ISSN: 2376-2136 (Print)
ISSN: 2376-2144 (Online)

Trends in Renewable Energy

Volume 6, Issue 2, June 2020

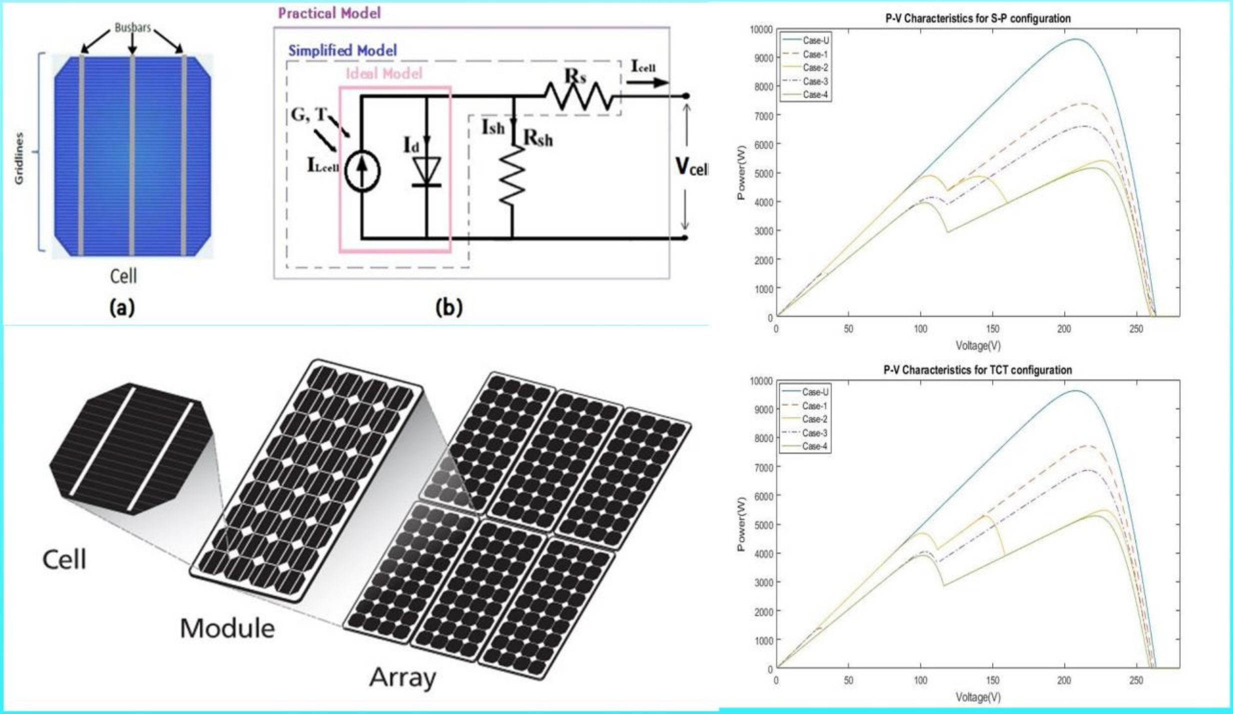

Cover image: Solar Photovoltaic Array Configurations with Partial Shaded Modules, see article by Raju and Chengaiah in this issue.

futureenergysp.com
thefutureenergy.org

Trends in Renewable Energy

ISSN: 2376-2136 (Print)   ISSN: 2376-2144 (Online)

http://futureenergysp.com/

Trends in Renewable Energy is an open accessed, peer-reviewed semi-annual journal publishing reviews and research papers in the field of renewable energy technology and science.

The aim of this journal is to provide a communication platform that is run exclusively by scientists working in the renewable energy field. Scope of the journal covers: Bioenergy, Biofuel, Biomass, Bioprocessing, Biorefinery, Biological waste treatment, Catalysis for energy generation, Energy conservation, Energy delivery, Energy resources, Energy storage, Energy transformation, Environmental impact, Feedstock utilization, Future energy development, Green chemistry, Green energy, Microbial products, Physico-chemical process for Biomass, Policy, Pollution, Renewable energy, Smart grid, Thermo-chemical processes for biomass, etc.

The Trends in Renewable Energy publishes the following article types: peer-reviewed reviews, mini-reviews, technical notes, short-form research papers, and original research papers.

The article processing charge (APC), also known as a publication fee, is fully waived for the Trends in Renewable Energy.

Editorial Team of Trends in Renewable Energy

EDITOR-IN-CHIEF

Dr. Bo Zhang	Prof., School of Chemical Engineering & Pharmacy, Wuhan Institute of Technology, China
Dr. Changyan Yang	Prof., School of Chemical Engineering & Pharmacy, Wuhan Institute of Technology, China

HONORARY CHAIRMEN

Dr. Yong Wang	Voiland Distinguished Professor, The Gene and Linda Voiland School of Chemical Engineering and Bioengineering, Washington State University, United States
Dr. Mahendra Singh Sodha	Professor, Lucknow University; Former Vice Chancellor of Devi Ahilya University, Lucknow University, and Barkatulla University; Professor/Dean/HOD/Deputy Director at IIT Delhi; Padma Shri Award; India
Dr. Elio Santacesaria	Professor of Industrial Chemistry, CEO of Eurochem Engineering srl, Italy

VICE CHAIRMEN

Dr. Mo Xian	Prof., Assistant Director, Qingdao Institute of BioEnergy and Bioprocess Technology, Chinese Academy of Sciences, China

EDITORS

Dr. Yiu Fai Tsang,	Associate Prof., Department of Science and Environmental Studies, The Education University of Hong Kong
Dr. Melanie Sattler	Dr. Syed Qasim Endowed Professor, Dept. of Civil Engineering, University of Texas at Arlington, United States
Dr. Attila Bai	Associate Prof., University of Debrecen, Hungary
Prof. Christophe Pierre Ménézo	University of Savoy Mont-Blanc, France
Dr. Moinuddin Sarker	MCIC, FICER, MInstP, MRSC, FARSS., VP of R & D, Head of Science/Technology Team, Natural State Research, Inc., United States
Dr. Suzana Yusup	Associate Prof., Biomass Processing Laboratory, Centre for Biofuel and Biochemical Research, Green Technology Mission Oriented Research, Universiti Teknologi PETRONAS, Malaysia
Dr. Zewei Miao	Global Technology Development, Monsanto Company, United States
Dr. Hui Wang	Pfizer Inc., United States
Dr. Shuangning Xiu	North Carolina Agricultural and Technical State University, United States
Dr. Junming XU	Associate Prof., Institute of Chemical Industry of Forest Products, China Academy of Forest, China
Dr. Hui Yang	Prof., College of Materials Science and Engineering, Nanjing Tech University, China
Dr. Ying Zhang	Associate Prof., School of Chemistry and Materials Science, University of Science and Technology of China, China
Dr. Ming-Jun Zhu	Prof., Assistant Dean, School of Bioscience & Bioengineering, South China University of Technology, China

EDITORIAL BOARD

Dr. Risahbh Dev Shukla	Dean and Associate Prof., Department of Electrical Engineering, Budge Budge Institute of Technology Kolkata, India
Dr. Neeraj Gupta	Indian Institute of Technology Roorkee, India
Dr. Elena Lucchi	Politecnico di Milano, Italy
Dr. Muhammad Mujtaba Asad	Faculty of Technical and Vocational Education, Universiti Tun Hussein Onn Malaysia, Malaysia
Dr. Afzal Sikander	Department of Instrumentation and Control Engineering, Dr. B. R.

	Ambedkar National Institute of Technology, India
Dr. Padmanabh Thakur	Professor and Head, Department of Electrical Engineering, Graphic Era University, India
Dr. K. DHAYALINI	Professor, Department of Electrical and Electronics Engineering, K. Ramakrishnan College of Engineering, Tamilnadu, India
Shangxian Xie	Texas A&M University, United States
Dr. Tanmoy Dutta	Sandia National Laboratories, United States
Dr. Efstathios Stefos	Pontifical Catholic University of Ecuador, Faculty of Exact and Natural Sciences, School of Physical Sciences and Mathematics, Ecuador
Dr. Xin Wang	Miami University, United States
Dr. Rami El-Emam	Assist. Prof., Faculty of Engineering, Mansoura University, Egypt
Dr. Rameshprabu Ramaraj	School of Renewable Energy, Maejo University, Thailand
Dr. ZAFER ÖMER ÖZDEMİR	Kirklareli University, Technology Faculty, Turkey
Dr. Vijay Yeul	Chandrapur Super Thermal Power Station, India
Dr. Mohanakrishna Gunda	VITO - Flemish Institute for Technological Research, Belgium
Dr. Shuai Tan	Georgia Institute of Technology, United States
Shahabaldin Rezania	Universiti Teknologi Malaysia (UTM), Malaysia
Dr. Madhu Sabnis	Contek Solutions LLC, Texas, United States
Dr. Qiangu Yan	Mississippi State University, United States
Dr. Mustafa Tolga BALTA	Associate Prof., Department of Mechanical Engineering, Faculty of Engineering, Aksaray University, Turkey
Dr. María González Alriols	Associate Prof., Chemical and Environmental Engineering Department, University of the Basque Country, Spain
Dr. Nattaporn Chaiyat	Assist. Prof., School of Renewable Energy, Maejo University, Thailand
Dr. Nguyen Duc Luong	Institute of Environmental Science and Engineering, National University of Civil Engineering, Vietnam
Mohd Lias Bin Kamal	Faculty of Applied Science, Universiti Teknologi MARA, Malaysia
Dr. N.L. Panwar	Assistant Prof., Department of Renewable Energy Engineering, College of Technology and Engineering, Maharana Pratap University of Agriculture and Technology, India
Dr. Caio Fortes	BASF, Brazil
Dr. Flavio Prattico	Department of Methods and Models for Economics, Territory and Finance, Sapienza University of Rome, Italy
Dr. Wennan ZHANG	Docent (Associate Prof.) and Senior Lecturer in Energy Engineering, Mid Sweden University, Sweden
Dr. Ing. Stamatis S. Kalligeros	Assistant Prof., Hellenic Naval Academy, Greece
Carlos Rolz	Director of the Biochemical Engineering Center, Research Institute at Universidad del Valle, Guatemala
Ms. Lilias Makashini	Copperbelt University, Zambia
Dr. Ali Mostafaeipour	Assistant Prof., Industrial Engineering Department, Yazd University, Iran
Dr. Camila da Silva	Prof., Maringá State University, Brazil
Dr. Anna Skorek-Osikowska	Silesian University of Technology, Poland
Dr. Shek Atiqure Rahman	Sustainable and Renewable Energy Engineering, College of Engineering, University of Sharjah, Bangladesh
Dr. Emad J Elnajjar	Associate Prof., Department of Mechanical Engineering, United Arab Emirates University, United Arab Emirates
Osamah Siddiqui	University of Ontario Institute of Technology, Canada
Dr. Rupendra Kumar Pachauri	Assistant Prof., Electrical and Electronics Engineering Department, University of Petroleum and Energy Studies, India
Dr. Jun Mei	School of Chemistry and Physics, Science and Engineering Faculty, Queensland University of Technology, Australia
Dr. Valeria Di Sarli	Institute for Research on Combustion, National Research Council of Italy, Italy
Dr. Utkucan Şahin	Assistant Prof., Department of Energy Systems Engineering, Faculty of Technology, Muğla Sıtkı Koçman University, Turkey
Dr. ALIASHIM ALBANI	School of Ocean Engineering, Universiti Malaysia Terengganu, Malaysia
Dr. Ashwini Kumar	Assistant Prof., College of Engineering, HSBPVT's Parikrama Group of Institutions, India
Dr. Hasan AYDOGAN	Associate Prof., Mechanical Engineering Department, Selcuk University, Turkey
Dr. Jiekang Wu	Professor, School of Automation, Guangdong University of Technology, China
Dr. Ong Huei Ruey	DRB-HICOM University of Automotive, Malaysia

Dr. Miguel Ángel Reyes Belmonte	IMDEA Energy Institute, Spain
Dr. Chitra Venugopal	Associate Professor in Electrical Engineering, University of Trinidad and Tobago, Trinidad
Dr. Amit Kumar Singh	Assistant Prof., Instrumentation & Control Engineering Department, Dr. B.R.A. National Institute of Technology, India
Dr. Suvanjan Bhattacharyya	University of Pretoria, South Africa
Dr. Karunesh Tiwari	Babu Banarasi Das University, India
Dr. Sharadrao A. Vhanalkar	Karmaveer Hire Arts, Science, Commerce and Education College, India
Dr. Prasenjit Chatterjee	Assistant Prof. and Head, MCKV Institute of Engineering, India
Dr. S. Balamurugan	Mindnotix Technologies, India
Dr. Mohammad Nurunnabi	University of Oxford, United Kingdom
Dr. Kenneth Okedu	Caledonian College of Engineering, Oman
Dr. Cheng Zhang	Sr. Materials Engineer, Medtronic, Inc., United States
Dr. Chandani Sharma	Assistant Prof., Department of Electrical Engineering, Graphic Era University, India
Dr. Kashif Irshad	Assistant Prof., Mechanical Engineering Department, King Khalid University, Saudi Arabia
Dr. Abhijit Bhagavatula	Principal Lead Engineer, Southern Company Services, United States
Dr. S. Sathish	Associate Prof., Department of Mechanical Engineering, Hindustan University, India
Mr. A. Avinash	Assistant Prof., KPR Institute of Engineering & Technology, India
Mr. Bindeshwar Singh	Assistant Prof., Kamla Nehru Institute of Technology, India
Dr. Yashar Hashemi	Tehran Regional Electric Company, Iran
Dr. Navanietha Krishnaraj R	South Dakota School of Mines and Technology, United States
Dr. SANDEEP GUPTA	JECRC University, India
Dr. Shwetank Avikal	Graphic Era Hill University, India
Dr. Xianglin Zhai	Poochon Scientific LLC, United States
Dr. Rui Li	Assistant Prof., College of Engineering, China Agricultural University, China
Dr. Adam Elhag Ahmed	National Nutrition Policy Chair, Department of Community Services, College of Applied Medical Sciences, King Saud University, Saudi Arabia
Dr. Jingbo Li	Massachusetts Institute of Technology, United States
Dr. Srikanth Mutnuri	Associate Prof., Department of Biological Sciences, Associate Dean for International Programmes and Collaboration, Birla Institute of Technology & Science, India
Dr. Bashar Malkawi	S.J.D., Associate Prof., College of Law, University of Sharjah, United Arab Emirates
Dr. Simona Silvia Merola	Istituto Motori - National Research Council of Naples, Italy
Dr. Hakan Caliskan	Faculty of Engineering, Department of Mechanical Engineering, Usak University, Turkey

Table of Contents

Volume 6, Issue No. 2, June 2020

Articles

Trends in Renewable Energy
OPEN ACCESS ISSN: 2376-2144
Peer-Reviewed Article futureenergysp.com/index.php/tre

Global Solar Radiation Characteristics at Calabar and Port Harcourt Cities in Nigeria

Solomon Okechukwu Amadi[a*], Timothy Dike[a], and Samuel Chukwujindu Nwokolo[b]

[a]*Dept of Physics, Geology & Geophysics, Alex Ekwueme Federal University, Ndufu-Alike, Nigeria*
[b]*Dept of Physics, Faculty of Physical Sciences, University of Calabar, Nigeria*

Received February 22, 2020; Accepted March 27, 2022; Published April 7, 2020

This study analyzed the inter-annual variability in solar radiation at Port Harcourt and Calabar, aiming at improving knowledge of solar resources. For the investigation, monthly mean global solar radiation data for fifteen years (2000 – 2014) was collected from Nigerian Meteorological Agency (NIMET), and the monthly mean extraterrestrial solar radiation was determined using globally recognized standard relation. The clearness index parameter was employed for characterizing the spatial variability of solar radiation for Calabar and Port Harcourt. The statistics of the monthly mean solar radiation deviations of Port Harcourt and Calabar was tested using the Kolmogorov–Smirnov method. The test results showed that they are normally distributed random variables. Furthermore, the analysis of sequential properties showed that the coefficients of the auto-correlation with lag 1 are significant for both stations. The auto-correlation coefficients with lag 1, though usually not significant, are negative for both stations. The auto regression lag 1 (AR-1) is the recommended procedure (model equation) for generating monthly solar radiation synthetic time series, with auto-correlation coefficients varying from 0.30 to 0.47 for both stations in the South-South of Nigeria.

Keywords: Global solar radiation; Clearness index; Extraterrestrial solar radiation; Calabar; Nigeria

1. Introduction

A wide range of solar energy applications, including modeling, design of solar crop dryers, and photovoltaic system sizing, requires a huge amount of knowledge of global solar radiation. The daily solar radiation intensity is normally among the variables collected by weather stations. The important role played by knowledge sharing in the subject of solar radiation and its subsequent exploitation has necessitated the need to develop ways of predicting the incident solar radiation in the interest of the regions of the globe like tropical Africa, where routine measurements are lacking in spite of the huge availability of solar energy in the region [1]. As the fossil fuel reserves suffer severe depletion, it becomes imperative that alternative energy resources should be explored and utilized with high conversion efficiency to help bridge the wide gap between energy supply and energy demand [2]. For sub-Saharan African countries such as Nigeria, the economic and efficient utilization of solar energy has become inevitable because of the abundance and reliability of solar energy resource. Augustine and Nnabuchi [3] estimated that Nigeria has approximately 3,000 hours of annual sunshine. Offiong [4] stated that the mean daily solar radiation received in Nigeria is up to 20MJ/m²/day. This, however,

**Corresponding author:* solomonokeamadi@gmail.com

Tr Ren Energy, 2020, Vol.6, No.2, 111-130. doi: 10.17737/tre.2020.6.2.00114

depends on the location and the time of the year. Despite this huge amount of solar energy, Nigeria with a rural population of over 97,000 inhabitants [5], still has her population suffering deprivation from conventional energy due to poor infrastructural facilities and subsequent unreliability in energy supply.

Solar energy is among the most important alternative energy resources with excellent potentials for utilization in both rural and urban communities. Having vast knowledge of the distribution of solar energy at a geographical location is significant for the creation and advancement of new solar energy devices with improved efficiency [6]. Data on solar radiation is a basic requirement for conducting feasibility studies with respect to solar energy systems. Augustine and Nnabuchi [3] opined that the knowledge of solar energy acquired over a long period ought to be applicable not only to the site where the radiation data was collected, but also to other locations with similar climates.

Nigeria is located between Latitude 4°N and 14°N. This vantage position enables the country to receive a vast amount of solar energy throughout the year. Solar radiation data can be accessed in a variety of forms depending on choice and application. Several scholars [1, 2, 4, 6] have emphasized the importance of solar radiation data in the design and operation of efficient solar energy devices which are anchored on accurate and detailed information of solar radiation climatology. The diurnal and seasonal patterns of both the hourly/daily clearness and the cloudiness indices were clearly shown in the datasets. Okogbue *et al* [7] investigated the optical sky conditions in some selected locations in the major ecological zones of Nigeria using monthly global solar irradiance data for an interval not less than 20 years. Many empirical studies on the portioning of solar irradiance have been presented for various regions of the world [8].

Solar irradiance is defined as the power per unit area (W/m^2) received from the sun in the form of electromagnetic radiation within the range of wavelength that the measuring instrument can detect. When the solar irradiance is integrated over time, it is referred to as solar irradiation, insolation, or solar exposure. Nevertheless, for practical purposes, it is apt to often use insolation and irradiance interchangeably. Irradiance may be measured on top of the atmosphere or at the earth's surface after atmospheric attenuation effects of absorption, reflection and scattering. Irradiance measured on top of the atmosphere depends on such factors as distance from the sun, the solar cycle, and changes in cross-cycle. In addition, irradiance on the earth's surface is affected by the tilt of the measuring surface, the solar altitude, and the conditions of the atmosphere. Solar radiation is radiant energy which the sun emits, essentially electromagnetic energy. Almost half of the radiation is contained in the visible wave band of the electromagnetic spectrum (www.sciencedaily.com/terms/solar_radiation htm). The other half mostly lies in the near-infrared band, while some lie in the ultraviolet region of the spectrum. The aim of the study is to characterize the global solar radiation at Port Harcourt and Calabar in South-South Nigeria using 15 years' data (2000–2014).

2. Study Area

Port Harcourt and Calabar have a tropical climate with wet and dry seasons. Two distinct wet seasons are observed: the more intense season is observed from April to July whereas a less intense one occurs from September to November. At the peak of the wet season, the meteorological condition at the stations is wet about half the time. Port Harcourt and Calabar experience a dry season (when rain falls less than two days in a month) in August, as well as from December to March. This second part of dry season is accompanied by Harmattan winds which originate from the Sahara Desert and have their peak from December to early February. Port Harcourt and Calabar have a fairly small temperature range, generally between 33°C and 21°C. The hottest month is March, when the mean diurnal temperatures reach about 29°C. July is the coldest month with a mean temperature of about 25°C [9]. The geographical information of the study area is presented in Table 1, while the map showing the distance between the locations under study (Port Harcourt and Calabar) is shown in Fig. 1.

Table 1. Meteorological stations

Station name	Latitude	Longitude	Elevation.
Calabar	4.71' N	8.55' E	62.3 m
Port Harcourt	4.40' N	7.17' E	19.55 m

3. Methodology

3.1 Data

The monthly mean daily ground - measured global solar radiation data used for this study (Port Harcourt and Calabar) was obtained from the Nigeria Meteorological Agency, Oshodi Lagos [10]. The data accessed covered a period of fifteen years (2000-2014) for Port Harcourt and Calabar. The monthly mean daily extraterrestrial solar radiation (H_O) is the solar radiation received by horizontal surface during a day at the top of the atmosphere, calculated using the procedure for monthly mean extraterrestrial solar radiation shown in Table 2 and expressed theoretically as:

$$H_O = \frac{24}{\pi} I_{SC}\left(1 + 0.033\cos\frac{360n}{365}\right) \times \left(\cos\phi\cos\delta\sin\omega_S + \frac{2\pi\omega_S}{360}\sin\phi\sin\delta\right) \quad (1)$$

The mean sunrise hour angle (ω_s) can be evaluated as:

$$\omega_s = \cos^{-1}\left[\tan\delta\tan\phi\right] \quad (2)$$

$$\delta = 23.45\sin\left[\frac{360(n+284)}{365}\right] \quad (3)$$

where ϕ represents the latitude, δ is the solar declination and n is the number of days of the year beginning from first January. I_{SC} is the solar constant and other symbols retain their meanings in the usual notation.

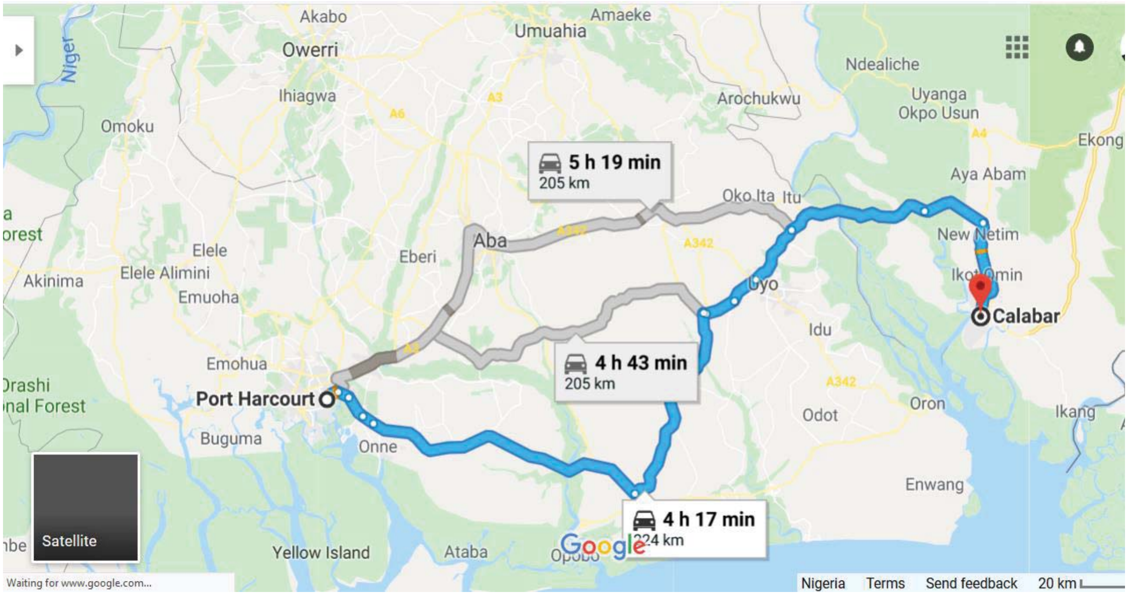

Fig. 1. Map showing distance between Port Harcourt and Calabar

Table 2. Representative day of each month for calculation of the monthly mean extraterrestrial solar radiation for Port Harcourt and Calabar [11]

Month	n for i^{th} day of the month	Representative day	n	δ
January	1	17	17	-20.9
February	i+31	16	47	-13.0
March	i+59	16	75	-2.4
April	i+90	15	105	9.4
May	i+120	15	135	18.8
June	i+151	11	162	23.1
July	i+181	17	198	21.2
August	i+212	16	228	13.5
September	i+243	15	258	2.2
October	i+273	15	288	-9.6
November	i+304	14	318	-18.9
December	i+334	10	344	-23.0

3.2 Data Analysis

In order to carry out the time series proposed for this study, astronomical trends were eliminated by dividing global solar radiation (H) by the extraterrestrial solar radiation (H_o). Trends removal in the global solar radiation was executed by subtracting the mean of the clearness index from the long-term monthly mean values of clearness indices for Port Harcourt and Calabar. Thus, the seasonal trend removal of solar radiation was evaluated using the following expressions.

$$kt' = kt - \langle kt \rangle \qquad (4)$$

Where kt' = deviations of monthly average of the daily clearness index; $\langle kt \rangle$ = grand average of kt , and kt = clearness index (*i.e.*, H/H_o). The Kolmogorov–Smirnov normality and total auto-correlation functions tests were equally used to determine the deviation and interannual variability of solar radiation at Port Harcourt and Calabar.

4. Results and Discussion

4.1 Results

The descriptive statistics of measured global solar radiation, calculated extraterrestrial solar radiation, and evaluated clearness indices for Port Harcourt and Calabar are shown in Tables 3 – 5. Figures 2 and 3 present inter-monthly deviations of clearness indices for Port Harcourt and Calabar. In Figures 4 – 16, the series of annual and monthly anomalies of clearness indices for Port Harcourt and Calabar are shown. Tables 6 and 7 together with Figures 17 and 18 present the total auto-correlation functions in deviation of km - <km> for Port Harcourt and Calabar. Figures 19 and 20 show the condition of normality of clearness index deviation for Calabar and Port Harcourt.

Table 3. Descriptive statistics of monthly mean daily global solar radiation (MJm^{-2}day^{-1}) for Port Harcourt and Calabar

	N	Range	Minimum	Maximum	Sum	Mean		Std. Deviation
	Statistic	Statistic	Statistic	Statistic	Statistic	Statistic	Std. Error	Statistic
Port Harcourt	12	5.16	12.87	18.03	185.88	15.4900	.44056	1.52616
Calabar	12	5.17	12.60	17.77	187.69	15.6408	.47382	1.64134
Valid N (listwise)	12							

Table 4. Descriptive Statistics of monthly mean daily extraterrestrial solar radiation (MJm^{-2}day^{-1}) for Port Harcourt and Calabar

	N	Range	Minimum	Maximum	Sum	Mean		Std. Deviation
	Statistic	Statistic	Statistic	Statistic	Statistic	Statistic	Std. Error	Statistic
Calabar	12	3.85	33.78	37.64	431.74	35.9784	.34991	1.21213
Port Harcourt	12	3.87	33.78	37.65	431.85	35.9878	.35078	1.21514
Valid N (listwise)	12							

Table 5. Descriptive Statistics of monthly mean daily clearness index for Port Harcourt and Calabar

	N	Range	Minimum	Maximum	Sum	Mean		Std. Deviation
	Statistic	Statistic	Statistic	Statistic	Statistic	Statistic	Std. Error	Statistic
Port Harcourt	12	.1635	.3541	.5176	5.1731	.431088	.0137923	.0477779
Calabar	12	.1656	.3444	.5100	5.2250	.435419	.0145954	.0505600
Valid N (listwise)	12							

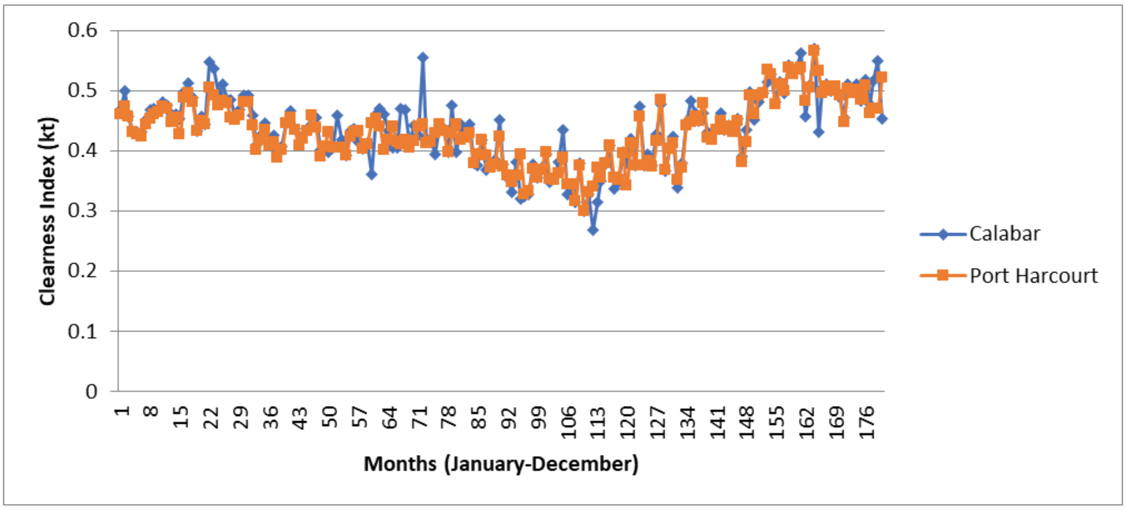

Fig. 2. Monthly mean daily clearness index (kt) deviation series for Port Harcourt and Calabar for January – December for fifteen years.

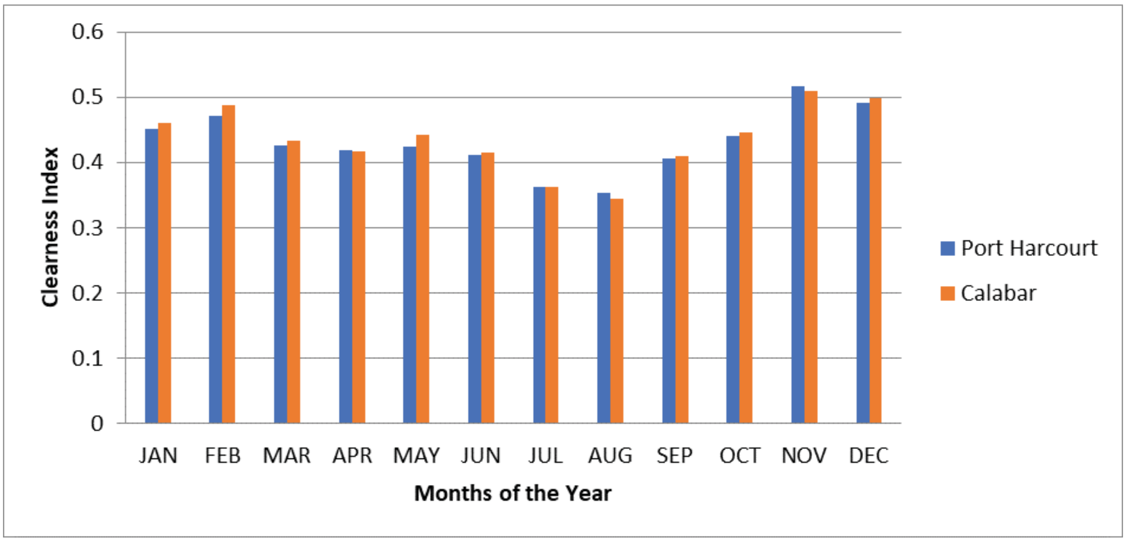

Fig. 3. Monthly mean daily clearness index deviation series for Port Harcourt and Calabar

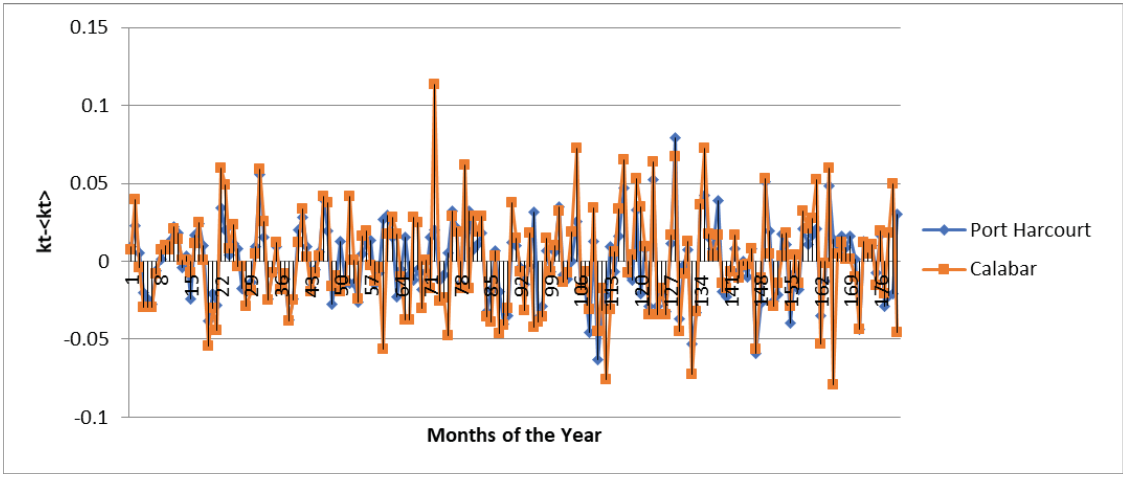

Fig. 4. Solar Radiation deviation series for Port Harcourt and Calabar for January – December for fifteen years. Kt =Annual monthly daily clearness index, <kt> = average of kt

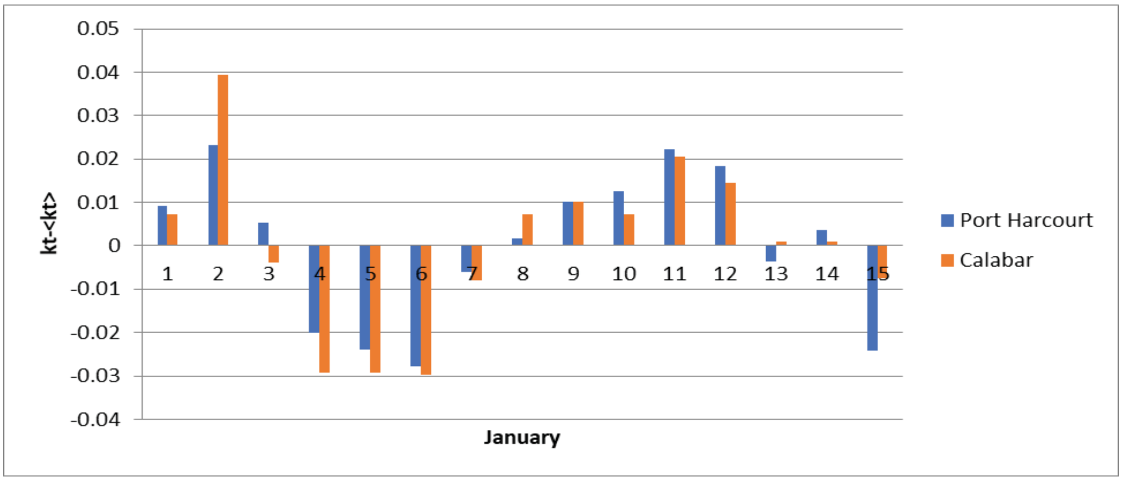

Fig. 5. Solar Radiation deviation series for Port Harcourt and Calabar for January for fifteen years. Kt = monthly mean daily clearness index, <kt> = mean of kt

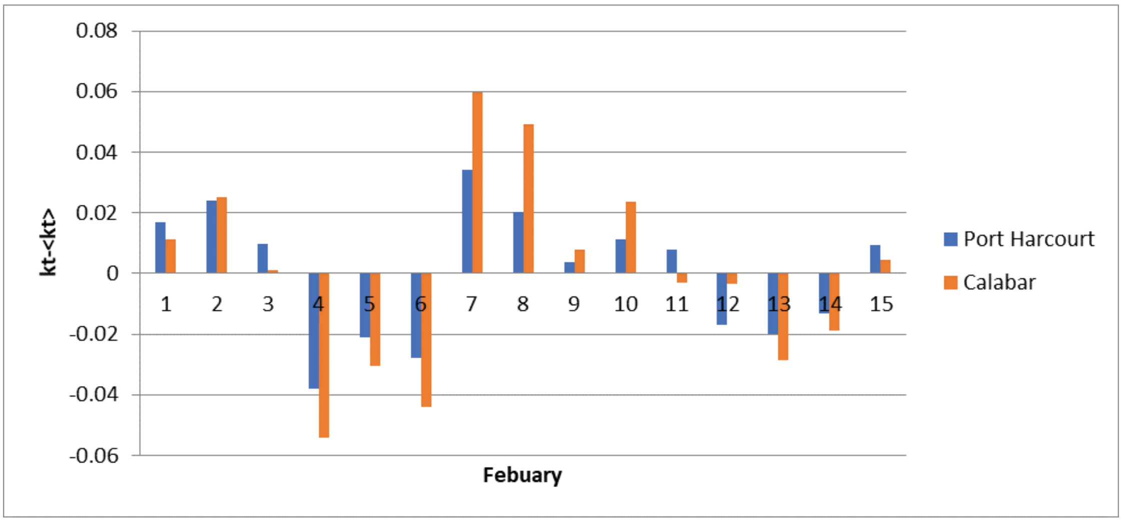

Fig. 6. Solar Radiation deviation series for Port Harcourt and Calabar for February for fifteen years. Kt = monthly mean daily clearness index, <kt> = mean of kt

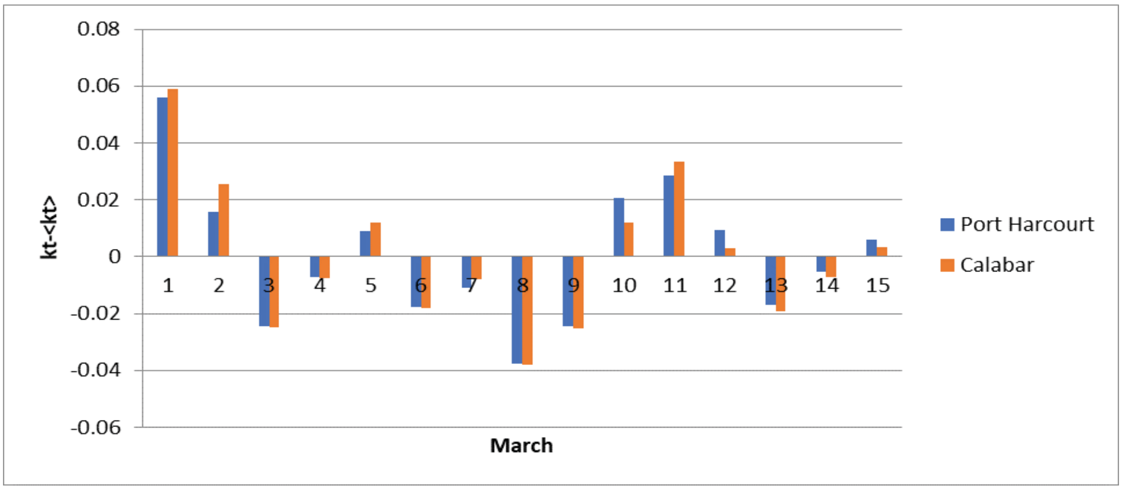

Fig. 7. Solar Radiation deviation series for Port Harcourt and Calabar for March for fifteen years. Kt = monthly mean daily clearness index, <kt> = mean of kt

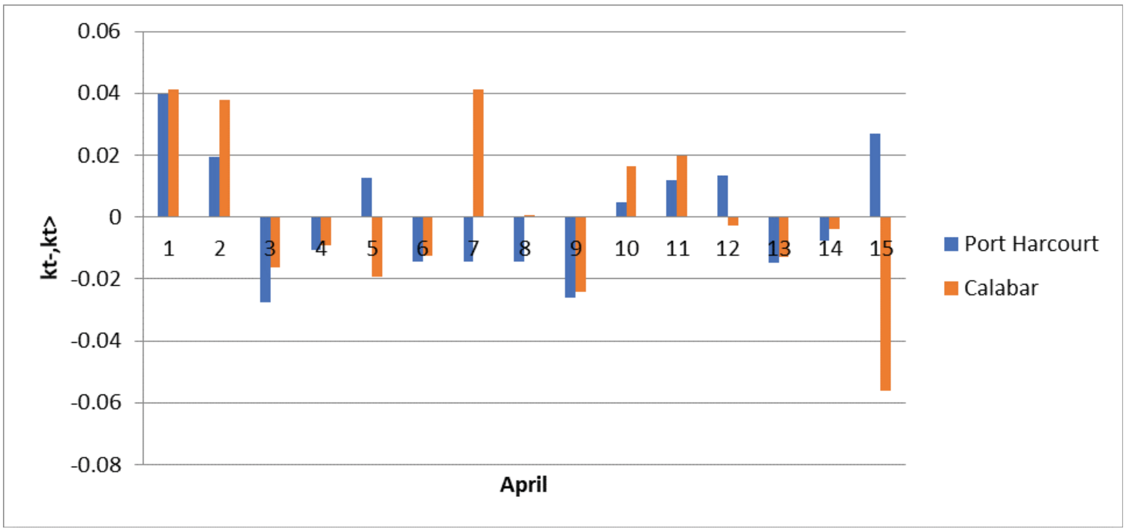

Fig. 8. Solar Radiation deviation series for Port Harcourt and Calabar for April for fifteen years. Kt = monthly mean daily clearness index, <kt> = mean of kt

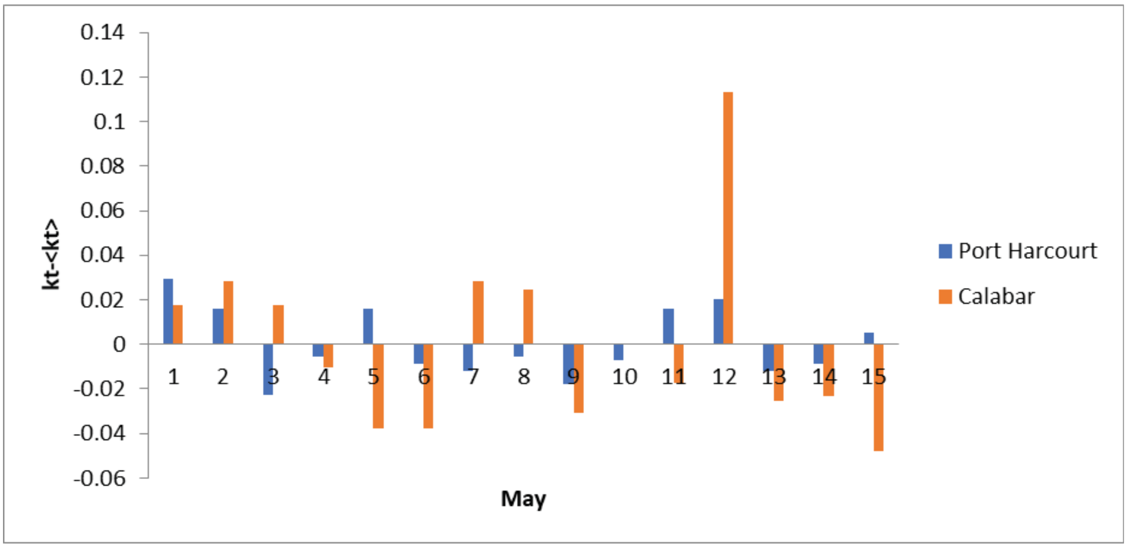

Fig. 9. Solar Radiation deviation series for Port Harcourt and Calabar for May for fifteen years. Kt = monthly mean daily clearness index, <kt> = mean of kt

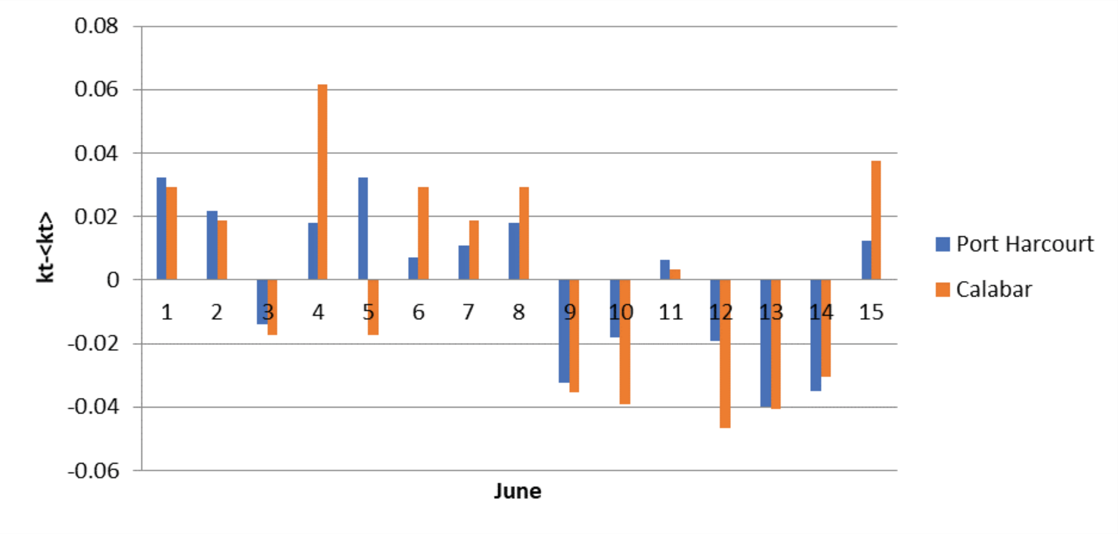

Fig. 10. Solar Radiation deviation series for Port Harcourt and Calabar for June for fifteen years. Kt = monthly mean daily clearness index, <kt> = mean of kt

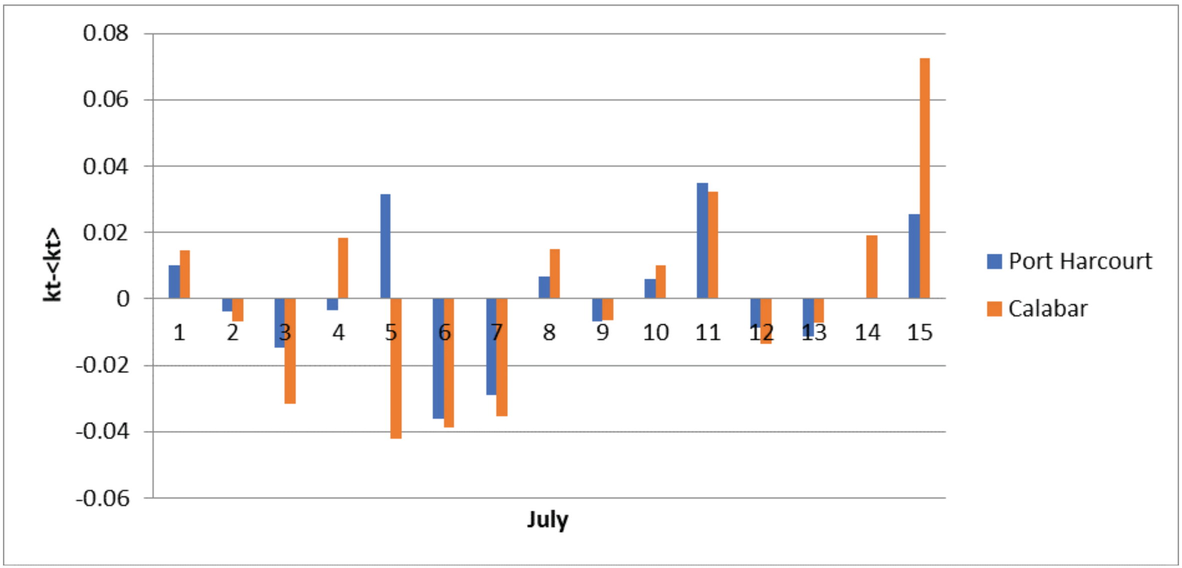

Fig. 11. Solar Radiation deviation series for Port Harcourt and Calabar for July for fifteen years. Kt = monthly mean daily clearness index, <kt> = mean of kt

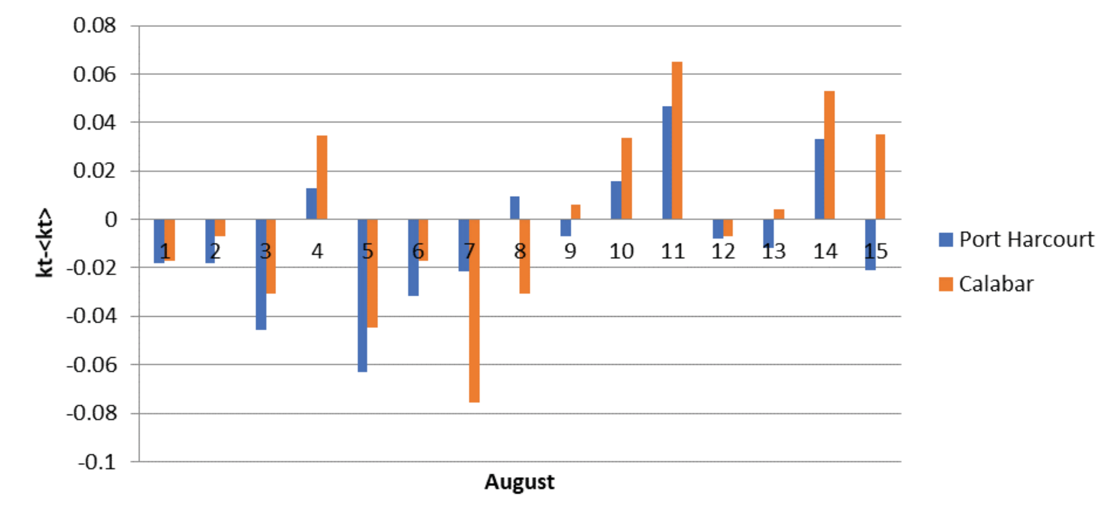

Fig. 12. Solar Radiation deviation series for Port Harcourt and Calabar for August for fifteen years. Kt = monthly mean daily clearness index, <kt> = mean of kt

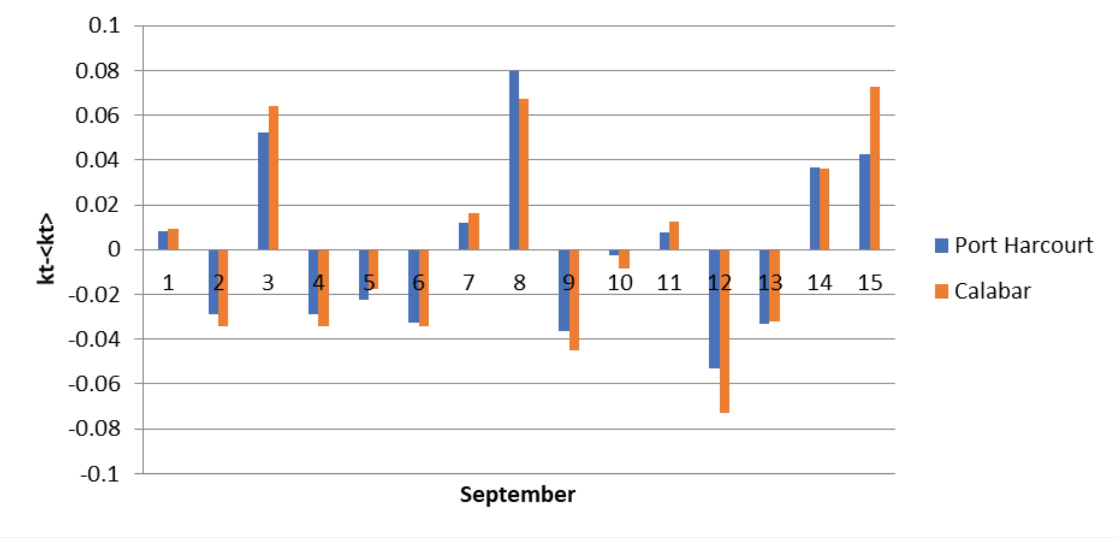

Fig. 13. Solar Radiation deviation series for Port Harcourt and Calabar for September for fifteen years.
Kt = monthly mean daily clearness index, <kt> = mean of kt

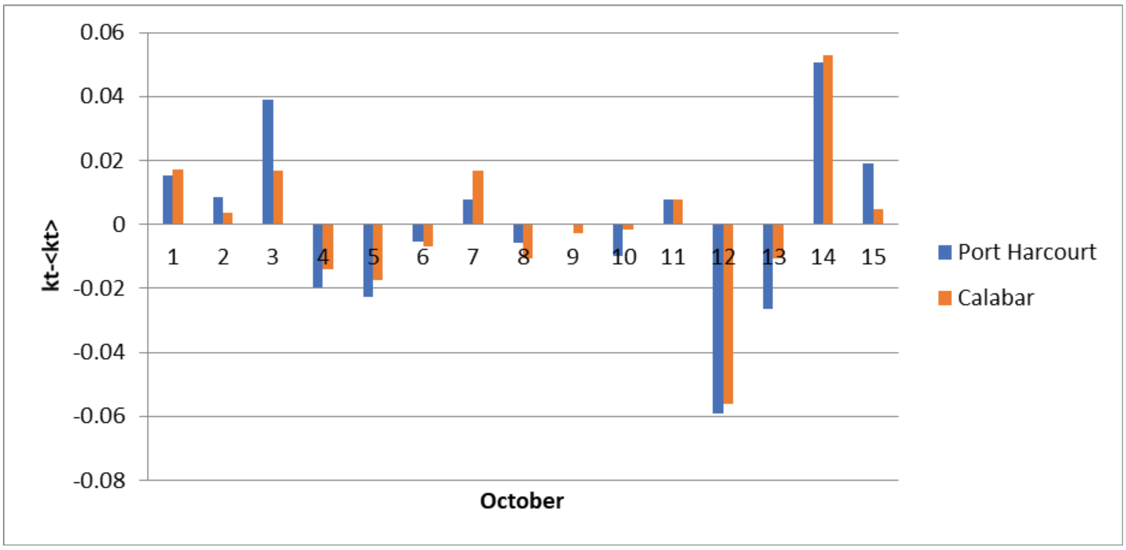

Fig. 14. Solar Radiation deviation series for Port Harcourt and Calabar for October for fifteen years.
Kt = monthly mean daily clearness index, <kt> = mean of kt

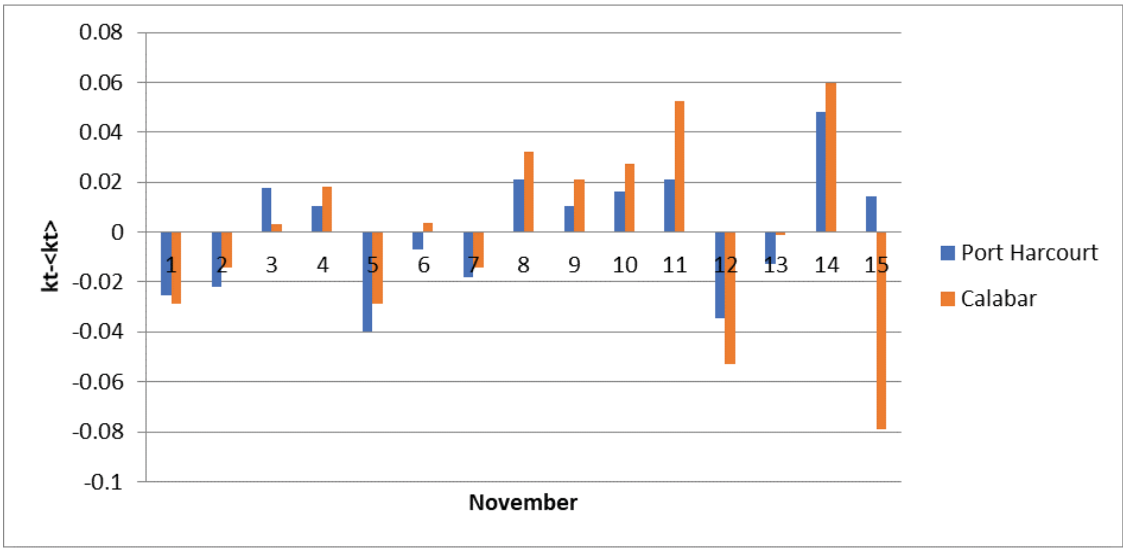

Fig. 15. Solar Radiation deviation series for Port Harcourt and Calabar for November for fifteen years.
Kt = monthly mean daily clearness index, <kt> = mean of kt

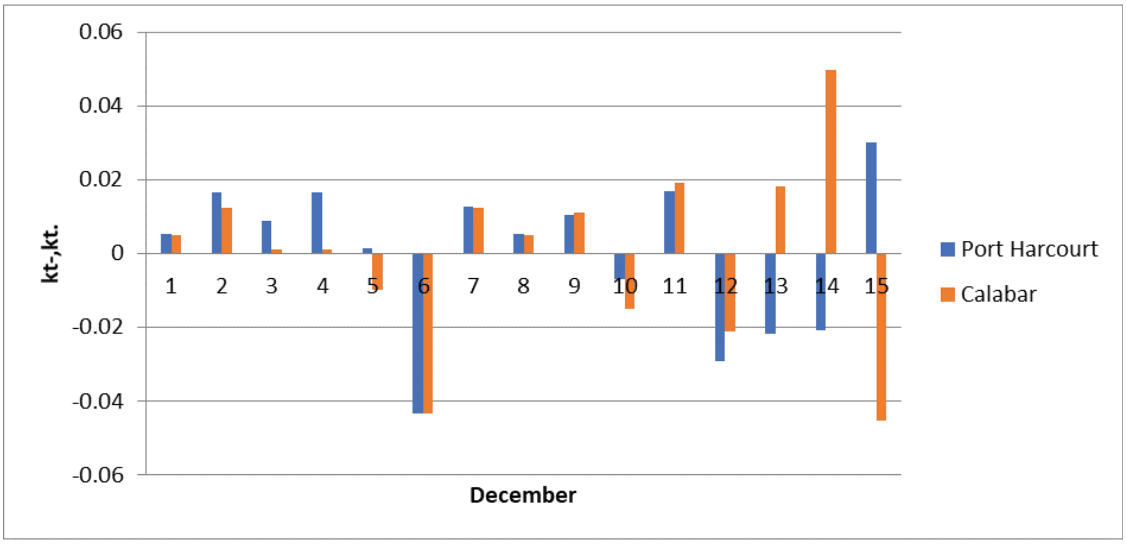

Fig. 16. Solar Radiation deviation series for Port Harcourt and Calabar for December for fifteen years.
Kt = monthly mean daily clearness index, <kt> = mean of kt

Table 6. Total auto-correlation function in deviation series of km - <km> for Port Harcourt

Lag	Autocorrelation	Std. Error[a]	Box-Ljung Statistic		
			Value	df	Sig.[b]
1	.108	.074	2.144	1	.143
2	-.216	.074	10.722	2	.005
3	-.106	.074	12.802	3	.005
4	.063	.073	13.537	4	.009
5	-.057	.073	14.135	5	.015
6	-.094	.073	15.794	6	.015
7	-.003	.073	15.796	7	.027
8	-.002	.072	15.796	8	.045
9	-.088	.072	17.269	9	.045
10	.006	.072	17.275	10	.068
11	.004	.072	17.278	11	.100
12	-.065	.072	18.094	12	.113
13	-.275	.071	32.933	13	.002
14	.154	.071	37.620	14	.001
15	.392	.071	68.054	15	.000
16	-.011	.071	68.077	16	.000

a. The underlying process assumed is independence (white noise).

b. Based on the asymptotic chi-square approximation.

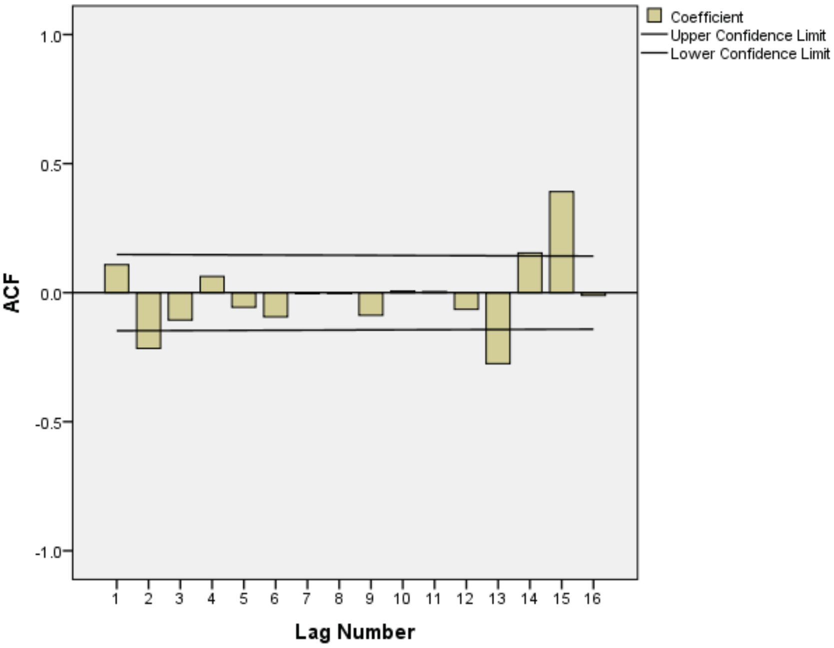

Fig. 17. Total auto-correlation function in deviation series of km - <km> for Port Harcourt

Table 7. Total auto-correlation function in deviation series of km - <km> for Calabar

Lag	Autocorrelation	Std. Error[a]	Box-Ljung Statistic		
			Value	df	Sig.[b]
1	.031	.074	.171	1	.679
2	-.149	.074	4.281	2	.118
3	-.135	.074	7.650	3	.054
4	-.013	.073	7.680	4	.104
5	-.014	.073	7.716	5	.173
6	-.115	.073	10.226	6	.115
7	-.015	.073	10.268	7	.174
8	-.078	.072	11.440	8	.178
9	.030	.072	11.611	9	.236
10	.019	.072	11.678	10	.307
11	.050	.072	12.158	11	.352
12	-.075	.072	13.256	12	.351
13	-.197	.071	20.874	13	.075
14	.070	.071	21.843	14	.082
15	.298	.071	39.448	15	.001
16	-.108	.071	41.764	16	.000

a. The underlying process assumed is independent (white noise).

b. Based on the asymptotic chi-square approximation.

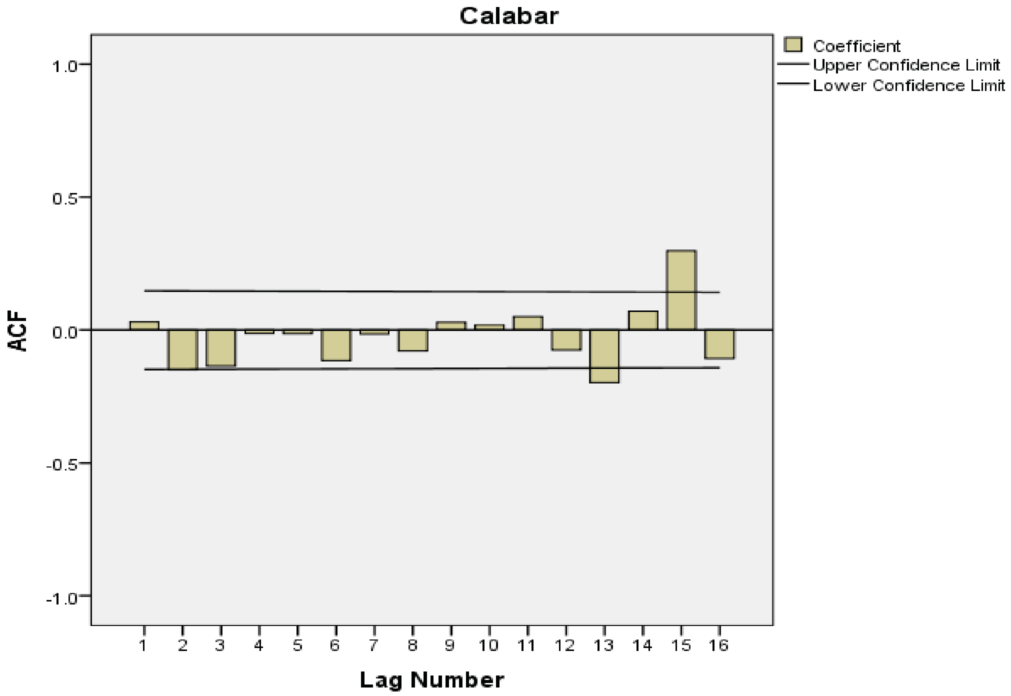

Fig. 18. Total auto-correlation function in deviation series of km - <km> for Calabar

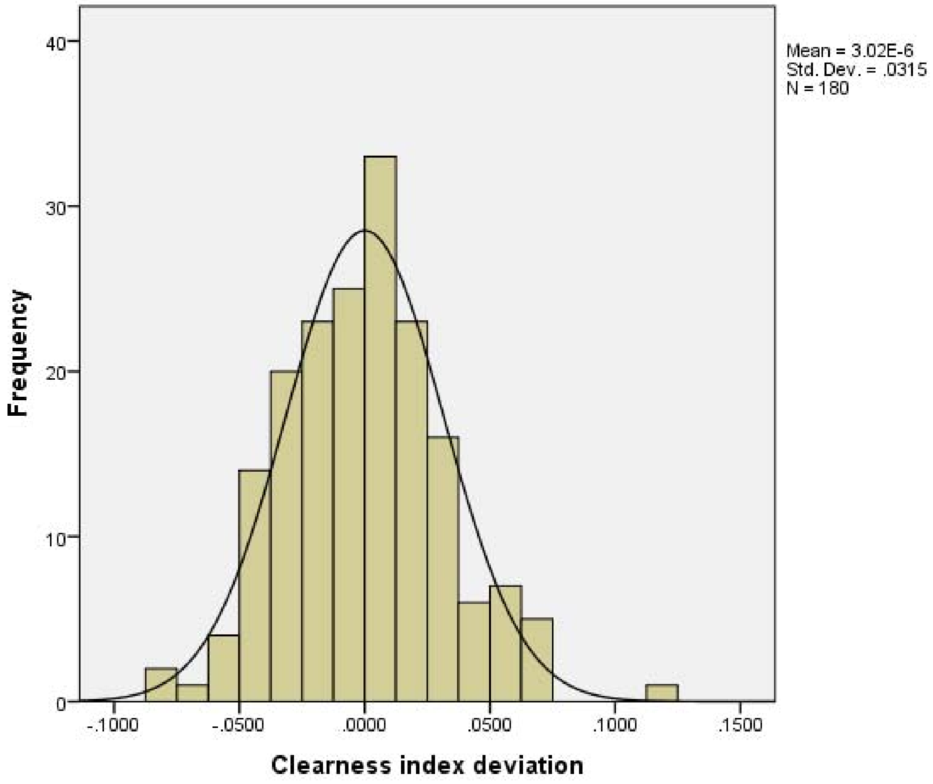

Fig. 19. Normality condition (Gaussian distribution) for clearness index deviation for Calabar

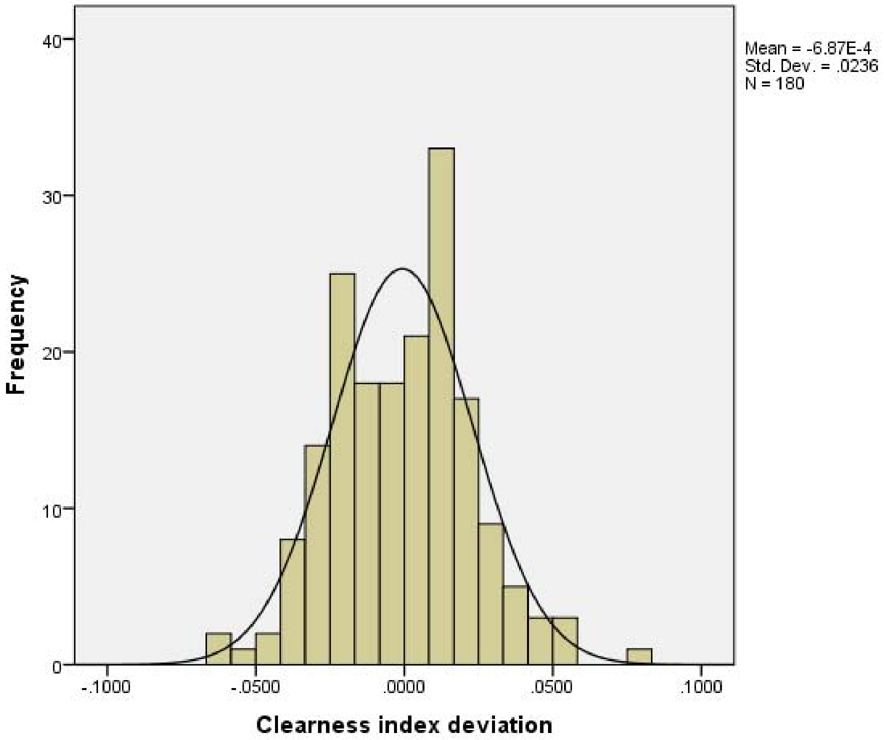

Fig. 20. Normality condition (Gaussian distribution) for clearness index deviation for Port Harcourt

4.2 Discussion

A close examination of Tables 3 and 4 shows that the maximum values of the monthly mean daily global solar radiation on a horizontal surface and the monthly mean daily extraterrestrial solar radiation for Port Harcourt are 18.03 $MJm^{-2}day^{-1}$ and 37.65 $MJm^{-2}day^{-1}$, respectively, whereas 17.77 $MJm^{-2}day^{-1}$ and 37.64 $MJm^{-2}day^{-1}$ were registered for Calabar, respectively. High values of monthly mean daily global solar radiation for the two cities were observed in the dry season months of November to April with peaks in November and February. There is a drop in December and January values of global solar radiation in the two cities, because of the Harmattan that reaches its peak from December to January. The months of occurrence is expected because high values of global solar radiation obtained during the dry season at the study location can be attributed to many contributory factors. The fact that the earth is closest to the sun in early January (The perihelion) than any other time is one significant factor. This observation is also attributed to the prevalence of low smog, low relative humidity, low cloud cover, low reflection, scattering and absorption by clouds together with low absorption of diffuse solar radiation and near infrared component of the solar spectrum during the November – February months. This period is markedly dry at these locations. Combination of all these factors enhances the global solar radiation and clearness index received at these locations. Furthermore, Harmattan is not usually severe in these areas compared to other cities further inland. Therefore, the aerosol mass loading that characterizes the Harmattan season (majorly months of November to February in Nigeria) is not seriously pronounced in these cities, thereby increasing greatly the intensity of daily global solar radiation on a flat surface within the months of November to February. Nevertheless, Harmattan reaches its peak from December to January in these cities, causing a drop in monthly average daily global solar radiation from December to January. The Harmattan season is usually connected with the prevalence of thick dust haze and early morning fog and mist resulted from the radiation cooling in the night under clear skies. This result is in agreement with Amadi *et al* [12], which observed that Calabar and Port Harcourt experience the highest number of sunshine hours in the November to February months. These results are also in consonance with the literature [13,14]. These trends are similar to the reports of several research in the region which lies within tropical rainforest zone of Nigeria [15-21].

It can be observed from Table 3 that the maximum global solar radiation received at Port Harcourt (18.03 $MJm^{-2}day^{-1}$) and Calabar (17.77 $MJm^{-2}day^{-1}$) are at par with each other. Similar observation also goes for the minimum values of global solar radiation received at the two cities (12.87 $MJm^{2}day^{-1}$ and 12.60 $MJm^{2}day^{-1}$) for Port Harcourt and Calabar, respectively. However, while the minimum was observed at Port Harcourt in July, it was observed at Calabar in August. A cursory look at Table 4 shows that the values of the maximum and minimum monthly mean daily global solar radiation received at Port Harcourt (37.65 $MJm^{2}day^{-1}$ and 33.78 $MJm^{2}day^{-1}$) and Calabar (37.64 $MJm^{2}day^{-1}$ and 33.78 $MJm^{2}day^{-1}$) are at par. Perhaps, the attenuation effects of aerosols, water vapour and low-level clouds on direct normal irradiance [22, 23] share some similar features in the two cities, since they are both coastal cities. Being coastal cities, they are highly affected by water drops aerosols, high load of sea salts and water vapour loads. The two cities are both administrative and commercialized with associated high load of atmospheric aerosols. Perhaps this explains why the clearness index variations and solar radiation deviation series in Figs 2, 3 and 4 follow the same pattern. However, Port Harcourt has more manufacturing concerns and is more industrialized. The city and its suburbs play host to many up-stream, middle-stream and down-stream oil industry activities being the hub of oil industry activities in Nigeria. The subsequent release of environmental pollutants such as greenhouse gases and aerosols (notably soot aerosols) would induce changes which determine to a great extent the degree of inter-annual variability of solar radiation and its components in the city. The result of higher attenuation effect of aerosols on solar radiation in Port Harcourt is vividly captured in Fig 3, where the monthly mean clearness indices of Calabar for the 15 years period is always higher than that of Port Harcourt, except for the months of July, August and November. This observation in Port Harcourt clearness index in July, August and November could be attributed to the indirect effects of aerosols on clouds and precipitation. Large aerosol particles are efficiently removed by the washout mechanism which occurs when such aerosols are cloud condensation nuclei. The cloud droplets that form on such aerosol particles return them to the earth's surface which is their main atmospheric sink. This scavenging of the atmospheric aerosols increases the atmospheric transparency in the peak of rainy season in July and August in the area. The semi-direct effect of aerosol has to do with aerosols of soot origin (particulate black carbon) which absorb solar radiation and re-radiate it as thermal radiation inside cloud layers. This consequently heats the air mass and evaporates cloud droplets [24]. This perhaps causes higher transmissivity of the Port Harcourt atmosphere than that of Calabar in November when the rains cease.

It also necessary to state that the degree of surrounding ecological factors such as tree canopies, forest, green fields and vegetation equally converts the direct component of global solar radiation into photosynthetically active radiation needed by plants and crops for manufacturing food in the areas [25-27]. Thus, these factors are equally fundamental parameters that modify the global solar radiation and inter-annual variability of monthly mean global solar radiation and clearness index deviations in Port Harcourt and Calabar irrespective of the fact that the extraterrestrial solar radiation, elevation and latitude of Calabar and Port Harcourt are similar, with both cities sharing the same eco-climatic zone. These deviations are shown in Figures 2 – 16.

The minimum values of extraterrestrial solar radiation (33.78 $MJm^{-2}day^{-1}$ and 33.78 $MJm^{-2}day^{-1}$) and global solar radiation (12.87 $MJm^{-2}day^{-1}$ and 12.60 $MJm^{-2}day^{-1}$) obtained during the rainy season in the months of July and August respectively for Port Harcourt and Calabar is equally expected for a tropical site [14]. The months in which they occur are also expected, because the atmosphere in those months is characterized by higher cloud cover, high relative humidity and associated scattering and absorption of direct and diffuse radiation in the solar wave band, thereby producing low amount of global solar radiation intercepted at the site. These trends align with the reports of many solar energy researchers in the region which is the tropical rainforest ecological zone of Nigeria [15-21].

The average of the monthly clearness index describes the percentage depletion of the incident global solar radiation by the sky, and therefore displays both the amount of available solar radiation and variations in the condition of the atmosphere at a particular locality. The prevailing clearness index variation is within the range of 0.35 – 0.45 for Port Harcourt and 0.34 – 0.46 for Calabar within the April to October months in the wet season; 0.43 - 0.52 for Port Harcourt and 0.44 – 0.51 for Calabar within the November to March months in the dry season, with an annual value of 0.43 for Port Harcourt and 0.44 for Calabar. The clearness index statistics is displayed in Table 5. These values are similar to some other reports in the same region of tropical rainforest eco-climatic zone of Nigeria [15-21].

Using the weather classification suggested by Iqbal [28] which are: (1) heavily overcast weather ($kt \leq 0.4$); (2) partly overcast weather ($0.4 \leq kt \leq 0.6$); and (3) clear weather ($kt \geq 7$), Port Harcourt and Calabar fall within the combination of heavily overcast weather and partly overcast weather. However, on the average, the cities have partly overcast weather. During the November to April months, the weather condition is clearly partly overcast. It was observed that global solar radiation varies directly with the clearness index and it increases very quickly as the heavily overcast sky becomes clearer. This is a demonstration that the clearness index has optimal control over global solar radiation at Port Harcourt and Calabar, Nigeria.

In Tables 6 and 7 and Figures 17 – 18, the illustrations of total auto-correlation functions for Port Harcourt and Calabar are displayed. The total auto-correlation shows vividly the seasonality of the coefficients; although showing some seasonality, it is much smaller. Where the auto-correlation coefficient with a given lag is situated externally in relation to the vertical lines, it can be confirmed, up to the 95% confidence level, that it is different from zero.

The solar radiation deviations analysis tested using the Kolmogorov–Smirnov method indicates that they are normally distributed random variables. Figures 19 – 20 show that for Port Harcourt and Calabar, the monthly mean solar radiation deviations are normally distributed. Furthermore, the analysis of sequential properties reveals that the autocorrelation coefficients with lag 1 are significant for Port Harcourt. In Calabar, the correlation of monthly values does not show any clear regional configuration; so it is pertinent to remark that in these cases, Calabar is related to Port Harcourt. Generally, the auto-correlation coefficients with lag 1, though they are not significant, are negative for almost all the Port Harcourt and Calabar. These trends are consistent with the reports of many solar energy researchers in Brazil [29-32].

CONCLUSIONS

In this study, the characteristics of inter-annual variability of solar radiation were analyzed for Port Harcourt and Calabar. To do this, fifteen years (2000 – 2014) monthly mean global solar radiation were collected from NIMET while the monthly mean extraterrestrial solar radiation were calculated from standard relation recognized globally. Clearness index parameter was employed for characterizing the spatial variability of solar radiation for Port Harcourt and Calabar. From the results, Calabar and Port Harcourt received similar amounts of solar radiation. However, the stations recorded different degrees of inter-annual variability over the fifteen years period. The result revealed that solar radiation at Calabar deviates more than that of Port Harcourt as a result of anthropogenic, environmental, geographical and ecological influence on the transmissivity and optical properties of the atmosphere. The statistics for the monthly average solar radiation deviations for Port Harcourt and Calabar were tested using the Kolmogorov–Smirnov method. The test results portray them as normally distributed random variables.

CONFLICTS OF INTEREST

The authors declare that there is no conflict of interests regarding the publication of this paper

REFERENCES

[1] Okogbue, E. C. and Adedokun, J. A. (2002). On the estimation of solar radiation in Ondo. *Nigerian Journal of Physics*, 14, 97-99.

[2] Aklaque, A. M., Firoz, A. and Wasim, M. A. (2009). Estimation of global and diffuse solar radiation for Hyderabad, Sindh, Pakistan. *Journal of Basic and Applied Science*, 5(2), 73-77.

[3] Augustine, C. and Nnabuchi, M. N. (2010). Analysis of some meteorological data for some selected cities in the eastern and southern zones of Nigeria. *African Journal of Environmental Science and Technology*, 4(2), 92-99.

[4] Offiong, A. (2003). Assessing the economic and environmental prospects of stand-by solar powered systems. *Nigeria. J. Applied Sci. and Env. Management*, 7(1), 37-42.

[5] Oti, M. I. (1995). Design, manufacture and installation of multi-bladed wind mill. *NJSE*, 13, 110-117.

[6] Chegaar, M. and Chibani, A. (2000). A simple method for computing global solar radiation. *Rev. Energ. Ren. Chem*, 111-115.

[7] Okogbue, E. C., Adedokun, J. A. and Holmgren, B. (2009). Hourly and daily clearness index and diffuse fraction at a tropical station, Ile-Ife, Nigeria. *Int. J. Climatol.* 29(8), 1035-1047.

[8] Udo, S. O. and Aro, T. O. (2000). New empirical relationships for determining global PAR from measurements of global solar radiation, infrared radiation or sunshine duration. *Int. J. Climatol.*, 20, 1265-1274.

[9] Nwokolo, S.C. and Ogbulezie, J. C. (2017). A comprehensive review of empirical models for estimating global solar radiation in Africa. *Renewable and Sustainable Energy Reviews*, 78, 955-995. DOI: https://doi.org/10.1016/j.rser.2017.04.101

[10] Nigeria Meteorological Agency (NiMet) *http://www.nimet.gov.ng/*.

[11] Klein, S. A. (1977). Calculation of monthly average insolation on tilted surfaces. *Solar Energy*, 19(4), 325-329. DOI: https://doi.org/10.1016/0038-092X(77)90001-9

[12] Amadi, S. O., Udo, S. O., and Ewona, I. O. (2014). The spatial and temporal variability of sunshine hours in Nigeria (1961–2012). *IOSR J. Appl. Phys*, 6(6), 1-10. DOI: 10.9790/4861-06630110

[13] Babatunde, E. B. (2001). Solar radiation modeling for a tropical station, llorin, Nigeria. Ph.D. Thesis

[14] Babatunde, E. B., and Aro, T. O. (2001). Characteristic variations of global (total) solar radiation at Ilorin, Nigeria. *Nigeria Journal Solar Energy*, 9, 157 - 173.

[15] Maduekwe, A. A. L., and Chendo, M. A. C. (1995). Predicting the components of the total hemispherical solar radiation from sunshine duration measurements in Lagos, Nigeria. *Renewable Energy*, 6(7), 807-812. DOI: https://doi.org/10.1016/0960-1481(95)91008-2

[16] Fagbenle, R. O. (1993). Total solar radiation estimates in Nigeria using a maximum-likelihood quadratic fit. *Renewable Energy*, 3(6), 813-817. DOI: https://doi.org/10.1016/0960-1481(93)90089-Y

[17] Falayi, E., Adepitan, J., and Rabiu, A. (2008). Empirical models for the correlation of global solar radiation with meteorological data for Iseyin, Nigeria. *International journal of physical sciences*, 3(9), 210-216.

[18] Adaramola, M. S. (2012). Estimating global solar radiation using common meteorological data in Akure, Nigeria. *Renewable Energy*, 47, 38-44. DOI: https://doi.org/10.1016/j.renene.2012.04.005

[19] Ohunakin, O. S., Adaramola, M. S., Oyewola, O. M., and Fagbenle, R. O. (2013). Correlations for estimating solar radiation using sunshine hours and temperature measurement in Osogbo, Osun State, Nigeria. *Frontiers in Energy*, 7(2), 214-222. DOI: 10.1007/s11708-013-0241-2

[20] Okundamiya, M. S., Emagbetere, J. O., and Ogujor, E. A. (2016). Evaluation of various global solar radiation models for Nigeria. *International Journal of Green Energy*, 13(5), 505-512. DOI: 10.1080/15435075.2014.968921

[21] Ayodele, T. R., and Ogunjuyigbe, A. S. O. (2016). Performance assessment of empirical models for prediction of daily and monthly average global solar radiation: the case study of Ibadan, Nigeria. *International Journal of Ambient Energy*, 38(8), 803-813. DOI: 10.1080/01430750.2016.1222961

[22] Cornejo, L., Martín-Pomares, L., Alarcon, D., Blanco, J., and Polo, J. (2018). A through analysis of solar irradiation measurements in the region of Arica Parinacota, Chile. *Renewable Energy*, 112, 197-208. DOI: https://doi.org/10.1016/j.renene.2017.04.012

[23] Polo, J., and Estalayo, G. (2015). Impact of atmospheric aerosol loads on Concentrating Solar Power production in arid-desert sites. *Solar Energy*, 115, 621-631. DOI: https://doi.org/10.1016/j.solener.2015.03.031

[24] Ramanathan, V., Crutzen, P. J., Kiehl, J. T. and Rosenfeld, D. (2001). Aerosols, climate and the hydrological cycle. *Science*, 294, 2119-2124.

[25] Spitters, C. J., and Musabilha, V. M. M. (1986). The Conservative Ratio of Photosynthetically Active to Total Radiation in the Tropics. *Journal of Applied Ecology*, 19(3), 853-858. DOI: 10.2307/2403287

[26] Black, J. N. (1954). The distribution of solar radiation over the Earth's surface. *Archiv für Meteorologie, Geophysik und Bioklimatologie, Serie B*, 7(2), 165-189. DOI: 10.1007/BF02243320

[27] Cartledge, O. (1973). Solar Radiation Climate in a Subtropical Region. *Nature Physical Science*, 242(114), 11-12. DOI: 10.1038/physci242011a0

[28] Iqbal, M. (1980). Prediction of hourly diffuse solar radiation from measured hourly global solar radiation on a horizontal surface. Solar Energy, 24(5), 491-503.

[29] Tiba, C., and Fraidenraich, N. (2004). Analysis of monthly time series of solar radiation and sunshine hours in tropical climates. *Renewable Energy*, 29(7), 1147-1160. DOI: https://doi.org/10.1016/j.renene.2003.11.016

[30] Aguiar, R., and Boland, J. (1999). Interannual variability of meteorological parameters in temperate climates. In: *1999 ISES Solar World Congress*, G. Grossman, ed., Elsevier, pp: I-353.

[31] Aguiar, R. J., Collares-Pereira, M., and Conde, J. P. (1988). Simple procedure for generating sequences of daily radiation values using a library of Markov transition matrices. *Solar Energy*, 40(3), 269-279. DOI: https://doi.org/10.1016/0038-092X(88)90049-7

[32] Graham, V. A., Hollands, K. G. T., and Unny, T. E. (1988). A time series model for Kt with application to global synthetic weather generation. *Solar Energy*, 40(2), 83-92. DOI: https://doi.org/10.1016/0038-092X(88)90075-8

Trends in Renewable Energy
OPEN ACCESS ISSN: 2376-2144
Peer-Reviewed Article
futureenergysp.com/index.php/tre

Mathematical Analysis of Solar Photovoltaic Array Configurations with Partial Shaded Modules

*V. Bala Raju, Dr. Ch. Chengaiah

Dept. of EEE, SV University College of Engg., Tirupati, India

Received February 24, 2020; Accepted April 22, 2020; Published April 28, 2020

Solar-based photovoltaic (SPV) cells produce power from sunlight through the photovoltaic effect. The yield voltage of a single PV cell is small, so the voltage is extended by interfacing PV cells in series arrangement known as PV module or panel. Solar PV array comprises of series and parallel connections of modules in the grid structure with a few columns and rows. The various kinds of SPV array configurations or topologies are shaped by changing the number of electrical connections between module to module in an array. This paper presents the mathematical examination of 6×6 size regular SPV array configurations, including Total-Cross-Tied, Parallel, Honey-Comb, Series-Parallel, Series, Bridge-Linked types beneath un-shading case, and different proposed shading cases (primarily short narrow, short wide, long narrow, and long wide shadings). The electrical proportionate circuit of the SPV array setups was analyzed by Kirchhoff's laws at distinctive nodes and loops in a sun powered PV array. The location of global maximum power point (GMPP) was determined hypothetically and distinguished in Matlab/simulation software at various shading conditions.

Keywords: Photovoltaic cell; Module; Array; Configurations; Shaded modules; Row currents; PV array power.

1. Introduction

The expanded electrical energy demand around the world, ecological issues, and the global warming effect due to the use of fossil fuels have brought about the developing selection of sustainable power sources for power generation. Sustainable power source is an elective wellspring of electrical energy for providing the necessary energy demand. Among all renewable energy sources, the photovoltaic (PV) system has a more preferred position than other sources, because of the most recent improvement in PV innovation, value drop of PV modules or panels, rugged and simple in design requiring very little maintenance, subsidies provided by the government, no pollution *etc.* [1]. Solar-based PV (SPV) power is gotten by the immediate transformation strategy for sunlight into power. The exhibition of the SPV system relies upon solar-based irradiance, shading effect, maturing impact, temperature, and degradation impacts, and so on. The most influencing factors are temperature and solar-based irradiance [2-3]. The sun-oriented PV system has a unique extreme power point (MPP) under uniform irradiance case, and numerous peaks happen under non-uniform irradiance cases, for example, local peaks, global peaks. This global peak point is considered on the yield P-V characteristics [4].

*Corresponding author: vbrajuu@gmail.com

Tr Ren Energy, 2020, Vol.6, No.2, 131-155. doi: 10.17737/tre.2020.6.2.00115

Solar-oriented PV cells can straightforwardly convert the sun powered capacity into the electrical power and be associated through various interconnections of cells to achieve more power. The sun-based PV panel or module is shaped by arranging PV cells in series, while the PV array is framed by the series and parallel association of PV panels. The quantity of interconnections between modules in a array are changed to make the diverse SPV exhibit association topologies, for example, Series, Bridge-Link, Parallel, Total-Cross-Tied (TCT), Series-Parallel, and Honey-Comb types [5]. Among all topologies, TCT has least mismatch, low shading losses, and high producing yield power [6]. Many researchers have introduced literature reviews on solar PV array configurations under incomplete shading conditions [7-10].

This paper presents the mathematical examination of a 6×6 SPV array arrangement under four shading cases including short narrow (SN), long wide (LW), short wide (SW) and long narrow (LN) shadings, and one un-shading case (U). The mathematical examination of a 6×6 size regular designs was gotten from Kirchhoff's laws, *i.e.*, Kirchhoff's current law (KCL) was applied at hubs, and Kirchhoff's voltage law (KVL) was applied at closed loops.

This paper initially discusses the modeling of a single diode photovoltaic cell, module, and array in Section 2. Different conventional SPV arrangements are introduced in Section 3. In Sections 4 and 5, the numerical investigation of conventional type configurations under the non-shading case and four shading cases and furthermore reproduction results for a 6×6 array designs are introduced. In Section 6, conclusions are given.

2. Modeling of Solar Photovoltaic System

2.1 Modeling of Photovoltaic Cell, Module, and Array

Sun oriented photovoltaic cells directly convert photon energy from sun based irradiance into DC electricity through the photovoltaic effect. Each cell generates a small amount of the current, and these cells are connected in series to form a single module or panel and produce higher currents. The combination of series and parallel connected PV panels forms a SPV array.

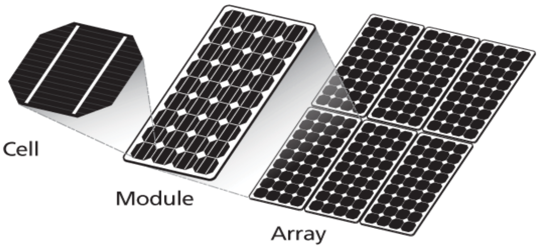

Figure 1. Formation of the solar PV cell to an array.

Figure 1 shows the formation of the SPV array with several cells and modules. The simplified models of single diode PV cell and PV array are shown in Figure 2 and

Figure 3, respectively. The solar PV array is made by series-connected (N_S) and parallel connected (N_P) PV panels.

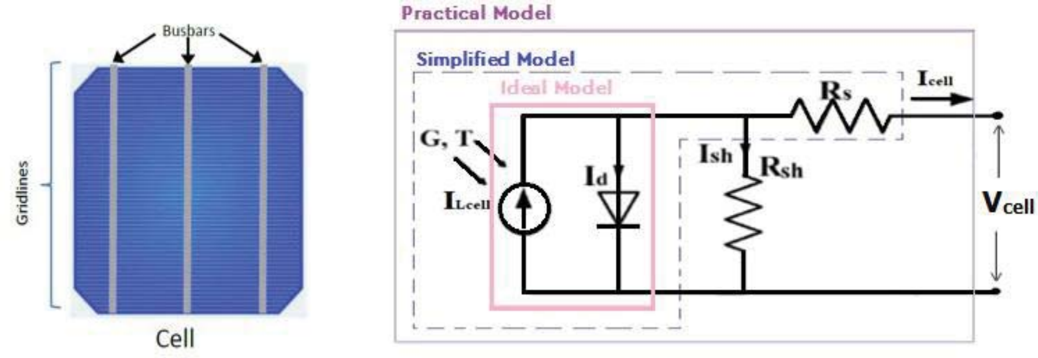

(a) **(b)**

Figure 2. (a) Single diode solar PV cell (b) Equivalent circuit of a PV cell

The mathematical representation of a PV cell is given in Equation 1 [11].

$$I_{cell} = I_{Lcell} - I_0 \left[exp \left\{ \frac{q(V_{cell} + I_{cell}R_S)}{KaT_c} \right\} - 1 \right] - \frac{(V_{cell} + I_{cell}R_S)}{R_{SH}} \quad \dots\dots\dots(1)$$

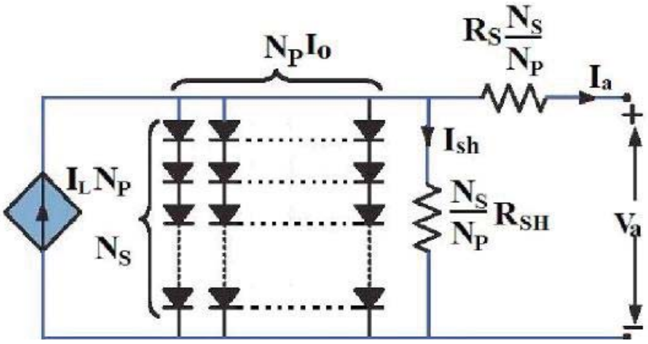

Figure 3. Circuit of solar photovoltaic array

The mathematical representation of the PV module given in Equation 2,

$$I_m = I_L - I_0 \left[exp \left\{ \frac{q(V_m + I_m R_S)}{n_s KaT_c} \right\} - 1 \right] - \frac{(V_m + I_m R_S)}{R_{SH}} \quad \dots\dots\dots(2)$$

where I_L is the current generated by the module light, represented as

$$I_L = \frac{G}{G_0} [I_{LSTC} + K_{isc}(T_c - T_{STC})] \quad \dots\dots\dots(3)$$

where, K_{isc} is the module short circuit co-efficient, I_{LSTC} the current generated by the module light at STC (Standard Test Conditions). G is the incident irradiance, and G_0 is the standard irradiation. I_m and V_m are output current and voltage of PV module, I_{cell} and

V_{cell} are output current and voltage of a single diode PV cell, I_{Lcell} is photo generated current of a solar PV cell and I_0 is reverse saturation current.

The simplified mathematical equation of PV array [10-11] is given by

$$I_a = N_P.I_L - N_P.I_0\left[exp\left\{\frac{q(V_a + \frac{N_S}{N_P}I_aR_S)}{N_sKaT_c}\right\} - 1\right] - \frac{(V_a + \frac{N_S}{N_P}I_aR_S)}{\frac{N_S}{N_P}.R_{SH}} \quad \ldots\ldots(4)$$

where, N_P and N_S are the total number of parallel and series connected panels in the SPV array, R_{SH} and R_S are parallel and series resistances of the module, V_a and I_a are the voltage and current of the SPV array. I_L denotes the photo-electric current, I_o is reverse saturation current, q: charge, a: diode ideality factor, k: Boltzmann constant and T is the temperature of the solar cell at STC.

The above set of equations is used to model the PV array to simulate I-V and P-V characteristics with the help of parameters in the datasheet of a solar PV module.

3. Solar PV Array Configurations

3.1 Conventional Solar PV Array Configurations

There are six basic PV array configurations available which are known as a conventional type of configurations or topologies. From this conventional type, hybrid PV array topologies are developed by combining any two conventional type configurations. The primary conventional configurations of PV array are [12]:

a. Simple Series (SS) connection
b. Series-Parallel (S-P) connection
c. Bridge-Linked (B-L) connection
d. Simple Parallel (SP) connection
e. Total-Cross-Tied (T-C-T) connection
f. Honey-Comb (H-C) connection configuration.

Figure 4 shows the conventional array configurations of a 6×6 size solar PV array.

Simple-Series (SS): In this connection, one module is connected to another module like a series connection, as shown in Figure 4(a). In a series connection, the total voltage is the sum of each module voltages, so the output array voltage is high in a SS topology.

Simple-Parallel (P): In this connection, all SPV modules are parallel connected, as shown in Figure 4(b). In a parallel connection, the total current is the sum of each module currents, so the output array current is high in a parallel topology.

Series-Parallel (SP): In this type, the number of series-connected modules called strings is connected to form a series-parallel (SP) topology, as displayed in Figure 4(c).

Bridge-Link (BL): This BL topology is adapted from a wheat-stone bridge, and this scheme is derived from the bridge rectifier connections, as shown in Figure 4(e).

Honey-Comb (HC): In this connection, solar PV panels are connected in hexagon shape by the honeycomb architecture, as shown in Figure 4(f).

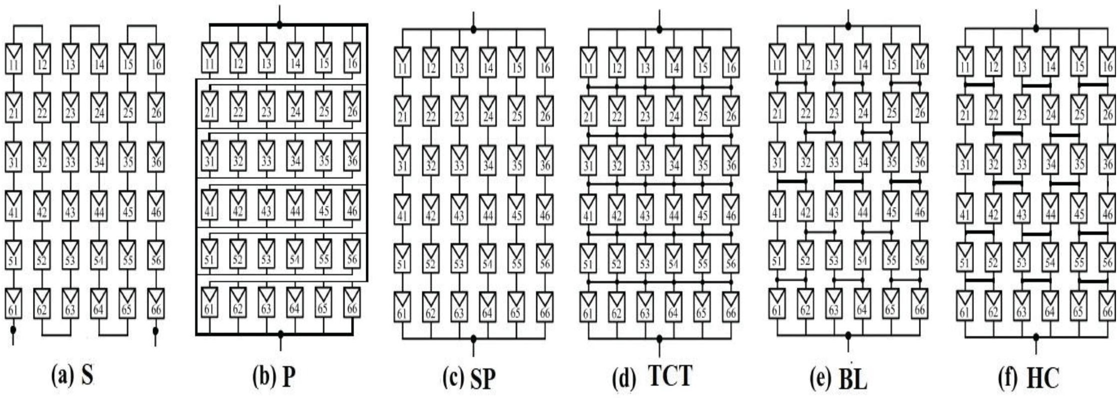

(a) S (b) P (c) SP (d) TCT (e) BL (f) HC

Figure 4. 6×6 Solar PV array conventional configurations

Total-Cross-Tied (TCT): This TCT connection is formed by establishing the electrical contacts or ties among the rows and columns of the S-P connection topology, as shown in Figure 4(d).

In this TCT connection, SPV modules are connected in matrix form. The labeled number **mn** in matrix form indicates; first index **m** represents the row number and second index **n** represents the column number. For example, in a 6×6 connected SPV array 1st row consists of PV modules labeling from 11 (1st row and 1st column) to 16 (1st row and 6th column) , and the 1st column consists of modules from 11 (1st row and 1st column) to 61 (6th row and 1st column), as shown in Figure 4.

4. Mathematical Analysis of SPV Array Configurations

In this section, mathematical examination is performed for a 6×6 size PV array conventional configuration, appeared in Figures 5 to 10. The mathematical is performed with the assistance of Kirchhoff's laws, *i.e.*, Kirchhoff's current law is applied at nodes and Kirchhoff's voltage law is applied at closed loops.

4.1 Different Interconnection Array Configurations

(i) Simple Series Configuration

The simplest topology or configuration of the PV system is Simple Series connection type, as shown in Figure 5. Where I_{PV} and V_{PV} are the current and voltage of the PV array.

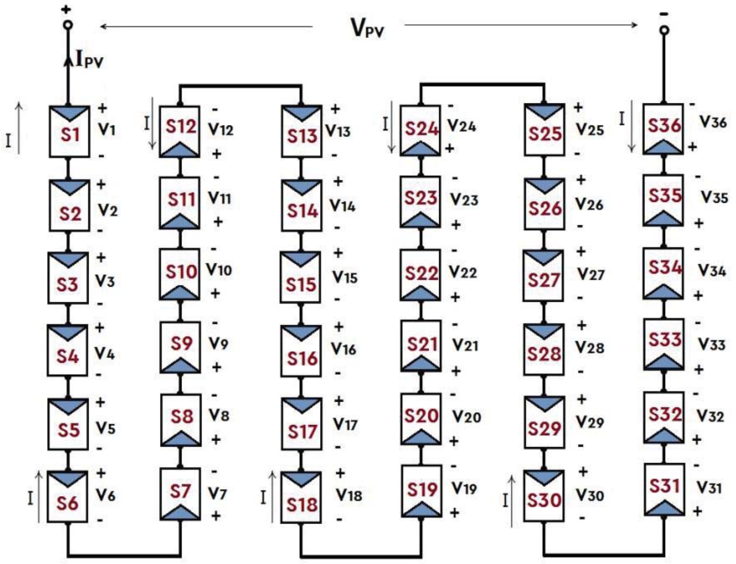

Figure 5. 6×6 Simple Series configuration

In a series connection, the same current flowing through the 36 modules in the array. Apply KVL for one closed loop in the Simple Series topology and the KVL equation is written as,

$$\sum_{n=1}^{36} V_n = V_{PV} \qquad ----(5)$$

where n is the number of modules in an array configuration.

It is noted that a 6×6 array of SS connection has 36 module voltages and the one array current.

i.e., $$\boldsymbol{V_{PV}} = V_1 + V_2 + \cdots .. + V_{36} \qquad ----(6)$$

$$\boldsymbol{I_{PV}} = I \qquad ----(7)$$

(ii) Simple Parallel Configuration

The simple parallel configuration is shown in Figure 6. Where**,** I_{PV} and V_{PV} are the array current and voltage.

In a parallel configuration, all the modules have the same voltage (In any parallel, the circuit voltages are equal), *i.e.*, $V_1=V_2=\dots\dots\dots = V_{36} = V$ as shown in Figure 6 and different currents. Apply KCL at different nodes, then

$$\sum_{n=1}^{36} I_n = I_{PV} \qquad ---(8)$$

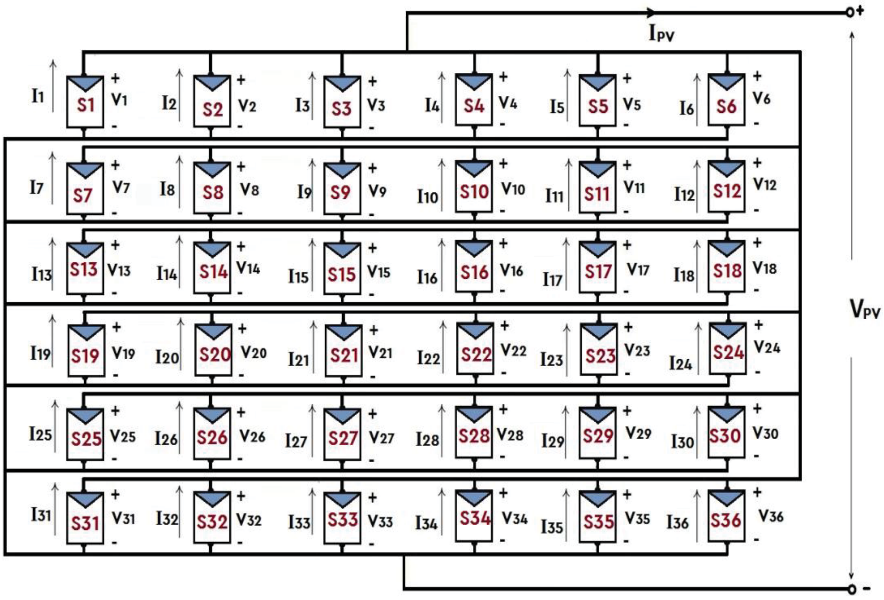

Figure 6. 6×6 Simple Parallel configuration

Where **n** is the number of modules in an array configuration. It is noted that a 6×6 array of parallel connection has 36 module currents and the one array voltage.

i.e.,

$$\boldsymbol{V_{PV}} = V_1 = V_2 = \cdots = V_{36} = \boldsymbol{V} \qquad ---(9)$$

$$\boldsymbol{I_{PV}} = I_1 + I_2 + \cdots \ldots\ldots\ldots + I_{36} \qquad ---(10)$$

(iii) Series-Parallel Configuration

The circuit of Series-Parallel (S-P) configuration of modules in an array is shown in Figure 7. This topology has four parallel strings, and each contains nine series-connected modules.

The total array current I_{PV} is equal to the sum of the six-string currents.

i.e.,

$$\boldsymbol{I_{PV}} = I_1 + I_2 + I_3 + I_4 + I_5 + I_6 \qquad ---(11)$$

The six parallel string voltages are equal to the array voltage. Apply KVL at parallel strings, then the equations are given by,

$$\sum_{n=1}^{6} V_n = \sum_{n=7}^{12} V_n = \sum_{n=13}^{18} V_n = \sum_{n=19}^{24} V_n = \sum_{n=25}^{30} V_n = \sum_{n=31}^{36} V_n = \boldsymbol{V_{PV}} \qquad ----(12)$$

The SP configuration has 36 module voltages and four-string currents. SP configuration voltages and currents in 1st, 2nd,3rd, 4th,5th, 6th columns are V_1 to V_6, V_7 to V_{12}, V_{13} to V_{18}, V_{19} to V_{24}, V_{25} to V_{30}, V_{31} to V_{36} and I_1, I_2, I_3, I_4, I_5, I_6, respectively, which are shown in Figure 7.

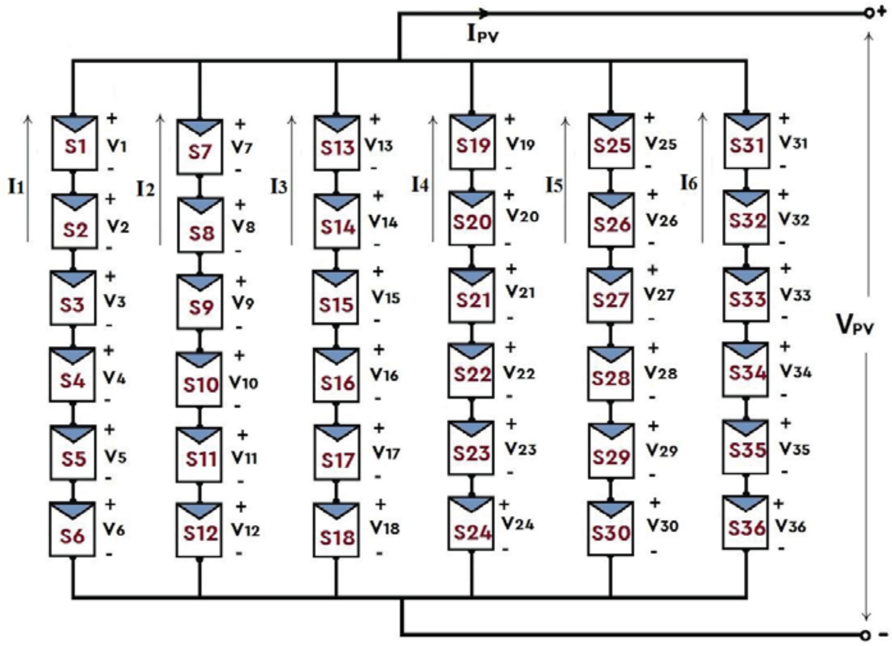

Figure 7. 6×6 Series-Parallel configuration

(iv) Total-Cross-Tied Configuration

The solar PV array with TCT configuration is shown in Figure 8. The voltage of 6 parallel modules at the mth row is V_m.
where,

$$m = \begin{cases} n & \text{for } 1 \le n \le 6 \\ n-6 & \text{for } 7 \le n \le 12 \\ n-12 & \text{for } 13 \le n \le 18 \\ n-18 & \text{for } 19 \le n \le 24 \\ n-24 & \text{for } 25 \le n \le 30 \\ n-30 & \text{for } 30 \le n \le 36 \end{cases}$$

The array voltage V_{PV} is equal to the sum of six rows of individual module voltages:

$$\boldsymbol{V}_{\mathbf{PV}} = \sum_{m=1}^{6} V_m \qquad ----(13)$$

$$\boldsymbol{V}_{\mathbf{PV}} = \boldsymbol{V_1} + \boldsymbol{V_2} + \boldsymbol{V_3} + \boldsymbol{V_4} + \boldsymbol{V_5} + \boldsymbol{V_6}$$

Where,

$$\boldsymbol{V_1} = \mathrm{v}_1 = \mathrm{v}_7 = \mathrm{v}_{13} = \mathrm{v}_{19} = \mathrm{v}_{25} = \mathrm{v}_{31}$$
$$\boldsymbol{V_2} = \mathrm{v}_2 = \mathrm{v}_8 = \mathrm{v}_{14} = \mathrm{v}_{20} = \mathrm{v}_{21} = \mathrm{v}_{32}$$
$$\boldsymbol{V_3} = \mathrm{v}_3 = \mathrm{v}_9 = \mathrm{v}_{15} = \mathrm{v}_{21} = \mathrm{v}_{22} = \mathrm{v}_{33}$$
$$\boldsymbol{V_4} = \mathrm{v}_4 = \mathrm{v}_{10} = \mathrm{v}_{16} = \mathrm{v}_{22} = \mathrm{v}_{23} = \mathrm{v}_{34}$$
$$\boldsymbol{V_5} = \mathrm{v}_5 = \mathrm{v}_{11} = \mathrm{v}_{17} = \mathrm{v}_{23} = \mathrm{v}_{24} = \mathrm{v}_{35}$$
$$\boldsymbol{V_6} = \mathrm{v}_6 = \mathrm{v}_{12} = \mathrm{v}_{18} = \mathrm{v}_{24} = \mathrm{v}_{25} = \mathrm{v}_{36}$$

Apply KCL at nodes 1 to 5, as shown in Figure 8.

$$\sum_{m=0}^{5}\left(I_{6.m+q} - I_{6.m+(q+1)}\right) = 0;\ q = 1,2,3,4,5; \qquad ----(14)$$

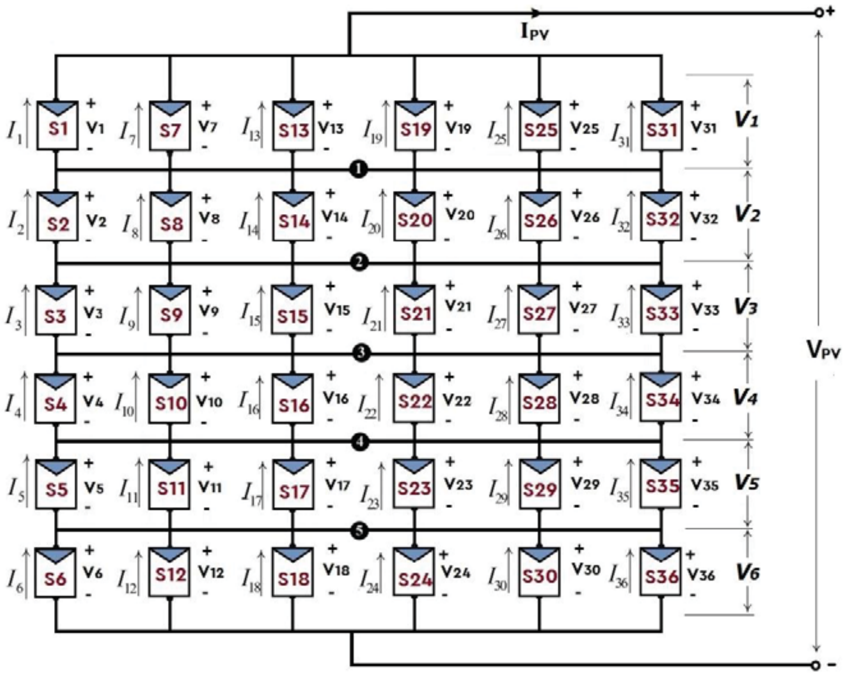

Figure 8. 6×6 Total-Cross-Tied configuration

The TCT topology has 36 module currents and 6 module voltages, as shown in Figure 8. TCT configuration has currents in 1st,2nd,3rd,4th,5th,6th columns, which are I_1 to I_6, I_7 to I_{12}, I_{13} to I_{18}, I_{19} to I_{24}, I_{25} to I_{30}, I_{31} to I_{36}, and voltages in 1st row to 6th rows are V_1 to V_6.

(v) Bridge-linked Connection Configuration

The solar PV array with B-L configuration is shown in Figure 9. The module currents and voltages are I_m and V_p, respectively. The subscripts *m, p* are related to module number n, where,

$$m = \begin{cases} 1 & \text{for n} = 1,2 \\ 2 & \text{for n} = 3,4 \\ 3 & \text{for n} = 5,6 \\ \text{n} - 3; & \text{for } 7 \le \text{n} \le 30; \\ 28 & \text{for n} = 31,32 \\ 29 & \text{for n} = 33,34 \\ 30 & \text{for n} = 35,36; \end{cases} \qquad p = \begin{cases} \text{n} & \text{for } 1 \le \text{n} \le 12 \\ \text{n} - 6 & \text{for n} = 13,18 \\ \text{n} - 1 & \text{for } 14 \le \text{n} \le 17 \\ \text{n} - 2 & \text{for } 19 \le \text{n} \le 24 \\ \text{n} - 8 & \text{for n} = 25,30 \\ \text{n} - 4 & \text{for n} = 31,36 \end{cases}$$

In this BL type connection topology, 30 module currents and 32 voltages across modules. Figure 9 shows the 12 nodes in the BL topology.

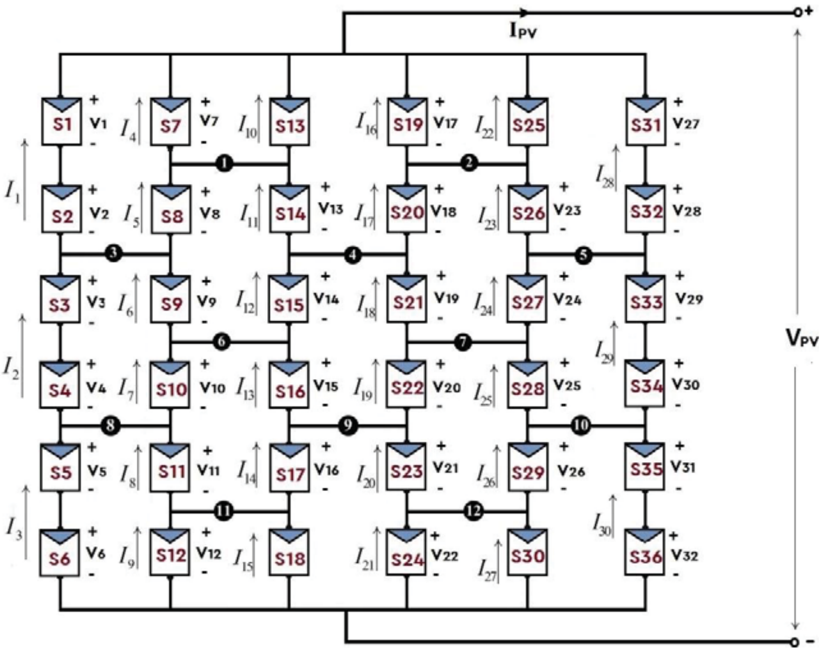

Figure 9. 6×6 Bridge-Linked configuration

The node numbers 3 and 8 at the left column, apply the KCL at node points:

$$I_m + I_q - I_{m+1} - I_{q+1} = 0;\ m = 1,2 \qquad ---(15)$$

where the subscript *q* is related to *m* by,

$$q = \begin{cases} 5 & \text{for m} = 1 \\ 7 & \text{for m} = 2 \end{cases}$$

Similarly, apply KCL for the nodes 1, 6, 11 between 2nd & 3rd column and nodes 4 , 9 between 3rd & 4th columns,

$$I_m + I_{m+6} - I_{m+1} - I_{m+7} = 0;\ \ m = 4,6,8,11,13,16,18,20 \qquad ---(16)$$

For the node numbers 5,10 between 5th and 6th columns, apply the KCL at node points:

$$I_m + I_q - I_{m+1} - I_{q+1} = 0;\ m = 23,25 \qquad ---(17)$$

in which the subscripts *q* and *m* relate to each other by,

$$q = \begin{cases} 28 & \text{for m} = 23 \\ 29 & \text{for m} = 25 \end{cases}$$

Figure 9 shows the loops and each loop contains four modules, apply KVL for the loops:

$$\begin{aligned}
&V_p + V_{p+1} - V_{p+6} - V_{p+7} = 0; && p = 1,3,5 \\
&V_p + V_{p+1} - V_{p+5} - V_{p+6} = 0; && p = 8,10 \\
&V_{p+6} + V_p - V_{p+10} - V_{p+11} = 0; && p = 7,17 \\
&V_p + V_{p+1} - V_{p+5} - V_{p+6} = 0; && p = 14,18,20,24 \\
&V_{p+4} + V_p - V_{p+9} - V_{p+10} = 0; && p = 12,22
\end{aligned} \qquad ---(18)$$

Finally, apply the KVL for six modules loop in the 1st column is given by

$$\sum_{p=1}^{6} V_p = \boldsymbol{V_{PV}} \qquad --- (19)$$

The 6×6 BL configuration has 32 voltages and 30 currents which are shown in Figure 9. BL configuration voltages and currents in 1st, 2nd,3rd, 4th, 5th,6th columns are V_1 to V_6, V_7 to V_{12}, V_{13} to V_{16}, V_{17} to V_{22}, V_{23} to V_{26}, V_{27} to V_{32} and I_1 to I_3, I_4 to I_9, I_{10} to I_{15}, I_{16} to I_{21}, I_{22} to I_{27}, I_{28} to I_{30}, respectively.

(vi) Honey-Comb Connection Configuration

The PV array with HC connection configuration is shown in Figure 10. The module currents and voltages are I_m and V_p, respectively. The subscripts *m*, *p* are related to module number n.

where,

$$m = \begin{cases} 1 & \text{for } n = 1 \\ 2 & \text{for } n = 2,3,4 \\ 3 & \text{for } n = 5 \\ 4 & \text{for } n = 6 \\ n-2 & \text{for } 7 \le n \le 31 \\ 30 & \text{for } n = 32,33,34 \\ 31 & \text{for } n = 35 \\ 32 & \text{for } n = 36 \end{cases}; \quad p = \begin{cases} n; & \text{for } 1 \le n \le 6 \\ 1; & \text{for } n = 7 \\ n-1; & \text{for } n = 8,9,10 \\ 5; & \text{for } n = 11 \\ 6; & \text{for } n = 12 \\ n-3; & \text{for } n = 13,14 \\ 8; & \text{for } n = 15 \\ n-4; & \text{for } n = 16,17,18 \\ 10; & \text{for } n = 19 \end{cases}; \quad p = \begin{cases} n-5; & \text{for } n = 20,21,22 \\ 13; & \text{for } n = 23 \\ 14; & \text{for } n = 24 \\ n-7; & \text{for } n = 25,26 \\ 16; & \text{for } n = 27 \\ n-8; & \text{for } n = 28,29,30 \\ 18; & \text{for } n = 31 \\ n-9; & \text{for } n = 32,33,34 \\ 21; & \text{for } n = 35 \\ 22; & \text{for } n = 36 \end{cases}$$

In the HC connection type topology, the total number of nodes is 13. Apply KCL for each node,

$$I_m + I_q - I_{m+1} - I_{q+1} = 0; \;\; m = 1,2,3,6,7,11,14,15,18,19,23,26,27 \quad \ldots\ldots(20)$$

and the subscript *q* is related to *m* given by

$$q = \begin{cases} 5 & m = 1 \\ 8 & m = 2 \\ 9 & m = 3 \\ 12 & m = 6 \end{cases}; \quad q = \begin{cases} 13 & m = 7 \\ 17 & m = 11 \\ 20 & m = 14 \\ 21 & m = 15 \end{cases}; \quad q = \begin{cases} 24 & m = 18 \\ 25 & m = 19 \\ 29 & m = 23 \\ 30 & m = 26 \\ 31 & m = 27 \end{cases}$$

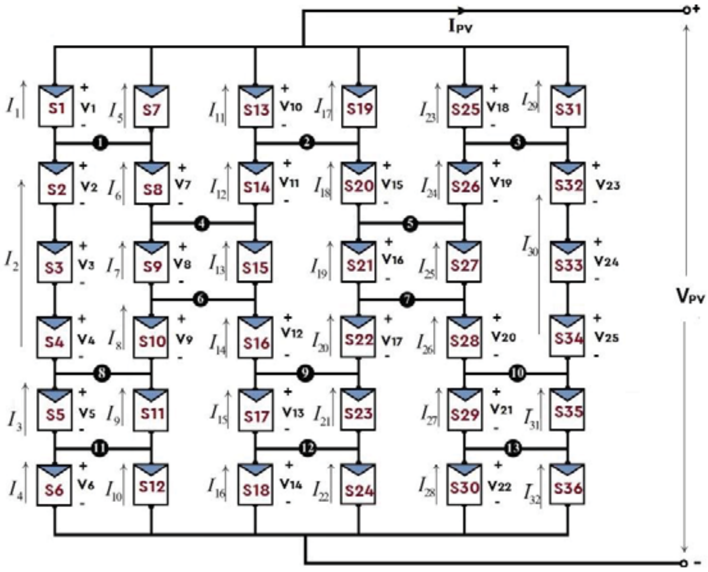

Figure 10. 6×6 Honey-Comb configuration

Then apply KVL to six or four modules in a loop,

$$\begin{aligned} &V_p + V_{p+1} + V_{p+2} - V_q - V_{q+1} - V_{q+2} = 0; \quad (\boldsymbol{p}, \boldsymbol{q}) = (\mathbf{2}, \mathbf{7}) \\ &V_q + V_p - V_{p+3} - V_{p+4} = 0; \qquad (p, q) = (7,1) \& \ (15,10) \\ &V_p + V_{p-3} + V_{p+1} - V_{p+4} - V_{p+5} - V_{p+6} = 0; \quad p = 11,19 \\ &V_p + V_{p-4} + V_{p-3} - V_q - V_{q+1} - V_{q+2} = 0; \ (p, q) = (9,12) \ \& \ (17,20) \end{aligned} \quad ---(21)$$

Finally, apply KVL for the six modules loop in the left column is given as,

$$\sum_{n=1}^{6} V_n = \boldsymbol{V_{PV}} \qquad ---(22)$$

In 6×6, HC configuration has 25 module voltages and 32 currents, as shown in Figure 10. HC configuration has voltages and currents in 1st, 2nd, 3rd, 4th, 5th, 6th columns are V_1 to V_6, V_7 to V_9, V_{10} to V_{14}, V_{15} to V_{17}, V_{18} to V_{22}, V_{23} to V_{25} and I_1 to I_4, I_5 to I_{10}, I_{11} to I_{16}, I_{17} to I_{22}, I_{23} to I_{28}, I_{29} to I_{32}, respectively.

Mathematical analysis of 6×6 PV connection configurations is tabulated in Table 1. Where P_{PV}, V_{PV} and I_{PV} are the output power, voltage and current of the SPV array respectively, V and I are the voltage and current output of a single PV module respectively.

4.2 Generation of Power Across the TCT array configuration

In this section, the power generation of SPV array with TCT configuration is discussed and output voltage, current and power of an array are theoretically calculated.

The current *I* generated by a single solar module at any irradiance G is given as,

$$\boldsymbol{I} = \left(\frac{G}{G_o}\right).I_m \qquad ----(23)$$

where *G* is irradiance at shading condition, and G_0 is the standard irradiance of 1000 W/m^2. If the solar module receives full irradiance, the output current of the module is more and vice-versa.

The PV array voltage V_{PV} is given as the summation of individual module voltages in the rows in an array, *i.e.*,

$$\boldsymbol{V_{PV}} = \sum_{p=1}^{n} V_{mp} \qquad ----(24)$$

where V_{mp} is the maximum module voltage at pth row. In a 6x6 TCT SPV array configuration, number of rows are 6, each row voltage is Vm (the maximum module voltage), so the total voltage of an array is equal to the sum of row voltage. By neglecting the voltage drop across diodes, the SPV array voltage is given as,

$$\boldsymbol{V_{PV}} = V_{m1} + V_{m2} + V_{m3} + V_{m4} + V_{m5} + V_{m6}$$

where, $V_{m1}\ to\ V_{m6}$ are the maximum voltage of parallel connected modules in rows. Each row has 6 number of modules are connected in parallel and the row voltage is equal to V_m (total voltage is same as individual voltages in parallel connection), then

$$\boldsymbol{V_{PV}} = 6\,V_m \qquad ----(25)$$

By applying the Kirchhoff's current law, the output current of an TCT SPV array configuration (current across each node in an array) is given by,

$$\boldsymbol{I_{PV}} = \sum_{q=1}^{n}\left(I_{pq} - I_{(p+1)q}\right) = 0\,; \quad where, p = 1,2,\dots,(n-1) \quad ----(26)$$

where, **p** and **q** are the number of rows and columns of the SPV array.

For a 6×6 solar PV array TCT configuration, the number of rows is six are connected in series and number of modules per row is 6 are connected in parallel. The total array current is the sum of six number of module currents in each row given as,

$$\boldsymbol{I_{PV}} = I_{m1} + I_{m2} + I_{m3} + I_{m4} + I_{m5} + I_{m6}$$

where, $I_{m1}\ to\ I_{m6}$ are the maximum current of parallel connected modules in rows. Each row has 6 number of modules are connected in parallel and maximum current of each module is equal to I_m (total current is the sum of individual module currents in parallel connection), then

$$I_{PV} = 6\, I_m \qquad ----(27)$$

where **Im** is the maximum generated current of each PV module in an array.
Under un-shaded conditions, the power output of a 6×6 Solar PV TCT array is given as,

$$P_{PV} = V_{PV}.I_{PV} = 6V_m.6I_m = 36V_m.I_m \qquad ----(28)$$

Table 1. Parameters (V, I and P) of a 6×6 SPV Array Topologies

Configurations	OUTPUT		
	Array Voltage V_{PV} (V)	Array Current I_{PV} (A)	Array Power P_{PV} (W)
Simple Series	$V_{PV} = \sum_{n=1}^{36} V_n = 36\,V$	$I_{PV} = I$	$P_{PV} = 36\,VI$
Simple Parallel	$V_{PV} = V$	$I_{PV} = \sum_{n=1}^{36} I_n = 36\,I$	$P_{PV} = 36\,VI$
Series-Parallel	$V_{PV} = \sum_{n=1}^{6} V_n = 6\,V$	$I_{PV} = \sum_{n=1}^{6} I_n = 6\,I$	$P_{PV} = 36\,VI$
Total-Cross-Tied	$V_{PV} = \sum_{n=1}^{6} V_n = 6\,V$	$I_{PV} = \sum_{n=1}^{6} I_n = 6\,I$	$P_{PV} = 36\,VI$
Bridge-Link	$V_{PV} = \sum_{n=1}^{6} V_n = 6\,V$	$I_{PV} = I_1 + I_4 + I_{10} + I_{16} + I_{22} + I_{28} = 6\,I$	$P_{PV} = 36\,VI$
Honey-Comb	$V_{PV} = \sum_{n=1}^{6} V_n = 6\,V$	$I_{PV} = I_1 + I_5 + I_{11} + I_{17} + I_{23} + I_{29} = 6\,I$	$P_{PV} = 36\,VI$

5. Mathematical Analysis of Partial Shaded SPV Array with TCT Configurations

5.1 Row Currents and Output Powers of the SPV Array with TCT topology

Figure 12 shows the partially shaded modules in the 6×6 PV array with TCT configurations [13-14]. For mathematical analysis of 6×6, TCT configuration calculates the currents in each row, array voltage, and array power [12]. The row currents are given as

$$I_{Rp} = \sum_{n=1}^{6} S_{pn} I_m = S_{p1} I_m + S_{p2} I_m + S_{p3} I_m + S_{p4} I_m + S_{p5} I_m + S_{p6} I_m \qquad ---(29)$$

$$where,\ S_{p1} = \left(\frac{G_{p1}}{G_o}\right),\ S_{p2} = \left(\frac{G_{p2}}{G_o}\right),\ S_{p3} = \left(\frac{G_{p3}}{G_o}\right), S_{p4} = \left(\frac{G_{p4}}{G_o}\right), S_{p5} = \left(\frac{G_{p5}}{G_o}\right),\ S_{p6} = \left(\frac{G_{p6}}{G_o}\right) \qquad --(30)$$

where p is row number, G_0 is the standard irradiance of 1000 W/m^2, G_{p1} is the Pth row and 1st column irradiance value in W/m^2.

The 1st-row current is given as,

$$\boldsymbol{I_{R1}} = \sum_{n=1}^{6} S_{1n}I_m = S_{11}I_m + S_{12}I_m + S_{13}I_m + S_{14}I_m + S_{15}I_m + S_{16}I_m \qquad ---(31)$$

$$Where, S_{11} = \left(\frac{G_{11}}{G_o}\right), S_{12} = \left(\frac{G_{12}}{G_o}\right), S_{13} = \left(\frac{G_{13}}{G_o}\right),\ S_{14} = \left(\frac{G_{14}}{G_o}\right),\ S_{15} = \left(\frac{G_{15}}{G_o}\right),\ S_{16} = \left(\frac{G_{16}}{G_o}\right)$$

The 2nd, 3rd,4th, 5th, and 6th-row currents are given as,

$$\boldsymbol{I_{R2}} = \sum_{n=1}^{6} S_{2n}I_m = S_{21}I_m + S_{22}I_m + S_{23}I_m + S_{24}I_m + S_{25}I_m \ + S_{26}I_m --- (32)$$

$$\boldsymbol{I_{R3}} = \sum_{n=1}^{6} S_{3n}I_m = S_{31}I_m + S_{32}I_m + S_{33}I_m + S_{34}I_m + S_{35}I_m \ + S_{36}I_m --- (33)$$

$$\boldsymbol{I_{R4}} = \sum_{n=1}^{6} S_{4n}I_m = S_{41}I_m + S_{42}I_m + S_{43}I_m + S_{44}I_m + S_{45}I_m \ + S_{46}I_m --- (34)$$

$$\boldsymbol{I_{R5}} = \sum_{n=1}^{6} S_{5n}I_m = S_{51}I_m + S_{52}I_m + S_{53}I_m + S_{54}I_m + S_{55}I_m \ + S_{56}I_m --- (35)$$

$$\boldsymbol{I_{R6}} = \sum_{n=1}^{6} S_{6n}I_m = S_{61}I_m + S_{62}I_m + S_{63}I_m + S_{64}I_m + S_{65}I_m \ + S_{66}I_m --- (36)$$

Since the currents are different in each row, so two or more peaks occur in output characteristics (P-V curves). In the TCT SPV array configuration, the global MPP, is the product of voltage and current of each row. The array current depends on the irradiance, and the array voltage is the same for all the rows by neglecting the voltage drop across the diodes. Solar PV array output voltage and power are given as,

$$\boldsymbol{V_{PV}} = 6\,V_m \qquad ----(37)$$

$$\boldsymbol{P_{PV}} = \ V_{PV}.I_{PV} = 36.V_{PV}.I_{PV} \qquad ----(38)$$

The theoretical calculations of current, voltage, and power of TCT array topology are tabulated in Table 2.

5.3 Generation and Location of Global MPP for Shaded PV Array TCT Topology

The SPV array with TCT configuration under various shading cases are shown in Figure 12 [13]. For mathematical analysis of partially shaded conventional TCT configurations [15], four partial shading patterns are shown in Figure 11 and the irradiance of shaded panels is 500 W/m^2 are considered. There are mainly,

(a) Short Narrow shading (SNS)
(b) Short Wide shading (SWS)
(c) Long Narrow shading (SNS)
(d) Long Wide shading (SNS)
(e) Un-shaded Case (U)

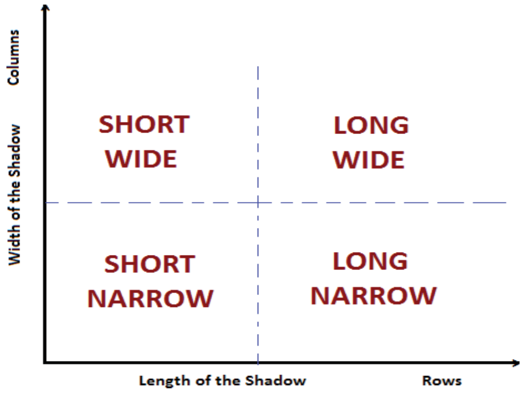

Figure 11. Types of shading cases

(a) Short Narrow Shading (SNS)

The short narrow type of shading scenario is observed in Figure 12(a). For formulating the location of Global Maximum Power Point (GMPP) in the output P-V characteristics theoretically, first calculate the currents in each row of the SPV array. From Figure 12(a), the 1st-row current is calculated from Equation 31,

$$\boldsymbol{I_{R1}} = \left(\frac{G_{11}}{G_o}\right) I_m + \left(\frac{G_{12}}{G_o}\right) I_m + \left(\frac{G_{13}}{G_o}\right) I_m + \left(\frac{G_{14}}{G_o}\right) I_m + \left(\frac{G_{15}}{G_o}\right) I_m + \left(\frac{G_{16}}{G_o}\right) I_m$$

where, $G_{11} = G_{12} = G_{13} = G_{14} = G_{15} = G_{16} =$ irradiances at shading and G_0 is the standard irradiance of 1000W/m^2.

From Figure 12(a): In short narrow shading, PV panels in 1st, 2nd and 3rd rows are under full uniform irradiation level of 1000 W/m^2, while the remaining rows are under different irradiance of 500 W/m^2. The current generated by the 1st, 2nd, and 3rd rows are calculated as follows:

$$\boldsymbol{I_{R1}} = \boldsymbol{I_{R2}} = \boldsymbol{I_{R3}} = \left(\frac{1000}{1000}\right) I_m + \left(\frac{1000}{1000}\right) I_m + \left(\frac{1000}{1000}\right) I_m + \left(\frac{1000}{1000}\right) I_m + \left(\frac{1000}{1000}\right) I_m + \left(\frac{1000}{1000}\right) I_m = 6\ I_m \text{ ---}\boldsymbol{\textit{(i)}}$$

Modules in row 4th, 5th and 6th are shaded and the corresponding row currents are given by,

$$\boldsymbol{I_{R4}} = \boldsymbol{I_{R5}} = \boldsymbol{I_{R6}} = \left(\frac{1000}{1000}\right) I_m + \left(\frac{1000}{1000}\right) I_m + \left(\frac{1000}{1000}\right) I_m + \left(\frac{500}{1000}\right) I_m + \left(\frac{500}{1000}\right) I_m + \left(\frac{500}{1000}\right) I_m = 4.5\ I_m \text{--}\boldsymbol{\textit{(ii)}}$$

From the row currents given in *i* and *ii*, it is observed that the currents in different rows are changing from 4.5 I_m *to* 6 I_m. Due to these varying currents, multiple peaks are generated in the output characteristics.

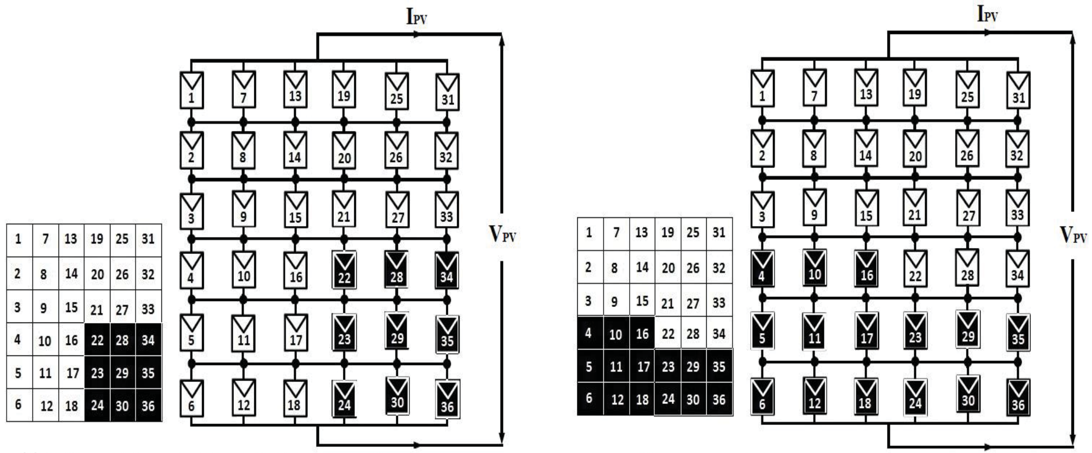

(a) Short Narrow Shading (SNS) on Modules of 6x6 Solar PV Array in TCT Configuration

(b) Short Wide Shading (SWS) on Modules of 6x6 Solar PV Array in TCT Configuration

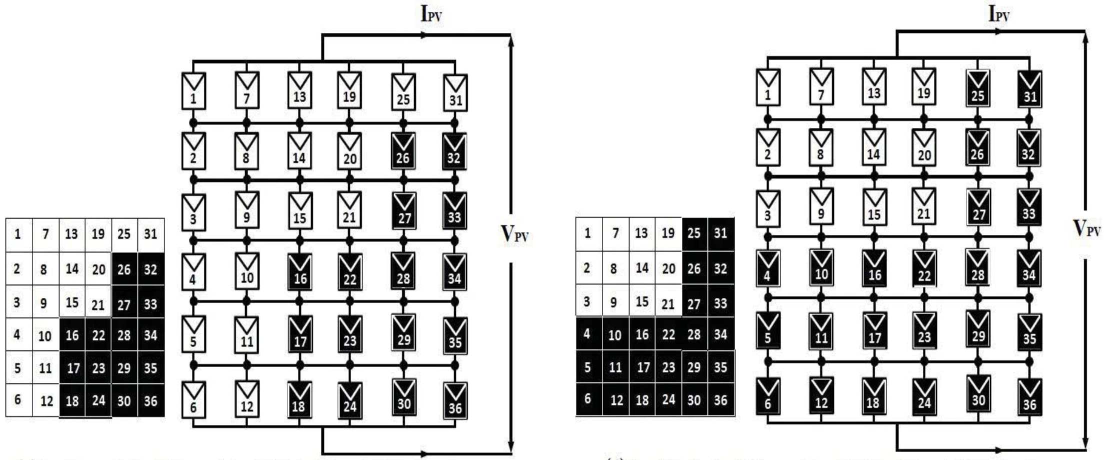

(c) Long Narrow Shading (LNS) on modules of 6x6 Solar PV Array in TCT Configuration

(d) Long Wide Shading (LWS) on modules of 6x6 Solar PV Array in TCT Configuration

Figure 12. 6×6 Solar array with TCT configuration under various shading conditions

The maximum generated power of SPV array configuration under uniform irradiance of 1000 W/m^2 is given as

$$\boldsymbol{P_{PV}} = V_{PV}.I_{PV} = 6\,V_m.6\,I_m = 36\,V_m I_m \qquad \text{---- (39)}$$

where V_m is the maximum voltage. In the TCT topology, there are six series-connected modules, the voltage across the PV Array is $6V_m$ and the array current is $4.5I_m$, due to the limitation of the array current in series-connected modules in the array topology. There is no module bypassed through the bypass diode, so the array voltage is $6V_m$.

In the TCT topology under short narrow shading case without bypassing the solar modules, the total array output power is given as

$$\boldsymbol{P_{PV,TCT}} = (6\,V_m) * (4.5\,I_m) = 27\,V_m I_m \qquad \text{----(40)}$$

(b) Short Wide Shading (SWS)

The short wide shading pattern can be observed in Figure 12(b). In this shading case, PV modules in 1st, 2nd, 3rd rows receive an irradiance of 1000 W/m^2, while the remaining modules in rows are under shaded with solar irradiance of 500 W/m^2. The current generated by the 1st, 2nd, and 3rd rows are calculated as follows:

$$\boldsymbol{I_{R1}} = \boldsymbol{I_{R2}} = \boldsymbol{I_{R3}} = \left(\frac{1000}{1000}\right) I_m + \left(\frac{1000}{1000}\right) I_m + \left(\frac{1000}{1000}\right) I_m + \left(\frac{1000}{1000}\right) I_m + \left(\frac{1000}{1000}\right) I_m + \left(\frac{1000}{1000}\right) I_m = 6\ I_m$$

Modules in row 4th, 5th and 6th are shaded. Corresponding row currents are given by,

$$\boldsymbol{I_{R4}} = \left(\frac{500}{1000}\right) I_m + \left(\frac{500}{1000}\right) I_m + \left(\frac{500}{1000}\right) I_m + \left(\frac{1000}{1000}\right) I_m + \left(\frac{1000}{1000}\right) I_m + \left(\frac{1000}{1000}\right) I_m = 4.5\ I_m$$

$$\boldsymbol{I_{R5}} = \boldsymbol{I_{R6}} = \left(\frac{500}{1000}\right) I_m + \left(\frac{500}{1000}\right) I_m + \left(\frac{500}{1000}\right) I_m + \left(\frac{500}{1000}\right) I_m + \left(\frac{500}{1000}\right) I_m + \left(\frac{500}{1000}\right) I_m = 3\ I_m$$

(c) Long Narrow Shading (LNS)

The long narrow shading pattern can be observed in Figure 12(c). In this shading case, PV modules in 1st row receive irradiance of 1000 W/m^2, while the remaining modules in rows are shaded with an irradiance of 500 W/m^2. Then the current in 1st row is calculated as follows:

$$\boldsymbol{I_{R1}} = \left(\frac{1000}{1000}\right) I_m + \left(\frac{1000}{1000}\right) I_m + \left(\frac{1000}{1000}\right) I_m + \left(\frac{1000}{1000}\right) I_m + \left(\frac{1000}{1000}\right) I_m + \left(\frac{1000}{1000}\right) I_m = 6\ I_m$$

PV Modules in 2nd,3rd,4th,5th and 6th rows are under shading, and corresponding row currents are given by,

$$\boldsymbol{I_{R2}} = \boldsymbol{I_{R3}} = \left(\frac{1000}{1000}\right) I_m + \left(\frac{1000}{1000}\right) I_m + \left(\frac{1000}{1000}\right) I_m + \left(\frac{1000}{1000}\right) I_m + \left(\frac{500}{1000}\right) I_m + \left(\frac{500}{1000}\right) I_m = 5\ I_m$$

$$\boldsymbol{I_{R4}} = \boldsymbol{I_{R5}} = \boldsymbol{I_{R6}} = \left(\frac{1000}{1000}\right) I_m + \left(\frac{1000}{1000}\right) I_m + \left(\frac{500}{1000}\right) I_m + \left(\frac{500}{1000}\right) I_m + \left(\frac{500}{1000}\right) I_m + \left(\frac{500}{1000}\right) I_m = 4\ I_m$$

(d) Long Wide Shading (LWS)

The LWS shading case is observed in Figure 12(d). Assume shading modules have irradiance of 500 W/m^2. In this type of shading case, all rows are shaded. From Figure 9(d): In long wide shading, PV modules in all rows are under shaded with solar irradiance of 500 W/m^2. The current generated by the 1st, 2nd, 3rd, 4th, 5th, and 6th rows are calculated as follows: Row current is calculated from Equation 31.

$$\boldsymbol{I_{R1}} = \boldsymbol{I_{R2}} = \boldsymbol{I_{R3}} = \left(\frac{\mathbf{1000}}{\mathbf{1000}}\right) I_m + \left(\frac{1000}{1000}\right) I_m + \left(\frac{1000}{1000}\right) I_m + \left(\frac{1000}{1000}\right) I_m + \left(\frac{500}{1000}\right) I_m + \left(\frac{500}{1000}\right) I_m = 5\ I_m$$

The PV modules in 4, 5, 6th rows are shaded, and corresponding row currents are given by,

$$\boldsymbol{I_{R4}} = \boldsymbol{I_{R5}} = \boldsymbol{I_{R6}} = \left(\frac{500}{1000}\right) I_m + \left(\frac{500}{1000}\right) I_m + \left(\frac{500}{1000}\right) I_m + \left(\frac{500}{1000}\right) I_m + \left(\frac{500}{1000}\right) I_m + \left(\frac{500}{1000}\right) I_m = 3\ I_m$$

The currents generated in six rows in an array configuration are different due to non-uniform irradiance falling on the modules in an array configuration, which results in the multiple peaks occur on the output P–V characteristics. The location of global MPP in output PV characteristics of conventional array topologies under different shading cases are tabulated in Tables 2 and 3, and the module currents in each row are based on the order in which modules were bypassed. By neglecting the voltage drops across the diodes and voltage variations across individual rows, then

The voltage of PV array is given as, $\boldsymbol{V_{PV}}=6\ V_m$.
Total Array power is given as, $\boldsymbol{P_{PV}} = V_{PV} \cdot I_{PV}$. ----(41)

In Table 2, the array current I_{PV}^* denotes the minimum of six-row currents due to series connection of six modules, and the current is limited to minimum row current. Only the minimum current will flow through the array configurations[16-17].

(e) Un-Shaded Case-U:

In the un-shade case, 36 PV modules in a 6×6 array TCT configuration receive uniform irradiance of 1000 W/m^2.The parameters are calculated under uniform irradiance case by equation 24 to 28,

The array current $\mathbf{V_{PV}} = 6\ I_m$
array voltage $\mathbf{I_{PV}} = 6\ V_m$ and
array power $\mathbf{P_{PV}} = 36\ V_m.I_m$. ----(42)

5.3 Theoretical Calculations and Discussions

In this paper, mathematical analysis of a 6×6 size, solar based PV array configurations is performed under four shading cases including short narrow, short wide, long narrow, and long wide types of partial shadings, as appeared in Figures 12(a) to 12(d). Table 3 demonstrates the hypothetical figuring to determine the maximum global power for the Total-Cross-Tied PV array design. Under uniform irradiance implies the non-shading case, the TCT configuration has an extreme maximum array power of 36 $V_m I_m$; while in shading cases, the currents in each row are different because of progress in irradiance on the PV modules in an array and corresponding power also changed. In the case of short narrow shading (SNS), the minimum current is 4.5 I_m from the rows 4th, 5th, 6th, and remaining row currents are equal to 6 I_m. Modules are connected in series due to this; the current is limited to the minimum current of rows[16-17], so the array current is 4.5 I_m, and array voltage is 6 V_m. The resultant array power is 27 $V_m I_m$. In the remaining three shading cases, the energy yield of the PV array TCT configuration is less than the SNS case. The theoretical results are tabulated in Table 3 for the TCT 6×6 PV array configuration. In series connections, high voltages are generated by PV modules and high currents are produced in parallel connections. In S-P and TCT connections, the output power of the array is more under short narrow case as compared to other shading cases.

From the mathematical analysis of a 6×6 size solar PV array configurations, it can be concluded that:

* In the simple series connection type of configuration, under uniform irradiance case, the maximum current (I_m) is produced by the SPV modules of an array. Under shading cases, limitation due to the minimum current of 0.5 I_m (is determined from Equation 31) with an irradiance of 500 W/m^2, the voltage is V_m and neglect voltage drops across diodes. The resultant array power is only 18 $V_m.I_m$, while in uniform case it is 36 V_mI_m.
* In the simple parallel connection type of configurations, under uniform irradiance case the maximum current (I_m) is produced in each parallel connected modules in the PV array. Under shading cases, different currents are created and determined from Equation 31. In the short narrow case, the array current and voltage is 31.5 I_m and V_m, and neglect voltage drops across diodes. The resultant array power is only 31.5 $V_m.I_m$, though in uniform case it is 36 V_mI_m.
* In the Series-Parallel connection type of configurations, under uniform irradiance case the array current is the aggregate of six-string currents (series connection of modules), *i.e.*, 6 I_m, array voltage is 6 V_m, and the resultant array power is 36 $V_m.I_m$. Under the short narrow case, because of shading with irradiance of 500 W/m^2, the array current is 4.5 I_m, the array voltage across 6 PV modules is 6 V_m, and the resulting array power is 27 V_mI_m.
* In the TCT connection type of configurations, under uniform irradiance case, the array current, the voltage, and the power are 6 I_m, 6 V_m, and 36 $V_m.I_m$, respectively. In short narrow shading case, row 4, 5, 6 has a minimum current of 4.5 I_m, and the voltage is 6 V_m (neglecting voltage drops across the diodes). When the rows in the configuration are connected in series, because of limitation in series current, the array current is limited to 4.5 I_m and the resultant power is 27 $V_m.I_m$.
* In the B-L connection type of configurations, under uniform irradiance case, the maximum array current in parallel strings is 6 I_m, the voltage is 6 V_m and the array power is 36 $V_m.I_m$. Under different shading cases, the output power of the array is changed.
* In the H-C connection type of configurations, under uniform irradiance case, the array current is 6 I_m, the voltage is 6 V_m and the power is 36 V_mI_m. The output power of an array configuration is changed, and it depends upon the shading pattern.

Theoretical calculations of different solar PV array configurations are presented in Table 2 and 3.

Table 2. Theoretical calculations of the location of GMPP in PV array with S, P and S-P configurations under irradiance of 500 W/m^2

Configuration	**Simple Series**			**Simple Parallel**			**Series-Parallel**		
Shadow Cases	**Array Current (I_{PV})**	**Array Voltage (V_{PV})**	**Array Power (P_{PV})**	**Array Current (I_{PV})**	**Array Voltage (V_{PV})**	**Array Power (P_{PV})**	**Array Current (I_{PV})**	**Array Voltage (V_{PV})**	**Array Power (P_{PV})**
Uniform case	$I_{PV} = I_m$	36 V_m	36 V_m. I_m	I_{PV} =36 I_m	V_m	36 V_m. I_m	I_{PV} = 6 I_m	6 V_m	36 V_m. I_m
Short Narrow	I_{PV} = 0.5 I_m	36 V_m	18 V_m. I_m	I_{PV} =31.5 I_m	V_m	31.5 V_m. I_m	I_{PV} = 4.5 I_m	6 V_m	27 V_m. I_m
Short Wide	I_{PV} = 0.5 I_m	36 V_m	18 V_m. I_m	I_{PV} =28.5 I_m	V_m	28.5 V_m. I_m	I_{PV} = 3 I_m	6 V_m	18 V_m. I_m
Long Narrow	I_{PV} = 0.5 I_m	36 V_m	18 V_m. I_m	I_{PV} =28 I_m	V_m	28 V_m. I_m	I_{PV} = 4 I_m	6 V_m	24 V_m. I_m
Long Wide	I_{PV} = 0.5 I_m	36 V_m	18 V_m. I_m	I_{PV} =24 I_m	V_m	24 V_m. I_m	I_{PV} = 3 I_m	6 V_m	18 V_m. I_m

Table 3. Theoretical calculations of the location of GMPP in SPV Array with TCT configuration under irradiance of 500 W/m^2

Shading Cases	Order of row currents in which the modules are bypassed (I_R)	Array Voltage (V_R)	Array Power ($P_{PV} = V_R.\ I_R$)	Location of GMPP (P_{PV})
Un-Shaded Case (U)	$I_{R6} = 6\ I_m$	$6\ V_m$	$36\ V_m.\ I_m$	***$36\ V_m.\ I_m$***
	$I_{R5} = 6\ I_m$	$6\ V_m$	$36\ V_m.\ I_m$	
	$I_{R4} = 6\ I_m$	$6\ V_m$	$36\ V_m.\ I_m$	
	$I_{R3} = 6\ I_m$	$6\ V_m$	$36\ V_m.\ I_m$	
	$I_{R2} = 6\ I_m$	$6\ V_m$	$36\ V_m.\ I_m$	
	$I_{R1} = 6\ I_m$	$6\ V_m$	$36\ V_m.\ I_m$	
Short Narrow Shading (SNS)	***$I_{R6} = 4.5\ I_m$***	***$6\ V_m$***	***$27\ V_m.\ I_m$***	***$27\ V_m.\ I_m$***
	$I_{R5} = 4.5\ I_m$	$5\ V_m$	$22.5\ V_m.\ I_m$	
	$I_{R4} = 4.5\ I_m$	$4\ V_m$	$18\ V_m.\ I_m$	
	$I_{R3} = 6\ I_m$	$3\ V_m$	$18\ V_m.\ I_m$	
	$I_{R2} = 6\ I_m$	$2\ V_m$	$12\ V_m.\ I_m$	
	$I_{R1} = 6\ I_m$	V_m	$6\ V_m.\ I_m$	
Short Wide Shading (SWS)	***$I_{R6} = 3\ I_m$***	***$6\ V_m$***	***$18\ V_m.\ I_m$***	***$18\ V_m.\ I_m$***
	$I_{R5} = 3\ I_m$	$5\ V_m$	$15\ V_m.\ I_m$	
	$I_{R4} = 4.5\ I_m$	$4\ V_m$	$18\ V_m.\ I_m$	
	$I_{R3} = 6\ I_m$	$3\ V_m$	$18\ V_m.\ I_m$	
	$I_{R2} = 6\ I_m$	$2\ V_m$	$12\ V_m.\ I_m$	
	$I_{R1} = 6\ I_m$	V_m	$6\ V_m.\ I_m$	
Long Narrow Shading (LNS)	***$I_{R6} = 4\ I_m$***	***$6\ V_m$***	***$24\ V_m.\ I_m$***	***$24\ V_m.\ I_m$***
	$I_{R5} = 4\ I_m$	$5\ V_m$	$20\ V_m.\ I_m$	
	$I_{R4} = 4\ I_m$	$4\ V_m$	$16\ V_m.\ I_m$	
	$I_{R3} = 5\ I_m$	$3\ V_m$	$15\ V_m.\ I_m$	
	$I_{R2} = 5\ I_m$	$2\ V_m$	$10\ V_m.\ I_m$	
	$I_{R1} = 6\ I_m$	V_m	$6\ V_m.\ I_m$	
Long Wide Shading (LWS)	***$I_{R6} = 3\ I_m$***	***$6\ V_m$***	***$18\ V_m.\ I_m$***	***$18\ V_m.\ I_m$***
	$I_{R5} = 3\ I_m$	$5\ V_m$	$15\ V_m.\ I_m$	
	$I_{R4} = 3\ I_m$	$4\ V_m$	$12\ V_m.\ I_m$	
	$I_{R3} = 5\ I_m$	$3\ V_m$	$15\ V_m.\ I_m$	
	$I_{R2} = 5\ I_m$	$2\ V_m$	$10\ V_m.\ I_m$	
	$I_{R1} = 5\ I_m$	V_m	$6\ V_m.\ I_m$	

5.4 Simulation Results

The 6×6 solar PV array conventional topologies, mainly S-P, TCT, BL, HC types of models, are developed and simulated in Matlab/Simulink software. The Vikram solar ELDORA 270W [P_{max} is 270W] panel specifications are used in simulation of a 6×6 size SPV array with S-P, TCT, BL and HC configurations under SNS,SWS,LNS,LWS shading cases. The simulation results are tabulated in Table 4, and the maximum PV array powers observed in the TCT topology are 7714 W, 5478 W, 6865 W, and 5284 W under proposed four shading cases, respectively. The output characteristics (V-P) of different array configurations are appeared in Figures 13 to 16.

Table 4. Simulation results of a 6×6 solar PV array configurations under different shading cases

Configuration Vs Shading Cases	Series-Parallel (S-P)	Total-Cross-Tied (TCT)	Bridge-Linked (BL)	Honey-Comb (HC)
	Array Power-P_{PV} (W)			
Uniform case	9620	9620	9620	9620
Short Narrow	***7384***	***7714***	***7565***	***7414***
Short Wide	5412	5478	5407	5434
Long Narrow	6604	6865	6765	6732
Long Wide	5154	5284	5206	5223

i. S-P Configuration P-V Characteristics

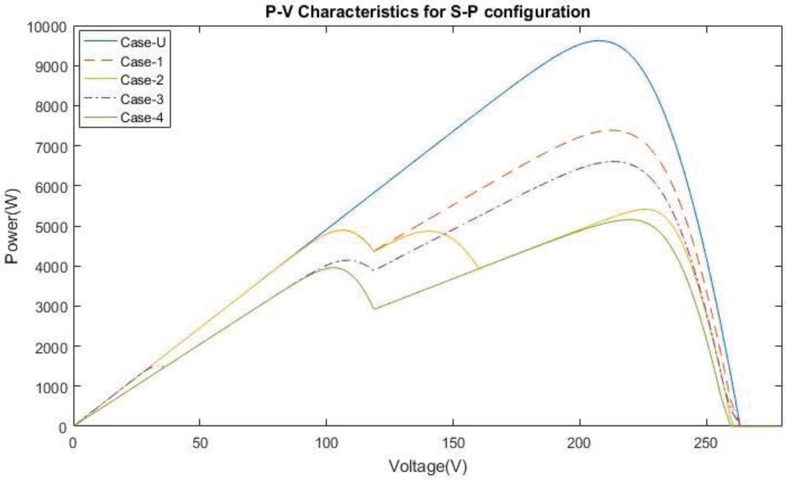

Figure 13. PV Curves for S-P type connection

ii. TCT Configuration P-V Characteristics

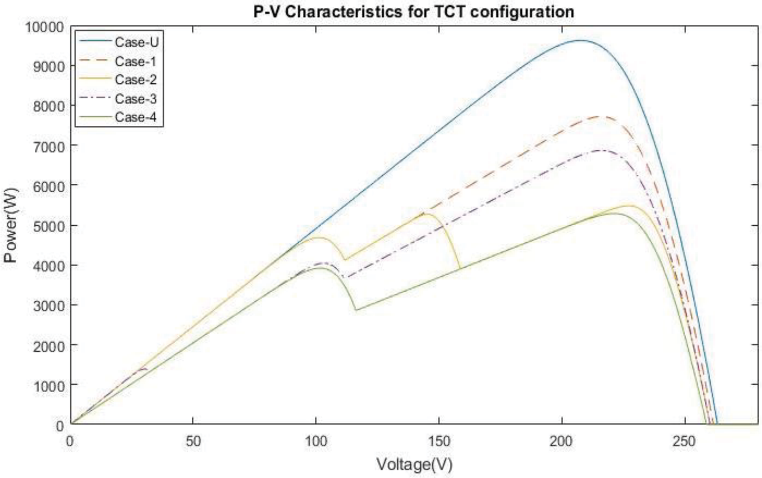

Figure 14. PV Curves for TCT type connection

iii. B-L Configuration P-V Characteristics

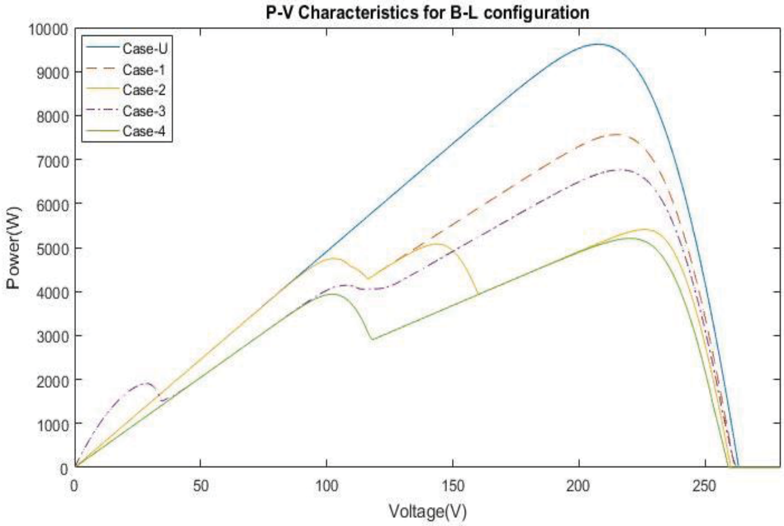

Figure 15. PV Curves for B-L type connection

iv. H-C Configuration P-V Characteristics

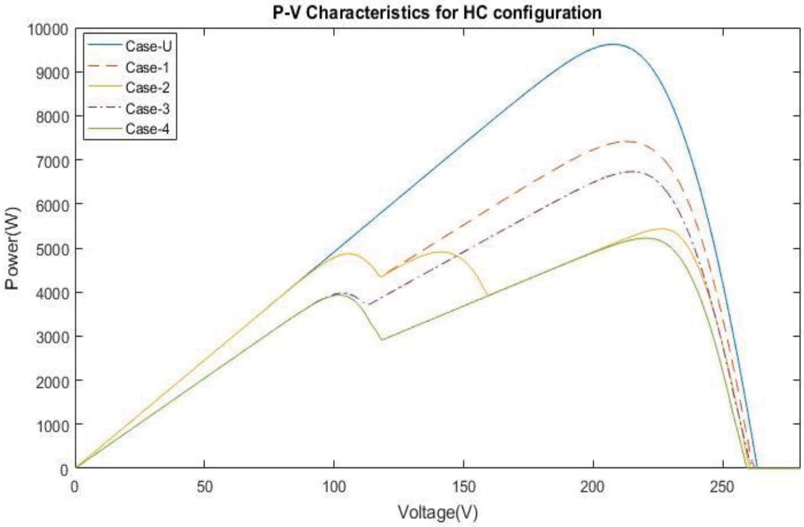

Figure 16. PV Curves for HC type connection

6. CONCLUSIONS

In this paper, mathematical investigation of conventional solar PV array configurations in particularly SS, P, SP, TCT, BL and HC types under uniform irradiance case, *i.e.*, non-shading case and proposed partial shading cases including short narrow, short wide, long narrow and long wide shading cases are presented. The 6×6 size solar PV array configurations are considered for examining under non-shading and partial shading cases. Under various shading cases, each row current is determined based on the order of row currents, in which the modules are bypassed for the identification of a global peak power position in the output characteristics of different PV array configurations. This mathematical analysis is based on the KVL and KCL equations of a different module connections in a PV array. From the theoretical calculations and simulation analysis, the array output power is greater in TCT configuration under short narrow shading conditions. It can be concluded that the energy yield of an array relies upon the shading pattern in the SPV array configurations.

CONFLICTS OF INTEREST

The authors declare that there is no conflict of interests regarding the publication of this paper.

REFERENCES

[1] Fahrenbruch, A., and Bube, R. (2012). *Fundamentals of solar cells: photovoltaic solar energy conversion*, Elsevier

[2] Dirk, A., Assmann, D., Laumanns, U., and Uh, D. (2006). *Renewable energy: a global review of technologies, policies and markets*, Routledge

[3] Kumar, A., Pachauri, R. K., and Chauhan, Y. K. Experimental analysis of SP/TCT PV array configurations under partial shading conditions. In: *Proc., 2016 IEEE 1st International Conference on Power Electronics, Intelligent Control and Energy Systems (ICPEICES)*, pp: 1-6. DOI: 10.1109/icpeices.2016.7853403

[4] Bingöl, O., and Özkaya, B. (2018). Analysis and comparison of different PV array configurations under partial shading conditions. *Solar Energy*, 160, 336-343. DOI: 10.1016/j.solener.2017.12.004

[5] Pendem, S. R., and Mikkili, S. (2018). Modelling and performance assessment of PV array topologies under partial shading conditions to mitigate the mismatching power losses. *Solar Energy*, 160, 303-321. DOI: 10.1016/j.solener.2017.12.010

[6] Nguyen, D., and Lehman, B. A reconfigurable solar photovoltaic array under shadow conditions. In: *Proc., 2008 Twenty-Third Annual IEEE Applied Power Electronics Conference and Exposition*, IEEE, pp: 980-986

[7] Parlak, K. Ş. (2014). PV array reconfiguration method under partial shading conditions. *International Journal of Electrical Power & Energy Systems*, 63, 713-721. DOI: 10.1016/j.ijepes.2014.06.042

[8] Rani, B. I., Ilango, G. S., and Nagamani, C. (2013). Enhanced power generation from PV array under partial shading conditions by shade dispersion using Su Do Ku configuration. *IEEE Transactions on sustainable energy*, 4(3), 594-601

[9] Wang, Y.-J., and Hsu, P.-C. (2011). An investigation on partial shading of PV modules with different connection configurations of PV cells. *Energy*, 36(5), 3069-3078. DOI: 10.1016/j.energy.2011.02.052

[10] Tatabhatla, V. M. R., Agarwal, A., and Kanumuri, T. (2019). Improved power generation by dispersing the uniform and non-uniform partial shades in solar photovoltaic array. *Energy Conversion and Management*, 197, 111825. DOI: 10.1016/j.enconman.2019.111825

[11] Krishna, G. S., and Moger, T. (2019). Enhancement of maximum power output through reconfiguration techniques under non-uniform irradiance conditions. *Energy*, 187, 115917. DOI: 10.1016/j.energy.2019.115917

[12] Raju, V.B., and Chengaiah, Ch. (2019). Performance Analysis of Conventional, Hybrid and Optimal PV Array Configurations of Partially Shaded Modules. *International Journal of Engineering and Advanced Technology*, 9(1), 3061-3073. DOI: 10.35940/ijeat.A1661.109119

[13] Chao, K.-H., Lai, P.-L., and Liao, B.-J. (2015). The optimal configuration of photovoltaic module arrays based on adaptive switching controls. *Energy Conversion and Management*, 100, 157-167. DOI: 10.1016/j.enconman.2015.04.080

[14] Zhu, L., Li, Q., Chen, M., Cao, K., and Sun, Y. (2019). A simplified mathematical model for power output predicting of Building Integrated Photovoltaic under partial shading conditions. *Energy Conversion and Management*, 180, 831-843. DOI: https://doi.org/10.1016/j.enconman.2018.11.036

[15] Belhachat, F., and Larbes, C. (2015). Modeling, analysis and comparison of solar photovoltaic array configurations under partial shading conditions. *Solar Energy*, 120, 399-418. DOI: https://doi.org/10.1016/j.solener.2015.07.039

[16] Xiaoguang Liu and Yuefeng Wang. Reconfiguration Method to Extract more Power from Partially Shaded Photovoltaic Arrays with Series-Parallel Topology. Energies 2019, 12, 1439; DOI:10.3390/en12081439

[17] F. Spertino and J. S. Akilimali. Are Manufacturing I-V and P-V Mismatch and Reverse Currents Key Factors in Large Photovoltaic Arrays?. *IEEE Transactions on Industrial Electronics,* vol. 56, pp. 4520-4531, 2009. DOI: 10.1109/TIE.2009.2025712

Trends in Renewable Energy
OPEN ACCESSISSN:2376-2144
Peer-Reviewed Article
futureenergysp.com/index.php/tre

Business Analytics and IT in Smart Grid – Part 1: The Impact of Measurement Differences on the iSHM Class Map Footprints of Overhead Low-Voltage Broadband over Power Lines Topologies

Athanasios G. Lazaropoulos[1,2,*]

1: School of Electrical and Computer Engineering / National Technical University of Athens / 9 Iroon Polytechniou Street / Zografou, GR 15780
2: Department of Industrial Design and Production Engineering / School of Engineering / University of West Attica / 250 Thivon & P. Ralli / Athens, GR 12244

Received March 25, 2020; Accepted May 4, 2020; Published May 10, 2020

Due to the smart grid (SG) operation, the power utilities are dealing with a cataclysm of big data that demands advanced information technology (IT) infrastructure and business analytics while one cause of this growth is the nature of the power grid operation that demands real-time measurements. In [1], [2], the theoretical framework and the numerical results for the interoperability of Deterministic Hybrid Model (DHM), initial Statistical Hybrid Model (iSHM), the definition procedure and the class maps have been presented for the overhead low-voltage broadband over power lines (OV LV BPL) networks as well as the iSHM footprints. On the basis of the five real indicative OV LV BPL topologies of [1], [2], the impact of measurement differences that follow either continuous uniform distributions (CUDs) or normal distributions (NDs) of different intensities is first highlighted on iSHM footprints.

Keywords: Smart Grid; Broadband over Power Lines (BPL) networks; Power Line Communications (PLC); Distribution and Transmission Power Grids; Capacity, Statistics; Business Analytics; IT; Modeling

---

*Corresponding author: AGLazaropoulos@gmail.com

Tr Ren Energy, 2020, Vol.6, No.2, 156-186. doi: 10.17737/tre.2020.6.2.00117

Nomenclature

AWGN	Additive White Gaussian Noise
BPL	Broadband over Power Lines
BPMN	Business Process Model and Notation
CASD	Channel Attenuation Statistical Distribution
CDF	Cumulative Density Function
CS2 module	Coupling Scheme version 2 module
CUD	Continuous Uniform Distribution
DHM	Deterministic Hybrid Model
EMI	ElectroMagnetic Interference
ICT	Information and Communication Technology
IPSD limits	Injected Power Spectral Density Limits
IT	Information Technology
iSHM	initial Statistical Hybrid Model
LOS	Line-of-Sight
LV	Low Voltage
L1PMA	L1 Piecewise Monotonic Approximation
L2WPMA	L2 Weighted Piecewise Monotonic Approximation
MLE	Maximum Likelihood Estimator
mSHM	modified Statistical Hybrid Model
MTL	Multiconductor Transmission Line
ND	Normal Distribution
OV	Overhead
PSD	Power Spectral Density
PDF	Probability Density Function
SG	Smart Grid
SHM	Statistical Hybrid Model
TIM	Topology Identification Methodology
TL	Transmission Line
WtG	Wire-to-Ground

1. Introduction

To support various SG applications, the vintage transmission and distribution power grids need to obtain additional intelligence by rendering ITs as their key aspect [1]-[3]. Actually, the supported SG applications impose a big data challenge that requires IT infrastructure and advanced business analytics techniques in order to face with the vast amounts of data and their analytics [4], [5]. The adoption of the available SG ICT solutions may help towards the support of reliable and secured bi-directional data communications across the entire power grid, better power grid monitoring and management, further data integration of other power grid related sources, the improvement of power grid efficiency and the deal with fervent issues of modern energy networks [6]. Among the available SG ICT solutions, BPL networks attract the great attention from the stakeholders among the other available communications technologies since these networks can exploit the already installed wired power grid infrastructure without the need for additional wiring costs except for the ones that are related with network equipment [7]-[9].

As the operation of BPL networks is concerned across the power grid, a lot of evolution steps took place recently by focusing on the statistical processing of the communications channel that is proven to be a hostile medium for communications as the infrastructure and the equipment of transmission and distribution power grids are designed to deliver power rather information [1], [10]-[14]. On the basis of the well-validated DHM for transmission and distribution power grids [10], [11], [15]-[18], the proposed SHM framework, which consists of its iSHM and mSHM versions, has recently been proposed in [19]-[21]. Also, new tools that are integrated with SHM and further exploit its operation are available in [1], [2], [22]-[24], namely: (i) *The definition procedure*: This procedure enriches the existing BPL topology classes with virtual BPL topology subclasses statistically defined in terms of the applied SHM version and its corresponding successful CASD parameter pairs (i.e, MLEs and CDF for iSHM and mSHM CASDs, respectively); (ii) *The class maps*: 2D contour plots illustrate the borders between adjacent BPL topology classes while CASD parameter pairs with the corresponding BPL topology subclass average capacities are represented on the class map; and (iii) *The class map footprints of critical events of the operation of power grids*: The real OV LV BPL topologies, the real OV LV BPL topologies with a sole branch line fault and the real OV LV BPL topologies with a single hook for energy theft can be illustrated as superimposed white areas upon the class maps for given power grid type, SHM version, CASD, coupling scheme, IPSD limits and noise levels. In accordance with [2], the most descriptive class map footprints are the iSHM ones, which are going to be exploited in this paper, since their representation depends on a straightforward procedure rather than the approximation of mSHM ones. Until now, the results of iSHM and its accompanying tools have exploited as inputs the theoretical numerical results came from the operation of DHM.

Already been mentioned in [25]-[29], measurement differences between the experimental and theoretical results may occur due to a number of practical reasons and "real-life" difficulties thus having as a result the influence of the DHM numerical results in terms of the transfer function and capacity and, from now on, the destabilization of the entire iSHM framework operation (*i.e.*, iSHM results as well as the accompanying tools). In accordance with [25], [26], [29], [30], a typical scenario to take into account measurement differences during the BPL network analysis is their handling as error distributions such as CUDs and NDs that are superimposed to the coupling scheme transfer function theoretical numerical results of DHM. In this paper, the impact of measurement differences as CUDs and NDs on the iSHM framework operation is first assessed through the iSHM class map footprints of a list of real indicative OV LV BPL topologies.

The rest of this paper is organized as follows: In Section II, the interaction among DHM, iSHM, the definition procedure, the class maps and footprints of OV LV BPL topologies is briefly outlined. Section III deals with the measurement differences and the mathematics concerning the integration of the corresponding measurement difference CUDs and NDs in SHM and its accompanying tools. In Section IV, the numerical results regarding the impact of measurement differences on the iSHM footprints of the aforementioned real indicative OV LV BPL topologies are shown. Section V concludes this paper.

2. The Basics of DHM, iSHM, the Definition Procedure, the Class Maps and the Footprints of OV LV BPL Topologies

Prior to examine the interaction of DHM, iSHM, the definition procedure, the class maps and the footprints of OV LV BPL topologies, brief details concerning the applied OV LV MTL configuration and indicative OV LV BPL topologies are given in Sec.2.1. Helpful operation details for DHM, iSHM, the definition procedure, the class maps and the footprints of OV LV BPL topologies are reported in Secs 2.2-2.7, respectively.

2.1 OV LV MTL Configuration and Indicative OV LV BPL Topologies

As the BPL signal propagation is examined, the typical OV LV MTL configuration that is applied in this paper is shown in Fig. 1(a) of [1]. Note that the applied OV LV MTL configuration consists of four parallel non-insulated conductors (*i.e.*, $n^{\mathrm{OVLV}}=4$), which are hung in vertical arrangement. More details concerning the MTL configuration dimensions, the conductor dimensions and the conductor structure are given in [18], [31] while the ground properties and the role of ground during the BPL signal propagation over OV power lines are detailed in [10], [18], [32]-[36].

As the BPL signal transmission is studied, the typical OV LV BPL topology that is used in this paper is shown in Fig. 1(b) of [1]. In fact, the examined typical OV LV BPL topology is the division result of OV LV BPL networks into simpler topologies of fixed end-to-end connection length (say, 1000m in this paper) but different topological characteristics (say, number of branches, distances between branches and branch lengths) that depend on the underlying power grid. In accordance with [37], [38], [18], [39], five OV LV BPL topology classes (*i.e.*, “LOS”, rural, suburban, urban A and urban B) with their respective representative OV LV BPL topologies, which act as the real indicative OV LV BPL topologies of this paper, can be defined so that a classification of all OV LV BPL topologies (*i.e.*, either real or virtual ones) can be made in terms of their capacity. In Table 1 of [1], the five real indicative OV LV BPL topologies of this paper are reported as well as their topological characteristics.

2.2 DHM

With reference to BPMN diagrams of iSHM [1], [19], [21], it is evident that the numerical results of DHM act as the cornerstone of iSHM, class maps and footprints. DHM is a well validated model that has extensively been employed to examine the behavior of various transmission and distribution BPL networks [10], [11], [15]-[18], [32], [40]-[43]. In general terms, DHM consists of four interconnected submodules; say, two internal submodules (*i.e.*, the bottom-up and top-down approach modules) and two external ones (*i.e.*, the coupling scheme and the capacity computation modules). The numerical results of DHM that are of interest for iSHM and its tools of this paper are the transfer function and the capacity for given BPL topology, MTL configuration, coupling scheme, EMI policy and noise level. Mathematically, the output of the interconnection of the aforementioned internal submodules is the $n^{\mathrm{OVLV}} \times n^{\mathrm{OVLV}}$ line channel transfer function matrix

$$\mathbf{H}^{\mathrm{OVLV}}\{\cdot\} = \mathbf{T}_{\mathrm{V}}^{\mathrm{OVLV}} \cdot \mathbf{H}^{\mathrm{OVLV,m}}\{\cdot\} \cdot \left(\mathbf{T}_{V}^{\mathrm{OVLV}}\right)^{-1} \tag{1}$$

where $\mathbf{H}^{\mathrm{OVLV,m}}\{\cdot\}$ is the $n^{\mathrm{OVLV}} \times n^{\mathrm{OVLV}}$ modal channel transfer function matrix that mainly depends on the examined OV LV MTL configuration and OV LV BPL topology and $\mathbf{T}_{\mathrm{V}}^{\mathrm{OVLV}}$ is a $n^{\mathrm{OVLV}} \times n^{\mathrm{OVLV}}$ matrix that depends on the frequency, the physical properties of the TLs and the geometry of the OV LV MTL configuration. With reference to eq. (1), the output of the coupling scheme module is the coupling scheme channel transfer function that relates output and input BPL signal through

$$H^{\mathrm{OVLV},C}\{\cdot\} = [\mathbf{C}^{\mathrm{out}}]^{\mathrm{OVLV},C} \cdot \mathbf{H}^{\mathrm{OVLV}}\{\cdot\} \cdot [\mathbf{C}^{\mathrm{in}}]^{\mathrm{OVLV},C} \tag{2}$$

for given coupling scheme where $[\cdot]^{\mathrm{c}}$ denotes the applied coupling scheme among the supported coupling schemes of CS2 module [44], [45], $\mathbf{C}^{\mathrm{in}}$ is the input coupling $n^{\mathrm{OVLV}} \times 1$ column vector that deals with the BPL signal injection interface and is defined by the applied coupling scheme and $\mathbf{C}^{\mathrm{out}}$ is the ouput coupling $1 \times n^{\mathrm{OVLV}}$ line vector that deals with the BPL signal extraction interface and is also defined by the applied coupling scheme. With reference to eq. (2), the output of the capacity computation module is the capacity C that is given by [1], [37], [46], [47]

$$C = f_s \sum_{q=1}^{Q} \log_2 \left\{1 + \left[\frac{\langle p(f_q)\rangle_{\mathrm{L}}}{\langle N(f_q)\rangle_{\mathrm{L}}} \cdot \left|H^{\mathrm{OVLV,C}}(f_q)\right|^2\right]\right\} \tag{3}$$

$$f_q = 3\mathrm{MHz} + (q-1) \cdot f_s,\ q = 1, \ldots, Q \tag{4}$$

$$\mathbf{f} = [f_1 \quad \cdots \quad f_q \quad \cdots \quad f_Q],\ q = 1, \ldots, Q \tag{5}$$

where f_q is the flat-fading subchannel start frequency, f_s is the flat-fading subchannel frequency spacing, Q is the number of subchannels in the examined 3-30MHz frequency range, $\mathbf{f}$ is the 1×Q line vector that consists of the flat-fading subchannel start frequencies f_q, $p(\cdot)$ is the applied IPSD limits in dBm/Hz, $N(\cdot)$ is the applied AWGN PSD levels in dBm/Hz and $\langle\cdot\rangle_{\mathrm{L}}$ is an operator that converts dBm/Hz into a linear power ratio (W/Hz). More details concerning the applied coupling scheme, IPSD limits and AWGN PSD levels are given in [1], [2].

2.3 iSHM

Already been mentioned, SHM consists of iSHM and mSHM. With reference to the BPMN diagrams of iSHM and mSHM [1], [19], iSHM consists of six Phases (*i.e.*, Phase A-F) while each Phase is clearly defined in terms of its procedure and the input / output files.

In accordance with [19] and with reference to Fig. 2(a) of [1], the operation of iSHM can be described through the concatenation of six Phases (*i.e.*, Phases A-F).

The input of iSHM, which coincides with the input parameters of its Phase A, is the topological characteristics of the examined real indicative OV LV BPL topologies, the applied coupling scheme, IPSD limits and AWGN PSD levels. The output of iSHM, which coincides with the output of Phase F, is the capacity range of each OV LV BPL topology main subclass for given CASD when each OV LV BPL topology main subclass consists of its representative real indicative OV LV BPL topology from Phase A and P statistically equivalent virtual OV LV BPL topologies to the real indicative one in terms of CASD MLEs. Note that iSHM may support five CASDs with their corresponding MLEs (*i.e.*, Gaussian, Lognormal, Wald, Weibull and Gumbel CASDs) while each CASD exhibits different performance depending on the input parameters of Phase A.

In accordance with [2], the performance of iSHM CASDs is assessed in terms of the best percentage change and average percentage change results that are performance capacity metrics. By evaluating the CASD approximation accuracy to the real capacity results, the best CASD is chosen for iSHM and are further applied during the definition procedure, class maps and footprints.

2.4 The Definition Procedure and Class Maps

As already been identified in [23], [24], [48], OV LV BPL topology classes are underrepresented since iSHM only exploits the five main OV LV BPL topology subclasses in order to define the respective classes for given CASD. The definition procedure, which has been introduced in [48], clearly solves this issue by statistically defining and inserting virtual indicative OV LV BPL topologies with their respective subclasses in the existing five OV LV BPL topology classes of iSHM by appropriately computing MLEs of iSHM CASDs. An appropriate flowchart that describes the definition procedure of iSHM for OV LV BPL networks is given in Fig. 3(a) of [1].

In accordance with [48], as the definition procedure of iSHM is concerned, it consists of eleven steps (*i.e.*, FL1.01-FL1.11) that can be further categorized into three groups (*i.e.*, Group 1.A-1.C). The input of the iSHM definition procedure is the five main OV LV BPL topology subclasses with their respective representative real indicative OV LV BPL topologies for given CASD. The output of the iSHM definition procedure is the class map that is a 2D contour plot where (i) each CASD parameter pair is corresponded to its OV LV BPL topology subclass average capacity; (ii) real and virtual OV LV BPL topology subclasses are described by corresponding CASD parameter pairs; (iii) the borders between the OV LV BPL topology classes are illustrated; and (iv) by taking into the capacity arrangement of OV LV BPL topology subclasses and the borders between the OV LV BPL topology classes, OV LV BPL topology class areas can be demonstrated.

In Secs 2.3 and 2.4, DHM, iSHM, definition procedure and class maps have been presented that form all together an interconnected system but with specified settings. The set of the default operation settings that are used in this paper are simply reported in Sec3.4 of [1] as a whole.

2.5 iSHM Footprints of Real OV LV BPL Topologies on Class Maps

The theoretical definition of footprints has been presented in [1] while the first numerical results concerning the application of footprints during critical events of the operation of OV LV power grids have been demonstrated in [2], say, the iSHM footprints of the real OV LV BPL topologies, of the OV LV BPL topologies with a sole branch line fault and of the OV LV BPL topologies with a single hook for energy theft.

As the iSHM footprints of the real OV LV BPL topologies are of interest in this paper, their computation is based on TIM that allows the accurate identification of an OV LV BPL topology with respect to its topological characteristics (*i.e.*, number of branches, length of branches, length of main distribution lines and branch terminations) by applying piecewise monotonic data approximations even if significant measurement differences may occur [49]-[51]. In fact, the computation of footprints is feasible by exploiting: (i) the OV LV BPL topology database of TIM that consists of OV LV BPL topologies with their respective theoretical and measured coupling scheme channel transfer functions when appropriate TIM BPL topology database specifications (e.g., the maximum number of branches, the length spacing for both branch distance and branch length and the maximum branch length) are assumed; and (ii) the computation of CASD MLEs of each OV LV BPL topology of the TIM BPL topology database for given best CASD for the preparation of the iSHM footprint [1]. As been demonstrated in [2], iSHM footprints of the real OV LV BPL topologies without measurement differences can be shown as areas of superimposed white spots upon the iSHM class maps for given power grid type, CASD, coupling scheme, IPSD limits and noise limits. By studying iSHM footprints of the real OV LV BPL topologies of [2], it is clear that the footprint extent of the real OV LV BPL topologies remains a small area of the respective class maps thus highlighting the significant and successful role of the respective definition procedures towards the enrichment of OV LV BPL topology classes with virtual OV LV BPL topologies.

Although iSHM footprints of the real OV LV BPL topologies graphically reveal the internal zones of the respective class maps where real OV LV BPL topologies can be located, the measurement differences during the computation of the coupling scheme transfer functions have been ignored in [2]. In this paper, the option of the TIM OV LV BPL topology database that considers measurement differences during the computation of coupling scheme transfer functions is activated thus allowing the impact assessment of measurement differences when various distributions are applied. In the following Section, the mathematics of the measurement difference distributions are reported as well as their interaction with DHM, iSHM, definition procedures, class maps and footprints. Note that although default operation settings have been assumed in Sec 2.4 of [2] for the interaction of iSHM footprints with the remaining set (*i.e.*, DHM, iSHM, definition procedures and class maps), there are no need for these assumptions here since the impact of measurement differences is going be studied with reference to the five real indicative OV LV BPL topologies of Table 1 of [1].

3. The Involvement of Measurement Differences from DHM to iSHM Footprints

In this Section, the way the measurement differences are taken into account in DHM are presented. In addition, the approach and the settings for the study of iSHM footprints when measurement differences are applied are reported.

3.1 Measurement Differences in DHM

From DHM to iSHM footprints, the theoretical computation of the coupling scheme channel transfer function, which is mathematically described in eq. (2), has been applied so far since no measurement differences have been assumed. However, a set of practical reasons and "real-life" conditions, which can be grouped into six categories [25], [27], [52], are taken into account in this paper so that the role and the effect of measurement differences can be further investigated. In accordance with [25], [27], [52] and eq. (2), the measured coupling scheme transfer function $\overline{H_{d1,d2,i}^{\text{OVLV},C,D}}\{\cdot\}$ after the consideration of measurement differences is determined by

$$\overline{H_{d1,d2,i}^{\text{OVLV},C,D}}\left(f_q\right) = H^{\text{OVLV},C}\left(f_q\right) + e_{d1,d2,i}^{D}\left(f_q\right),\ q=1,\ldots,Q,\ i=1,\ldots,I \qquad (6)$$

where $[\cdot]^D$ denotes the applied measurement difference distribution –either CUD or ND–, $d1$ is the first parameter of the applied measurement difference distribution (the minimum value $-a_{\text{CUD}}$ or the mean μ_{ND} of CUD or ND, respectively), $d2$ is the second parameter of the applied measurement difference distribution (the maximum value a_{CUD} or the standard deviation σ_{ND} of CUD or ND, respectively), $e_{d1,d2,i}^{D}\left(f_q\right)$ is the measurement difference at frequency f_q for given measurement difference distribution, I is the number of different $1\times Q$ line vectors of measurement differences per applied measurement difference distribution, first and second parameter and i indicates the i^{th} among I line vectors of measurement differences. In this paper, 100 line vectors of measurement differences are going to be assumed per applied measurement difference distribution, first and second parameter (I=100).

3.2 Measurement Differences and Settings for the SHM Footprints

In order to highlight the impact of measurement differences on iSHM footprints for the five real indicative OV LV BPL topologies of Table 1 of [1], the iSHM class map that is shown in Fig. 1 of [2] is adopted as the graphical basis. With reference to the five real indicative OV LV BPL topologies of Table 1 of [1] and the BPMN diagrams of iSHM [1], [19], it is evident that the applied theoretical coupling scheme transfer functions are going to be replaced by the measured ones, which are described in eq. (6), thus directly affecting the output of DHM module of Phase A of the iSHM BPMN diagrams –see Fig. 2(a) of [1], respectively–.

To illustrate the impact of each line vector of measurement differences on the class maps of each real OV LV BPL topology of Table 1 of [1], the corresponding measured coupling scheme transfer function is accompanied by: (i) the respective MLEs of the Weibull CASD as described in iSHM BPMN diagram Phase C of Fig. 2(a) of [1] (*i.e.*, MLE computation module). Here, it should be noted that the Weibull CASD has been verified to be the best CASD for OV LV BPL topologies in [2]; and (ii) the capacity; when the default operation settings of Sec.3.4 of [1] are assumed.

As the iSHM footprint of each real OV LV BPL topology of Table 1 of [1] is considered for given measurement difference distribution, first and second parameter, the same procedure that is presented in [1] for the iSHM footprint of real OV LV BPL topologies is also followed here but with the following two differences: (i) Only the five real OV LV BPL topologies of Table 1 of [1] are used and not the entire TIM OV LV BPL topology database; and (ii) for each of the five real OV LV BPL topologies of Table 1 of [1], 100 white spots are expected to appear on Weibull CASD class maps as footprint that correspond to the respective combination of Weibull CASD MLEs and capacity of the 100 line vectors of measurement differences that are superimposed to the coupling scheme transfer function of each of the five real OV LV BPL topologies of Table 1 of [1].

4. Numerical Results and Discussion

In this Section, numerical results assessing the impact of measurement differences on iSHM footprints of OV LV BPL topologies are demonstrated. First, the effect of the different measurement distributions (*i.e.*, CUD or ND) is highlighted through the iSHM footprints for the five real OV LV BPL topologies of Table 1 of [1]. Second, the sensitivity of the aforementioned real OV LV BPL topologies to the measurement differences is revealed through their iSHM footprints. Third, for given real OV LV BPL topology, the effect of the intensity of measurement differences, say, the change of the first and second parameter values of the CUD and ND measurement distributions, on iSHM footprints is revealed.

4.1 iSHM Class Maps of OV LV BPL Topologies

In accordance with the iSHM definition [1], [19], [20], the CASD MLEs of iSHM are computed at the Phase C of Fig. 2(a) of [1]. As the default operation settings have been assumed in [1], MLEs of the Gaussian, Lognormal, Wald, Weibull and Gumbel CASDs of iSHM have been reported in Table 1 of [2] for the main subclasses of the real indicative OV LV BPL topologies of Table 1 of [1]. Their capacity estimation performance of CASDs of iSHM has been benchmarked via the percentage change and the average absolute percentage change of Table 2 of [2]. In accordance with Table 2 of [2], Weibull CASD performs the best performance among the available iSHM CASDs with respect to the percentage change and average absolute percentage change in all the examined OV LV BPL topology main subclasses. Therefore, only Weibull CASD is going to be applied during the following subsections. In accordance with [2], [23], [24], the iSHM class map of OV LV BPL topologies is plotted in Fig. 1 with respect to $\hat{a}_{\mathrm{MLE}}^{\mathrm{Weibull}}$, $\hat{\beta}_{\mathrm{MLE}}^{\mathrm{Weibull}}$ and the average capacity of each OV LV BPL topology subclass.

4.2 iSHM Footprints of Measurement Differences – The Effect of the Different Distributions of Measurement Differences on OV LV BPL Topologies

The impact of measurement differences on iSHM class maps of OV LV BPL topologies is examined via footprints. Actually, the effect of the different distributions of measurement differences (*i.e.*, CUD or ND) and the behavior of each of the real indicative OV LV BPL topologies when measurement differences are applied are going to be studied in this subsection. With reference to the iSHM class map of Fig. 1, the iSHM footprint of the real indicative OV LV BPL urban case A is illustrated as superimposed white spots on class maps in Fig. 2(a). Note that the CUD measurement difference of maximum value a_{CUD} of 3dB and 100 line vectors of random measurement differences of the aforementioned CUD are assumed during the preparation of Fig. 2(a). In Figs. 2(b)-(e), similar footprints with Fig. 2(a) are illustrated but for the case of urban case B, suburban case, rural case and "LOS" case, respectively, when the same 100 line vectors of measurement differences are applied. In Figs. 3(a)-(e), similar footprints with Figs. 2(a)-(e) are given but for the case of ND measurement differences of mean μ_{ND} and standard deviation σ_{ND} that are equal to 0dB and 3/2dB, respectively. Note that the same 100 line vectors of ND measurement differences are applied among Figs. 3(a)-(e).

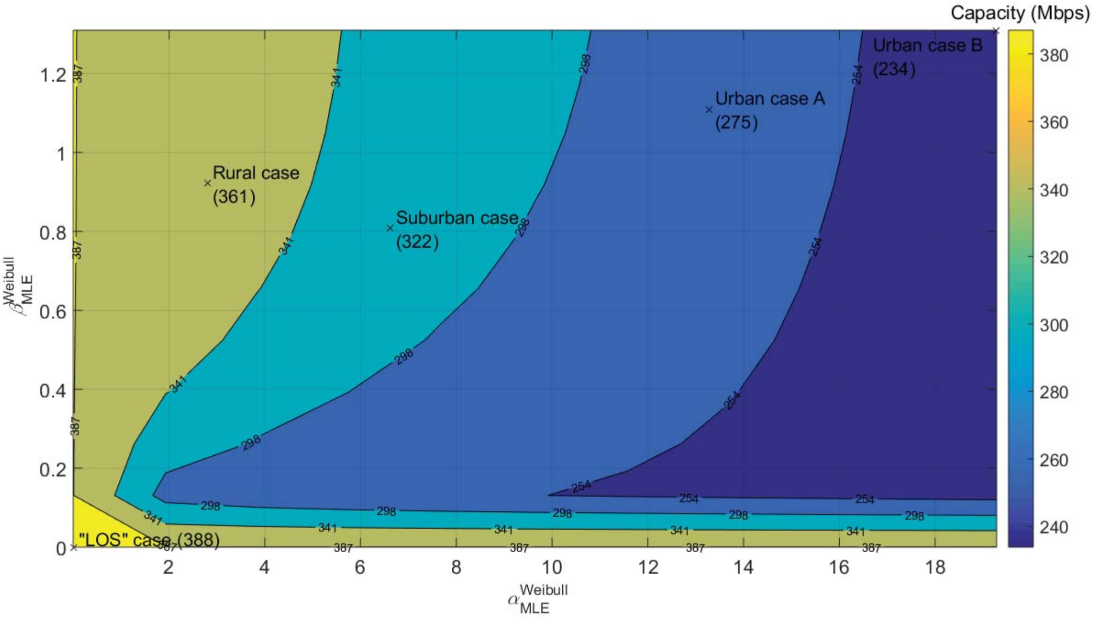

Fig. 1. iSHM class map of OV LV BPL topologies when 3-30MHz frequency band, WtG[1] coupling scheme and FCC Part 15 are assumed [2].

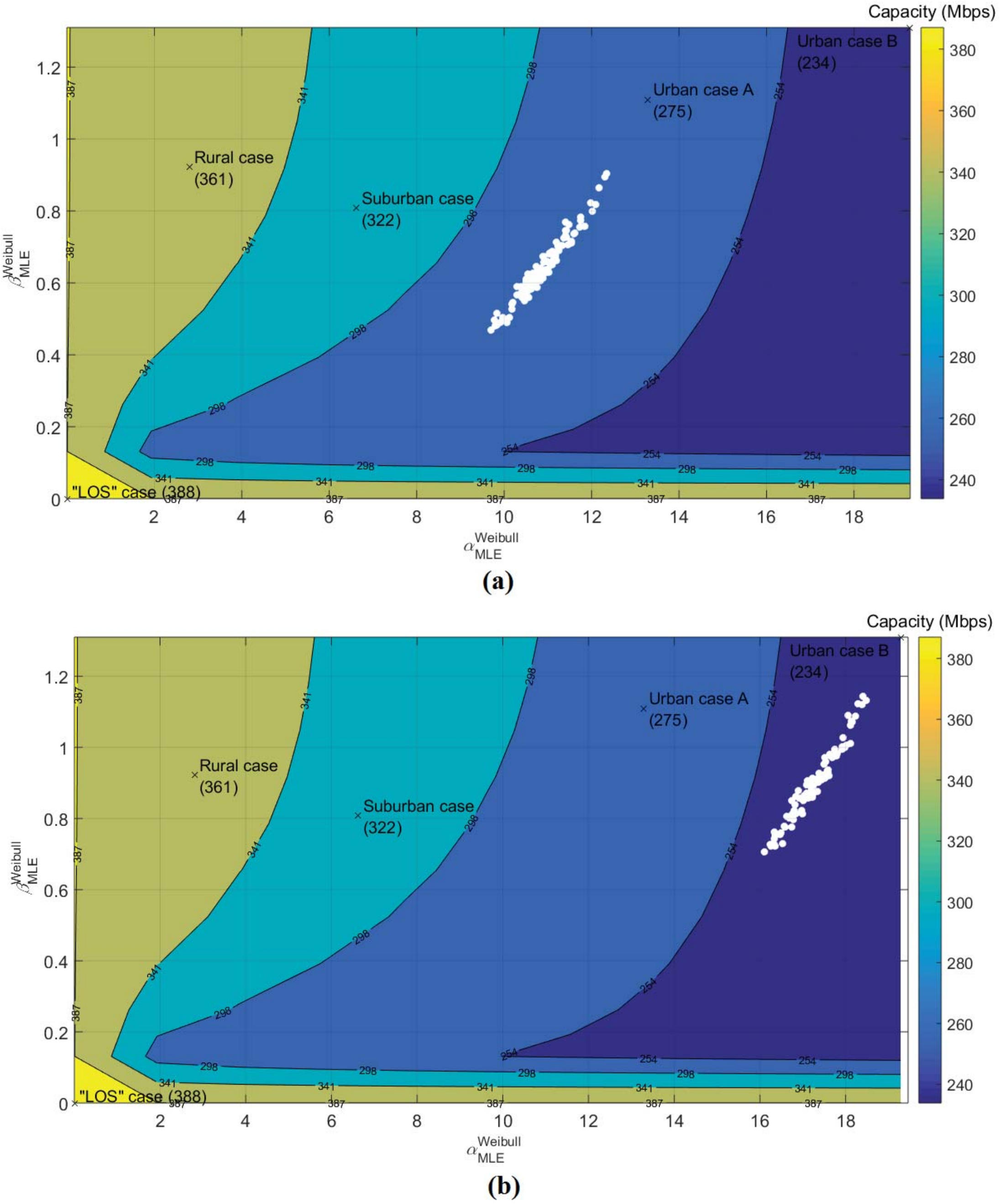
Capacity (Mbps)
380
360
340
320
300
280
260
240
Urban case B
(234)
Urban case A
(275)
Rural case
(361)
Suburban case
(322)
"LOS" case (388)
387
341
298
254
$\beta_{MLE}^{Weibull}$
0
0.2
0.4
0.6
0.8
1
1.2
$\alpha_{MLE}^{Weibull}$
2
4
6
8
10
12
14
16
18

(a)

(b)

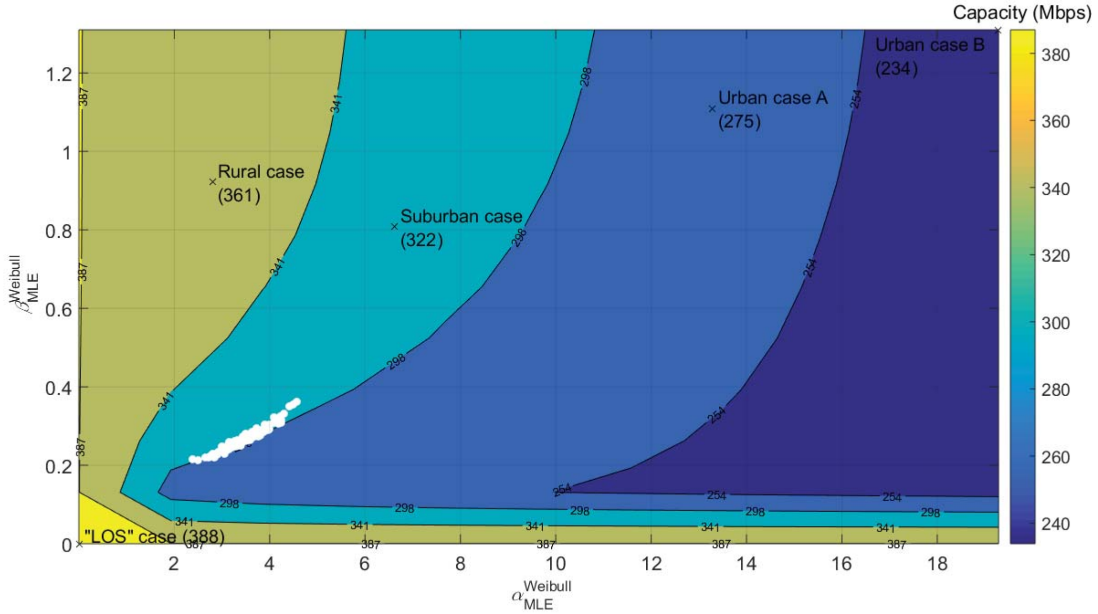
Capacity (Mbps)
380
360
340
320
300
280
260
240
Urban case B
(234)
Urban case A
(275)
Rural case
(361)
Suburban case
(322)
"LOS" case (388)
387
341
298
254
$\beta_{MLE}^{Weibull}$
1.2
1
0.8
0.6
0.4
0.2
0
2
4
6
8
10
12
14
16
18
$\alpha_{MLE}^{Weibull}$

(c)

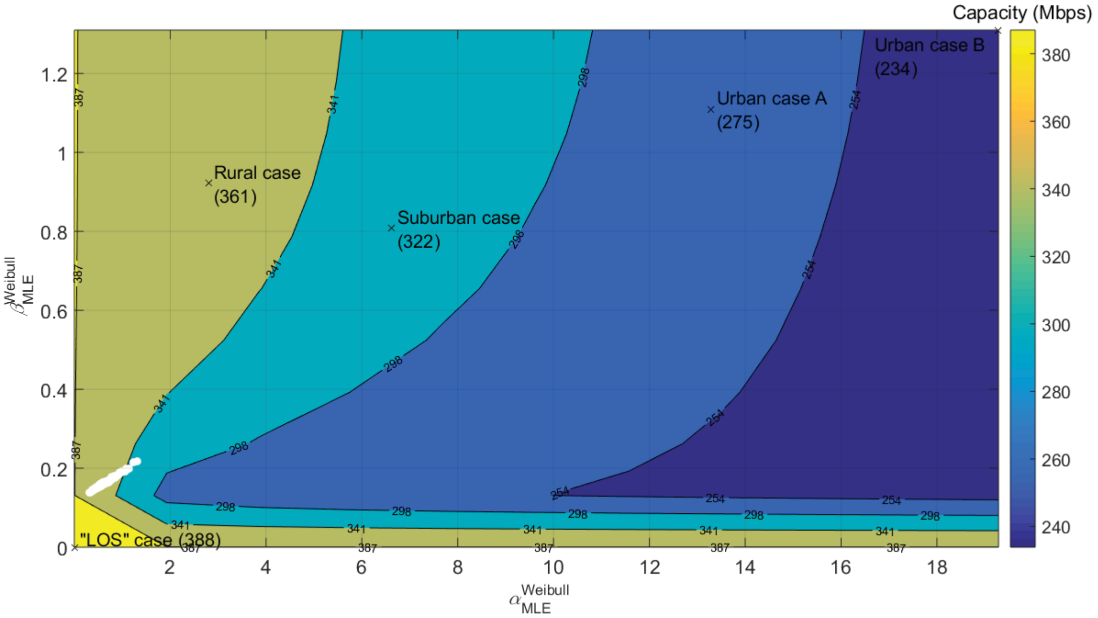
Capacity (Mbps)
380
360
340
320
300
280
260
240
Urban case B
(234)
Urban case A
(275)
Rural case
(361)
Suburban case
(322)
"LOS" case (388)
387
341
298
254
$\beta_{MLE}^{Weibull}$
1.2
1
0.8
0.6
0.4
0.2
0
2
4
6
8
10
12
14
16
18
$\alpha_{MLE}^{Weibull}$

(d)

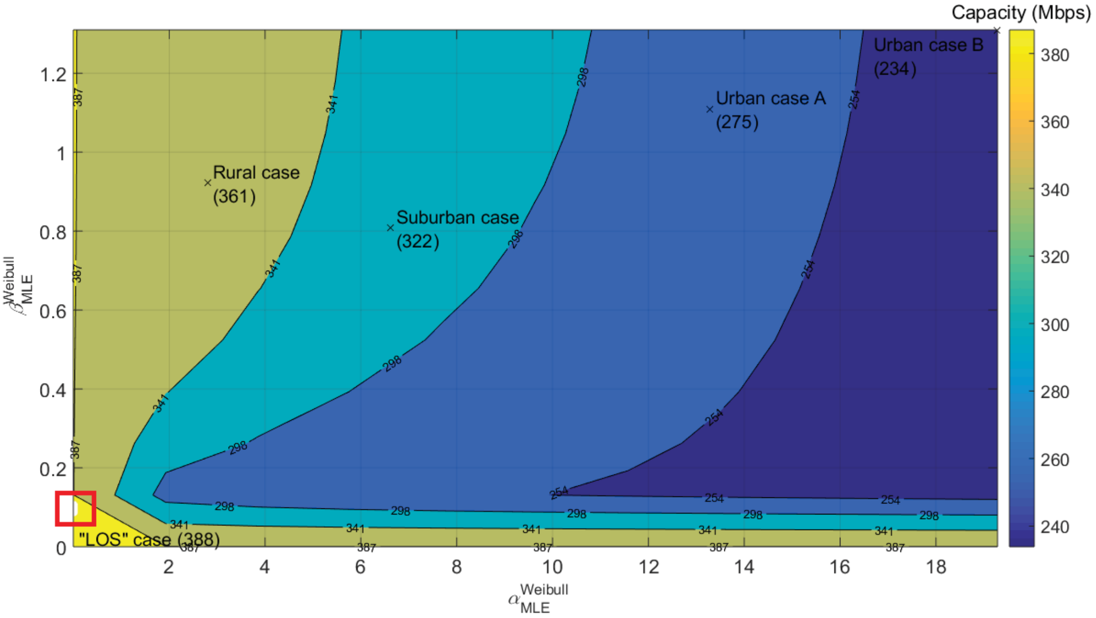

(e)

Fig. 2. iSHM footprints of the real indicative OV LV BPL topologies when 3-30MHz frequency band, WtG[1] coupling scheme, FCC Part 15 and CUD measurement differences of maximum value a_{CUD} = 3dB are assumed. (a) Urban case A. (b) Urban case B. (c) Suburban case. (d) Rural case. (e) "LOS" case.

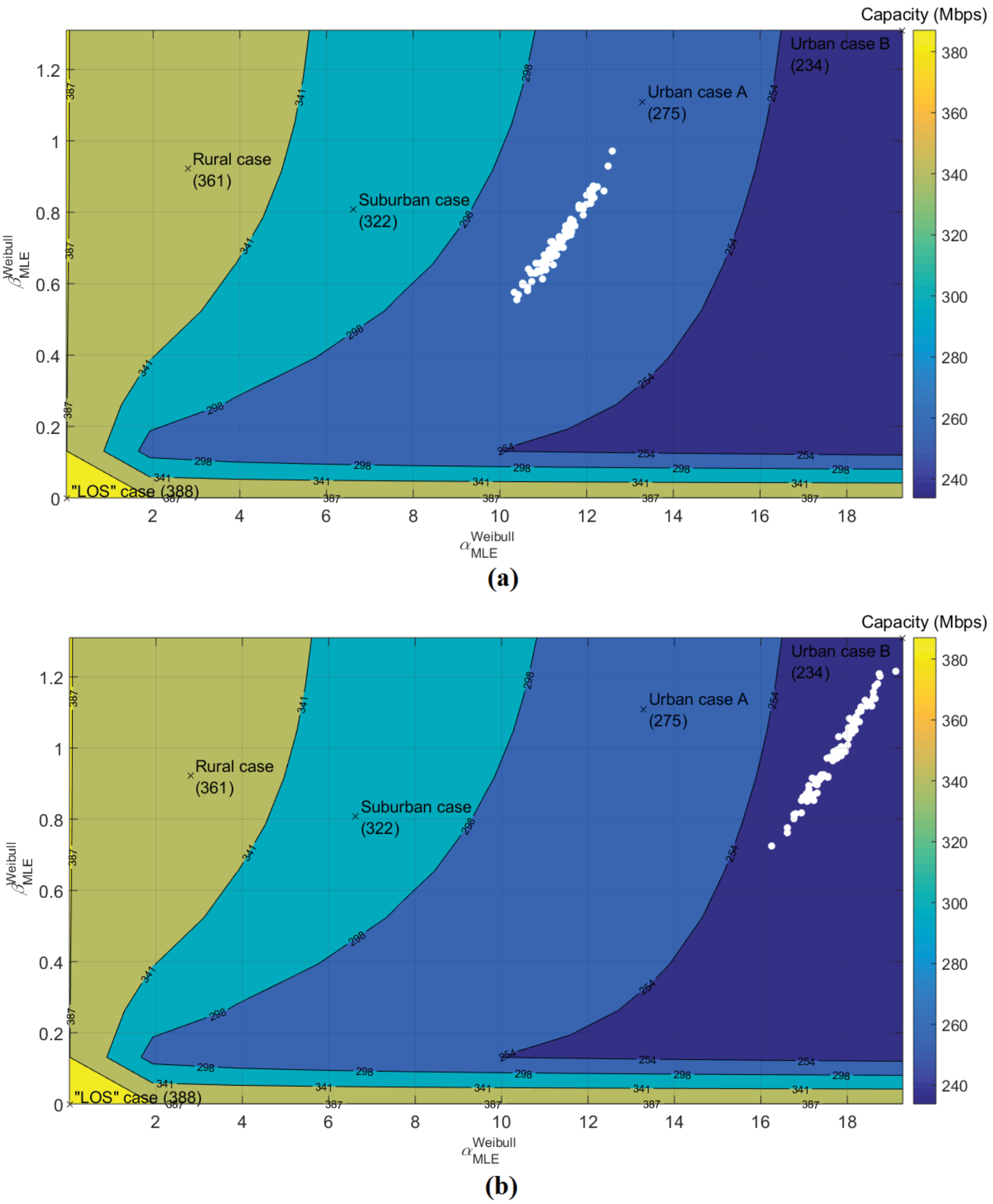
Capacity (Mbps)
380
360
340
320
300
280
260
240
Urban case B
(234)
Urban case A
(275)
Rural case
(361)
Suburban case
(322)
"LOS" case (388)
387
341
298
254
$\beta_{\mathrm{MLE}}^{\mathrm{Weibull}}$
$\alpha_{\mathrm{MLE}}^{\mathrm{Weibull}}$
0
0.2
0.4
0.6
0.8
1
1.2
2
4
6
8
10
12
14
16
18
(a)
(b)

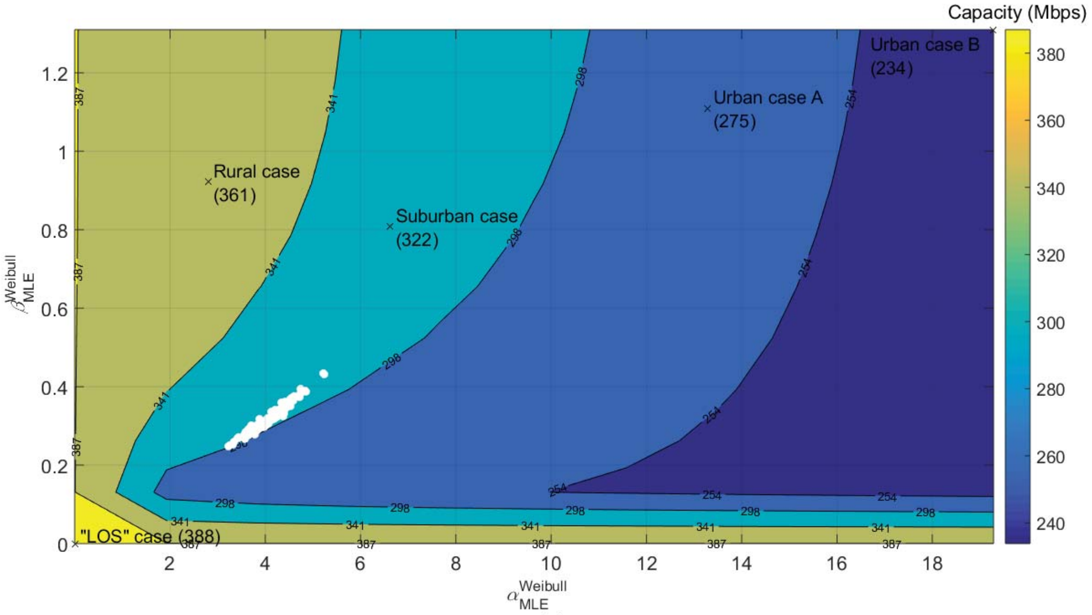
Capacity (Mbps)
380
360
340
320
300
280
260
240
Urban case B
(234)
Urban case A
(275)
Rural case
(361)
Suburban case
(322)
"LOS" case (388)
387
341
298
254
1.2
1
0.8
0.6
0.4
0.2
0
2
4
6
8
10
12
14
16
18
$\beta_{MLE}^{Weibull}$
$\alpha_{MLE}^{Weibull}$

(c)

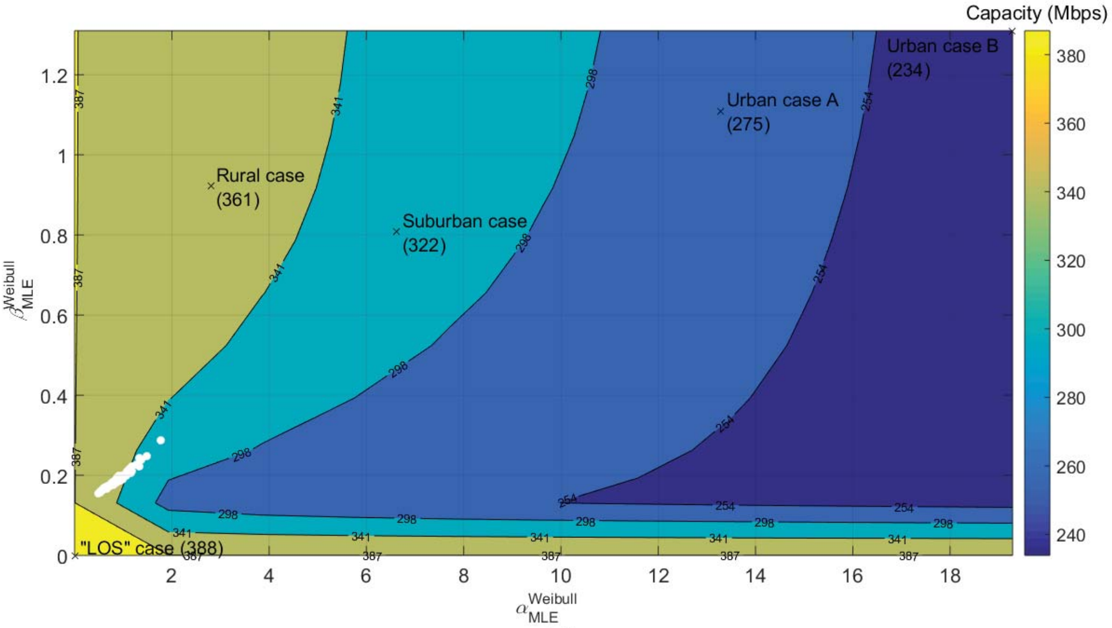
Capacity (Mbps)
380
360
340
320
300
280
260
240
Urban case B
(234)
Urban case A
(275)
Rural case
(361)
Suburban case
(322)
"LOS" case (388)
387
341
298
254
1.2
1
0.8
0.6
0.4
0.2
0
2
4
6
8
10
12
14
16
18
$\beta_{MLE}^{Weibull}$
$\alpha_{MLE}^{Weibull}$

(d)

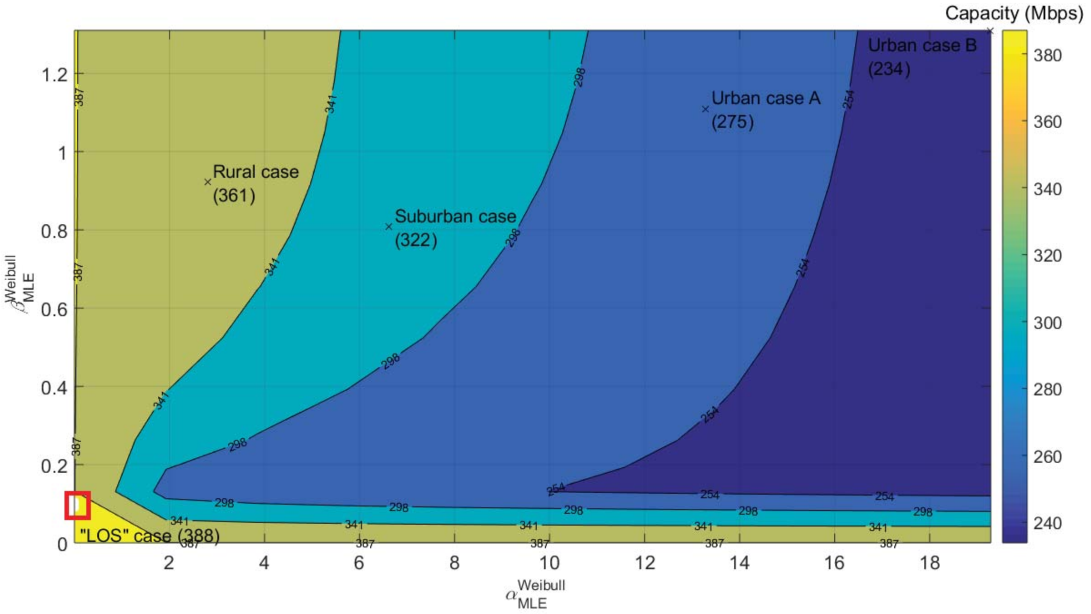

(e)

Fig. 3. Same plots but for ND measurement difference of mean μ_{ND} = 0dB and standard deviation σ_{ND} = 3/2dB.

By observing Figs. 2(a)-(e) and 3(a)-(e), several interesting observations can be made regarding the presence of measurement differences, namely:

- By comparing the aforementioned figures with Figs. 3(a) and 3(b) of [2], it is evident that the iSHM footprint behavior when measurement differences are applied present similarities to the behavior of OV LV BPL topologies with short branches for given OV LV BPL topology class. With reference to the theoretical values of $\hat{a}_{\text{MLE}}^{\text{Weibull}}$ and $\hat{\beta}_{\text{MLE}}^{\text{Weibull}}$ of the real indicative OV LV BPL topologies that act as the representative ones of classes, measurement differences tend to reduce the theoretical values of $\hat{a}_{\text{MLE}}^{\text{Weibull}}$ and $\hat{\beta}_{\text{MLE}}^{\text{Weibull}}$ of the representative OV LV BPL topologies thus forming the iSHM footprint as a diagonal white area of 100 white spots that is located at the lower left area of the examined class with approximate direction to the axis origin.
- As the location and the extent of the iSHM footprint are concerned for given OV LV BPL topology class, the footprint remains almost the same when the standard deviation σ_{ND} of ND measurement differences is approximately equal to the half of the maximum value a_{CUD} of CUD measurement differences while the mean value μ_{ND} of ND measurement differences is equal to zero. This fact can be explained by the distribution of PDFs of the previous CUD and ND measurement differences. Note that the mean μ_{ND} of ND measurement differences is assumed to be equal to 0, hereafter.
- As the maximum value a_{CUD} of CUD measurement differences and the standard deviation σ_{ND} of ND measurement differences remain low –say, Figs. 2(a)-(e) and 3(a)-(e)–, the footprint remains within the class area boundaries for given real indicative OV LV BPL topology.

- The direction of the footprint as well as its location can be explained by the management of the measurement differences with respect to the measured coupling scheme channel attenuation difference between each measured OV LV BPL topology and its respective theoretical “LOS” case [19]. More analytically, as the measured coupling scheme channel attenuation difference between each examined OV LV BPL topology and its respective theoretical “LOS” case is concerned, this should be remain greater or equal to zero (zero restriction of the measured coupling scheme channel attenuation difference). The zero restriction of the measured coupling scheme channel attenuation difference is a crucial condition for the fine iSHM procedure so that the MLE computation module of Phase C of iSHM BPMN diagram can operate and produce the Weibull MLEs of the examined OV LV BPL topology [19]. In accordance with [20], the coupling scheme channel attenuation differences are assumed to be equal to an arbitrarily low value, say 1×10^{-11}, instead of zero so that MLEs of Weibull CASD, which comprise natural logarithms and denominators, can be calculated.
- Depending on the intensity of measurement differences and the examined real indicative OV LV BPL topology, the zero restriction of the measured coupling scheme channel attenuation difference has as a result the greater concentration of channel attenuation difference values at zero that further affects the Weibull CASD approximation and its corresponding MLEs. In fact, as more channel attenuation difference values are located at zero, the approximated Weibull PDF tends to increase its maximum PDF value and to shift he location of the maximum PDF left tthat further entail simultaneously lower values of $\hat{a}_{\mathrm{MLE}}^{\mathrm{Weibull}}$ and $\hat{\beta}_{\mathrm{MLE}}^{\mathrm{Weibull}}$ with respect to the theoretical values of $\hat{a}_{\mathrm{MLE}}^{\mathrm{Weibull}}$ and $\hat{\beta}_{\mathrm{MLE}}^{\mathrm{Weibull}}$ for given real indicative OV LV BPL topology.
- The aforementioned zero restriction of the measured coupling scheme channel attenuation difference explains the dependence of the extent of the footprint on the multipath aggravation of the examined real indicative OV LV BPL topologies. Since coupling scheme transfer functions of less aggravated OV LV BPL topologies (*i.e.*, suburban and rural case) are closer to the “LOS” case, the zero restriction of the measured coupling scheme channel attenuation difference may be activated more frequently than in the cases of aggravated OV LV BPL topologies (*i.e.*, urban case A and B) when measurement differences are applied. Struggling to approximate the greater number of zero channel attenuation differences, the deeper notches due to the remaining measurement differences for given line vector have little effect to the approximated Weibull PDFs and, hence, small differences are expected to the Weibull CASD MLEs for the assumed line vectors of measurement differences thus entailing reduced sizes of the footprints of the less aggravated OV LV BPL topologies.
- As the OV LV BPL “LOS” case is examined as well as its iSHM footprint behavior when measurement differences are applied, the iSHM footprint of “LOS” case is located very close to the axes origin while its extent remains the smallest among the examined ones of real indicative OV LV BPL topologies. As measurement differences are superimposed to the coupling scheme channel attenuation of OV LV BPL “LOS” case, this has as effect almost the half of the measured coupling scheme channel attenuation difference values between the

measured OV LV BPL "LOS" case and the theoretical "LOS" case be equal to zero due to the zero restriction of the measured coupling scheme channel attenuation difference and the other half of the measured coupling scheme channel attenuation difference values be affected by the measurement differences. The latter values are responsible for the little shift of the iSHM footprint of "LOS" case with reference to the axis origin.

Until now, the impact of measurement differences on class maps of the real indicative OV LV BPL topologies has been investigated in terms of the relative location and the extent of the corresponding iSHM footprints. The most important characteristic of measurement differences that is their intensity is studied in the following subsection.

4.3 iSHM Footprints of Measurement Differences – The Effect of the Different Intensities of Measurement Differences on OV LV BPL Topologies

Higher intensities of measurement differences imply higher maximum values a_{CUD} and standard deviations σ_{ND} when CUD and ND measurement differences are applied, respectively. With reference to the iSHM class map of Fig. 1, the iSHM footprint of the real indicative OV LV BPL topology of urban case A is illustrated as superimposed spots on class maps in Fig. 4(a) when the maximum value a_{CUD} of CUD measurement differences ranges from 0B to 15dB. Conversely to Fig. 2(a), only one random line vector of measurement differences is applied for each maximum value a_{CUD} while the color of superimposed spots becomes redder as the maximum value a_{CUD} increases. In Figs. 4(b)-(e), similar footprints with Fig. 4(a) are illustrated but for the case of urban case B, suburban case, rural case and "LOS" case, respectively, when the same line vectors of measurement differences per maximum value a_{CUD} are applied. In Figs. 5(a)-(e), similar footprints with Figs. 4(a)-(e) are given but for the case of ND measurement differences where the mean μ_{ND} is equal to 0dB and the standard deviation σ_{ND} ranges from 0dB to 15/2dB, respectively. Note that the same line vectors of ND measurement differences per standard deviation σ_{ND} are applied in Figs. 5(a)-(e).

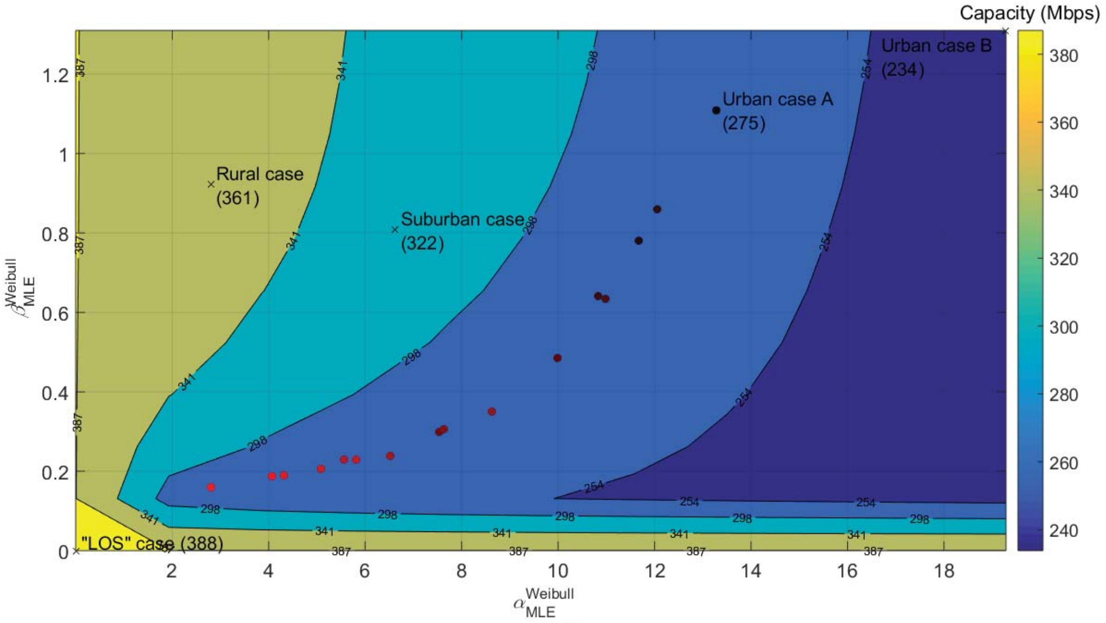
Capacity (Mbps)
380
360
340
320
300
280
260
240
Urban case B
(234)
Urban case A
(275)
Rural case
(361)
Suburban case
(322)
"LOS" case (388)
387
341
298
254
$\beta_{MLE}^{Weibull}$
$\alpha_{MLE}^{Weibull}$
0
0.2
0.4
0.6
0.8
1
1.2
2
4
6
8
10
12
14
16
18

(a)

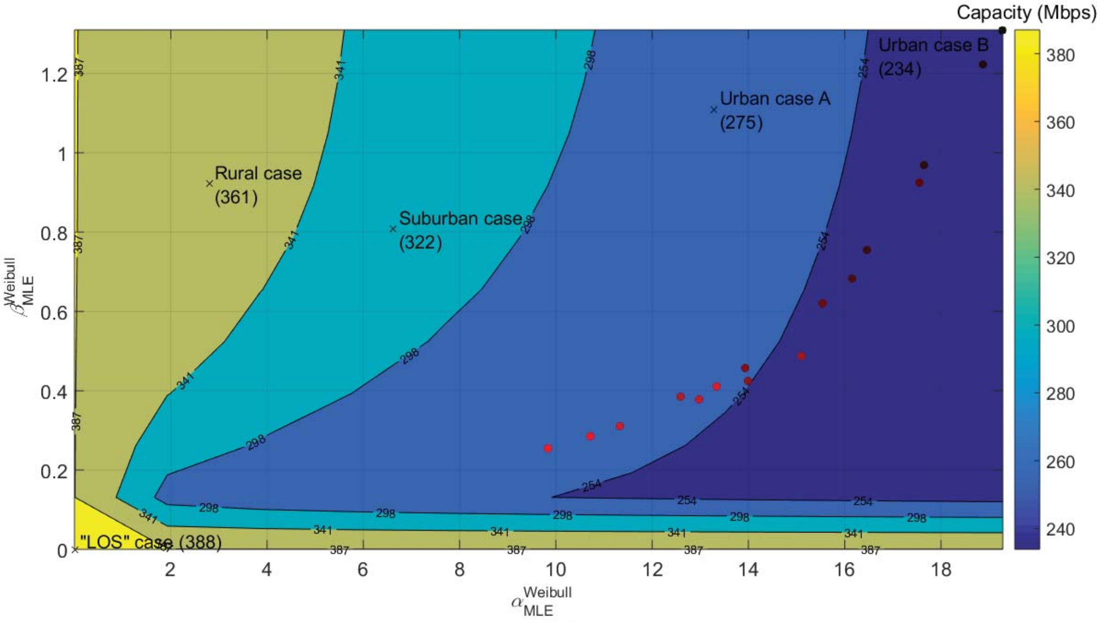
Capacity (Mbps)
380
360
340
320
300
280
260
240
Urban case B
(234)
Urban case A
(275)
Rural case
(361)
Suburban case
(322)
"LOS" case (388)
387
341
298
254
$\beta_{MLE}^{Weibull}$
$\alpha_{MLE}^{Weibull}$
0
0.2
0.4
0.6
0.8
1
1.2
2
4
6
8
10
12
14
16
18

(b)

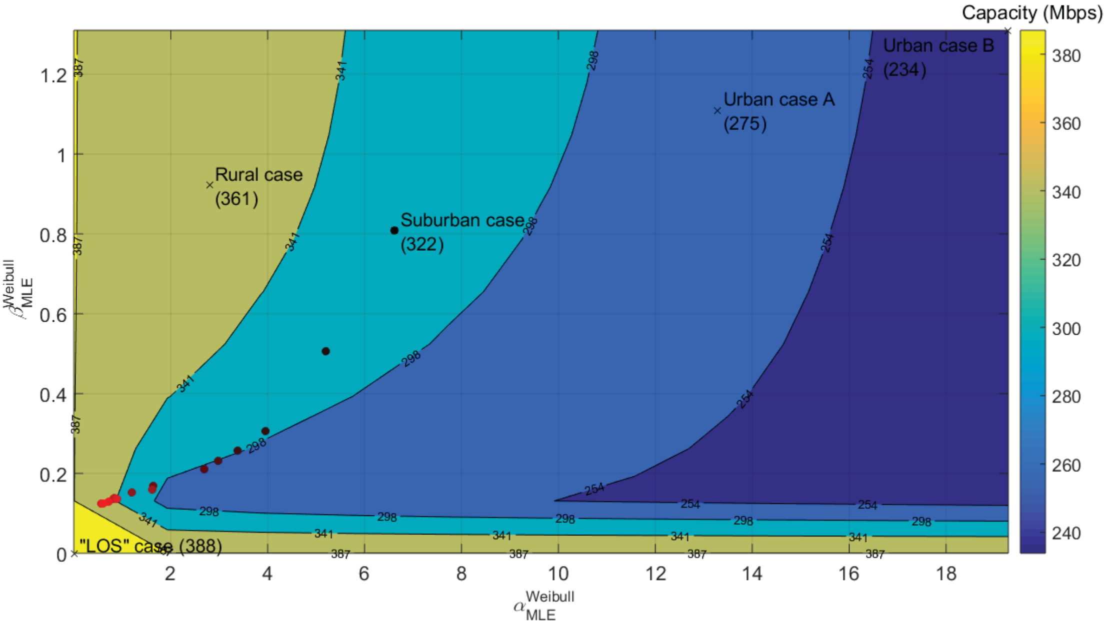
Capacity (Mbps)
380
360
340
320
300
280
260
240
Urban case B
(234)
Urban case A
(275)
Rural case
(361)
Suburban case
(322)
"LOS" case (388)
387
341
298
254
$\beta_{MLE}^{Weibull}$
$\alpha_{MLE}^{Weibull}$
0
0.2
0.4
0.6
0.8
1
1.2
2
4
6
8
10
12
14
16
18

(c)

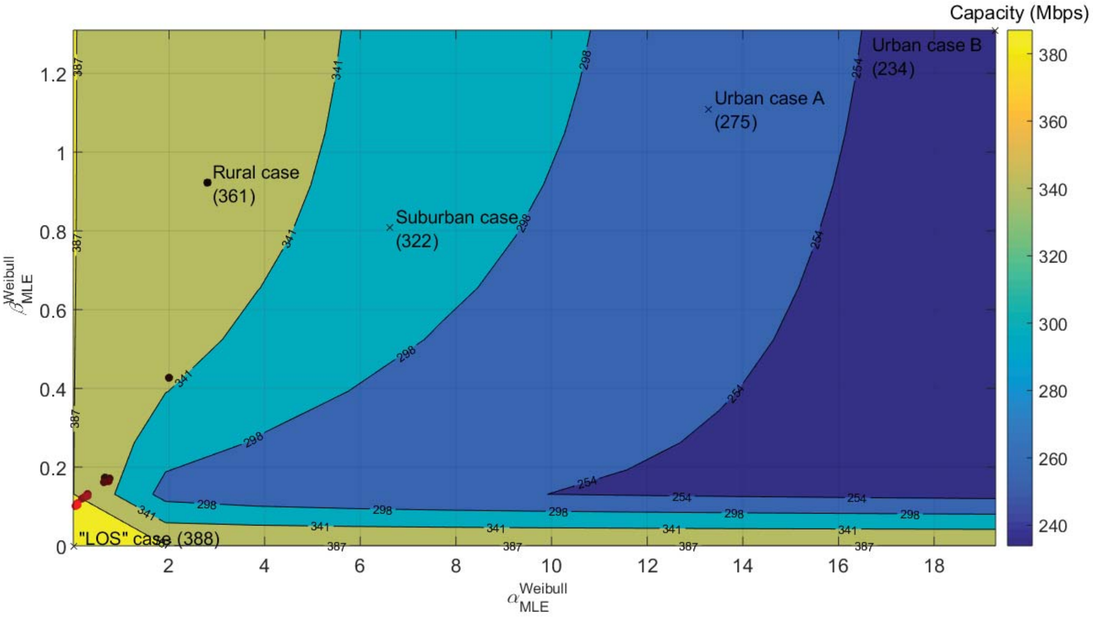
Capacity (Mbps)
380
360
340
320
300
280
260
240
Urban case B
(234)
Urban case A
(275)
Rural case
(361)
Suburban case
(322)
"LOS" case (388)
387
341
298
254
$\beta_{MLE}^{Weibull}$
$\alpha_{MLE}^{Weibull}$
0
0.2
0.4
0.6
0.8
1
1.2
2
4
6
8
10
12
14
16
18

(d)

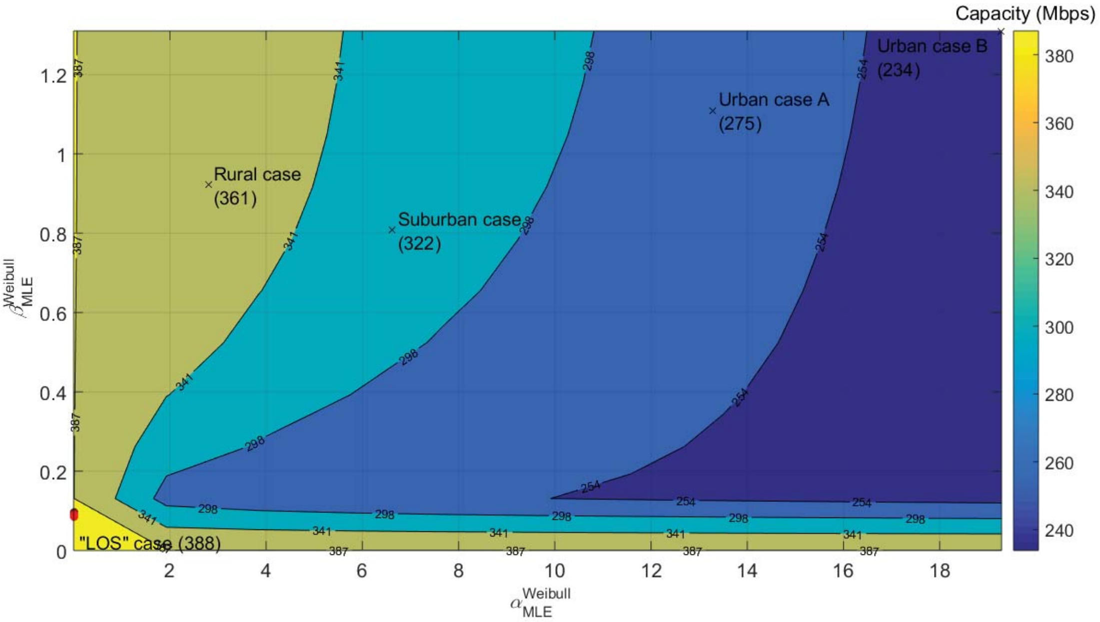

(e)

Fig. 4. iSHM footprints of the real indicative OV LV BPL topologies when 3-30MHz frequency band, WtG[1] coupling scheme, FCC Part 15 and CUD measurement differences of maximum value a_{CUD} that ranges from 0dB (black spot) to 15dB (red spot) are assumed. (i) Urban case A. (ii) Urban case B (iii) Suburban case (iv) Rural case (v) "LOS" case.

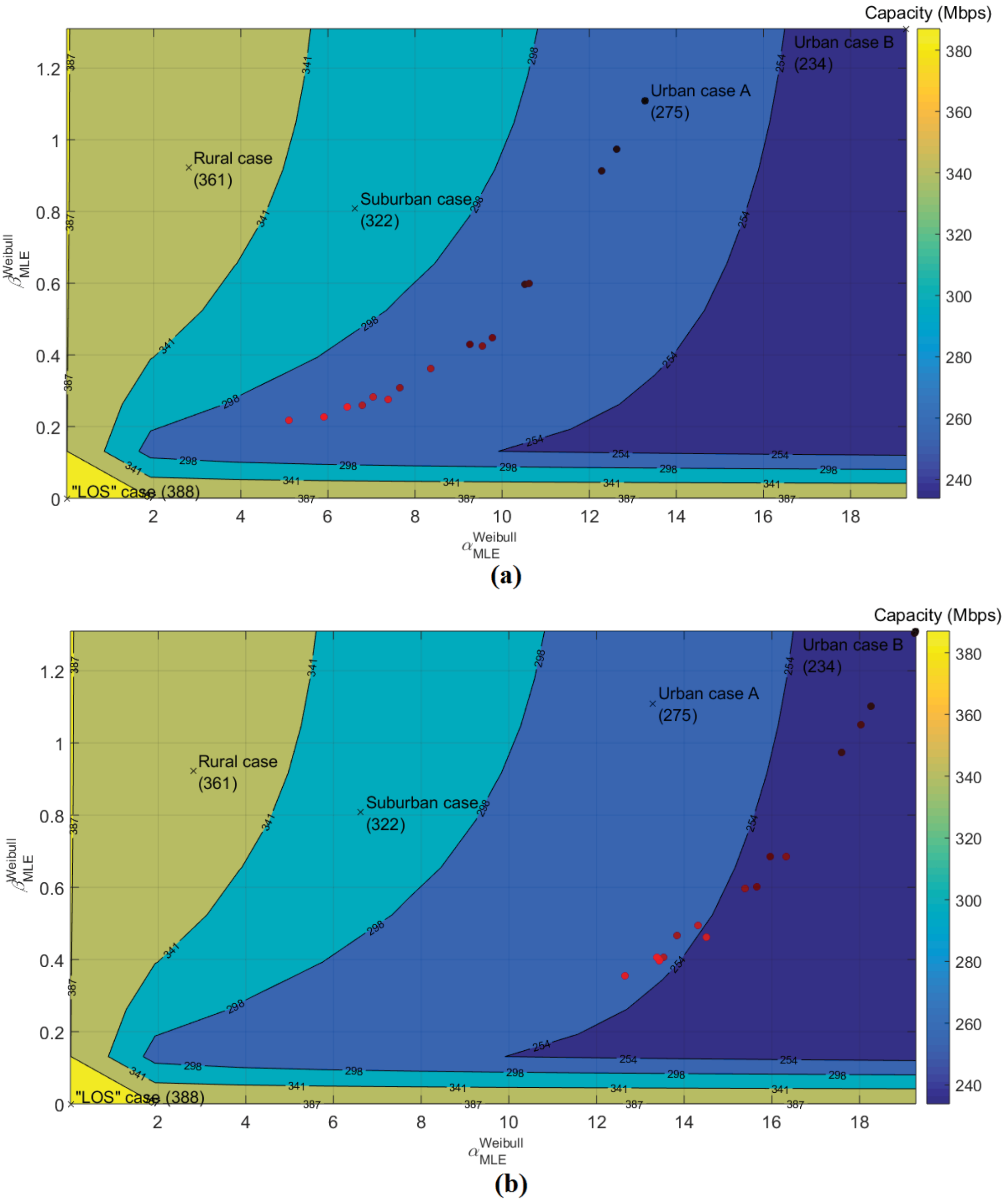
Capacity (Mbps)
380
360
340
320
300
280
260
240
Urban case B
(234)
Urban case A
(275)
Rural case
(361)
Suburban case
(322)
"LOS" case (388)
387
341
298
254
$\beta^{Weibull}_{MLE}$
1.2
1
0.8
0.6
0.4
0.2
0
$\alpha^{Weibull}_{MLE}$
2
4
6
8
10
12
14
16
18

(a)

(b)

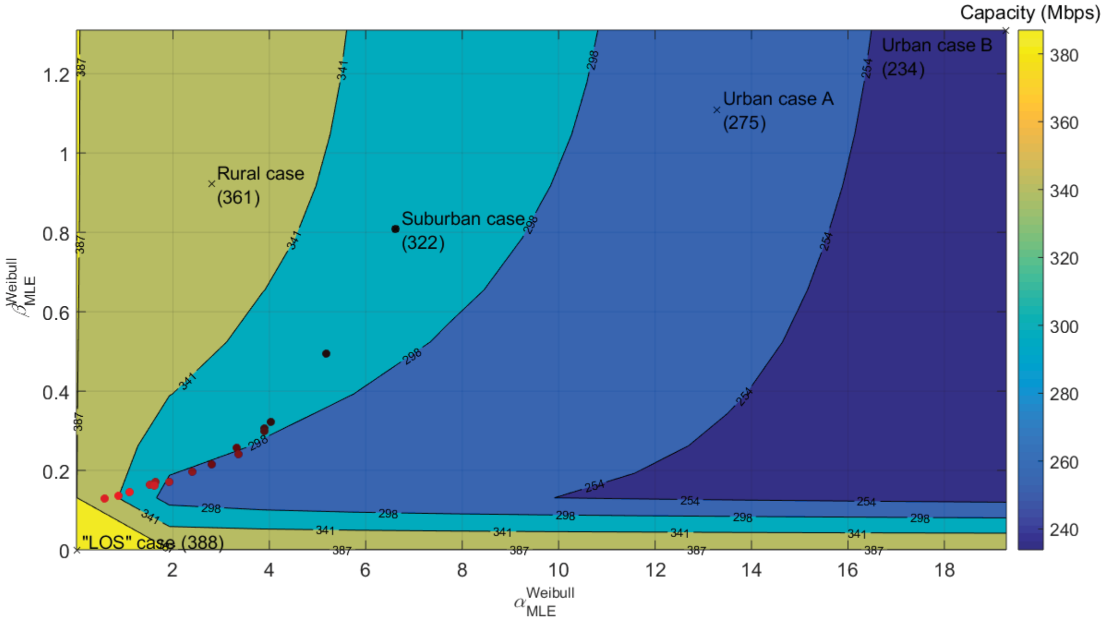
Capacity (Mbps)
380
360
340
320
300
280
260
240
Urban case B
(234)
Urban case A
(275)
Rural case
(361)
Suburban case
(322)
"LOS" case (388)
387
341
298
254
$\beta_{MLE}^{Weibull}$
1.2
1
0.8
0.6
0.4
0.2
0
2
4
6
8
10
12
14
16
18
$\alpha_{MLE}^{Weibull}$

(c)

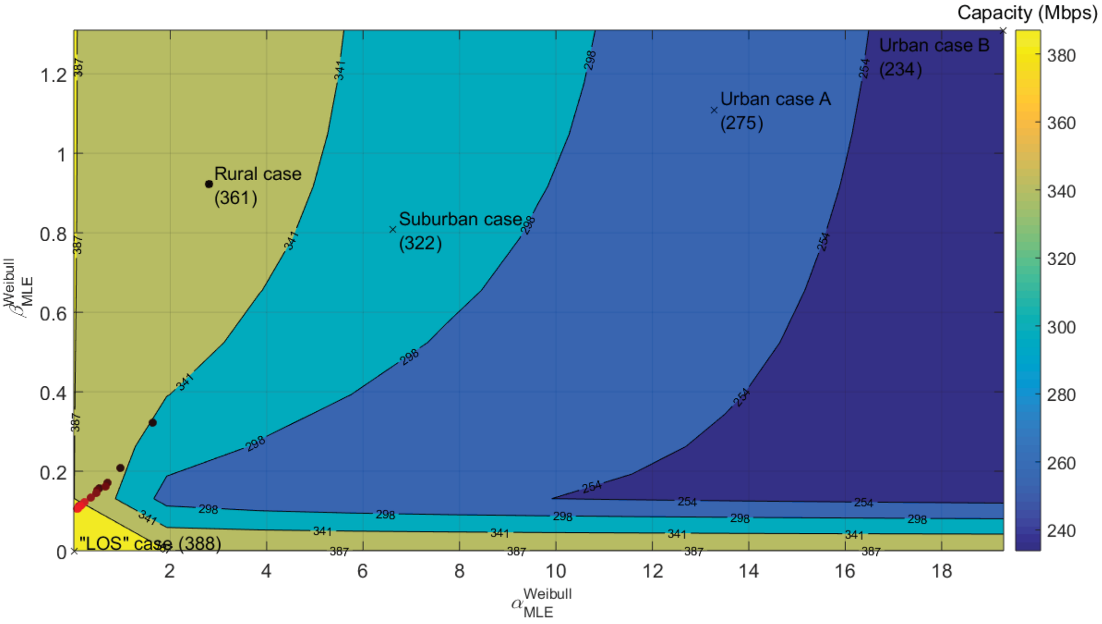
Capacity (Mbps)
380
360
340
320
300
280
260
240
Urban case B
(234)
Urban case A
(275)
Rural case
(361)
Suburban case
(322)
"LOS" case (388)
387
341
298
254
$\beta_{MLE}^{Weibull}$
1.2
1
0.8
0.6
0.4
0.2
0
2
4
6
8
10
12
14
16
18
$\alpha_{MLE}^{Weibull}$

(d)

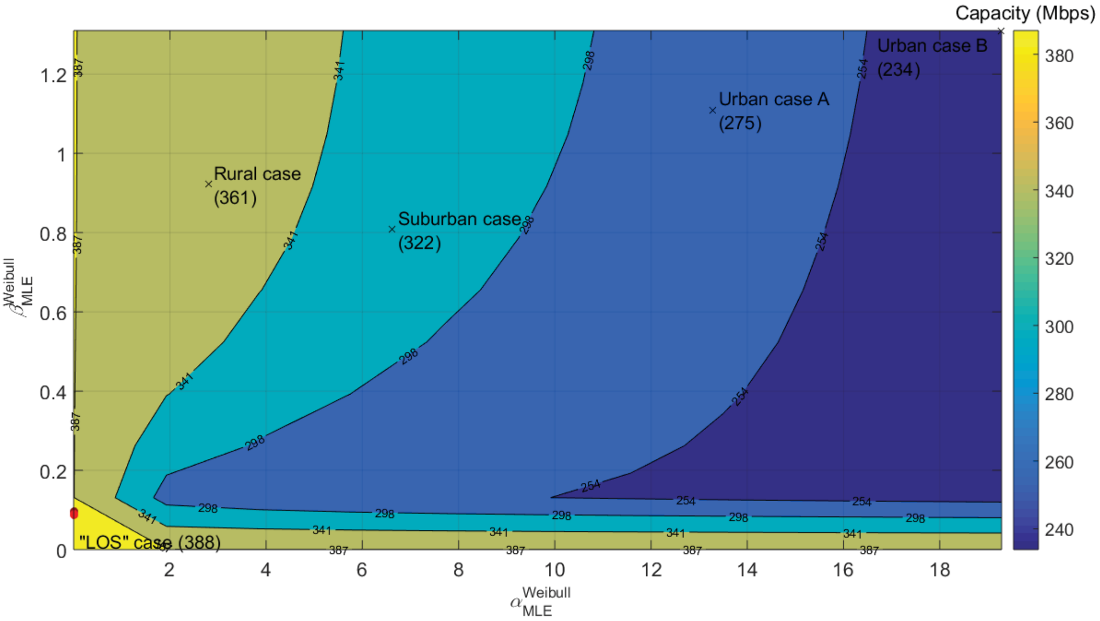

(e)

Fig. 5. Same plots but for ND measurement difference of mean μ_{ND} = 0dB and standard deviation σ_{ND} that ranges from 0dB (black spot) to 7.5dB (red spot).

By combining Figs. 4(a)-(e) and 5(a)-(e) with the respective figures of the previous subsections, interesting conclusions can be deduced regarding the behavior of iSHM footprints when measurement differences of different intensities are applied. More specifically:

- As the maximum value a_{CUD} of CUD measurement differences or standard deviation σ_{ND} of ND measurement differences increase, $\hat{a}^{\text{Weibull}}_{\text{MLE}}$ and $\hat{\beta}^{\text{Weibull}}_{\text{MLE}}$ of the measured real indicative OV LV BPL topologies simultaneously decrease. The iSHM footprint that is created from the increasing measurement differences, denoted hereafter as iSHM footprint due to the increasing measurement differences, starts from the theoretical values of $\hat{a}^{\text{Weibull}}_{\text{MLE}}$ and $\hat{\beta}^{\text{Weibull}}_{\text{MLE}}$ of the examined representative OV LV BPL topologies and tends to the iSHM footprint of "LOS" case that is located very close to the axes origin. The trend of the iSHM footprint due to the increasing measurement differences is explained by the fact that higher measurement differences force the measured coupling scheme channel attenuation of the real indicative OV LV BPL topologies to the zero restriction of the measured coupling scheme channel attenuation difference or to deeper spectral notches. Hence, the decrease of $\hat{a}^{\text{Weibull}}_{\text{MLE}}$ and $\hat{\beta}^{\text{Weibull}}_{\text{MLE}}$ of the measured real indicative OV LV BPL topologies compared with the respective theoretical ones is explained by the effort of the Weibull PDF to approximate the empirical PDFs of the measured coupling scheme channel attenuation differences.
- By observing Figs. 4(e) and 5(e), the iSHM footprint of the OV LV BPL "LOS" case due to the increasing measurement differences remains close to the axes origin. In fact, the distance of the iSHM footprint of the OV LV BPL "LOS" case from the axes origin when no measurement differences are applied is explained by

the fact that the coupling scheme channel attenuation differences is assumed to be equal to 1×10^{-11} instead of zero so that Weibull CASD MLEs can be calculated [19].

- The iSHM footprint due to the increasing measurement differences depends on the examined OV LV BPL topology class since its trend becomes steeper as more aggravated BPL topologies are studied. Actually, for high values of maximum value a_{CUD} of CUD measurement differences and standard deviation σ_{ND} of ND measurement differences, the iSHM footprint due to the increasing measurement differences can exceed the boundaries of the examined OV LV BPL topology class. As it was expected, the latter situation complicates either the identification of the examined OV LV BPL topology or the categorization of the examined OV LV BPL topology into the five classes.
- The significant Weibull MLEs distortion that is caused by the presence of high measurement differences may affect the monitoring and controlling of the OV LV power grid [28], [29]. To mitigate the measurement differences and preserve the validity of the collected data, piecewise monotonic data approximations, such as L1PMA [27] and L2WPMA [53], have been extensively applied in distribution and transmission BPL networks until now so that measured data can be filtered and restored. The future research is focused on the exploitation of the piecewise monotonic data approximations so that the lower left direction of the iSHM footprint due to measurement differences towards the axes origin can be inverted so that predictive tools that can exploit SHM footprints, such as the identification of OV LV BPL topologies and the detection of hooks for energy thefts [2], are not critically affected.

As been demonstrated, the operation of the SG produces big data whose wiser management may allow higher performances concerning the monitoring and controlling of the SG. Indeed, measurement differences combined with the real time operation are going to create a cataclysm of data that may mislead the existing predictive tools of the SG if they are not appropriately filtered. The interaction of iSHM footprints with piecewise monotonic data approximations may enhance the quality of business analytics of SG under the harsh real time conditions.

5. Conclusions

The numerical results concerning the behavior of iSHM footprints of the OV LV BPL networks when measurement differences are applied have been demonstrated as well as countermeasures proposals for ensuring the quality of business analytics and the tools of the SG. From iSHM footprints of the real indicative OV LV BPL topologies due to the increasing measurement differences, it has been verified that: (i) iSHM footprints of more aggravated OV LV BPL topologies (*i.e.*, urban case A and case B) are more sensitive to the measurement differences (higher extent of the corresponding iSHM footprints); (ii) When measurement differences remain relatively low, the iSHM footprint of the affected OV LV BPL topology remains within the corresponding class area boundaries; (iii) iSHM footprints due to the increasing measurement differences of all examined real OV LV BPL topologies present the same direction; say, towards the axes origin; (iv) As the measurement differences remain high, all affected OV LV BPL topologies tend to present similar Weibull CASD MLEs; and (v) High measurement differences jam the broadband tools of the SG, such as the topology identification technique via iSHM footprint, thus influencing the quality of business analytics of the SG. To mitigate the measurement differences and retrieve the theoretical iSHM footprint from the measured one, piecewise monotonic data approximations, such as L1PMA and L2WPMA, are investigated in [54], [55].

CONFLICTS OF INTEREST

The author declares that there is no conflict of interests regarding the publication of this paper.

References

[1] A. G. Lazaropoulos, "Statistical Channel Modeling of Overhead Low Voltage Broadband over Power Lines (OV LV BPL) Networks – Part 1: The Theory of Class Map Footprints of Real OV LV BPL Topologies, Branch Line Faults and Hook-Style Energy Thefts," *Trends in Renewable Energy*, vol. 6, no. 1, pp. 61-87, Mar. 2020. [Online]. Available: http://futureenergysp.com/index.php/tre/article/download/112/pdf

[2] A. G. Lazaropoulos, "Statistical Channel Modeling of Overhead Low Voltage Broadband over Power Lines (OV LV BPL) Networks – Part 2: The Numerical Results of Class Map Footprints of Real OV LV BPL Topologies, Branch Line Faults and Hook Style Energy Thefts," *Trends in Renewable Energy*, vol. 6, no. 1, pp. 88-109, Mar. 2020. [Online]. Available: http://futureenergysp.com/index.php/tre/article/download/113/pdf

[3] G. López, J. Matanza, D. de la Vega, M. Castro, A. Arrinda, J. I. Moreno, and A. Sendin, "The Role of Power Line Communications in the Smart Grid Revisited: Applications, Challenges, and Research Initiatives," *IEEE Access*, vol. 7, pp. 117346–117368, 2019.

[4] A. A. Munshi and A-R M. Yasser, "Big Data Framework for Analytics in Smart Grids," *Elsevier Electric Power Systems Research*, vol. 151, pp. 369-380, 2017.

[5] H. Daki, A. El Hannani, A. Aqqal, A. Haidine, and A. Dahbi, "Big Data management in smart grid: concepts, requirements and implementation," *Springer Journal of Big Data*, vol. 4, no. 1, pp. 1-19, 2017.

[6] A. H. Al-Badi, R. Ahshan, N. Hosseinzadeh, R. Ghorbani, and E. Hossain, "Survey of Smart Grid Concepts and Technological Demonstrations Worldwide Emphasizing on the Oman Perspective," *MDPI Applied System Innovation*, vol. 3, no. 1, 5, 2020.

[7] G. Artale, A. Cataliotti, V. Cosentino, D. Di Cara, R. Fiorelli, S. Guaiana, and G. Tinè, "A New Low Cost Coupling System for Power Line Communication on Medium Voltage Smart Grids," *IEEE Trans. on Smart Grid*, vol. 9, no. 4, pp. 3321-3329, 2018.

[8] L. González-Sotres, C. Mateo, P. Frías, C. Rodríguez-Morcillo, and J. Matanza, "Replicability Analysis of PLC PRIME Networks for Smart Metering Applications," *IEEE Trans. on Smart Grid*, vol. 9, no. 2, pp. 827-835, Mar. 2018.

[9] A. ElSamadouny, A. El Shafie, M. Abdallah, and N. Al-Dhahir, "Secure Sum-Rate-Optimal MIMO Multicasting Over Medium-Voltage NB-PLC Networks," *IEEE Trans. on Smart Grid*, vol. 9, no. 4, pp. 2954-2963, Jul. 2018.

[10] A. G. Lazaropoulos and P. G. Cottis, "Transmission characteristics of overhead medium voltage power line communication channels," *IEEE Trans. Power Del.*, vol. 24, no. 3, pp. 1164-1173, Jul. 2009.

[11] A. G. Lazaropoulos and P. G. Cottis, "Broadband transmission via underground medium-voltage power lines-Part I: transmission characteristics," *IEEE Trans. Power Del.*, vol. 25, no. 4, pp. 2414-2424, Oct. 2010.

[12] E. Biglieri, "Coding and modulation for a horrible channel," *IEEE Commun. Mag.*, vol. 41, no. 5, pp. 92–98, May 2003.

[13] M. Gebhardt, F. Weinmann, and K. Dostert, "Physical and regulatory constraints for communication over the power supply grid," *IEEE Commun. Mag.*, vol. 41, no. 5, pp. 84-90, May 2003.

[14] M. Götz, M. Rapp, and K. Dostert, "Power line channel characteristics and their effect on communication system design," *IEEE Commun. Mag.*, vol. 42, no. 4, pp. 78-86, Apr. 2004.

[15] A. G. Lazaropoulos and P. G. Cottis, "Capacity of overhead medium voltage power line communication channels," *IEEE Trans. Power Del.*, vol. 25, no. 2, pp. 723-733, Apr. 2010.

[16] A. G. Lazaropoulos and P. G. Cottis, "Broadband transmission via underground medium-voltage power lines-Part II: capacity," *IEEE Trans. Power Del.*, vol. 25, no. 4, pp. 2425-2434, Oct. 2010.

[17] A. G. Lazaropoulos, "Broadband transmission and statistical performance properties of overhead high-voltage transmission networks," *Hindawi Journal of Computer Networks and Commun.*, 2012, article ID 875632, 2012. [Online]. Available: http://www.hindawi.com/journals/jcnc/aip/875632/

[18] A. G. Lazaropoulos, "Towards Modal Integration of Overhead and Underground Low-Voltage and Medium-Voltage Power Line Communication Channels in the Smart Grid Landscape: Model Expansion, Broadband Signal Transmission Characteristics, and Statistical Performance Metrics (Invited Paper)," *ISRN Signal Processing*, vol. 2012, Article ID 121628, pp. 1-17, 2012. [Online]. Available: http://www.hindawi.com/isrn/sp/2012/121628/

[19] A. G. Lazaropoulos, "Statistical Broadband over Power Lines Channel Modeling – Part 1: The Theory of the Statistical Hybrid Model," *Progress in Electromagnetics Research C*, vol. 92, pp. 1-16, 2019. [Online]. Available: http://www.jpier.org/PIERC/pierc92/01.19012902.pdf

[20] A. G. Lazaropoulos, "Statistical Broadband over Power Lines (BPL) Channel Modeling – Part 2: The Numerical Results of the Statistical Hybrid Model," *Progress in Electromagnetics Research C*, vol. 92, pp. 17-30, 2019. [Online]. Available: http://www.jpier.org/PIERC/pierc92/02.19012903.pdf

[21] A. G. Lazaropoulos, "Enhancing the Statistical Hybrid Model Performance in Overhead and Underground Medium Voltage Broadband over Power Lines Channels by Adopting Empirical Channel Attenuation Statistical Distribution," *Trends in Renewable Energy*, vol. 5, no. 2, pp. 181-217, 2019. [Online]. Available: http://futureenergysp.com/index.php/tre/article/view/96/pdf

[22] A. G. Lazaropoulos, "The Role of Information Technology Department against the Hook Style Energy Theft in Smart Cities – Ad-Hoc Overhead Low-Voltage

Broadband over Power Lines (OV LV BPL) Networks," *Trends in Renewable Energy*, vol. 5, no. 2, pp. 117-150, Apr. 2019. [Online]. Available: http://futureenergysp.com/index.php/tre/article/download/93/pdf

[23] A. G. Lazaropoulos, "Virtual Indicative Broadband over Power Lines Topologies for Respective Subclasses by Adjusting Channel Attenuation Statistical Distribution Parameters of Statistical Hybrid Models – Part 2: Numerical Results for the Overhead and Underground Medium-Voltage Power Grids," *Trends in Renewable Energy*, vol. 5, no. 3, pp. 258-281, Aug. 2019. [Online]. Available: http://futureenergysp.com/index.php/tre/article/view/100/pdf

[24] A. G. Lazaropoulos, "Virtual Indicative Broadband over Power Lines Topologies for Respective Subclasses by Adjusting Channel Attenuation Statistical Distribution Parameters of Statistical Hybrid Models – Part 3: The Case of Overhead Transmission Power Grids," *Trends in Renewable Energy*, vol. 5, no. 3, pp. 282-306, Aug. 2019. [Online]. Available: http://futureenergysp.com/index.php/tre/article/view/101/pdf

[25] A. G. Lazaropoulos, "Measurement Differences, Faults and Instabilities in Intelligent Energy Systems–Part 1: Identification of Overhead High-Voltage Broadband over Power Lines Network Topologies by Applying Topology Identification Methodology (TIM)," *Trends in Renewable Energy*, vol. 2, no. 3, pp. 85-112, Oct. 2016. [Online]. Available: http://futureenergysp.com/index.php/tre/article/view/26/32

[26] A. G. Lazaropoulos, "Measurement Differences, Faults and Instabilities in Intelligent Energy Systems – Part 2: Fault and Instability Prediction in Overhead High-Voltage Broadband over Power Lines Networks by Applying Fault and Instability Identification Methodology (FIIM)," *Trends in Renewable Energy*, vol. 2, no. 3, pp. 113-142, Oct. 2016. [Online]. Available: http://futureenergysp.com/index.php/tre/article/view/27/33

[27] A. G. Lazaropoulos, "Best L1 Piecewise Monotonic Data Approximation in Overhead and Underground Medium-Voltage and Low-Voltage Broadband over Power Lines Networks: Theoretical and Practical Transfer Function Determination," Hindawi Journal of Computational Engineering, vol. 2016, Article ID 6762390, 24 pages, 2016. doi:10.1155/2016/6762390. [Online]. Available: https://www.hindawi.com/journals/jcengi/2016/6762390/cta/

[28] A. G. Lazaropoulos, "Power Systems Stability through Piecewise Monotonic Data Approximations – Part 1: Comparative Benchmarking of L1PMA, L2WPMA and L2CXCV in Overhead Medium-Voltage Broadband over Power Lines Networks," *Trends in Renewable Energy*, vol. 3, no. 1, pp. 2-32, Jan. 2017. [Online]. Available: http://futureenergysp.com/index.php/tre/article/view/29/34

[29] A. G. Lazaropoulos, "Power Systems Stability through Piecewise Monotonic Data Approximations – Part 2: Adaptive Number of Monotonic Sections and Performance of L1PMA, L2WPMA and L2CXCV in Overhead Medium-Voltage Broadband over Power Lines Networks," *Trends in Renewable Energy*, vol. 3, no. 1, pp. 33-60, Jan. 2017. [Online]. Available: http://futureenergysp.com/index.php/tre/article/view/30/35

[30] A. G. Lazaropoulos, "Main Line Fault Localization Methodology in Smart Grid – Part 2: Extended TM2 Method, Measurement Differences and L1 Piecewise Monotonic Data Approximation for the Overhead Medium-Voltage Broadband over Power Lines Networks Case," *Trends in Renewable Energy*, vol. 3, no. 3, pp.

26-61, Dec. 2017. [Online]. Available: http://futureenergysp.com/index.php/tre/article/view/37

[31] OPERA1, D44: Report presenting the architecture of plc system, the electricity network topologies, the operating modes and the equipment over which PLC access system will be installed, IST Integr. Project No 507667, Dec. 2005.

[32] P. Amirshahi and M. Kavehrad, "High-frequency characteristics of overhead multiconductor power lines for broadband communications," *IEEE J. Sel. Areas Commun.*, vol. 24, no. 7, pp. 1292-1303, Jul. 2006.

[33] P. Amirshahi, "Broadband access and home networking through powerline networks" Ph.D. dissertation, Pennsylvania State Univ., University Park, PA, May 2006.

[34] M. D'Amore and M. S. Sarto, "A new formulation of lossy ground return parameters for transient analysis of multiconductor dissipative lines," *IEEE Trans. Power Del.*, vol. 12, no. 1, pp. 303-314, Jan. 1997.

[35] M. D'Amore and M. S. Sarto, "Simulation models of a dissipative transmission line above a lossy ground for a wide-frequency range-Part I: Single conductor configuration," *IEEE Trans. Electromagn. Compat.*, vol. 38, no. 2, pp. 127-138, May 1996.

[36] M. D'Amore and M. S. Sarto, "Simulation models of a dissipative transmission line above a lossy ground for a wide-frequency range-Part II: Multi-conductor configuration," *IEEE Trans. Electromagn. Compat.*, vol. 38, no. 2, pp. 139-149, May 1996.

[37] A. G. Lazaropoulos, "Review and Progress towards the Capacity Boost of Overhead and Underground Medium-Voltage and Low-Voltage Broadband over Power Lines Networks: Cooperative Communications through Two- and Three-Hop Repeater Systems," *ISRN Electronics*, vol. 2013, Article ID 472190, pp. 1-19, 2013. [Online]. Available: http://www.hindawi.com/isrn/electronics/aip/472190/

[38] A. G. Lazaropoulos, "Broadband over Power Lines (BPL) Systems Convergence: Multiple-Input Multiple-Output (MIMO) Communications Analysis of Overhead and Underground Low-Voltage and Medium-Voltage BPL Networks (Invited Paper)," *ISRN Power Engineering*, vol. 2013, Article ID 517940, pp. 1-30, 2013. [Online]. Available: http://www.hindawi.com/isrn/power.engineering/2013/517940/

[39] A. G. Lazaropoulos, "Main Line Fault Localization Methodology (MLFLM) in Smart Grid–The Underground Medium- and Low-Voltage Broadband over Power Lines Networks Case," *Trends in Renewable Energy*, vol. 4, no. 1, pp. 15-42, Dec. 2017. [Online]. Available: http://futureenergysp.com/index.php/tre/article/view/45

[40] A. G. Lazaropoulos, "Towards Broadband over Power Lines Systems Integration: Transmission Characteristics of Underground Low-Voltage Distribution Power Lines," *Progress in Electromagnetics Research B*, vol. 39, pp. 89-114, 2012. [Online]. Available: http://www.jpier.org/PIERB/pierb39/05.12012409.pdf

[41] T. Sartenaer, "Multiuser communications over frequency selective wired channels and applications to the powerline access network" *Ph.D. dissertation*, Univ. Catholique Louvain, Louvain-la-Neuve, Belgium, Sep. 2004.

[42] T. Calliacoudas and F. Issa, ""Multiconductor transmission lines and cables solver," An efficient simulation tool for plc channel networks development,"

presented at the *IEEE Int. Conf. Power Line Communications and Its Applications*, Athens, Greece, Mar. 2002.

[43] T. Sartenaer and P. Delogne, "Deterministic modelling of the (Shielded) outdoor powerline channel based on the multiconductor transmission line equations," *IEEE J. Sel. Areas Commun.*, vol. 24, no. 7, pp. 1277-1291, Jul. 2006.

[44] A. G. Lazaropoulos, "Broadband Performance Metrics and Regression Approximations of the New Coupling Schemes for Distribution Broadband over Power Lines (BPL) Networks," *Trends in Renewable Energy*, vol. 4, no. 1, pp. 43-73, Jan. 2018. [Online]. Available: http://futureenergysp.com/index.php/tre/article/view/59/pdf

[45] A. G. Lazaropoulos, "New Coupling Schemes for Distribution Broadband over Power Lines (BPL) Networks," *Progress in Electromagnetics Research B*, vol. 71, pp. 39-54, 2016. [Online]. Available: http://www.jpier.org/PIERB/pierb71/02.16081503.pdf

[46] A. G. Lazaropoulos, "Underground Distribution BPL Connections with (N + 1)-hop Repeater Systems: A Novel Capacity Mitigation Technique," *Elsevier Computers and Electrical Engineering*, vol. 40, pp. 1813-1826, 2014.

[47] A. G. Lazaropoulos, "Deployment Concepts for Overhead High Voltage Broadband over Power Lines Connections with Two-Hop Repeater System: Capacity Countermeasures against Aggravated Topologies and High Noise Environments," *Progress in Electromagnetics Research B*, vol. 44, pp. 283-307, 2012. [Online]. Available: http://www.jpier.org/PIERB/pierb44/13.12081104.pdf

[48] A. G. Lazaropoulos, "Virtual Indicative Broadband over Power Lines Topologies for Respective Subclasses by Adjusting Channel Attenuation Statistical Distribution Parameters of Statistical Hybrid Models – Part 1: Theory," *Trends in Renewable Energy*, vol. 5, no. 3, pp. 237-257, Aug. 2019. [Online]. Available: http://futureenergysp.com/index.php/tre/article/view/99/pdf

[49] A. G. Lazaropoulos, "Improvement of Power Systems Stability by Applying Topology Identification Methodology (TIM) and Fault and Instability Identification Methodology (FIIM)–Study of the Overhead Medium-Voltage Broadband over Power Lines (OV MV BPL) Networks Case," *Trends in Renewable Energy*, vol. 3, no. 2, pp. 102-128, Apr. 2017. [Online]. Available: http://futureenergysp.com/index.php/tre/article/view/34

[50] I. C. Demetriou, "An application of best *L*1 piecewise monotonic data approximation to signal restoration," *IAENG International Journal of Applied Mathematics*, vol. 53, no. 4, pp. 226-232, 2013.

[51] I. C. Demetriou, "L1PMA: A Fortran 77 Package for Best L1 Piecewise Monotonic Data Smoothing," *Computer Physics Communications*, vol. 151, no. 1, pp. 315-338, 2003.

[52] A. G. Lazaropoulos, "Main Line Fault Localization Methodology in Smart Grid – Part 1: Extended TM2 Method for the Overhead Medium-Voltage Broadband over Power Lines Networks Case," *Trends in Renewable Energy*, vol. 3, no. 3, pp. 2-25, Dec. 2017. [Online]. Available: http://futureenergysp.com/index.php/tre/article/view/36

[53] I. C. Demetriou, "Algorithm 863: L2WPMA, a Fortran 77 package for weighted least-squares piecewise monotonic data approximation," *ACM Transactions on Mathematical Software (TOMS)*, vol. 33, no.1, pp. 6, 2007.

[54] A. G. Lazaropoulos, “Business Analytics and IT in Smart Grid – Part 2: The Qualitative Mitigation Impact of Piecewise Monotonic Data Approximations on the iSHM Class Map Footprints of Overhead Low-Voltage Broadband over Power Lines Topologies Contaminated by Measurement Differences,” *Trends in Renewable Energy*, vol. 6, no. 2, pp. 177-203, May 2020.
[55] A. G. Lazaropoulos, “Business Analytics and IT in Smart Grid – Part 3: New Application Aspect and the Quantitative Mitigation Analysis of Piecewise Monotonic Data Approximations on the iSHM Class Map Footprints of Overhead Low-Voltage Broadband over Power Lines Topologies Contaminated by Measurement Differences,” *Trends in Renewable Energy*, vol. 6, no. 2, pp. 204-223, May 2020.

Trends in Renewable Energy
OPEN ACCESS ISSN:2376-2144
Peer-Reviewed Article futureenergysp.com/index.php/tre

Business Analytics and IT in Smart Grid – Part 2: The Qualitative Mitigation Impact of Piecewise Monotonic Data Approximations on the iSHM Class Map Footprints of Overhead Low-Voltage Broadband over Power Lines Topologies Contaminated by Measurement Differences

Athanasios G. Lazaropoulos[1,2,*]

1: School of Electrical and Computer Engineering / National Technical University of Athens / 9 Iroon Polytechniou Street / Zografou, GR 15780
2: Department of Industrial Design and Production Engineering / School of Engineering / University of West Attica / 250 Thivon & P. Ralli / Athens, GR 12244

Received March 25, 2020; Accepted May 4, 2020; Published May 13, 2020

Business analytics and IT infrastructure preserve the integrity of the smart grid (SG) operation against the flood of big data that may be susceptible to faults, such as measurement differences. In [1], the impact of measurement differences that follow continuous uniform distributions (CUDs) of different magnitudes has been investigated via initial Statistical Hybrid Model (iSHM) footprints during the operation of overhead low-voltage broadband over power lines (OV LV BPL) networks. In this companion paper, the mitigation efficiency of piecewise monotonic data approximations, such as L1PMA and L2WPMA, is qualitatively assessed in terms of iSHM footprints when the aforementioned measurement difference CUD of different intensities are applied.

Keywords: Smart Grid; Broadband over Power Lines (BPL) networks; Power Line Communications (PLC); Distribution and Transmission Power Grids; Capacity, Statistics; Business Analytics; IT; Modeling

**Corresponding author:* AGLazaropoulos@gmail.com

Tr Ren Energy, 2020, Vol.6, No.2, 187-213. doi: 10.17737/tre.2020.6.2.00118

Nomenclature

BPL	Broadband over Power Lines
BPMN	Business Process Model and Notation
CASD	Channel Attenuation Statistical Distribution
CUD	Continuous Uniform Distribution
DHM	deterministic hybrid model
FIIM	Fault and Instability Identification Methodology
HS-DET method	hook style energy theft detection method
IP	Internet Protocol
IT	Information Technology
iSHM	initial Statistical Hybrid Model
LOS	Line-of-Sight
LV	Low Voltage
L1PMA	L1 Piecewise Monotonic Approximation
L2WPMA	L2 Weighted Piecewise Monotonic Approximation
MLE	Maximum Likelihood Estimator
ND	Normal Distribution
OV	Overhead
PES	Percent Error Sum
SG	Smart Grid
SHM	Statistical Hybrid Model
TIM	Topology Identification Methodology
WtG	Wire-to-Ground

1. Introduction

During the recent years, the transformation of the traditional power grid to the SG urges the installation of a parallel advanced IP-based communications network enhanced with a plethora of broadband applications and business analytics [1]-[14]. Among the available communications solutions that can support this communications network, BPL networks can play an important role since they exploit the already installed wired power grid infrastructure [4], [15]-[23].

However, big data that overwhelm SG are susceptible to errors that can affect business analytics and decisions based on them. Indeed, as the operation of BPL networks is concerned across SG, the already installed wired power grid infrastructure is a hostile medium for communications as it is designed to deliver power rather information [19], [21], [24]-[27]. As the BPL channel modeling is concerned, the recently proposed iSHM, which is based on the well-validated DHM, can be deployed for the broadband channel description of transmission and distribution power grids [19]-[23], [28]-[31]. Also, a plethora of related broadband iSHM tools, such as the definition procedure, the class maps and the iSHM footprints, have been so far demonstrated and tested in order to assist the operation of iSHM towards a more accurate statistical description of the communications channel [32]-[35]. Except for the communications channel itself, measurement differences between the experimental and theoretical results during the channel attenuation determination, briefly denoted as measurement differences, may occur due to a number of practical reasons and “real-life” difficulties that may critically influence iSHM operation, the interaction of broadband iSHM tools with iSHM and finally the SG big data with the related decisions.

Actually, the impact of measurement differences that can be treated as CUDs has been assessed through the iSHM footprints for a list of real indicative OV LV BPL topologies in [1] while appropriate countermeasures that are based on piecewise monotonic data approximations and iSHM footprints are first presented and assessed in this companion paper. The numerical results of [1] confirmed the nasty impact of measurement differences on the behavior of iSHM footprints of the OV LV BPL topologies since high measurement differences may jam the SG broadband tools, such as the topology identification technique and energy theft identification, which are based on the analysis of iSHM footprints. To restore the affected iSHM footprints and to preserve the quality of business analytics, piecewise monotonic data approximations, such as L1PMA [36] and L2WPMA [37], which have been successfully applied in distribution and transmission BPL networks for the mitigation of measurement differences in broadband applications of TIM [8], FIIM [8] and HS-DET method [38], can also be applied in iSHM footprints so that the contaminated measured data can be partially restored and the approximated iSHM footprints tend to be gathered close to the respective theoretical values.

The rest of this paper is organized as follows: Section II synopsizes the mathematics of measurement differences. Also, the piecewise monotonic data approximations of interest, say L1PMA and L2WPMA, are briefly outlined. L1PMA and L2WPMA mitigation character is analyzed in mathematical terms as well as their involvement in the iSHM operation and iSHM footprints. In Section III, the numerical results regarding the mitigation impact of piecewise monotonic data approximations against the measurement differences on the iSHM footprints are shown. Section IV concludes this paper.

2. Measurement Differences and Countermeasures in DHM and iSHM Footprints

In accordance with [1], measurement differences affect the iSHM performance since they are mathematically superimposed on the numerical results of DHM, which is the core element of the Phase A of the BPMN diagram of iSHM [29]. First, a synopsis of the mathematical involvement of the CUD measurement differences in DHM is provided. Second, a presentation of the two piecewise monotonic data approximations of interest, say L1PMA and L2WPMA, is presented as well as the required mathematics.

2.1 Measurement Differences in DHM and iSHM Footprint Operation Settings

Due to practical reasons and "real-life" conditions [36], [39], [40], measurement differences may be observed among the theoretical and measured coupling scheme transfer functions for given OV LV BPL topology and coupling scheme. In accordance with [1], [36], [39], [40], these measurement differences can be decently treated either as CUDs of variable maximum value a_{CUD} or as NDs of variable standard deviation σ_{ND} when the mean value μ_{ND} is assumed to be equal to zero. Since measurement differences $e^{D}_{d1,d2,i}\{\cdot\}$ that follow the aforementioned distributions are added to the theoretical coupling scheme transfer function $H^{\mathrm{OVLV},C}\{\cdot\}$, the measured coupling scheme transfer function $\overline{H^{\mathrm{OVLV},C,D}_{d1,d2,i}}\{\cdot\}$ can be determined by [1], [6], [41]

$$\overline{H^{\mathrm{OVLV},C,D}_{d1,d2,i}}\left(f_q\right) = H^{\mathrm{OVLV},C}\left(f_q\right) + e^{D}_{d1,d2,i}\left(f_q\right),\ q=1,\ldots,Q,\ i=1,\ldots,I \tag{1}$$

where $[\cdot]^{C}$ denotes the applied coupling scheme, $[\cdot]^{D}$ denotes the applied measurement difference distribution –either CUD of this paper or ND–, f_q is the flat-fading subchannel start frequency, Q is the number of subchannels in the examined frequency range, $d1$ is the first parameter of the applied measurement difference distribution (*i.e.*, the minimum value $-a_{\mathrm{CUD}}$ of CUD), $d2$ is the second parameter of the applied measurement difference distribution (*i.e.*, the maximum value a_{CUD} of CUD), $H^{\mathrm{OVLV},C}\left(f_q\right)$ is the theoretical coupling scheme transfer function at frequency f_q for given coupling scheme, $e^{D}_{d1,d2,i}\left(f_q\right)$ is the measurement difference at frequency f_q for given measurement difference distribution, I is the number of different $1\times Q$ line vectors of measurement differences per applied measurement difference distribution, first and second parameter and i indicates the i^{th} among I line vectors of measurement differences.

2.2 Piecewise Monotonic Data Approximations and iSHM Footprints

Piecewise monotonic data approximations have extensively been applied in transmission and distribution BPL topologies during various critical broadband applications that require the mitigation of measurement differences in order to ensure the smooth operation of the power grid [36], [39], [42]-[46]. A synthesis of suitable quantitative performance metrics has been proposed and benchmarked so far, such as PES, fault PES and ΔPES, for the mitigation of measurement differences during the BPL channel attenuation determination [44], [14]. During the preparation of the improved iSHM footprints, piecewise monotonic data approximations are going to filter the numerical results of DHM that are contaminated by measurement differences between the Phases A and B of the BPMN diagram of iSHM [29]. From the available piecewise monotonic data approximations [37], [42], [47]-[51], L1PMA and L2WPMA are applied in this paper while the corresponding iSHM footprints can be considered as new qualitative performance metrics.

As L1PMA is integrated in BPMN diagram of iSHM, L1PMA receives as input the measured OV LV BPL coupling scheme transfer function data from Phase A and gives as output the corresponding approximated data that are further delivered to Phase B of the BPMN diagram of iSHM. By exploiting the piecewise monotonicity property of OV LV BPL coupling scheme transfer functions, L1PMA decomposes the input data into separate monotonous sections between the adjacent turning points (primary extrema) [49], [50]. The main advantage of L1PMA is its mitigation performance against the uncorrelated measurement differences generated by CUDs by identifying and ignoring the few large measurement differences [36], [42], [44]. In programming terms, by having developed and exploiting the appropriate MATLAB - Octave / Fortran interface, L1PMA Fortran software package, which is freely available in [52], gives the best fit of the measured OV LV BPL coupling scheme transfer function data given the number of monotonic sections (*i.e.*, either user- or computer-defined).

As L2WPMA is regarded, L2WPMA holds the same position with L1PMA in the BPMN diagram of iSHM. Similarly to L1PMA, appropriate Fortran software package that interoperates with the existing MATLAB - Octave module is freely available online in [37]. L2WPMA operates in a same way to L1PMA since L2WPMA decomposes the examined input measured data contaminated by measurement differences into separate monotonous sections between its primary extrema [37], [42], [44]. Conversely to L1PMA, L2WPMA exploits the first divided of input data while it minimizes the weighted sum of the square of the measurement differences by requiring specific number of sign changes that are defined either by user or the computer.

Note that the default operation settings, which are described in Sec 3.4 of [24] and Sec. 3.2 of [1], that regulate the interconnected operation from DHM to iSHM footprints are also assumed in this paper. In order to allow the application of piecewise monotonic data approximations, the only mandatory change concerning the assumed default operation settings has to do with the required BPL frequency range; due to restrictions in the number of monotonic sections and sign changes imposed by the Fortran software packages of L1PMA and L2WPMA, respectively, the BPL frequency range and flat-fading subchannel frequency spacing are assumed to be equal to 3-30MHz and 1MHz, respectively. Therefore, the number of flat-fading subchannels Q is equal to 27 while the flat-fading subchannel start frequencies are given by

$$f_q = 3\text{MHz} + (q-1) \times 1\text{MHz},\ q=1,\ldots,Q \tag{2}$$

Note that small differences are expected to appear in iSHM class maps and iSHM footprints of OV LV BPL topologies of [1] due to the aforementioned changes of BPL frequency range settings but the generality of the mitigation measurement difference analysis remains valid.

As the mathematics of piecewise monotonic data approximations is considered, the approximated coupling scheme transfer function can be expressed as

$$\overline{\overline{H_{d1,d2,\imath}^{\mathrm{OVLV},C,D,P}}}\left(f_q\right) = P\left\{\overline{H_{d1,d2,\imath}^{\mathrm{OVLV},C,D}}\left(f_q\right)\right\},\ q=1,\ldots,Q,\ i=1,\ldots,I \tag{3}$$

where $[\cdot]^P$ denotes the applied piecewise monotonic data approximation, say L1PMA and L2WPMA, and $P\{\cdot\}$ synopsizes the aforementioned procedure for given piecewise monotonic data approximation that is anyway executed by the corresponding software package.

3. Numerical Results and Discussion

In this Section, numerical results that qualitatively assesses the mitigation impact of piecewise monotonic data approximations against measurement differences on iSHM footprints of OV LV BPL topologies are demonstrated. First, the countermeasures effect of L1PMA and L2WPMA is qualitatively benchmarked for given intensity of the measurement difference CUD. Second, the impact of the user-defined numbers of L1PMA monotonic sections and L2WPMA sign changes is graphically assessed with respect to the mitigation of measurement differences. Third, the mitigation performance of L1PMA and L2WPMA is finally qualitatively assessed against the measurement differences of increasing intensity.

3.1 iSHM Class Maps of OV LV BPL Topologies

In accordance with the BPMN diagram of iSHM [29], the CASD MLEs of iSHM are computed at the Phase C of Fig. 2(a) of [24]. In accordance with [35], Weibull CASD MLEs are going to be used in this paper since Weibull CASD performs the best performance among the available iSHM CASDs with reference to the percentage change and average absolute percentage change when OV LV BPL topology main subclasses are examined. In accordance with [33]-[35], the iSHM class map of OV LV BPL topologies, which acts as the graphical basis for the demonstration of iSHM footprints due to measurement differences, is plotted in Fig. 1 with respect to $\hat{a}_{\mathrm{MLE}}^{\mathrm{Weibull}}$, $\hat{\beta}_{\mathrm{MLE}}^{\mathrm{Weibull}}$ and the average capacity of each OV LV BPL topology subclass when the default operation settings of [1], [24] and the modified BPL frequency range settings of Sec.2.2 are assumed.

By comparing Fig. 1 with Fig. 1 of [1], differences are observed in capacity borders and the location of the real indicative OV LV BPL topologies of Table 1 of [24] since different frequency range properties from those of [1] are assumed in this paper in order to allow the fine operation of L1PMA and L2WPMA [44]. Also, to focus on the demonstration of the mitigation impact results of piecewise monotonic data approximations, only one real indicative OV LV BPL topology of the main subclasses of Table 1 of [24], say, urban case A, is going to be examined in this paper. According to [1], aggravated OV LV BPL topologies, such as urban case A and B, that are characterized by intense multipath environments, are more sensitive to measurement differences as unveiled in iSHM footprints of [1] and for that reason urban case A is arbitrarily chosen to be investigated in this paper. Note that the real indicative OV LV BPL rural case is located outside the $\hat{\beta}_{\mathrm{MLE}}^{\mathrm{Weibull}}$ upper limit of Fig. 1 due to the aforementioned frequency range properties.

3.2 iSHM Footprints due to Measurement Differences and the Countermeasures of Piecewise Monotonic Data Approximations

The impact of measurement differences on iSHM class maps of OV LV BPL topologies can be examined via the iSHM footprints as well as the effect of the proposed countermeasures. The mitigation impact of piecewise monotonic approximations can be checked by the comparison of the iSHM footprint due to measurement differences and the iSHM footprint after the application of the countermeasures in terms of the footprint size reduction, direction to the axes origin and mitigation shift.

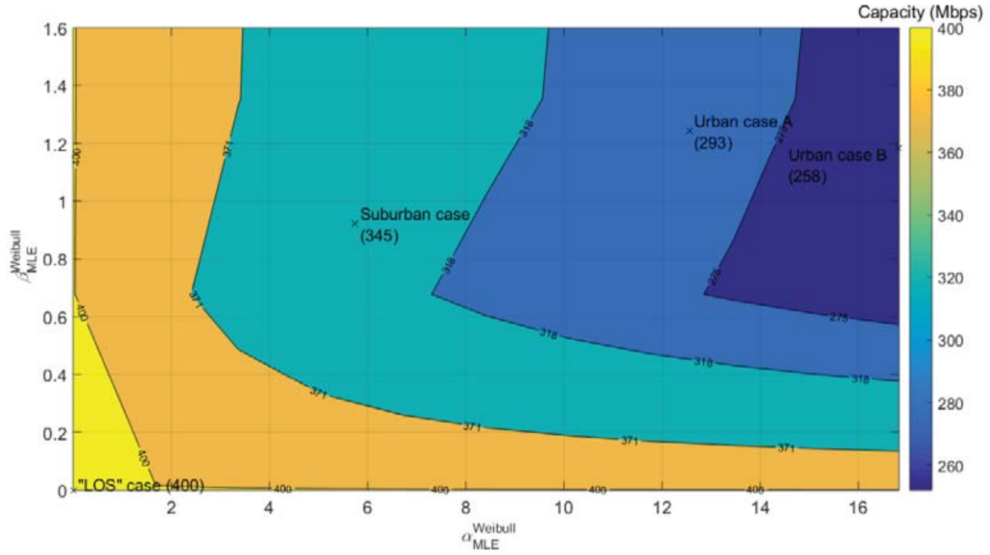

Fig. 1. iSHM class map of OV LV BPL topologies when 3-30MHz frequency band, 1MHz frequency subchannel spacing, WtG^{1} coupling scheme and FCC Part 15 are assumed [35].

With reference to the iSHM class map of Fig. 1, the iSHM footprint due to measurement differences of the arbitrary 5dB maximum value a_{CUD} for the real indicative OV LV BPL urban case A is illustrated in Fig. 2 as superimposed white circles on the iSHM class map. Also, in Fig. 2, the iSHM footprint after the application of L1PMA against the aforementioned measurement differences is shown as superimposed cyan squares when 4 monotonic sections are assumed. Note that 100 line vectors of random measurement differences of the aforementioned CUD are assumed during the preparation of Fig. 2 that imply 100 white circles and 100 respective cyan squares. In Fig. 3, similar iSHM footprints with Fig. 2 are illustrated but for the application of L2WPMA when 4 sign changes and the same 100 line vectors of measurement differences are assumed.

By comparing iSHM footprints due to measurement differences of Figs 2 and 3 with Fig. 3(a) of [1], it is obvious that the fewer data of the numerical results of DHM of this paper render the iSHM footprint due to measurements more sensitive to the measurement differences and more segmented. The destructive result of measurement differences is justified by the extent of the iSHM footprint due to measurement differences that starts from the neighborhood of the theoretical values of $\hat{a}_{\mathrm{MLE}}^{\mathrm{Weibull}}$ and $\hat{\beta}_{\mathrm{MLE}}^{\mathrm{Weibull}}$ of the real indicative OV LV BPL urban case A and reaches up to the OV LV BPL rural class topology.

As the L1PMA is applied, its mitigation efficiency against the measurement differences is visible by the shift of the iSHM footprint towards the up right direction due to the L1PMA application near to the theoretical values of $\hat{a}_{\mathrm{MLE}}^{\mathrm{Weibull}}$ and $\hat{\beta}_{\mathrm{MLE}}^{\mathrm{Weibull}}$ of the real indicative OV LV BPL urban case A. Indeed, cyan squares that come from the L1PMA application are located closer to the theoretical values of $\hat{a}_{\mathrm{MLE}}^{\mathrm{Weibull}}$ and $\hat{\beta}_{\mathrm{MLE}}^{\mathrm{Weibull}}$ of the real indicative OV LV BPL urban case A compared with the white circles supported by the measurement differences. In Fig. 3, same results regarding the iSHM footprint of the approximated data are observed after the L2WPMA application.

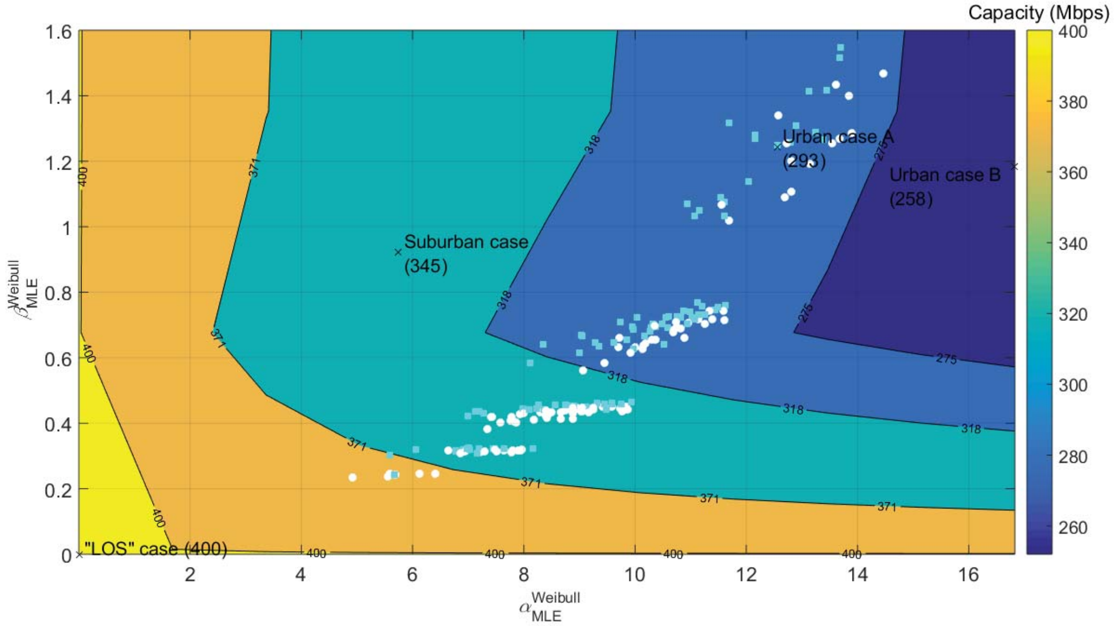

Fig. 2. iSHM footprints of the real indicative OV LV BPL urban case A when 3-30MHz frequency band, 1MHz frequency subchannel spacing, WtG^1 coupling scheme, FCC Part 15, CUD measurement differences of maximum value a_{CUD} = 5dB (white circles) are assumed and L1PMA of 4 monotonic sections (cyan squares) is applied.

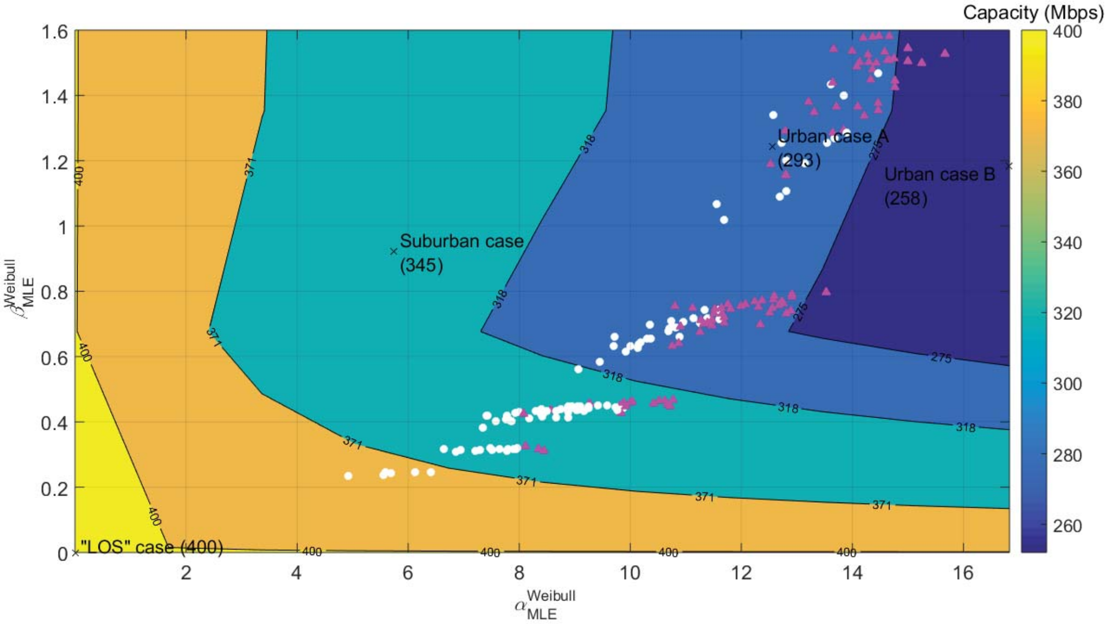

Fig. 3. Same plot with Fig. 2 but for L2WPMA of 4 sign changes (magenta triangles).

Until now, the mitigation impact of measurement differences on class maps has been investigated in terms of the relative location and the extent of the corresponding iSHM footprints due to the application of L1PMA and L2WPMA. In the following subsection, the impact of monotonic sections and sign changes of L1PMA and L2WPMA, respectively, is assessed against the measurement differences for given measurement difference intensity.

3.3 The Role of Monotonic Sections and Sign Changes against the Measurement Differences

In accordance with [42], [44], the selection of the numbers of monotonic sections for L1PMA and of the sign changes for L2WPMA has a critical effect during their application and their mitigation effect against the measurement differences. In order to highlight the importance of the right selection of the number of L1PMA monotonic sections and of L2WPMA sign changes, various strategies have been applied that exploit either the deterministic definition or the adaptive one until now [36], [39], [42]-[44].

Similarly to Fig. 2, the iSHM footprint due to measurement differences of the arbitrary 6dB maximum value a_{CUD} for the real indicative OV LV BPL urban case A is illustrated in Fig. 4(a). Also, in Fig. 4(a), the iSHM footprint due to the application of L1PMA against the aforementioned measurement differences is shown as superimposed cyan squares when 1 monotonic section is assumed. In Figs. 4(b)-(i), similar footprints with Fig. 4(a) are illustrated but for the number of monotonic sections ranging from 2 to 9, respectively. In Figs. 5(a)-(i), similar footprints with Figs. 4(a)-(i) are illustrated but for the application of L2WPMA when sign changes range from 1 to 9, respectively, and the same 100 line vectors of measurement differences are assumed in Figs. 4(a)-(i) and 5(a)-(i).

From Figs. 4(a)-(i) and 5(a)-(i), it is obvious that the careful selection of L1PMA monotonic sections and L2WPMA sign changes may have different impact on the mitigation of measurement differences whereas a bad selection may even make the approximated data worse than the measured ones. Indeed, as the L1PMA monotonic sections are concerned, the predefined number of monotonic sections forces L1PMA to create a pattern of specific monotonic sections for the approximated coupling scheme transfer function data by appropriately filtering the examined measured coupling scheme transfer function data. On the basis of the predefined number of monotonic sections, the L1PMA concept is that measurement differences that mainly disrupt the pattern for the examined measured coupling scheme transfer function data are ignored thus delivering the approximated coupling scheme transfer function data for given number of monotonic sections. A relatively high number of monotonic sections, which is significantly greater than the number of monotonic sections of the theoretical coupling scheme channel attenuation data (e.g., greater than 8 monotonic sections in Fig. 4), can have the opposite results to the expected ones due to the overapproximation of the measured data; say, in this case, a significant number of contaminated data by measurement differences should be taken into account so that the number of monotonic sections of the approximated coupling scheme transfer function data agrees with the predefined number of monotonic sections. The overapproximation of the measured data, which comes from the application of relatively high numbers of monotonic sections, can be observed in iSHM footprints in the cases where cyan squares of the approximated coupling scheme transfer function data start to coincide with the white circles of the measured coupling scheme transfer function data. Conversely, when significantly lower number of monotonic sections is assumed (e.g., 1 or 2 monotonic sections in Fig. 4), an average value of the measured coupling scheme transfer function data is expected.

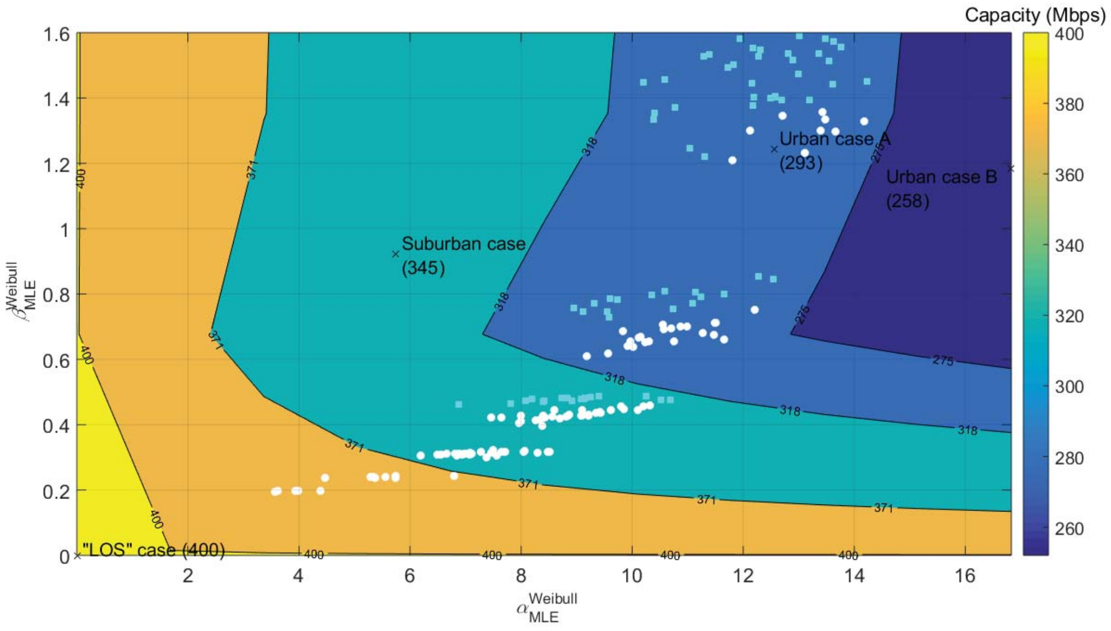
Capacity (Mbps)
400
380
360
340
320
300
280
260
1.6
1.4
1.2
1
0.8
0.6
0.4
0.2
0
$\beta^{Weibull}_{MLE}$
2
4
6
8
10
12
14
16
$\alpha^{Weibull}_{MLE}$
Urban case A
(293)
Urban case B
(258)
Suburban case
(345)
"LOS" case (400)
400
371
318
275

(a)

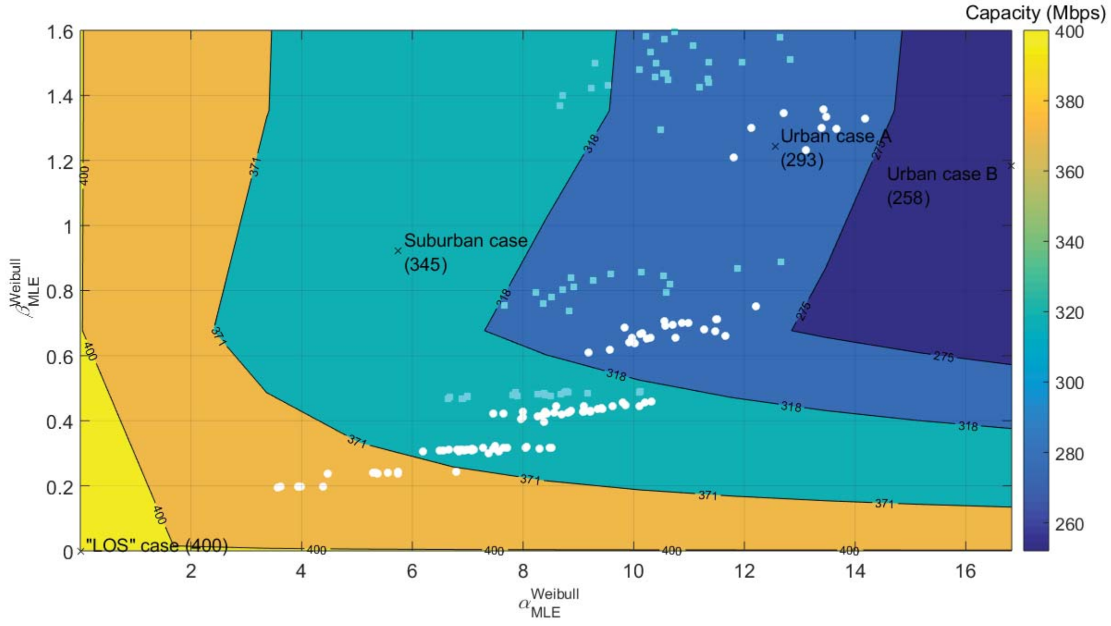
Capacity (Mbps)
400
380
360
340
320
300
280
260
1.6
1.4
1.2
1
0.8
0.6
0.4
0.2
0
$\beta^{Weibull}_{MLE}$
2
4
6
8
10
12
14
16
$\alpha^{Weibull}_{MLE}$
Urban case A
(293)
Urban case B
(258)
Suburban case
(345)
"LOS" case (400)
400
371
318
275

(b)

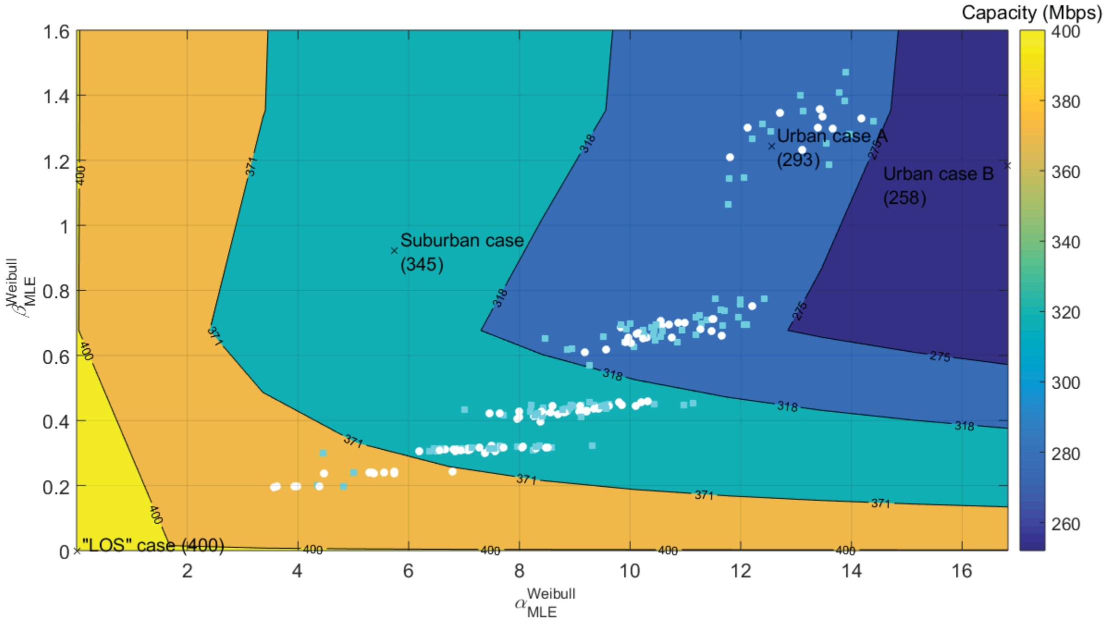
Capacity (Mbps)
400
380
360
340
320
300
280
260
1.6
1.4
1.2
1
0.8
0.6
0.4
0.2
0
$\beta_{MLE}^{Weibull}$
2
4
6
8
10
12
14
16
$\alpha_{MLE}^{Weibull}$
Urban case A (293)
Urban case B (258)
Suburban case (345)
"LOS" case (400)
400
371
318
275

(c)

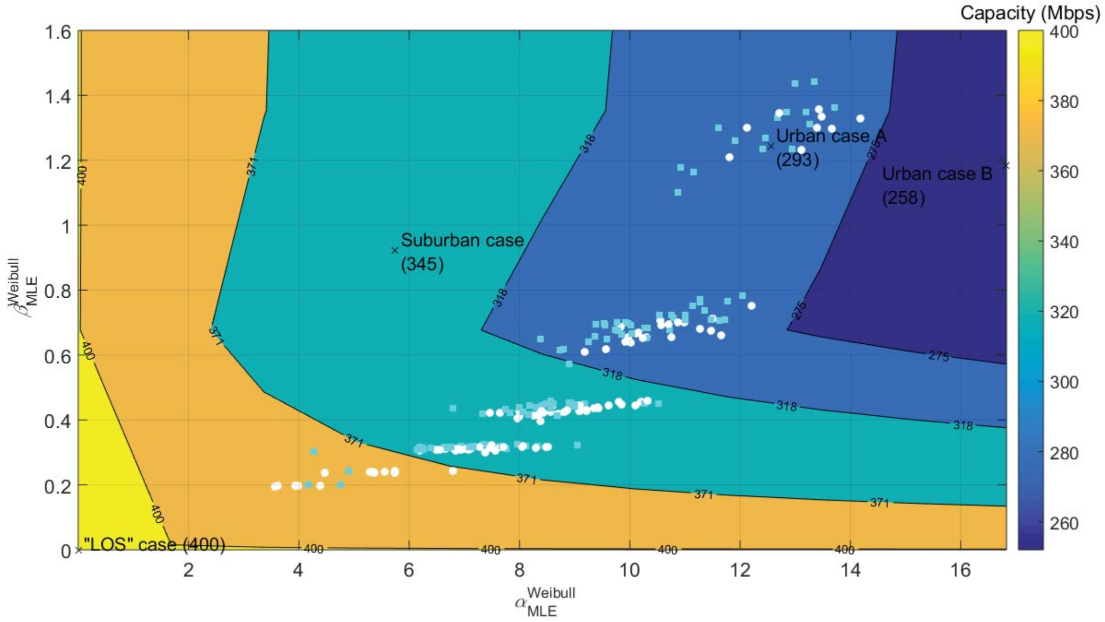
Capacity (Mbps)
400
380
360
340
320
300
280
260
1.6
1.4
1.2
1
0.8
0.6
0.4
0.2
0
$\beta_{MLE}^{Weibull}$
2
4
6
8
10
12
14
16
$\alpha_{MLE}^{Weibull}$
Urban case A (293)
Urban case B (258)
Suburban case (345)
"LOS" case (400)
400
371
318
275

(d)

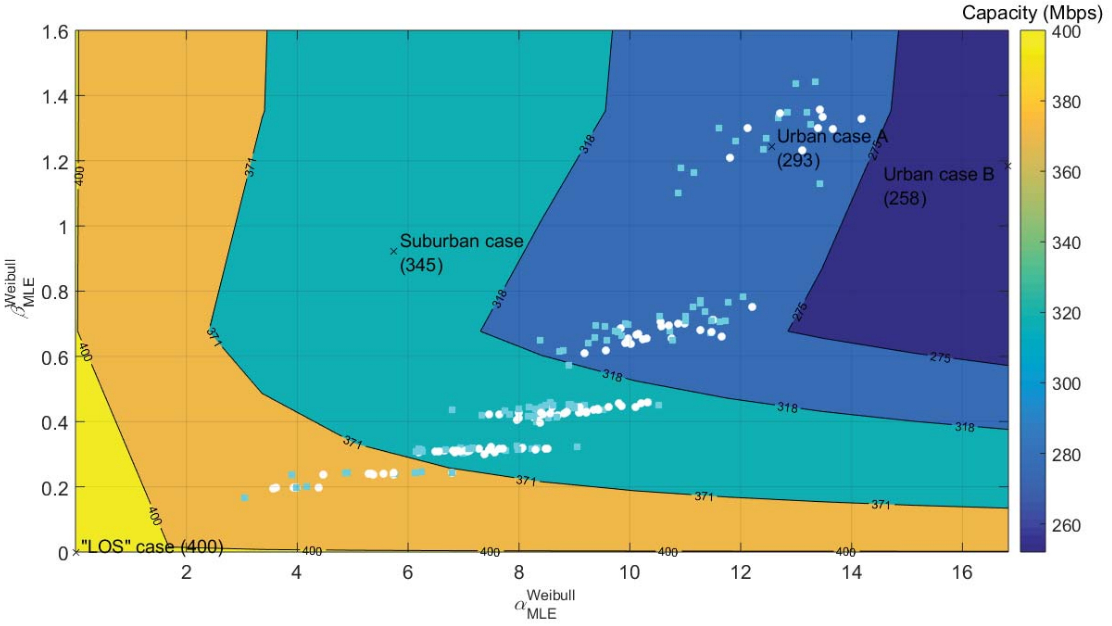
Capacity (Mbps)
400
380
360
340
320
300
280
260
1.6
1.4
1.2
1
0.8
0.6
0.4
0.2
0
$\beta^{Weibull}_{MLE}$
2
4
6
8
10
12
14
16
$\alpha^{Weibull}_{MLE}$
Urban case A
(293)
Urban case B
(258)
Suburban case
(345)
"LOS" case (400)
400
371
318
275

(e)

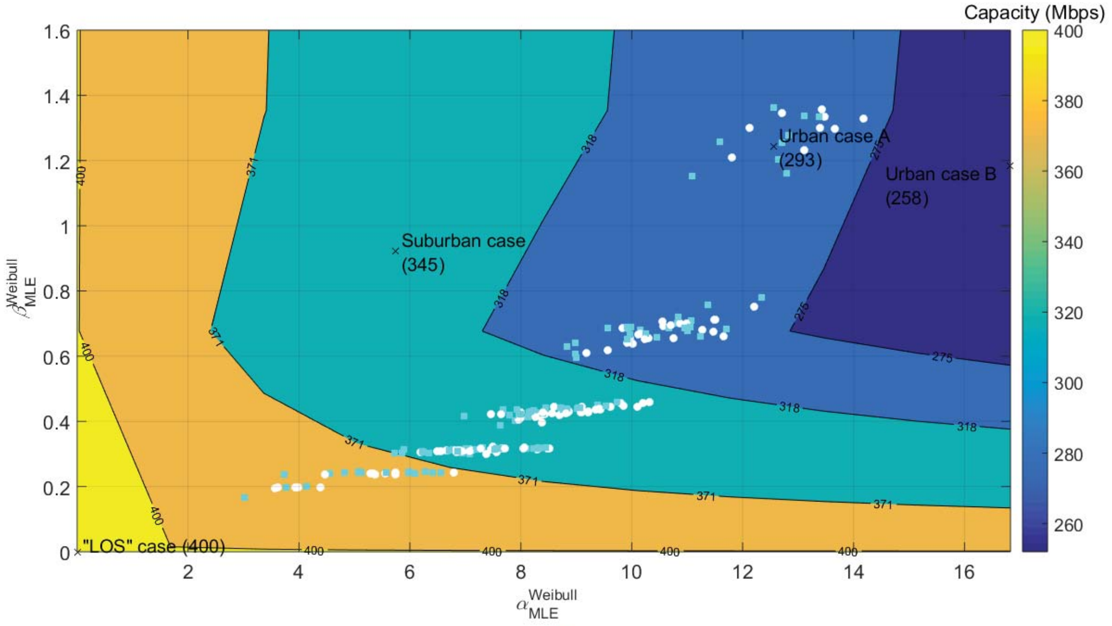
Capacity (Mbps)
400
380
360
340
320
300
280
260
1.6
1.4
1.2
1
0.8
0.6
0.4
0.2
0
$\beta^{Weibull}_{MLE}$
2
4
6
8
10
12
14
16
$\alpha^{Weibull}_{MLE}$
Urban case A
(293)
Urban case B
(258)
Suburban case
(345)
"LOS" case (400)
400
371
318
275

(f)

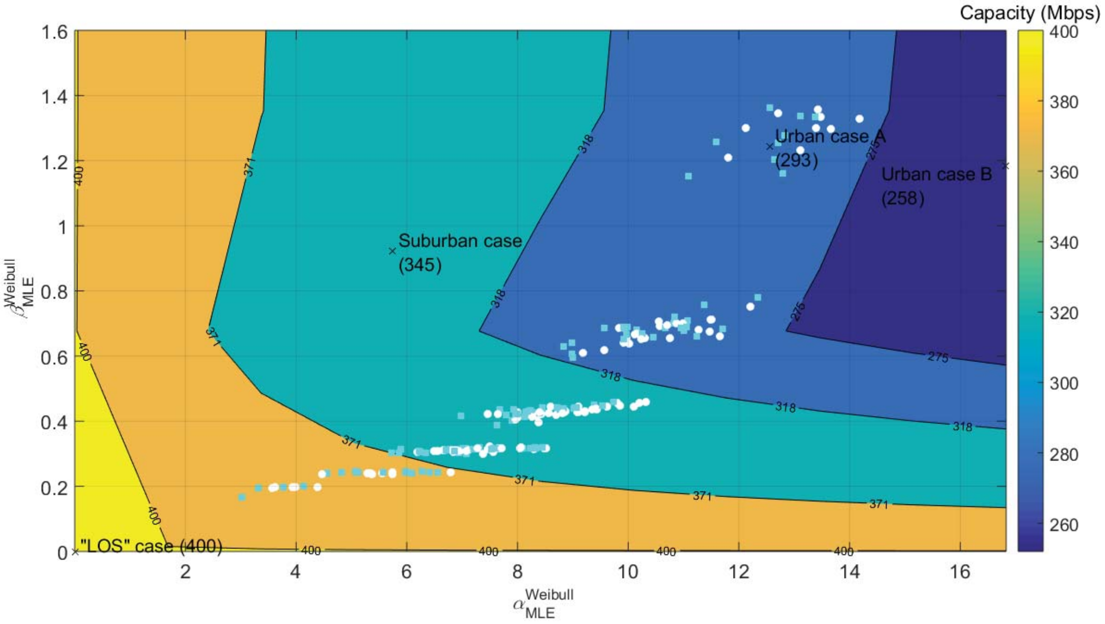
Capacity (Mbps)
400
380
360
340
320
300
280
260
Urban case A
(293)
Urban case B
(258)
Suburban case
(345)
"LOS" case (400)
371
318
275
400
$\beta^{Weibull}_{MLE}$
$\alpha^{Weibull}_{MLE}$
0
0.2
0.4
0.6
0.8
1
1.2
1.4
1.6
2
4
6
8
10
12
14
16

(g)

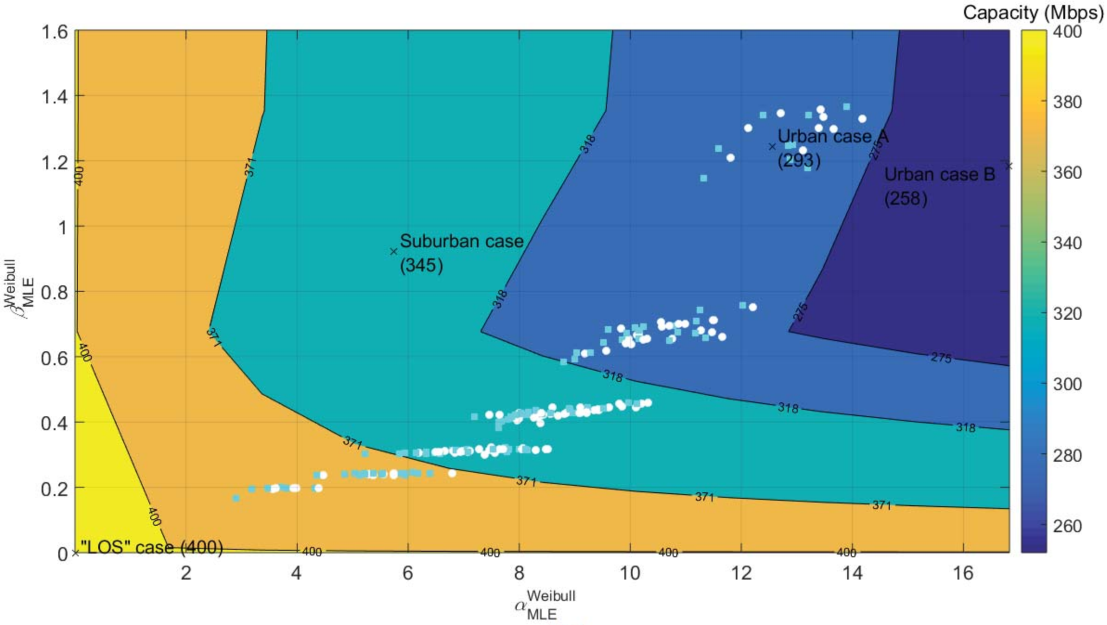
Capacity (Mbps)
400
380
360
340
320
300
280
260
Urban case A
(293)
Urban case B
(258)
Suburban case
(345)
"LOS" case (400)
371
318
275
400
$\beta^{Weibull}_{MLE}$
$\alpha^{Weibull}_{MLE}$
0
0.2
0.4
0.6
0.8
1
1.2
1.4
1.6
2
4
6
8
10
12
14
16

(h)

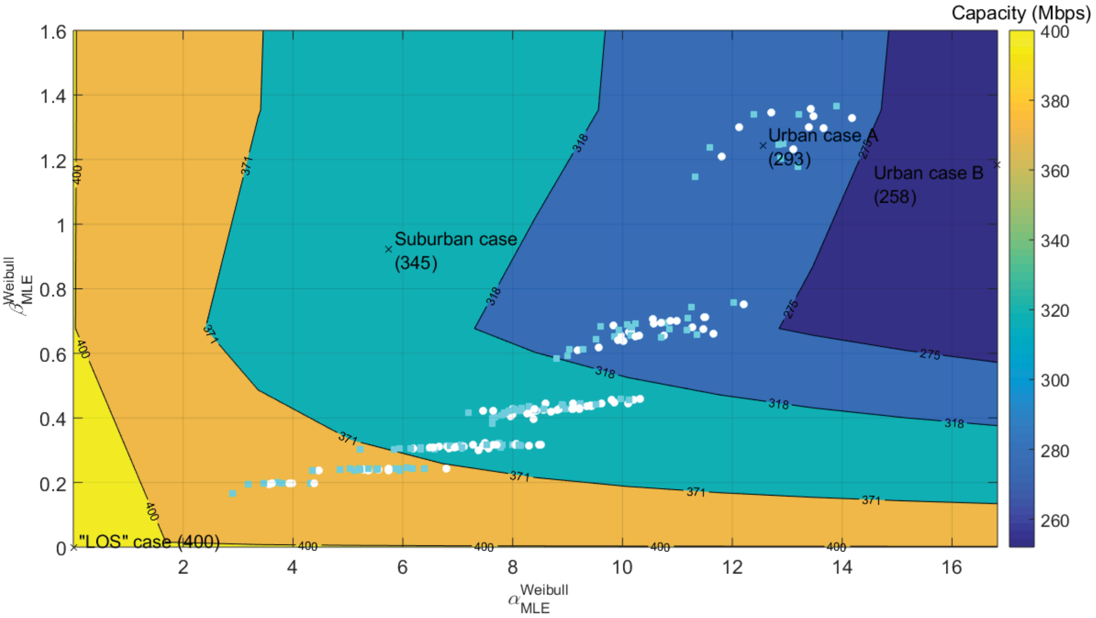

(i)

Fig. 4. iSHM footprints of the real indicative OV LV BPL urban case A when 3-30MHz frequency band, 1MHz frequency subchannel spacing, WtG[1] coupling scheme, FCC Part 15, CUD measurement differences of maximum value a_{CUD} = 6dB (white circles) are assumed and various L1PMA monotonic sections (cyan squares) is applied. (a) 1 monotonic section. (b) 2 monotonic sections. (c) 3 monotonic sections. (d) 4 monotonic sections. (e) 5 monotonic sections. (f) 6 monotonic sections. (g) 7 monotonic sections. (h) 8 monotonic sections. (i) 9 monotonic sections.

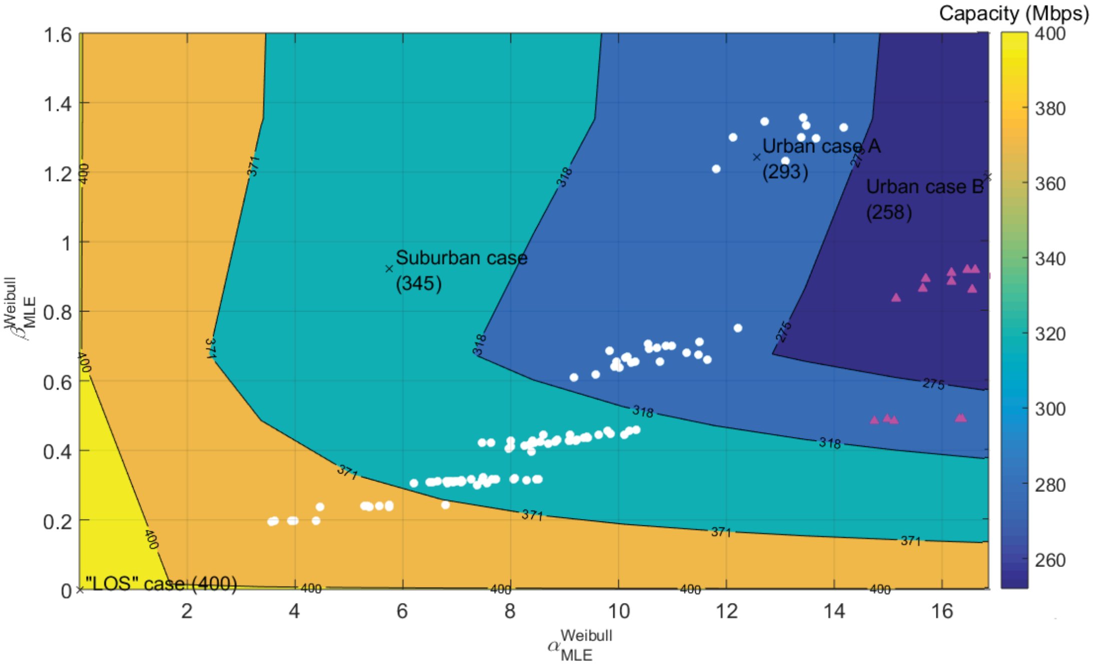
Capacity (Mbps)
400
380
360
340
320
300
280
260
1.6
1.4
1.2
1
0.8
0.6
0.4
0.2
0
$\beta_{MLE}^{Weibull}$
2
4
6
8
10
12
14
16
$\alpha_{MLE}^{Weibull}$
Urban case A
(293)
Urban case B
(258)
Suburban case
(345)
"LOS" case (400)
400
371
318
275

(a)

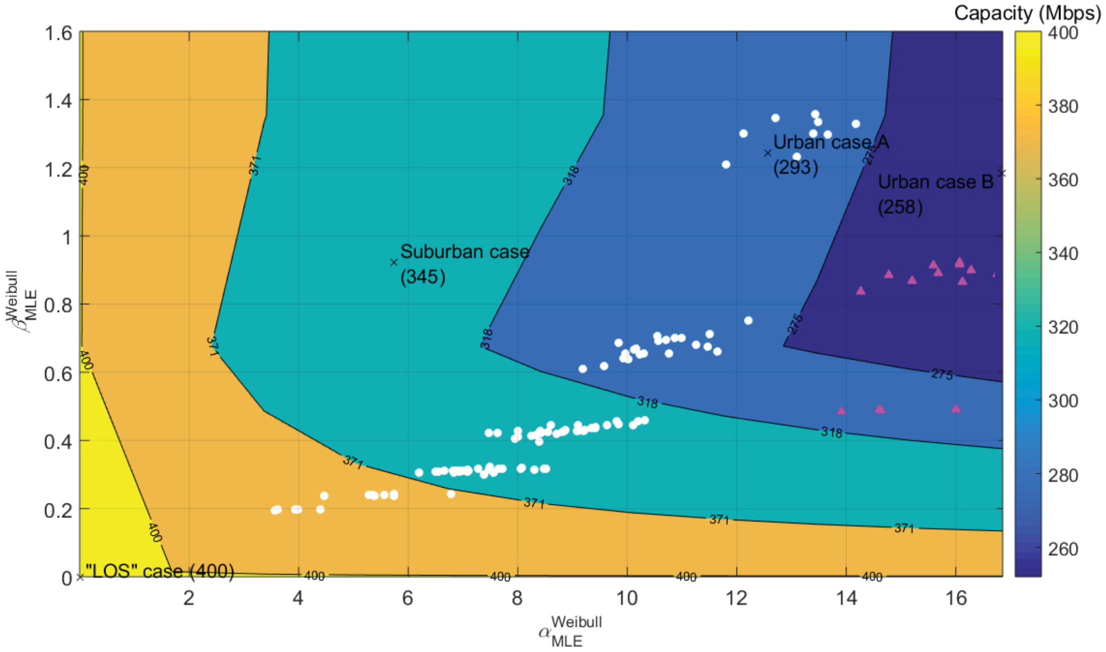
Capacity (Mbps)
400
380
360
340
320
300
280
260
1.6
1.4
1.2
1
0.8
0.6
0.4
0.2
0
$\beta_{MLE}^{Weibull}$
2
4
6
8
10
12
14
16
$\alpha_{MLE}^{Weibull}$
Urban case A
(293)
Urban case B
(258)
Suburban case
(345)
"LOS" case (400)
400
371
318
275

(b)

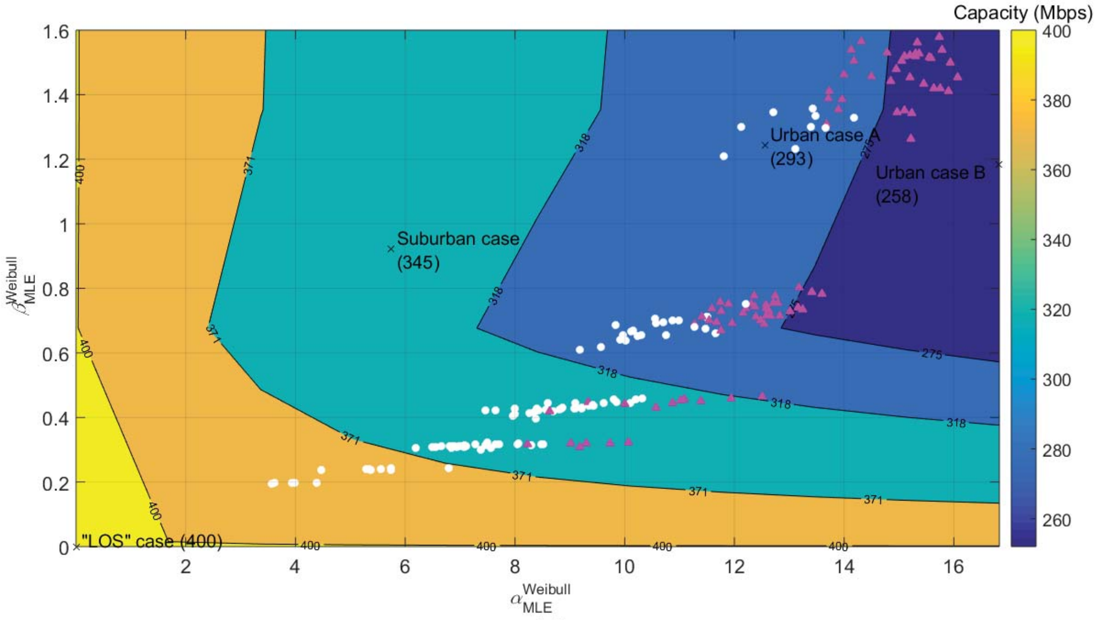
Capacity (Mbps)
400
380
360
340
320
300
280
260
1.6
1.4
1.2
1
0.8
0.6
0.4
0.2
0
$\beta_{MLE}^{Weibull}$
2
4
6
8
10
12
14
16
$\alpha_{MLE}^{Weibull}$
Suburban case
(345)
Urban case A
(293)
Urban case B
(258)
"LOS" case (400)
400
371
318
275

(c)

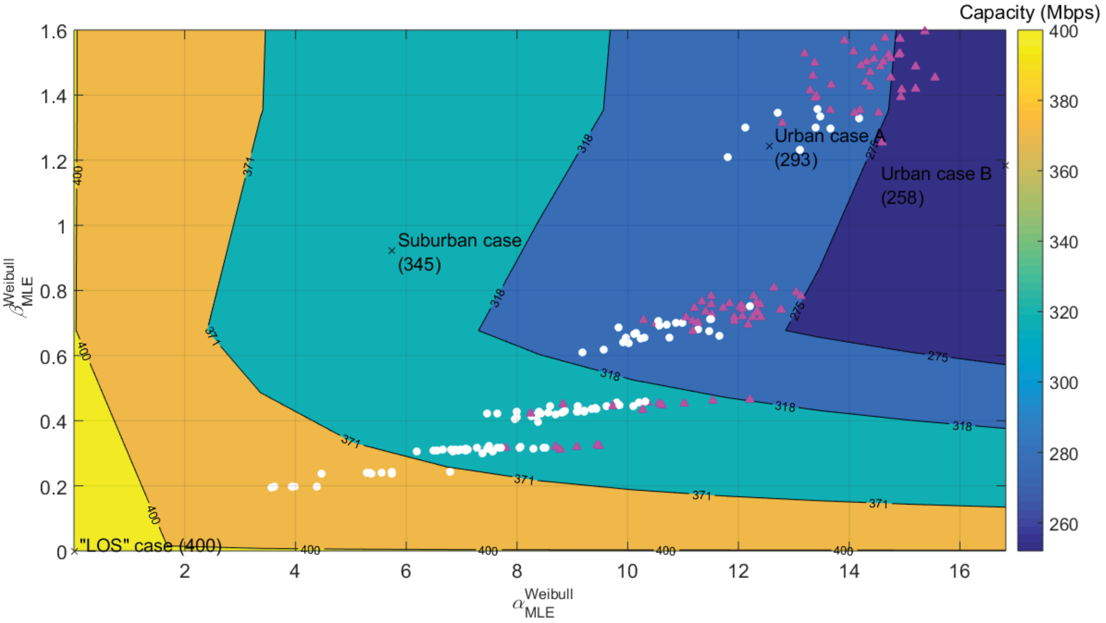
Capacity (Mbps)
400
380
360
340
320
300
280
260
1.6
1.4
1.2
1
0.8
0.6
0.4
0.2
0
$\beta_{MLE}^{Weibull}$
2
4
6
8
10
12
14
16
$\alpha_{MLE}^{Weibull}$
Suburban case
(345)
Urban case A
(293)
Urban case B
(258)
"LOS" case (400)
400
371
318
275

(d)

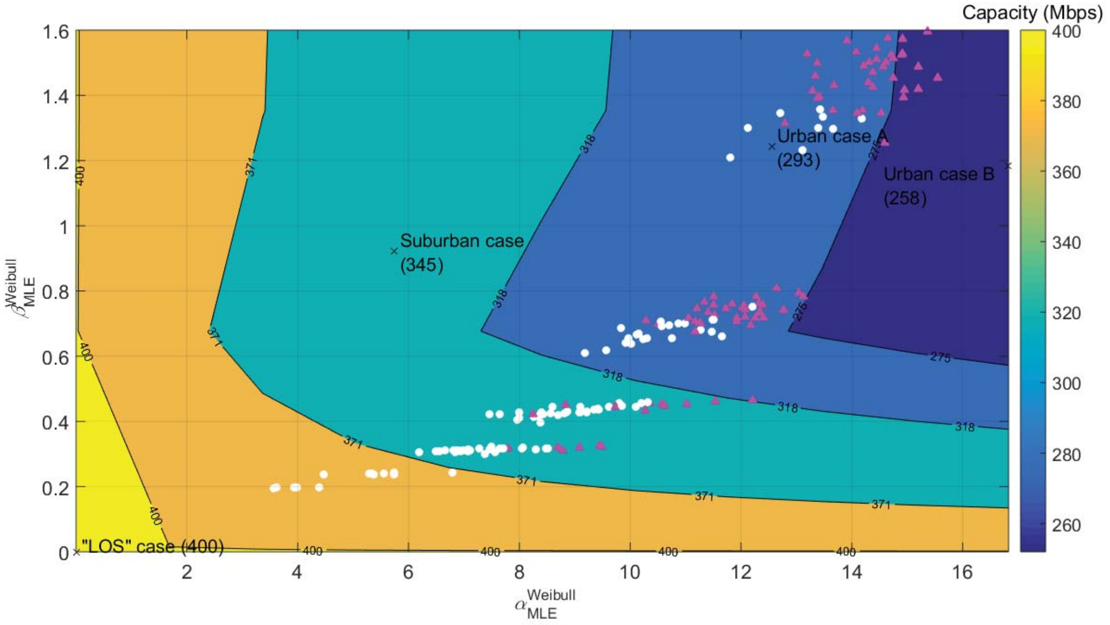
Capacity (Mbps)
400
380
360
340
320
300
280
260
1.6
1.4
1.2
1
0.8
0.6
0.4
0.2
0
2
4
6
8
10
12
14
16
$\beta_{MLE}^{Weibull}$
$\alpha_{MLE}^{Weibull}$
"LOS" case (400)
Suburban case
(345)
Urban case A
(293)
Urban case B
(258)
371
318
275
400

(e)

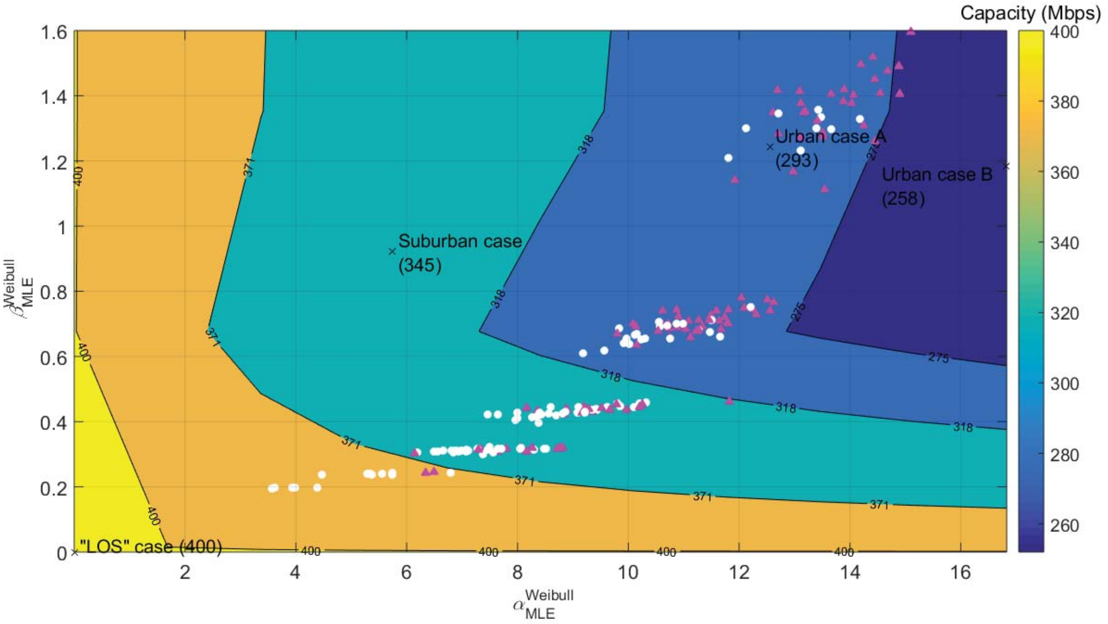
Capacity (Mbps)
400
380
360
340
320
300
280
260
1.6
1.4
1.2
1
0.8
0.6
0.4
0.2
0
2
4
6
8
10
12
14
16
$\beta_{MLE}^{Weibull}$
$\alpha_{MLE}^{Weibull}$
"LOS" case (400)
Suburban case
(345)
Urban case A
(293)
Urban case B
(258)
371
318
275
400

(f)

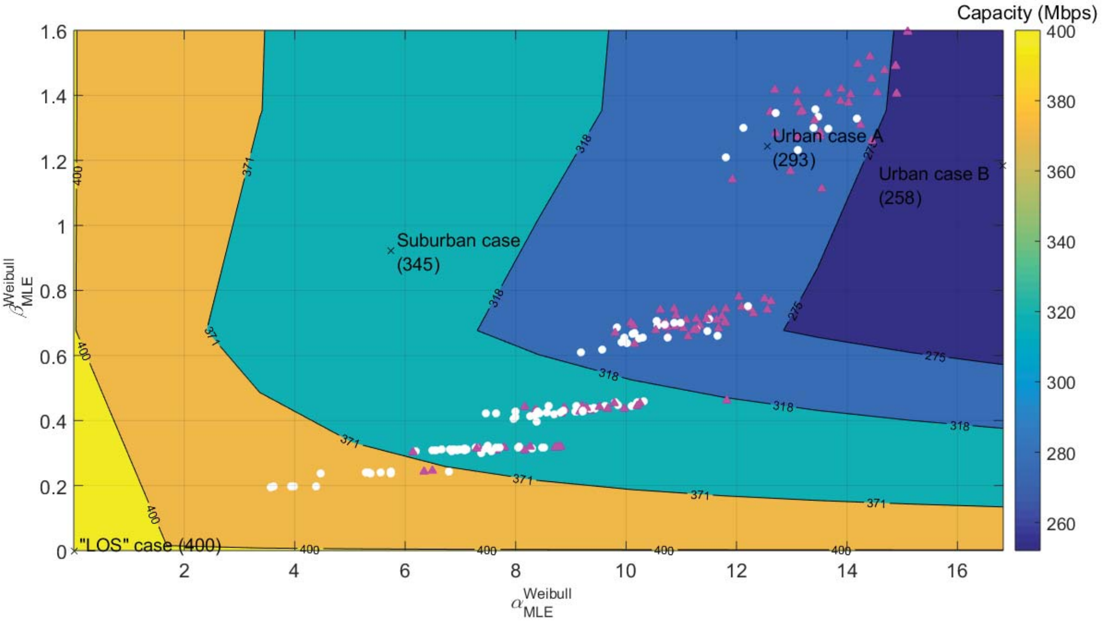
Capacity (Mbps)
400
380
360
340
320
300
280
260
1.6
1.4
1.2
1
0.8
0.6
0.4
0.2
0
2
4
6
8
10
12
14
16
$\beta^{Weibull}_{MLE}$
$\alpha^{Weibull}_{MLE}$
Suburban case
(345)
Urban case A
(293)
Urban case B
(258)
"LOS" case (400)
400
371
318
275

(g)

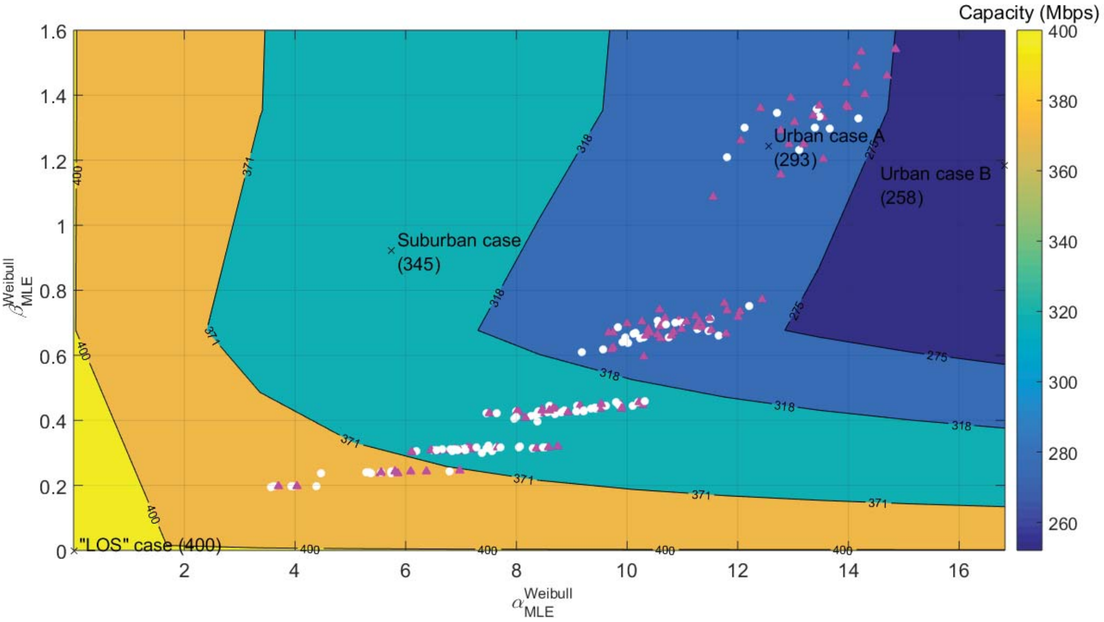
Capacity (Mbps)
400
380
360
340
320
300
280
260
1.6
1.4
1.2
1
0.8
0.6
0.4
0.2
0
2
4
6
8
10
12
14
16
$\beta^{Weibull}_{MLE}$
$\alpha^{Weibull}_{MLE}$
Suburban case
(345)
Urban case A
(293)
Urban case B
(258)
"LOS" case (400)
400
371
318
275

(h)

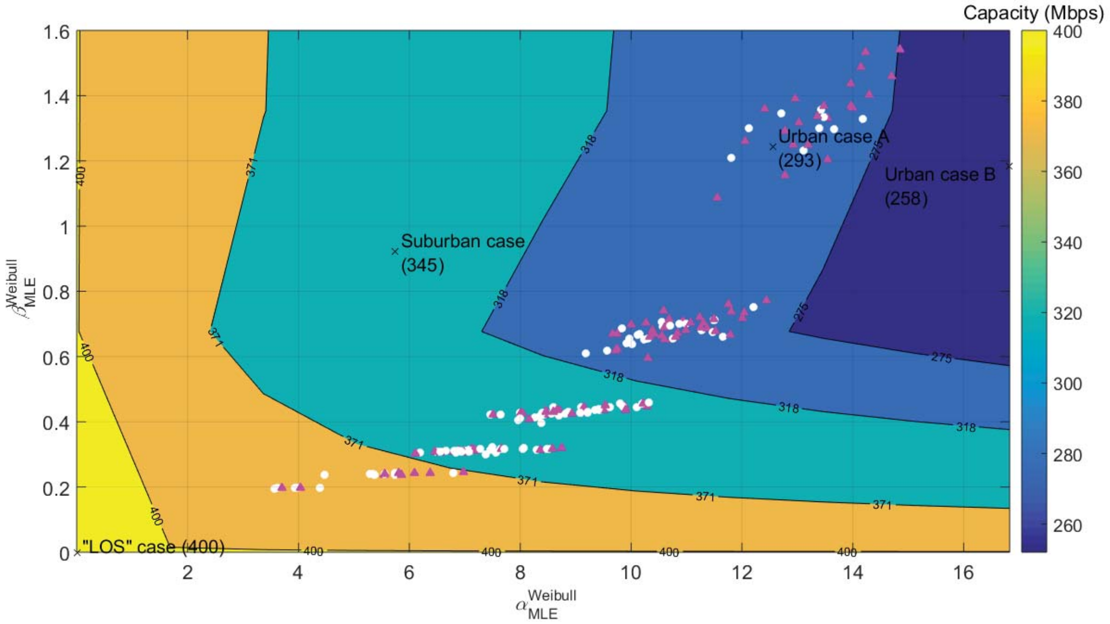

(i)

Fig. 5. Same plots with Fig. 4 but for L2WPMA of different sign changes (magenta triangles). (a) 1 sign change. (b) 2 sign changes. (c) 3 sign changes. (d) 4 sign changes. (e) 5 sign changes. (f) 6 sign changes. (g) 7 sign changes. (h) 8 sign changes. (i) 9 sign changes.

L1PMA approximations of very low monotonic sections are revealed in iSHM footprints by the significantly higher distances between the white circles and the respective cyan squares that can anyway lead to a safe mitigation of measurement differences. Same results concerning the selection of L2WPMA sign changes are observed in L2WPMA iSHM footprints. Anyway, a successful selection of L1PMA monotonic sections or L2WPMA sign changes is characterized by corresponding iSHM footprint whose cyan squares or magenta triangles are located closer to the sign of the real indicative OV LV BPL urban case A than the white circles of the measured coupling scheme transfer function data. In the rest of this paper, 1 monotonic section and 5 sign changes are assumed for the application of L1PMA and L2WPMA, respectively, by visually comparing Figs. 4(a)-(i) and 5(a)-(i), respectively.

In accordance with [36], [39], [42]-[44], the numbers of L1PMA monotonic sections and L2WPMA sign changes should be based mainly on the inherent properties of the examined theoretical coupling scheme transfer function data and secondarily on the intensity of measurement differences only for little adjustments. As the stochastic definition of the numbers of L1PMA monotonic sections and L2WPMA sign changes is applied in this paper, the aforementioned secondary dependence can be neglected. Therefore the 1 L1PMA monotonic section and 5 L2WPMA sign changes are assumed to act as constants for the following respective L1PMA and L2WPMA approximations. In the following subsection, the mitigation efficiency of L1PMA and L2WPMA against different intensities of measurement differences is qualitatively assessed through respective iSHM footprints.

3.4 L1PMA and L2WPMA iSHM Footprints and Different Intensities of Measurement Differences

Higher intensities of measurement differences entail higher maximum values a_{CUD} for the CUD measurement differences that are applied in this subsection. With reference to the iSHM class map of Fig. 1, the iSHM footprint due to measurement differences of the real indicative OV LV BPL urban case A is illustrated as a set of circles of various reddish colors in Fig. 6 when the maximum value a_{CUD} of CUD measurement differences ranges from 0B to 15dB. In contrast with Figs. 4(a)-(i), only one random line vector of measurement differences, say, the first one, is applied per each maximum value a_{CUD} while the color of the superimposed circles becomes redder as the maximum value a_{CUD} increases. Given the random line vector of measurement differences of maximum value a_{CUD} and its corresponding circle of the iSHM footprint, L1PMA approximates the corresponding measured coupling scheme transfer function data with the assumed 1 monotonic section of Sec.3.3 while the respective approximated coupling scheme transfer function data are illustrated as a square of the same color with the circle color it comes from and a cyan perimeter as well as a connecting line of the same color with the circle color between the circle and the square. In Fig. 7, similar iSHM footprint with Fig. 6 is shown but for the case of L2WPMA when the 5 sign changes of Sec.3.3 are assumed and triangles with magenta perimeter are plotted instead of the L1PMA squares.

From Figs. 6 and 7, it is clear that the increasing maximum value a_{CUD} of CUD measurement differences imposes the simultaneous decrease of $\hat{a}_{\mathrm{MLE}}^{\mathrm{Weibull}}$ and $\hat{\beta}_{\mathrm{MLE}}^{\mathrm{Weibull}}$ of the measured data of the real indicative OV LV BPL urban case A. In accordance with [1], the redder circles that come from the application of higher maximum values a_{CUD} are located closer to the axes origin rather than to the $\hat{a}_{\mathrm{MLE}}^{\mathrm{Weibull}}$ and $\hat{\beta}_{\mathrm{MLE}}^{\mathrm{Weibull}}$ of the theoretical data of the real indicative OV LV BPL urban case A. Hence, the iSHM footprint due to the increasing measurement differences starts from the neighborhood of the theoretical values of $\hat{a}_{\mathrm{MLE}}^{\mathrm{Weibull}}$ and $\hat{\beta}_{\mathrm{MLE}}^{\mathrm{Weibull}}$ of the real indicative OV LV BPL urban case A and tends to the axes origin in a down-left diagonal direction. The goal of the application of piecewise monotonic data approximations is to reverse the previous diagonal direction of red circles and to bring the approximated respective red L1PMA squares and L2WPMA triangles: (i) back to the OV LV BPL urban case A topology class as primary objective; and (ii) as close as possible to the theoretical values of $\hat{a}_{\mathrm{MLE}}^{\mathrm{Weibull}}$ and $\hat{\beta}_{\mathrm{MLE}}^{\mathrm{Weibull}}$ as secondary but more accurate objective.

In order to qualitatively assess the performance of L1PMA and L2WPMA against the increasing measurement differences, the location and the distance of L1PMA squares and L2WPMA triangles that come from the respective circles of the measured data are tracked. In the vast majority of the cases, squares and triangles are located closer to the theoretical values of $\hat{a}_{\mathrm{MLE}}^{\mathrm{Weibull}}$ and $\hat{\beta}_{\mathrm{MLE}}^{\mathrm{Weibull}}$ of the real indicative OV LV BPL urban case A compared against the respective circles of the measured data. More analytically, in the examined cases where high measurement differences are applied, the L1PMA mitigation of measurement differences is important since from the six circles that are located at OV LV BPL rural and "LOS" topology classes, no squares remain inside the aforementioned classes. Similarly, L2WPMA countermeasures against measurement differences achieve to mitigate five out of the five circles that are located at OV LV BPL rural and

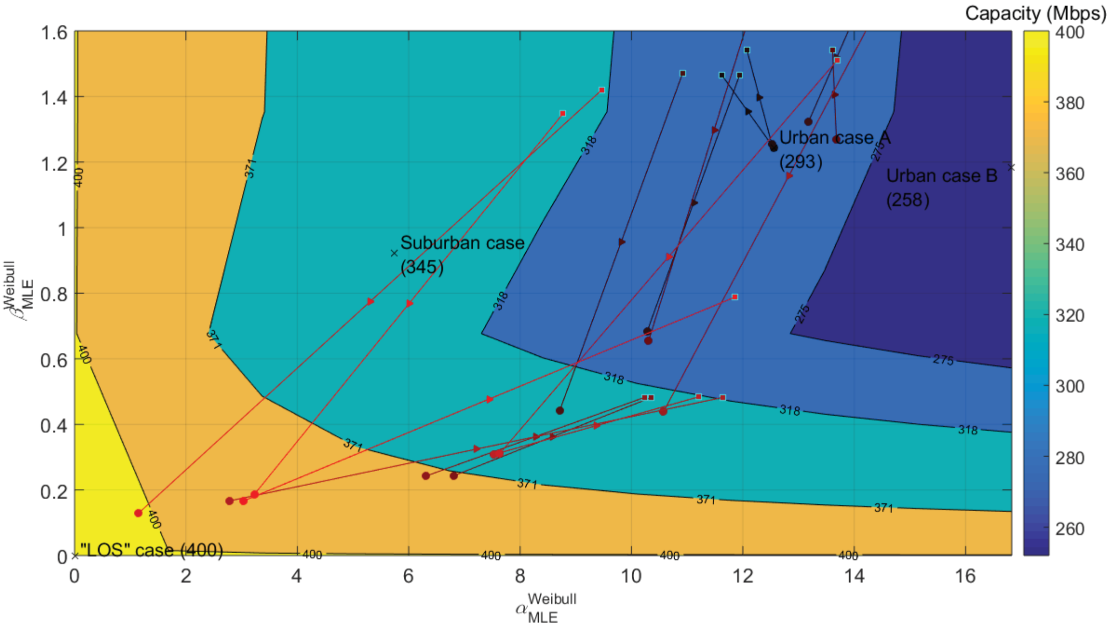

Fig. 6. iSHM footprints of the real indicative OV LV BPL topologies when 3-30MHz frequency band, WtG[1] coupling scheme, FCC Part 15, 1 monotonic section of L1PMA and CUD measurement differences of maximum value a_{CUD} that ranges from 0dB (black spot) to 15dB (red spot) are assumed.

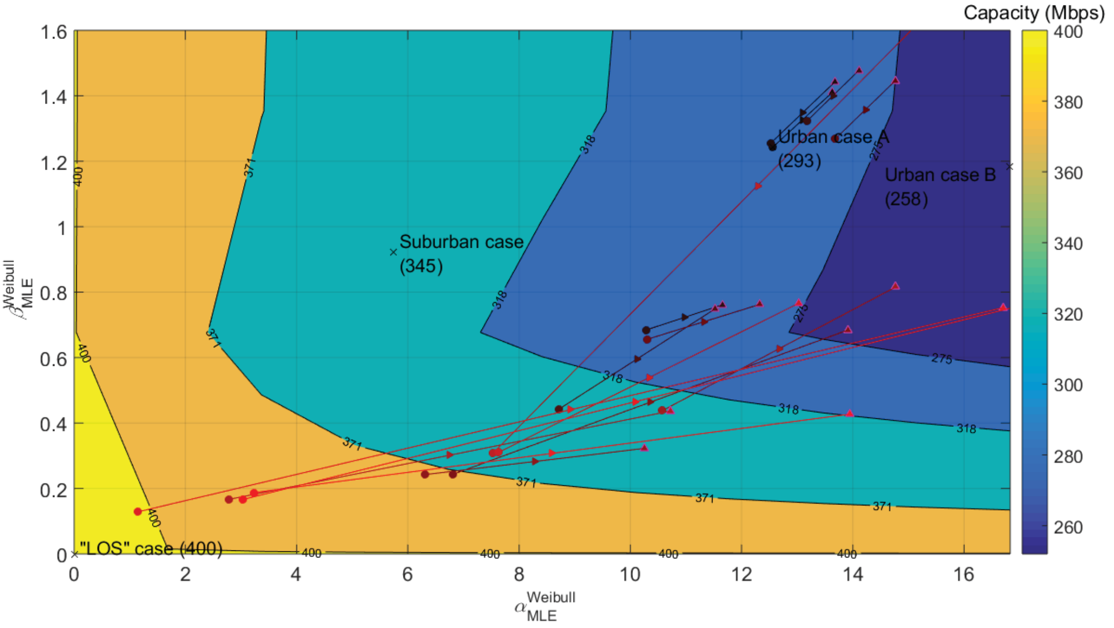

Fig. 7. Same plots but for 5 sign changes of L2WPMA.

“LOS” topology classes. In addition, from the 16 available circles, 6 of them are located at the OV LV BPL urban case A topology class when 8 squares and 9 triangles are present in the visible part of the previous class after the application of L1PMA and L2WPMA, respectively. Anyway, the connecting lines with their triangle signs at their middle reveal the performance of L1PMA and L2WPMA against the measurement differences while the mitigation efficiency becomes more significant when measurement differences are higher. Anyway, the promising results regarding the mitigation of higher measurement differences by L1PMA and L2WPMA was expected after the determination of respective monotonic sections and sign changes in Sec.3.3.

In this subsection, the qualitative assessment of piecewise monotonic data approximations via iSHM footprints has revealed their strong potential against measurement differences of increasing intensity. The obvious evolution of this piece of research is the proposal of a quantitative assessment of the mitigation impact of piecewise monotonic data approximations based on iSHM footprints in [53] so that a more confident selection of L1PMA monotonic sections and L2WPMA sign changes can be achieved.

4. Conclusions

To ensure the reliability of data that feed the business analytics and the tools of the SG, the mitigation performance of L1PMA and L2WPMA against measurement differences has been qualitatively assessed via iSHM footprints for OV LV BPL topologies. Indeed, L1PMA and L2WPMA iSHM footprints present significant improvement concerning their extent and their distance from Weibull CASD MLEs of the real indicative OV LV BPL urban case A when they are compared against iSHM footprints due to measurement differences. Also, it has been verified that the fine selection of L1PMA monotonic sections and L2WPMA sign changes plays critical role towards a successful mitigation of measurement differences. In addition, the proposed countermeasures of applying L1PMA and L2WPMA have been proven to be a valuable tool against high measurement differences since the mitigation efficiency in these cases is important. Finally, the qualitative assessment of piecewise monotonic data approximations has been validated via iSHM footprints but the continuation of the research in [53] focuses on the proposal of quantitative metrics for iSHM footprints that allows the more precise selection of L1PMA monotonic sections and L2WPMA sign changes on the basis of the available iSHM footprints.

CONFLICTS OF INTEREST

The author declares that there is no conflict of interests regarding the publication of this paper.

References

[1] A. G. Lazaropoulos, “Business Analytics and IT in Smart Grid – Part 1: The Impact of Measurement Differences on the iSHM Class Map Footprints of Overhead Low-Voltage Broadband over Power Lines Topologies,” *Trends in Renewable Energy*, vol. 6, no. 2, pp. 146-176, May 2020.

[2] A. G. Lazaropoulos, “Factors Influencing Broadband Transmission Characteristics of Underground Low-Voltage Distribution Networks,” *IET Commun.*, vol. 6, no. 17, pp. 2886-2893, Nov. 2012.

[3] F. Aalamifar and L. Lampe, "Optimized WiMAX profile configuration for smart grid communications," *IEEE Transactions on Smart Grid*, vol. 8, no. 6, pp. 2723-2732, 2017.

[4] A. G. Lazaropoulos, "Deployment Concepts for Overhead High Voltage Broadband over Power Lines Connections with Two-Hop Repeater System: Capacity Countermeasures against Aggravated Topologies and High Noise Environments," *Progress in Electromagnetics Research B*, vol. 44, pp. 283-307, 2012. [Online]. Available: http://www.jpier.org/PIERB/pierb44/13.12081104.pdf

[5] A. G. Lazaropoulos, "Towards Broadband over Power Lines Systems Integration: Transmission Characteristics of Underground Low-Voltage Distribution Power Lines," *Progress in Electromagnetics Research B*, vol. 39, pp. 89-114, 2012. [Online]. Available: http://www.jpier.org/PIERB/pierb39/05.12012409.pdf

[6] A. G. Lazaropoulos, "Broadband Performance Metrics and Regression Approximations of the New Coupling Schemes for Distribution Broadband over Power Lines (BPL) Networks," *Trends in Renewable Energy*, vol. 4, no. 1, pp. 43-73, Jan. 2018. [Online]. Available: http://futureenergysp.com/index.php/tre/article/view/59/pdf

[7] A. G. Lazaropoulos, "Wireless Sensor Network Design for Transmission Line Monitoring, Metering and Controlling Introducing Broadband over PowerLines-enhanced Network Model (BPLeNM)," *ISRN Power Engineering*, vol. 2014, Article ID 894628, 22 pages, 2014. doi:10.1155/2014/894628. [Online]. Available: http://www.hindawi.com/journals/isrn.power.engineering/2014/894628/

[8] A. G. Lazaropoulos, "Improvement of Power Systems Stability by Applying Topology Identification Methodology (TIM) and Fault and Instability Identification Methodology (FIIM)–Study of the Overhead Medium-Voltage Broadband over Power Lines (OV MV BPL) Networks Case," *Trends in Renewable Energy*, vol. 3, no. 2, pp. 102-128, Apr. 2017. [Online]. Available: http://futureenergysp.com/index.php/tre/article/view/34

[9] A. G. Lazaropoulos, "Main Line Fault Localization Methodology in Smart Grid–Part 1: Extended TM2 Method for the Overhead Medium-Voltage Broadband over Power Lines Networks Case," *Trends in Renewable Energy*, vol. 3, no. 3, pp. 2-25, Dec. 2017. [Online]. Available: http://futureenergysp.com/index.php/tre/article/view/36

[10] A. G. Lazaropoulos, "Main Line Fault Localization Methodology in Smart Grid–Part 2: Extended TM2 Method, Measurement Differences and L1 Piecewise Monotonic Data Approximation for the Overhead Medium-Voltage Broadband over Power Lines Networks Case," *Trends in Renewable Energy*, vol. 3, no. 3, pp. 26-61, Dec. 2017. [Online]. Available: http://futureenergysp.com/index.php/tre/article/view/37

[11] A. G. Lazaropoulos, "Main Line Fault Localization Methodology in Smart Grid–Part 3: Main Line Fault Localization Methodology (MLFLM)," *Trends in Renewable Energy*, vol. 3, no. 3, pp. 62-81, Dec. 2017. [Online]. Available: http://futureenergysp.com/index.php/tre/article/view/38

[12] A. G. Lazaropoulos, "Main Line Fault Localization Methodology (MLFLM) in Smart Grid–The Underground Medium- and Low-Voltage Broadband over Power Lines Networks Case," *Trends in Renewable Energy*, vol. 4, no. 1, pp. 15-42,

Dec. 2017. [Online]. Available: http://futureenergysp.com/index.php/tre/article/view/45

[13] A. G. Lazaropoulos, "Smart Energy and Spectral Efficiency (SE) of Distribution Broadband over Power Lines (BPL) Networks – Part 1: The Impact of Measurement Differences on SE Metrics," *Trends in Renewable Energy*, vol. 4, no. 2, pp. 125-184, Aug. 2018. [Online]. Available: http://futureenergysp.com/index.php/tre/article/view/76/pdf

[14] A. G. Lazaropoulos, "Smart Energy and Spectral Efficiency (SE) of Distribution Broadband over Power Lines (BPL) Networks – Part 2: L1PMA, L2WPMA and L2CXCV for SE against Measurement Differences in Overhead Medium-Voltage BPL Networks," *Trends in Renewable Energy*, vol. 4, no. 2, pp. 185-212, Aug. 2018. [Online]. Available: http://futureenergysp.com/index.php/tre/article/view/77/pdf

[15] A. G. Lazaropoulos, "Underground Distribution BPL Connections with (N + 1)-hop Repeater Systems: A Novel Capacity Mitigation Technique," *Elsevier Computers and Electrical Engineering*, vol. 40, pp. 1813-1826, 2014.

[16] A. G. Lazaropoulos, "Review and Progress towards the Capacity Boost of Overhead and Underground Medium-Voltage and Low-Voltage Broadband over Power Lines Networks: Cooperative Communications through Two- and Three-Hop Repeater Systems," *ISRN Electronics*, vol. 2013, Article ID 472190, pp. 1-19, 2013. [Online]. Available: http://www.hindawi.com/isrn/electronics/aip/472190/

[17] A. G. Lazaropoulos, "Broadband over Power Lines (BPL) Systems Convergence: Multiple-Input Multiple-Output (MIMO) Communications Analysis of Overhead and Underground Low-Voltage and Medium-Voltage BPL Networks (Invited Paper)," *ISRN Power Engineering*, vol. 2013, Article ID 517940, pp. 1-30, 2013. [Online]. Available: http://www.hindawi.com/isrn/power.engineering/2013/517940/

[18] A. Nazem and M. R Arshad, "An Approach in Full Duplex Digital Multipoint Systems Using Large Signal Power Line Communication," *Bentham Recent Patents on Electrical & Electronic Engineering*, vol. 6, no. 2, pp. 138-146, 2013.

[19] A. G. Lazaropoulos and P. G. Cottis, "Transmission characteristics of overhead medium voltage power line communication channels," *IEEE Trans. Power Del.*, vol. 24, no. 3, pp. 1164-1173, Jul. 2009.

[20] A. G. Lazaropoulos and P. G. Cottis, "Capacity of overhead medium voltage power line communication channels," *IEEE Trans. Power Del.*, vol. 25, no. 2, pp. 723-733, Apr. 2010.

[21] A. G. Lazaropoulos and P. G. Cottis, "Broadband transmission via underground medium-voltage power lines-Part I: transmission characteristics," *IEEE Trans. Power Del.*, vol. 25, no. 4, pp. 2414-2424, Oct. 2010.

[22] A. G. Lazaropoulos and P. G. Cottis, "Broadband transmission via underground medium-voltage power lines-Part II: capacity," *IEEE Trans. Power Del.*, vol. 25, no. 4, pp. 2425-2434, Oct. 2010.

[23] A. G. Lazaropoulos, "Broadband transmission and statistical performance properties of overhead high-voltage transmission networks," *Hindawi Journal of Computer Networks and Commun.*, 2012, article ID 875632, 2012. [Online]. Available: http://www.hindawi.com/journals/jcnc/aip/875632/

[24] A. G. Lazaropoulos, “Statistical Channel Modeling of Overhead Low Voltage Broadband over Power Lines (OV LV BPL) Networks – Part 1: The Theory of Class Map Footprints of Real OV LV BPL Topologies, Branch Line Faults and Hook-Style Energy Thefts,” *Trends in Renewable Energy*, vol. 6, no. 1, pp. 61-87, Mar. 2020. [Online]. Available: http://futureenergysp.com/index.php/tre/article/download/112/pdf

[25] E. Biglieri, “Coding and modulation for a horrible channel,” *IEEE Commun. Mag.*, vol. 41, no. 5, pp. 92–98, May 2003.

[26] M. Gebhardt, F. Weinmann, and K. Dostert, “Physical and regulatory constraints for communication over the power supply grid,” *IEEE Commun. Mag.*, vol. 41, no. 5, pp. 84-90, May 2003.

[27] M. Götz, M. Rapp, and K. Dostert, “Power line channel characteristics and their effect on communication system design,” *IEEE Commun. Mag.*, vol. 42, no. 4, pp. 78-86, Apr. 2004.

[28] A. G. Lazaropoulos, “Towards Modal Integration of Overhead and Underground Low-Voltage and Medium-Voltage Power Line Communication Channels in the Smart Grid Landscape: Model Expansion, Broadband Signal Transmission Characteristics, and Statistical Performance Metrics (Invited Paper),” *ISRN Signal Processing*, vol. 2012, Article ID 121628, pp. 1-17, 2012. [Online]. Available: http://www.hindawi.com/isrn/sp/2012/121628/

[29] A. G. Lazaropoulos, “Statistical Broadband over Power Lines Channel Modeling – Part 1: The Theory of the Statistical Hybrid Model,” *Progress in Electromagnetics Research C*, vol. 92, pp. 1-16, 2019. [Online]. Available: http://www.jpier.org/PIERC/pierc92/01.19012902.pdf

[30] A. G. Lazaropoulos, “Statistical Broadband over Power Lines (BPL) Channel Modeling – Part 2: The Numerical Results of the Statistical Hybrid Model,” *Progress in Electromagnetics Research C*, vol. 92, pp. 17-30, 2019. [Online]. Available: http://www.jpier.org/PIERC/pierc92/02.19012903.pdf

[31] A. G. Lazaropoulos, “Enhancing the Statistical Hybrid Model Performance in Overhead and Underground Medium Voltage Broadband over Power Lines Channels by Adopting Empirical Channel Attenuation Statistical Distribution,” *Trends in Renewable Energy*, vol. 5, no. 2, pp. 181-217, 2019. [Online]. Available: http://futureenergysp.com/index.php/tre/article/view/96/pdf

[32] F. Pancaldi, F. Gianaroli, and G. M. Vitetta, “Equalization of Narrowband Indoor Powerline Channels for High Data Rate OFDM Communications,” *IEEE Trans. on Smart Grid*, vol. 9, no. 1, pp. 78-87, Jan. 2018.

[33] A. G. Lazaropoulos, “Virtual Indicative Broadband over Power Lines Topologies for Respective Subclasses by Adjusting Channel Attenuation Statistical Distribution Parameters of Statistical Hybrid Models – Part 2: Numerical Results for the Overhead and Underground Medium-Voltage Power Grids,” *Trends in Renewable Energy*, vol. 5, no. 3, pp. 258-281, Aug. 2019. [Online]. Available: http://futureenergysp.com/index.php/tre/article/view/100/pdf

[34] A. G. Lazaropoulos, “Virtual Indicative Broadband over Power Lines Topologies for Respective Subclasses by Adjusting Channel Attenuation Statistical Distribution Parameters of Statistical Hybrid Models – Part 3: The Case of Overhead Transmission Power Grids,” *Trends in Renewable Energy*, vol. 5, no. 3, pp. 282-306, Aug. 2019. [Online]. Available: http://futureenergysp.com/index.php/tre/article/view/101/pdf

[35] A. G. Lazaropoulos, “Statistical Channel Modeling of Overhead Low Voltage Broadband over Power Lines (OV LV BPL) Networks – Part 2: The Numerical Results of Class Map Footprints of Real OV LV BPL Topologies, Branch Line Faults and Hook Style Energy Thefts,” *Trends in Renewable Energy*, vol. 6, no. 1, pp. 88-109, Mar. 2020. [Online]. Available: http://futureenergysp.com/index.php/tre/article/download/113/pdf

[36] A. G. Lazaropoulos, “Best L1 Piecewise Monotonic Data Approximation in Overhead and Underground Medium-Voltage and Low-Voltage Broadband over Power Lines Networks: Theoretical and Practical Transfer Function Determination,” Hindawi Journal of Computational Engineering, vol. 2016, Article ID 6762390, 24 pages, 2016. doi:10.1155/2016/6762390. [Online]. Available: https://www.hindawi.com/journals/jcengi/2016/6762390/cta/

[37] I. C. Demetriou, “Algorithm 863: L2WPMA, a Fortran 77 package for weighted least-squares piecewise monotonic data approximation,” *ACM Transactions on Mathematical Software (TOMS)*, vol. 33, no.1, pp. 6, 2007.

[38] A. G. Lazaropoulos, “Detection of Energy Theft in Overhead Low-Voltage Power Grids – The Hook Style Energy Theft in the Smart Grid Era,” *Trends in Renewable Energy*, vol. 5, no. 1, pp. 12-46, Oct. 2018. [Online]. Available: http://futureenergysp.com/index.php/tre/article/view/81/pdf

[39] A. G. Lazaropoulos, “Measurement Differences, Faults and Instabilities in Intelligent Energy Systems–Part 1: Identification of Overhead High-Voltage Broadband over Power Lines Network Topologies by Applying Topology Identification Methodology (TIM),” *Trends in Renewable Energy*, vol. 2, no. 3, pp. 85-112, Oct. 2016. [Online]. Available: http://futureenergysp.com/index.php/tre/article/view/26/32

[40] A. G. Lazaropoulos, “Main Line Fault Localization Methodology in Smart Grid – Part 1: Extended TM2 Method for the Overhead Medium-Voltage Broadband over Power Lines Networks Case,” *Trends in Renewable Energy*, vol. 3, no. 3, pp. 2-25, Dec. 2017. [Online]. Available: http://futureenergysp.com/index.php/tre/article/view/36

[41] A. G. Lazaropoulos, “New Coupling Schemes for Distribution Broadband over Power Lines (BPL) Networks,” *Progress in Electromagnetics Research B*, vol. 71, pp. 39-54, 2016. [Online]. Available: http://www.jpier.org/PIERB/pierb71/02.16081503.pdf

[42] A. G. Lazaropoulos, “Power Systems Stability through Piecewise Monotonic Data Approximations – Part 1: Comparative Benchmarking of L1PMA, L2WPMA and L2CXCV in Overhead Medium-Voltage Broadband over Power Lines Networks,” *Trends in Renewable Energy*, vol. 3, no. 1, pp. 2-32, Jan. 2017. [Online]. Available: http://futureenergysp.com/index.php/tre/article/view/29/34

[43] A. G. Lazaropoulos, “Measurement Differences, Faults and Instabilities in Intelligent Energy Systems – Part 2: Fault and Instability Prediction in Overhead High-Voltage Broadband over Power Lines Networks by Applying Fault and Instability Identification Methodology (FIIM),” *Trends in Renewable Energy*, vol. 2, no. 3, pp. 113-142, Oct. 2016. [Online]. Available: http://futureenergysp.com/index.php/tre/article/view/27/33

[44] A. G. Lazaropoulos, “Power Systems Stability through Piecewise Monotonic Data Approximations – Part 2: Adaptive Number of Monotonic Sections and Performance of L1PMA, L2WPMA and L2CXCV in Overhead Medium-Voltage

Broadband over Power Lines Networks," *Trends in Renewable Energy*, vol. 3, no. 1, pp. 33-60, Jan. 2017. [Online]. Available: http://futureenergysp.com/index.php/tre/article/view/30/35

[45] A. G. Lazaropoulos, "Special Cases during the Detection of the Hook Style Energy Theft in Overhead Low-Voltage Power Grids through HS-DET Method – Part 1: High Measurement Differences, Very Long Hook Technique and "Smart" Hooks," *Trends in Renewable Energy*, vol. 5, no. 1, pp. 60-89, Jan. 2019. [Online]. Available: http://futureenergysp.com/index.php/tre/article/view/82/pdf

[46] A. G. Lazaropoulos, "Special Cases during the Detection of the Hook Style Energy Theft in Overhead Low-Voltage Power Grids through HS-DET Method – Part 2: Different Measurement Differences, Feint "Smart" Hooks and Hook Interconnection Issues," *Trends in Renewable Energy*, vol. 5, no. 1, pp. 90-116, Jan. 2019. [Online]. Available: http://futureenergysp.com/index.php/tre/article/view/83/pdf

[47] I. C. Demetriou, "A Decomposition Theorem for the Least Squares Piecewise Monotonic Data Approximation Problem," *Springer Approximation and Optimization*, pp. 119–134, 2019.

[48] I. C. Demetriou and M. J. D. Powell, "Least squares smoothing of univariate data to achieve piecewise monotonicity", *IMA Journal of Numerical Analysis*, vol. 11, no. 3, pp. 411-432, 1991.

[49] I. C. Demetriou, "An application of best *L*1 piecewise monotonic data approximation to signal restoration," *IAENG International Journal of Applied Mathematics*, vol. 53, no. 4, pp. 226-232, 2013.

[50] I. C. Demetriou, "L1PMA: A Fortran 77 Package for Best L1 Piecewise Monotonic Data Smoothing," *Computer Physics Communications*, vol. 151, no. 1, pp. 315-338, 2003.

[51] I. C. Demetriou, "L2CXCV: A Fortran 77 package for least squares convex/concave data smoothing," *Computer physics communications*, vol. 174, no.8, pp. 643-668, 2006.

[52] http://cpc.cs.qub.ac.uk/summaries/ADRF

[53] A. G. Lazaropoulos, "Business Analytics and IT in Smart Grid – Part 3: New Application Aspect and the Quantitative Mitigation Analysis of Piecewise Monotonic Data Approximations on the iSHM Class Map Footprints of Overhead Low-Voltage Broadband over Power Lines Topologies Contaminated by Measurement Differences," *Trends in Renewable Energy*, vol. 6, no. 2, pp. 204-223, May 2020.

Trends in Renewable Energy
OPEN ACCESS ISSN:2376-2144
Peer-Reviewed Article futureenergysp.com/index.php/tre

Business Analytics and IT in Smart Grid – Part 3: New Application Aspect and the Quantitative Mitigation Analysis of Piecewise Monotonic Data Approximations on the iSHM Class Map Footprints of Overhead Low-Voltage Broadband over Power Lines Topologies Contaminated by Measurement Differences

Athanasios G. Lazaropoulos[1,2,*]

1: School of Electrical and Computer Engineering / National Technical University of Athens / 9 Iroon Polytechniou Street / Zografou, GR 15780
2: Department of Industrial Design and Production Engineering / School of Engineering / University of West Attica / 250 Thivon & P. Ralli / Athens, GR 12244

Received March 25, 2020; Accepted May 4, 2020; Published May 14, 2020

Big data that overwhelm smart grid (SG) are susceptible to errors that can further affect business analytics and related human decisions. In [1], the impact of measurement differences that follow various distributions has been examined via initial Statistical Hybrid Model (iSHM) footprints while the mitigation impact of piecewise monotonic data approximations has been qualitatively assessed via corresponding iSHM footprints in [2]. In this companion paper, the potential of applying piecewise monotonic data approximations in the intrinsic procedure of iSHM rather than its inputs and the quantitative mitigation analysis of piecewise monotonic data approximations against measurement differences via iSHM footprints are proposed for the overhead low-voltage broadband over power lines (OV LV BPL) topologies.

Keywords: Smart Grid; Broadband over Power Lines (BPL) networks; Power Line Communications (PLC); Distribution and Transmission Power Grids; Capacity, Statistics; Business Analytics; IT; Modeling

**Corresponding author:* AGLazaropoulos@gmail.com

Tr Ren Energy, 2020, Vol.6, No.2, 214-233. doi: 10.17737/tre.2020.6.2.00119

Nomenclature

APDmd	Average Percent Distance computation of the Measurement Differences
APDna	Average Percent Distance computation of the New Aspect
APDta	Average Percent Distance computation of the Traditional Aspect
BPL	Broadband over Power Lines
BPMN	Business Process Model and Notation
CASD	Channel Attenuation Statistical Distribution
CUD	Continuous Uniform Distribution
DHM	deterministic hybrid model
EMI	ElectroMagnetic Interference
IP	Internet Protocol
IT	Information Technology
iSHM	initial Statistical Hybrid Model
LOS	Line-of-Sight
LV	Low Voltage
L1PMA	L1 Piecewise Monotonic Approximation
L2WPMA	L2 Weighted Piecewise Monotonic Approximation
MLE	Maximum Likelihood Estimator
MTL	Multiconductor Transmission Line
ND	Normal Distribution
OV	Overhead
SG	Smart Grid
TL	Transmission Line
WtG	Wire-to-Ground

1. Introduction

BPL technology is among the communications proposals that are going to transform the vintage power grid into an advanced IP-based communications network enhanced with a plethora of broadband applications and business analytics, the so called SG [1]-[8]. The main advantage of SG is the reception of a plethora of data concerning the metering, monitoring and controlling of its infrastructure and equipment thus allowing the authorized personnel and customers to take decisions that further affect the SG operation. It is evident that right decisions urge reliable data and towards that direction piecewise monotonic data approximations contribute to the restoration of the contaminated data by measurement differences in OV LV BPL networks [1], [7], [9]-[11].

In this paper, it is already known that measurement differences are observed between the experimental and theoretical results during the transfer function determination of OV LV BPL topologies and are due to a number of practical reasons and "real-life" difficulties. Actually, coupling scheme transfer function determination occurs in the well-validated DHM that is the introductory core element of the recently proposed and here applied iSHM that is deployed for the statistical broadband channel description of OV LV BPL topologies [12]-[20]. Business analytics of SG exploit a plethora of related broadband iSHM tools, such as the definition procedure, the class maps and the iSHM footprints whose results are critically affected by the coupling scheme transfer function data of DHM. More specifically, it has been shown in [1] that the behavior of iSHM footprints due to the measurement differences of the OV LV BPL networks may be sensitive even to low intensities of measurement differences. In accordance with [1], when high measurement differences occur the broadband iSHM tools, such as the topology identification technique and the energy theft detection via iSHM footprint, can be totally jammed thus influencing the quality of business analytics of the SG and the supported human decisions. To enhance the reliability of SG data, piecewise monotonic data approximations, such as L1PMA and L2WPMA, have been deployed against the measurement differences while their qualitative evaluation was done via the respective L1PMA and L2WPMA iSHM footprints in [2]. Indeed, L1PMA and L2WPMA can achieve significant measurement difference restoration concerning the extent and the distance of iSHM footprints from the theoretical Weibull CASD MLEs of the real indicative OV LV BPL urban case A. Note that the qualitative methodology of [2] examined the degree of shrinkage and stress of the iSHM footprints due to measurement differences by the applied piecewise monotonic data approximations towards the theoretical Weibull CASD MLEs of the real indicative OV LV BPL urban case A.

In this paper, first, a new aspect concerning the location of the application of piecewise monotonic data approximations inside the iSHM operation flowchart is proposed. Until now, piecewise monotonic data approximations have been applied right after the application of DHM to the coupling scheme transfer function data of the examined OV LV BPL topologies in order to suppress the measurement difference contamination at that location [7], [9], [21]-[28]. Since the result of the multipath aggravation of OV LV BPL topologies can be treated as a superposition of spectral notches of various depths and extents onto the coupling scheme transfer function of the OV LV BPL "LOS" case [14], [17], [29], piecewise monotonic data approximations can alternatively focus on the output results of the coupling scheme channel attenuation difference module Δ of iSHM that is anyway an internal iSHM procedure; the coupling scheme channel attenuation difference module Δ of iSHM gives as output the coupling scheme channel attenuation difference between each examined OV LV BPL topology and the OV LV BPL "LOS" case thus providing more uncorrelated data in comparison with the ones of the traditional aspect. The unbiased data of the coupling scheme channel attenuation difference module Δ of iSHM can be proven valuable for a more efficient application of piecewise monotonic data approximations under certain conditions [30]-[33].

Second, a quantitative methodology is proposed in this paper so that the assessment of the mitigation efficiency of piecewise monotonic data approximations against measurement differences can be feasible on the basis of the iSHM footprints of [2]. During the qualitative evaluation of L1PMA and L2WPMA in [2], it was clear that the critical intrinsic parameters of piecewise monotonic data approximations, such as L1PMA monotonic sections and L2WPMA sign changes, mainly affect the performance of piecewise monotonic data approximations against the measurement differences. The selection of the optimal numbers of L1PMA monotonic sections and L2WPMA sign changes has been made on the basis of the visual proximity of the respective L1PMA and L2WPMA iSHM footprints to the theoretical Weibull CASD MLEs for given real indicative OV LV BPL topology (say, real indicative OV LV BPL urban case A in [2]). Here, the evolution of the qualitative evaluation of the proximity is the proposal of a quantitative methodology that can compute the average distances of the piecewise monotonic data approximation iSHM footprints and iSHM footprints due to measurement differences and hence defines the critical intrinsic parameters of the piecewise monotonic data approximations by comparing and by sorting the gathered distances. Also, the new aspect, which is proposed in this paper, concerning the application of piecewise monotonic data approximations to the results of the coupling scheme channel attenuation difference module Δ of iSHM is also benchmarked through the new quantitative methodology.

The rest of this paper is organized as follows: Section II presents the mathematics of the new aspect regarding the application of piecewise monotonic data approximations to the results of the coupling scheme channel attenuation difference module Δ of iSHM. In Section III, the new quantitative methodology concerning the assessment of the mitigation efficiency of piecewise monotonic data approximations against measurement differences via iSHM footprints is presented. Section IV presents numerical results related with the application of the quantitative methodology and the new aspect of piecewise monotonic data approximation application location. Section V concludes this paper.

2. New Aspect of Application for the Piecewise Monotonic Data Approximations against Measurement Differences

With reference to the BPMN diagram of iSHM [34], iSHM consists of six Phases (*i.e.*, Phase A-F) while each Phase is clearly described by its procedure as well as its inputs and outputs. With reference to this BPMN diagram, Phase A consists of DHM that takes as inputs the examined real indicative OV LV BPL topology, the respective distribution MTL configuration and the applied coupling scheme while DHM results are the output of Phase A that is the theoretical coupling scheme transfer function

$H^{\mathrm{OVLV},C}\left(f_q\right)$, q=1,…,Q when measurement differences are not assumed where $[.]^{C}$ denotes the applied coupling scheme, f_q is the flat-fading subchannel start frequency and Q is the number of subchannels in the examined frequency range. When measurement differences are assumed during the preparation of iSHM footprints as in [1], [2], the measurement differences are treated as distributions; say, CUD of variable maximum value a_{CUD}. After the measurement difference consideration, the output of Phase A, which is afterwards exploited by the iSHM footprints, is the measured coupling scheme transfer function that is given by [1], [5], [35]

$$\overline{H_{d1,d2,i}^{\mathrm{OVLV},C,D}}\left(f_q\right) = H^{\mathrm{OVLV},C}\left(f_q\right) + e_{d1,d2,i}^{D}\left(f_q\right),\ q=1,\dots,Q,\ i = 1,\dots,I \tag{1}$$

where $[\cdot]^{D}$ denotes the applied measurement difference distribution –*i.e.*, CUD of this paper in accordance with [2]–, $d1$ is the first parameter of the applied measurement difference distribution (*i.e.*, the minimum value $-a_{\mathrm{CUD}}$ of CUD), $d2$ is the second parameter of the applied measurement difference distribution (*i.e.*, the maximum value a_{CUD} of CUD), $e_{d1,d2,i}^{D}\left(f_q\right)$ is the measurement difference at frequency f_q for given measurement difference distribution and I is the number of different $1 \times Q$ line vectors of measurement differences per applied measurement difference distribution, first and second parameter. Until now and during the preparation of iSHM footprints of [1], [2], piecewise monotonic data approximations are applied to the measured coupling scheme transfer function of eq. (1) having as a result the approximated coupling scheme transfer function that is given by

$$\overline{\overline{H_{d1,d2,i}^{\mathrm{OVLV},C,D,P}}}\left(f_q\right) = P\left\{\overline{H_{d1,d2,i}^{\mathrm{OVLV},C,D}}\left(f_q\right)\right\},\ q=1,\dots,Q,\ i = 1,\dots,I \tag{2}$$

where $[.]^{P}$ denotes the applied piecewise monotonic data approximation, say L1PMA or L2WPMA in this paper, and $P\{\cdot\}$ synopsizes the procedure of the applied piecewise monotonic data approximation. Therefore, the application of piecewise monotonic data approximations is concentrated in the Phase A of the BPMN diagram of iSHM while the results of the remaining Phases, which are illustrated as I L1PMA cyan squares or I L2WPMA magenta triangles on iSHM footprints of [2], are based on the approximated coupling scheme transfer function data.

In this paper, an application aspect of piecewise monotonic data approximations is proposed that has to do with the location of the application of piecewise monotonic data approximations across the Phases of the BPMN diagram of iSHM [34]. Conversely to the traditional case where piecewise monotonic data approximations are applied to the output results of the Phase A (say, the results of DHM), the new aspect of application suggests that the piecewise monotonic data approximations should be applied to the results of Phase B of the BPMN diagram of iSHM during the preparation of the iSHM footprints. More specifically, Phase B of the BPMN diagram should receive as input the output of the Phase A that is the measured coupling scheme transfer function $\overline{H_{d1,d2,i}^{\mathrm{OVLV},C,D}}\left(f_q\right)$ given by eq. (1). Phase B consists of the coupling scheme channel attenuation difference module Δ that computes the measured channel attenuation difference $\overline{\Delta\mathrm{A}_{i}^{\mathrm{G,C}}}\left(f_q\right)$ between the measured coupling scheme transfer function of the examined real indicative OV LV BPL topology, say, the real indicative OV LV BPL urban case A in this paper, and the theoretical coupling scheme transfer function of the OV LV BPL "LOS" case, namely

$$\overline{\Delta\mathrm{A}_{i}^{\mathrm{G,C}}}\left(f_q\right) = -\left[\overline{H_{d1,d2,i}^{\mathrm{OVLV},C,D}}\left(f_q\right) - H_{\text{"LOS" case}}^{\mathrm{OVLV},C}\left(f_q\right)\right],\ q=1,\dots,Q,\ i = 1,\dots,I \tag{3}$$

Note that the coupling scheme channel attenuation difference of eq. (3) always remains greater or equal to zero [34]. During the preparation of similar iSHM footprints of [1], [2] with the new aspect, piecewise monotonic data approximations are applied to the measured channel attenuation difference of eq. (3) having as a result the approximated channel attenuation difference given by

$$\overline{\overline{\Delta \mathrm{A}_{i}^{\mathrm{G,C}}}}\left(f_{q}\right)=P\left\{\overline{\Delta \mathrm{A}_{i}^{\mathrm{G,C}}}\left(f_{q}\right)\right\}, q=1,\ldots,Q,\ i=1,\ldots,I \tag{4}$$

Therefore, the application of piecewise monotonic data approximations during the new aspect leaves the results of the Phase A untouched whereas it focuses on the Phase B of the BPMN diagram of iSHM. Similarly to the traditional aspect, the results of the remaining Phases, which are based on the approximated channel attenuation difference data, are going to be illustrated as I L1PMA cyan squares or I L2WPMA magenta triangles on similar iSHM footprints to the ones of [2].

3. New Quantitative Methodology for Assessing the Mitigation Efficiency of Piecewise Monotonic Data Approximations against Measurement Differences via iSHM Footprints

In accordance with the BPMN diagram of iSHM [18] and during the preparation of iSHM footprints, Phase C computes all the related iSHM Weibull CASD MLEs of the examined real indicative OV LV BPL topology, namely either for the theoretical coupling scheme channel attenuation difference (i.e, $\hat{a}_{\mathrm{MLE,theor}}^{\mathrm{Weibull}}$ and $\hat{\beta}_{\mathrm{MLE,theor}}^{\mathrm{Weibull}}$) or the measured coupling scheme channel attenuation difference per measurement difference line vector i of eq. (3) (i.e, $\hat{a}_{\mathrm{MLE,meas},i}^{\mathrm{Weibull}}$ and $\hat{\beta}_{\mathrm{MLE,meas},i}^{\mathrm{Weibull}}$) or the approximated coupling scheme channel attenuation difference per measurement difference line vector *i* via the traditional aspect for given number of monotonic sections (or sign changes) (i.e, $\hat{a}_{\mathrm{MLE,approx,trad},i}^{\mathrm{Weibull}}$ and $\hat{\beta}_{\mathrm{MLE,approx,trad},i}^{\mathrm{Weibull}}$) or the approximated coupling scheme channel attenuation difference per measurement difference line vector *i* via the new aspect of eq. (4) for given number of L1PMA monotonic sections (or L2WPMA sign changes) (i.e, $\hat{a}_{\mathrm{MLE,approx,new},i}^{\mathrm{Weibull}}$ and $\hat{\beta}_{\mathrm{MLE,approx,new},i}^{\mathrm{Weibull}}$). In accordance with [36]-[38], the iSHM class map of OV LV BPL topologies, which acts as the graphical basis for the demonstration of all the kinds of iSHM footprints, is plotted in Fig. 1 of [2] with respect to $\hat{a}_{\mathrm{MLE}}^{\mathrm{Weibull}}$, $\hat{\beta}_{\mathrm{MLE}}^{\mathrm{Weibull}}$ and the average capacity of each OV LV BPL topology subclass when the default operation settings of [1], [34] and the modified BPL frequency range settings of [2] are assumed. Through the prism of iSHM footprints, the effect of measurement differences and the countermeasures of piecewise monotonic data approximations against the measurement differences have been illustrated in Figs. 2-7 of [2]. The qualitative assessment of piecewise monotonic data approximations via iSHM footprints has revealed their strong potential against measurement differences while the selection of the critical parameters of the numbers of L1PMA monotonic sections or L2WPMA sign changes can be made by visually assessing the proximity of the I Weibull CASD MLEs of their approximated coupling scheme transfer function data with respect to the theoretical Weibull CASD MLEs for given real indicative OV LV BPL topology.

In this paper, a quantitative methodology is proposed that benchmarks the measurement difference mitigation efficiency of piecewise monotonic data approximations in terms of the average percent distance of the I Weibull CASD MLEs of the approximated coupling scheme transfer function data with respect to the theoretical Weibull CASD MLEs for given real indicative OV LV BPL topology. To apply the new quantitative methodology with respect to iSHM footprints and to finally select the critical intrinsic parameters of the piecewise monotonic data approximations (*i.e.*, the number of L1PMA monotonic sections and L2WPMA sign changes) that perform the best measurement difference mitigation, the following steps should be followed, namely:

1. *APDmd*: Given the real indicative OV LV BPL topology and I measurement difference line vectors of the same intensity (*i.e.*, of the same maximum value a_{CUD} in this paper), the average percent distance of the measurement differences from the theoretical Weibull CASD MLEs is given by:

$$APDmd = 100\% \cdot \frac{\sum_{i=1}^{I} \sqrt{\left(\frac{\hat{a}_{\mathrm{MLE,meas},i}^{\mathrm{Weibull}} - \hat{a}_{\mathrm{MLE,theor}}^{\mathrm{Weibull}}}{\hat{a}_{\mathrm{MLE,theor}}^{\mathrm{Weibull}}}\right)^2 + \left(\frac{\hat{\beta}_{\mathrm{MLE,meas},i}^{\mathrm{Weibull}} - \hat{\beta}_{\mathrm{MLE,theor}}^{\mathrm{Weibull}}}{\hat{\beta}_{\mathrm{MLE,theor}}^{\mathrm{Weibull}}}\right)^2}}{I} \tag{5}$$

   This step is necessary because it evaluates the initial condition and defines the goal of all the iSHM footprints of the applied piecewise monotonic data approximations. Any countermeasures implemented should present average percent distances lower than the average percent distance of the measurement differences of eq. (5) so that these countermeasures are considered effective.

2. *APDta*: Given the real indicative OV LV BPL topology, I measurement difference line vectors of the same intensity and the number of L1PMA monotonic sections (or L2WPMA sign changes), the average percent distance of the approximated data of the traditional aspect from the theoretical Weibull CASD MLEs is given by:

$$APDta = 100\% \cdot \frac{\sum_{i=1}^{I} \sqrt{\left(\frac{\hat{a}_{\mathrm{MLE,approx,trad},i}^{\mathrm{Weibull}} - \hat{a}_{\mathrm{MLE,theor}}^{\mathrm{Weibull}}}{\hat{a}_{\mathrm{MLE,theor}}^{\mathrm{Weibull}}}\right)^2 + \left(\frac{\hat{\beta}_{\mathrm{MLE,approx,trad},i}^{\mathrm{Weibull}} - \hat{\beta}_{\mathrm{MLE,theor}}^{\mathrm{Weibull}}}{\hat{\beta}_{\mathrm{MLE,theor}}^{\mathrm{Weibull}}}\right)^2}}{I} \tag{6}$$

3. *APDna*: Similarly to *APDta*, given the real indicative OV LV BPL topology, I measurement difference line vectors of the same intensity and the number of L1PMA monotonic sections (or L2WPMA sign changes), the average percent distance between the approximated data of the new aspect and the theoretical Weibull CASD MLEs is given by:

$$APDna = 100\% \cdot \frac{\sum_{i=1}^{I} \sqrt{\left(\frac{\hat{a}_{\mathrm{MLE,approx,new},i}^{\mathrm{Weibull}} - \hat{a}_{\mathrm{MLE,theor}}^{\mathrm{Weibull}}}{\hat{a}_{\mathrm{MLE,theor}}^{\mathrm{Weibull}}}\right)^2 + \left(\frac{\hat{\beta}_{\mathrm{MLE,approx,new},i}^{\mathrm{Weibull}} - \hat{\beta}_{\mathrm{MLE,theor}}^{\mathrm{Weibull}}}{\hat{\beta}_{\mathrm{MLE,theor}}^{\mathrm{Weibull}}}\right)^2}}{I} \tag{7}$$

With reference to eqs. (5)-(7), it is obvious that interesting quantitative findings are going to be deduced in Sec. 4 where average percent distance comparisons can reveal: (i) the contamination degree due to the increasing measurement differences; (ii) the mitigation efficiency of the traditional aspect of the application of piecewise monotonic data approximations; (iii) the mitigation efficiency of the new aspect of the application of piecewise monotonic data approximations; and (iv) a benchmark comparison between the traditional aspect and the new one.

4. Numerical Results and Discussion

In this Section, numerical results that quantitatively assess the mitigation efficiency of piecewise monotonic data approximations against measurement differences on iSHM footprints of OV LV BPL topologies are first presented. On the basis of the proposed quantitative assessment, the new methodology of the average percent distance is going to be tested while this new methodology will assess L1PMA and L2WPMA for both aspects of application (*i.e.*, either the traditional aspect or the new one). Similarly to [2], the countermeasures effect of L1PMA and L2WPMA of the traditional and new aspects is quantitatively benchmarked for given intensity of the measurement difference CUD while the impact of the number of L1PMA monotonic sections and the L2WPMA sign changes is here quantitatively assessed with respect to the mitigation of measurement differences. Similarly to [2], only the real indicative OV LV BPL urban case A is examined and 100 measurement difference line vector (*i.e.*, I=100) are applied.

4.1 iSHM Footprints due to Measurement Differences and the Countermeasures of Piecewise Monotonic Data Approximations (Traditional Aspect vs New Aspect)

As already been mentioned, the iSHM class map of OV LV BPL topologies, which is depicted in [36]-[38], acts as the graphical basis for the demonstration of the various iSHM footprints and is shown in Fig. 1. Similarly to [2], the iSHM footprint due to measurement differences of the arbitrary 5dB maximum value a_{CUD} for the real indicative OV LV BPL urban case A is also depicted in Fig. 1 as superimposed white circles on the iSHM class map as well as the iSHM footprint due to the application of L1PMA of the traditional aspect against the aforementioned measurement differences is shown as superimposed cyan squares when 4 monotonic sections are assumed. In Fig. 2, similar figure with Fig. 1 is plotted but for the case of L2WPMA of the traditional aspect when 4 sign changes are applied and superimposed magenta triangles are shown instead of cyan squares. Note that Figs. 1 and 2 are the same with Figs. 2 and 3 of [2] for: (i) comparison reasons between the traditional and the new aspect; and (ii) the demonstration of the proposed quantitative analysis. In Figs. 3 and 4, same plots with the respective Figs. 1 and 2 but for the new aspect. Here, it should be reminded that an iSHM footprint due to zero measurement differences consists of I white circles that all circles coincide at the theoretical values $\hat{\alpha}_{\mathrm{MLE,theor}}^{\mathrm{Weibull}}$ and $\hat{\beta}_{\mathrm{MLE,theor}}^{\mathrm{Weibull}}$ of the real indicative OV LV BPL urban case A that is the optimum case and the iSHM footprint goal of the application of piecewise monotonic data approximations.

By comparing iSHM footprints of Figs 1-4, each iSHM footprint due to measurement differences consists of 100 white circles forming a segmented white region that starts from the theoretical values $\hat{\alpha}_{\mathrm{MLE,theor}}^{\mathrm{Weibull}}$ and $\hat{\beta}_{\mathrm{MLE,theor}}^{\mathrm{Weibull}}$ of the real indicative OV LV BPL urban case A where each white circle corresponds to one measurement difference line vector. Regardless of the applied aspect, each cyan square and each magenta triangle is the graphical approximation result on the iSHM footprint for each white circle when L1PMA and L2WPMA are applied, respectively.

In accordance with [2], the qualitative approximation success of L1PMA and L2WPMA has been evaluated by the upper right shift of the respective iSHM footprints towards the theoretical values $\hat{\alpha}_{\mathrm{MLE,theor}}^{\mathrm{Weibull}}$ and $\hat{\beta}_{\mathrm{MLE,theor}}^{\mathrm{Weibull}}$ of the real indicative OV LV BPL urban case A. Although the mitigation of measurement differences is clear after the application of the piecewise monotonic data approximations of both aspects, the qualitative assessment is not enough to recognize which of the iSHM footprints achieves the best mitigation. The quantitative methodology of Sec.3 can offer the required metrics to carefully benchmark the iSHM footprints after the application of piecewise monotonic data approximations and aspects of Figs. 1-4. The benchmark results of L1PMA and L2WPMA when traditional and new aspects are applied are reported in Table 1 after the application of the quantitative methodology of Sec. 3 to Figs. 1-4.

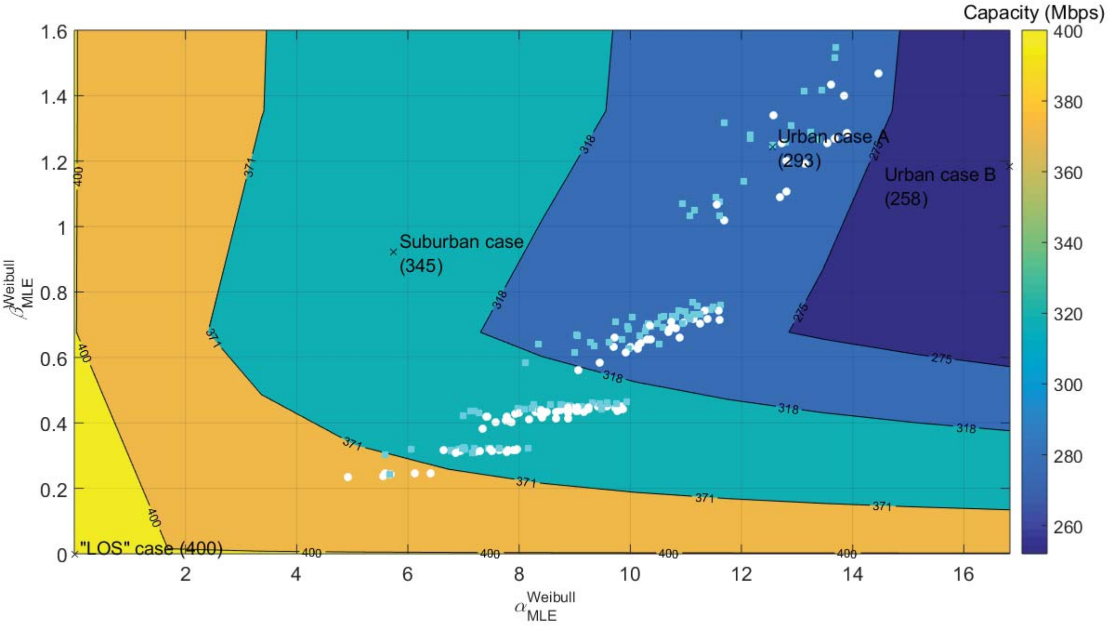

Fig. 1. iSHM footprints of the real indicative OV LV BPL urban case A when 3-30MHz frequency band, 1MHz frequency subchannel spacing, WtG[1] coupling scheme, FCC Part 15, CUD measurement differences of maximum value a_{CUD} = 5dB (white circles) are assumed and L1PMA of the traditional aspect of 4 monotonic sections (cyan squares) is applied [2].

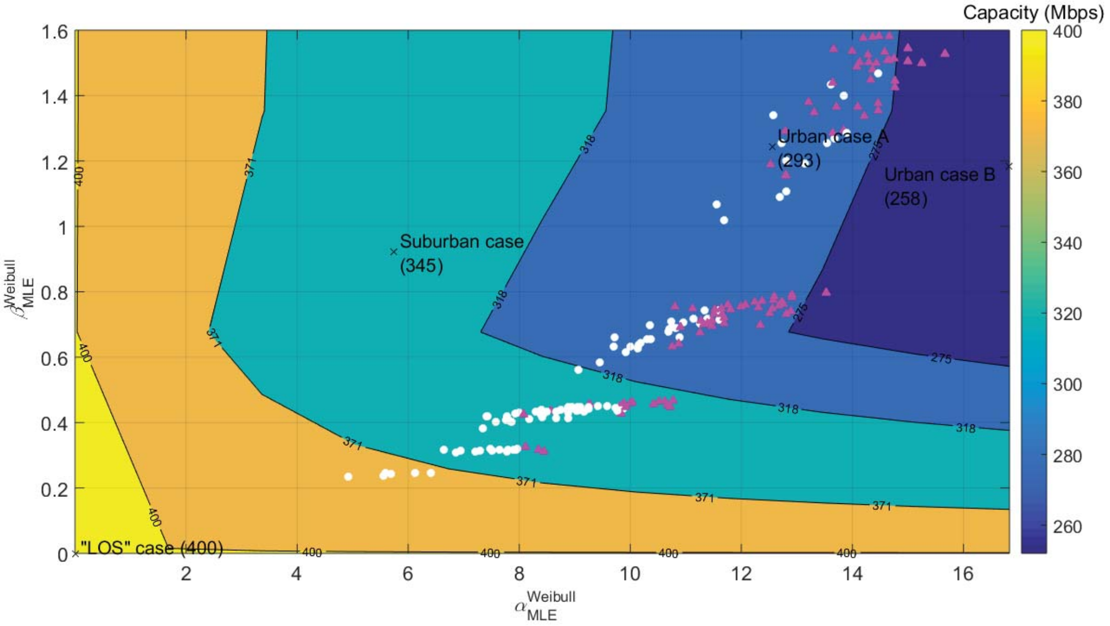

Fig. 2. Same plot with Fig. 1 but for L2WPMA of the traditional aspect of 4 sign changes (magenta triangles) [2].

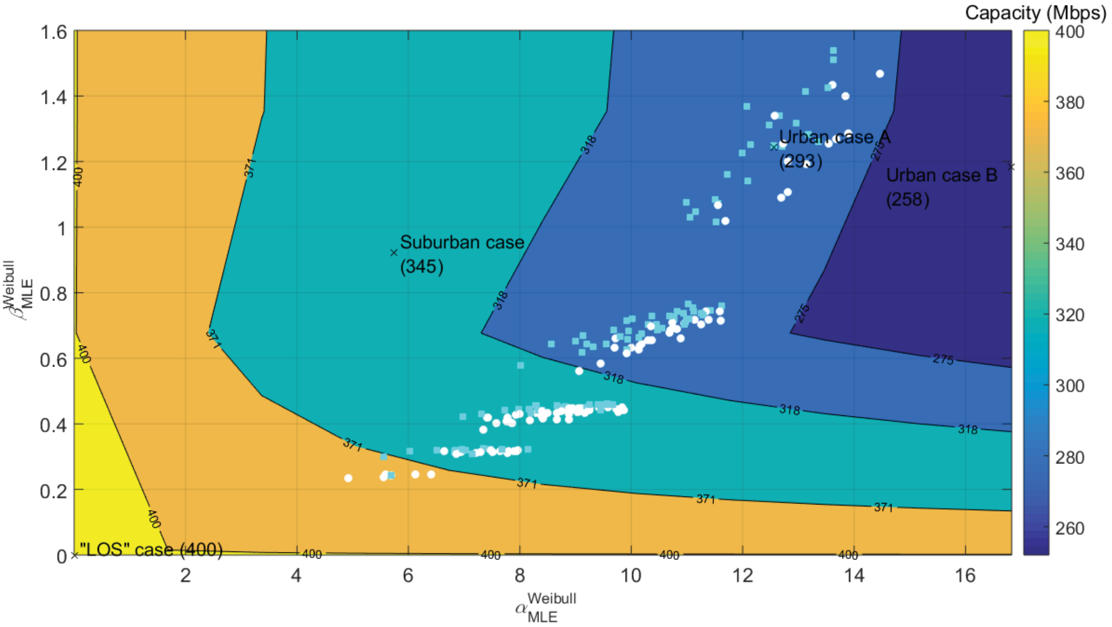

Fig. 3. Same plot with Fig. 1 but for L1PMA of the new aspect of 4 monotonic sections (cyan squares).

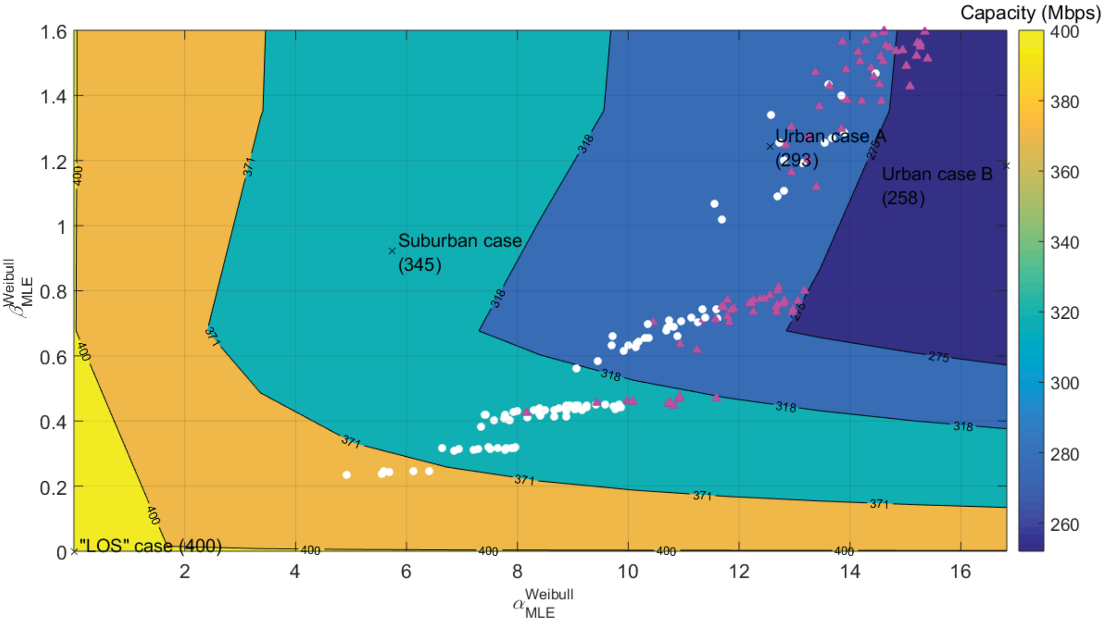

Fig. 4. Same plot with Fig. 2 but for L2WPMA of the new aspect of 4 sign changes (magenta triangles).

Table 1
Quantitative methodology benchmark results for L1PMA and L2WPMA when Traditional and New Aspects are Applied

Number of L1PMA Monotonic Sections / L2WPMA Sign Changes	**Measurement Differences (maximum value a_{CUD}=5dB)**	**Traditional Aspect**		**New Aspect**	
		L1PMA	**L2WPMA**	**L1PMA**	**L2WPMA**
	$APDmd$ (%)	**$APDta$ (%)**	**$APDta$ (%)**	**$APDna$ (%)**	**$APDna$ (%)**
4	61.22	53.90	38.67	51.98	36.09

By comparing the benchmark results of Table 1 with Figs. 1-4, it is evident that L1PMA and L2WPMA achieve to mitigate the measurement differences regardless of the aspect applied. Both piecewise monotonic data approximations of this paper shift their iSHM footprints up right in comparison with the iSHM footprint due to measurement differences. Note that the approximated iSHM footprints now lie closer to the theoretical values $\hat{a}_{\mathrm{MLE,theor}}^{\mathrm{Weibull}}$ and $\hat{\beta}_{\mathrm{MLE,theor}}^{\mathrm{Weibull}}$ of the real indicative OV LV BPL urban case A in comparison with the iSHM footprints due to measurement differences. Numerically, *APDmd* of the assumed measurement differences is equal to 61.22% whilst the worst performance of piecewise monotonic data approximations is achieved by L1PMA of the traditional aspect with *APDta* that is equal to 53.90%.

As the traditional and new aspects are here benchmarked, it is clear that the piecewise monotonic data approximations of the new aspect better mitigate the measurement differences in comparison with the respective ones of the traditional aspect. Numerically, L1PMA of the traditional aspect presents higher *APDta*, which is equal to 53.90%, in comparison with the *APDna* of L1PMA of the new aspect that is equal to 51.98%. Similarly, L2WPMA of the traditional aspect presents higher *APDta*, which is equal to 38.67%, in comparison with the *APDna* of L2WPMA of the new aspect that is equal to 36.09%. Anyway, the previous numerical results can also be observed in the previous Figs. 1-4. Piecewise monotonic data approximations of the new aspect handle more unbiased data in comparison with ones of the traditional aspect since the coupling scheme transfer function of the OV LV BPL "LOS" case acts as a background noise for the coupling scheme transfer function of the other OV LV BPL topologies. When 4 monotonic sections or sign changes are assumed, the best mitigation performance against measurement differences is achieved by L2WPMA of the new aspect.

From the previous analysis, it is evident that during the quantitative methodology there is no need for visually comparing the iSHM footprints due to the measurement differences and the iSHM footprints after the application of piecewise monotonic data approximations since APD metrics can securely allow the selection of the most suitable piecewise monotonic data approximation as well as its critical parameters for both aspects (*i.e.*, L1PMA monotonic sections or L2WPMA sign changes). Since the qualitative analysis has been fulfilled in [2], only tables of APD metrics are presented hereafter in order to assess the performance of the various versions of the piecewise monotonic data approximations. In the following subsection, the selection of the aforementioned critical parameters of piecewise monotonic data approximations is justified by the APD metrics and visually verified by Figs. 4(a)-(i) and 5(a)-(i) of [2].

4.2 The Quantitative Methodology for Defining the Number of L1PMA Monotonic Sections and L2WPMA Sign Changes

Already been identified in [2], [10], [26], [39], [40], the selection of the numbers of L1PMA monotonic sections and of L2WPMA sign changes has a significant impact on the mitigation performance of measurement differences. Also, this selection of the critical parameters of the piecewise monotonic data approximations can remain untouchable despite the different intensities of measurement differences applied with satisfactory performance unless adaptive techniques such those presented in [10], [11], [26], [39], [40] should be applied.

With reference to Figs. 4(a)-(i) and 5(a)-(i) of [2] as well as the proposed quantitative methodology of Sec. 3, APD metrics of: (i) the applied measurement differences of the arbitrary 6dB maximum value a_{CUD} for the real indicative OV LV BPL urban case A; and (ii) the piecewise monotonic data approximations of both the aspects; are here reported in Table 2 when the numbers of L1PMA monotonic sections and L2WPMA sign changes range from 1 to 9.

From Table 2, several interesting remarks that agree with the visual findings of Figs. 4(a)-(i) and 5(a)-(i) of [2], can be pointed out, namely:

- Depending on the number of L1PMA monotonic sections and L2WPMA sign changes, different mitigation performances can be observed among the available piecewise monotonic data approximations. The aforementioned result that is proven by the APD metrics of Table 2 has also been verified by the visual analysis of Figs. 4(a)-(i) and 5(a)-(i) of [2].
- As the application of L1PMA of the traditional aspect is concerned, its best mitigation performance with *APDta* of 38.48% is observed when one monotonic section is adopted. This *APDta* result is the best one among all the cases examined. Anyway, the same number of L1PMA monotonic sections has been verified for its mitigation performance by the visual examination of Figs. 4(a)-(i). As the number of monotonic sections increases so does *APDta* thus indicating that the relatively high intensity of measurement differences that is adopted in this subsection (*i.e.*, maximum value a_{CUD} of 6dB) requires the rough approximation provided by the assumption of 1 monotonic section. The overapproximation, which is defined in [2], occurs when the number of L1PMA monotonic sections of the traditional aspect is greater than 5 (*i.e.*, black background cells of the third and fourth columns of Table 2).
- As the application of L2WPMA of the traditional aspect is regarded, its best mitigation performance with *APDta* of 39.54% is observed when four or five sign changes are adopted. With reference to Fig. 5(e) of [2], the same number of L2WPMA sign changes has been validated for its mitigation performance by the visual examination. As the number of sign changes increases *APDta* first presents significant high values that are even higher than the respective *APDmds* (*i.e.*, black background cells of the fifth and sixth columns of Table 2), second starts to decrease till 39.54% of four or five sign changes and then increases tending to

Table 2
Quantitative methodology benchmark results for L1PMA and L2WPMA when Traditional and New Aspects are Applied for various Numbers of L1PMA Monotonic Sections and L2WPMA Sign Changes

Number of L1PMA Monotonic Sections / L2WPMA Sign Changes	**Measurement Differences (maximum value a_{CUD}=6dB)**	**Traditional Aspect**				**New Aspect**	
		L1PMA		**L2WPMA**		**L1PMA**	**L2WPMA**
	$APDmd$ (%)	**$APDta$ (%)**	**Reference Figure of [2]**	**$APDta$ (%)**	**Reference Figure of [2]**	**$APDna$ (%)**	**$APDna$ (%)**
1	68.63	38.48	Fig. 4(a)	111.58	Fig. 5(a)	40.19	118.94
2		45.98	Fig. 4(b)	99.64	Fig. 5(b)	44.01	106.67
3		57.67	Fig. 4(c)	51.58	Fig. 5(c)	55.63	45.94
4		58.17	Fig. 4(d)	39.54	Fig. 5(d)	55.95	39.37
5		62.04	Fig. 4(e)	39.54	Fig. 5(e)	59.57	39.37
6		69.46	Fig. 4(f)	46.25	Fig. 5(f)	68.06	39.69
7		69.51	Fig. 4(g)	46.25	Fig. 5(g)	68.11	39.69
8		71.46	Fig. 4(h)	55.15	Fig. 5(h)	70.94	46.72
9		71.46	Fig. 4(i)	55.15	Fig. 5(i)	70.94	46.72

a state of overapproximation. In contrast with L1PMA of the traditional aspect, L2WPMA tends to approximate the spectral notches of the coupling scheme transfer function data by avoiding the rough approximation of 1 monotonic section of L1PMA.

- As the application of L1PMA of the new aspect is concerned, its *APDna* behavior presents similarities with *APDta* of the L1PMA of the traditional aspect with respect to the number of monotonic sections. Indeed, the best *APDna* of the L1PMA of the new aspect is equal to 40.19% when one monotonic section is adopted. In all the numbers of monotonic sections examined, L1PMA of the new aspect presents better *APDna* than *APDta* of the L1PMA of the traditional aspect except the case of the one monotonic section. Anyway, L1PMA of the new aspect achieves to mitigate measurement differences of the maximum value a_{CUD} of 6dB even if 7 monotonic sections are assumed. Above 7 monotonic sections, its *APDna* exceeds *APDmd* (*i.e.*, black background cells of the seventh column of Table 2).
- As the application of L2WPMA of the new aspect is regarded, its best mitigation performance with *APDna* of 39.37% is observed when four or five sign changes are adopted that is the same number of sign changes of L2WPMA of the traditional aspect. Below 3 monotonic sections, its *APDna* exceeds *APDmd* (*i.e.*, black background cells of the eighth column of Table 2). For the monotonic sections that *APDna* is lower than *APDmd*, *APDna* of L2WPMA of the new

aspect always presents better values in comparison with *APDta* of L2WPMA of the traditional aspect.

Note that the numbers of 1 L1PMA monotonic section for both aspects and 5 L2WPMA sign changes for both aspects are going to be adopted in the following analysis. In accordance with [2], the aforementioned numbers can be treated as the basis for the respective piecewise monotonic data approximations regardless of the intensity of the measurement differences. In order to check the mitigation efficiency of L1PMA and L2WPMA of both aspects against different intensities of measurement differences, their performance is assessed through the quantitative methodology on the basis of respective iSHM footprints.

4.3 The Quantitative Methodology for L1PMA and L2WPMA iSHM Footprints of both Aspects when Different Intensities of Measurement Differences Occur

In accordance with Figs. 6 and 7 of [2], the mitigation performance of L1PMA and L2WPMA of the traditional aspect against the measurement differences has been visually proven to be important when measurement differences remain very high. Anyway, the promising results regarding the mitigation of higher measurement differences by L1PMA and L2WPMA of the traditional aspect was expected after the determination of respective monotonic sections and sign changes in Sec.3.3 of [2] for maximum value a_{CUD} of 6dB that is anyway sufficiently high. The aforementioned qualitative observations of [2] require the quantitative validation of this Section.

Unlike [2], in Table 3, APD metrics of: (i) the applied measurement differences of maximum values a_{CUD} that range from 0dB to 15dB for the real indicative OV LV BPL urban case A; and (ii) the results of the application of piecewise monotonic data approximations of both aspects; are here reported when the numbers of L1PMA monotonic sections and L2WPMA sign changes are equal to 1 and 5, respectively.

From Table 3, it is clear that the increasing maximum value a_{CUD} of CUD measurement differences entail significant increase of *APDmd*. Since L1PMA monotonic sections and L2WPMA sign changes have been defined when the relatively high measurement differences of Sec. 4.2 have been assumed, L1PMA and L2WPMA fail to mitigate the low measurement differences of maximum value a_{CUD} of 1dB and 2dB. Here, the philosophy of the adaptive monotonic sections and sign changes, which have been proposed in [10], [11], can also be applied in iSHM footprints so that even the low measurement differences of maximum value a_{CUD} of 1dB and 2dB can be mitigated by piecewise monotonic data approximations.

In contrast with the situation occurs during the study of the very low measurement differences, L1PMA and L2WPMA can safely mitigate measurement differences whose maximum value a_{CUD} remains higher than 2dB regardless of the aspect adopted. In fact, for the high measurement differences, L1PMA of the traditional aspect when one monotonic section is applied achieves the best *APDta* in comparison with the APD metrics of the other examined piecewise monotonic data approximations till approximately maximum values a_{CUD} of 10dB (cyan background cells of Table 3). For the very high measurement differences, L1PMA of the new aspect when one monotonic section is again applied starts to present the best *APDna* in comparison with the ones of the other examined piecewise monotonic data approximations. Anyway, the mitigation performance of all the examined piecewise monotonic data approximations mitigate measurement differences when maximum values a_{CUD} are greater than 2dB.

Table 3
Quantitative methodology benchmark results for L1PMA and L2WPMA when Traditional and New Aspects are Applied
(maximum value a_{CUD} ranges from 0dB to 15dB, numbers of L1PMA monotonic sections and L2WPMA sign changes are equal to 1 and 5, respectively)

Maximum Value a_{CUD} of Measurement Differences (dB)	**Measurement Differences**	**Traditional Aspect**		**New Aspect**	
		L1PMA	**L2WPMA**	**L1PMA**	**L2WPMA**
	$APDmd$ (%)	**$APDta$ (%)**	**$APDta$ (%)**	**$APDna$ (%)**	**$APDna$ (%)**
0	0	19.35	15.92	18.74	17.12
1	7.99	18.95	18.58	19.12	18.80
2	16.57	19.67	23.18	20.24	22.35
3	32.23	20.43	24.41	21.73	24.42
4	46.39	24.94	32.55	25.59	31.11
5	61.22	33.78	38.67	34.57	36.09
6	68.63	38.48	39.54	40.19	39.37
7	72.73	39.05	41.40	39.16	42.64
8	85.35	41.42	46.67	41.61	45.56
9	84.34	43.93	48.43	44.34	49.25
10	90.42	48.98	50.90	49.10	50.10
11	96.07	46.94	51.24	46.47	55.05
12	99.99	52.04	55.25	52.32	56.82
13	101.48	50.14	57.20	49.57	59.39
14	105.69	59.39	63.10	59.20	64.35
15	110.69	58.65	59.95	58.58	63.99

As L2WPMA is examined, mixed performance results occur between the traditional and new aspect. In general terms about L2WPMA, the traditional aspect is preferred when high measurement differences occur whereas the new aspect is used in the other cases.

Through the prism of the new quantitative methodology, it is evident that piecewise monotonic data approximations can easily mitigate measurement differences when piecewise monotonic data approximations are well calibrated in terms of their critical intrinsic parameters. Depending on the applied piecewise monotonic data approximations and the intensity of measurement differences as previously analyzed, the selection among the available piecewise monotonic data approximations and aspects changes.

5. Conclusions

After the proposal of the quantitative methodology of this companion paper, the reliability of BPL data that feed the business analytics and the tools of the SG is further enhanced. Towards the enhancement of the data quality and the data cleaning from the application of piecewise monotonic data approximations, such as L1PMA and

L2WPMA, the new aspect of applying piecewise monotonic data approximations can successfully mitigate measurement differences under conditions. With reference to iSHM footprints, it has been revealed that L1PMA and L2WPMA always mitigate measurements differences above a low threshold of 2dB while their performance becomes significant when measurement differences are important since the generated data of high measurement difference contamination are considered useless without a restoration. Finally, the interoperability of the qualitative and quantitative assessments of piecewise monotonic data approximations via iSHM footprints can be considered invaluable in order to ensure the data quality of the business analytics while the new aspects are added to the quiver of the available mitigation techniques against the measurement differences.

CONFLICTS OF INTEREST

The author declares that there is no conflict of interests regarding the publication of this paper.

References

[1] A. G. Lazaropoulos, "Business Analytics and IT in Smart Grid – Part 1: The Impact of Measurement Differences on the iSHM Class Map Footprints of Overhead Low-Voltage Broadband over Power Lines Topologies," *Trends in Renewable Energy*, vol. 6, no. 2, pp. 146-176, May 2020.

[2] A. G. Lazaropoulos, "Business Analytics and IT in Smart Grid – Part 2: The Qualitative Mitigation Impact of Piecewise Monotonic Data Approximations on the iSHM Class Map Footprints of Overhead Low-Voltage Broadband over Power Lines Topologies Contaminated by Measurement Differences," *Trends in Renewable Energy*, vol. 6, no. 2, pp. 177-203, May 2020.

[3] A. G. Lazaropoulos, "Factors Influencing Broadband Transmission Characteristics of Underground Low-Voltage Distribution Networks," *IET Commun.*, vol. 6, no. 17, pp. 2886-2893, Nov. 2012.

[4] A. G. Lazaropoulos, "Deployment Concepts for Overhead High Voltage Broadband over Power Lines Connections with Two-Hop Repeater System: Capacity Countermeasures against Aggravated Topologies and High Noise Environments," *Progress in Electromagnetics Research B*, vol. 44, pp. 283-307, 2012. [Online]. Available: http://www.jpier.org/PIERB/pierb44/13.12081104.pdf

[5] A. G. Lazaropoulos, "Broadband Performance Metrics and Regression Approximations of the New Coupling Schemes for Distribution Broadband over Power Lines (BPL) Networks," *Trends in Renewable Energy*, vol. 4, no. 1, pp. 43-73, Jan. 2018. [Online]. Available: http://futureenergysp.com/index.php/tre/article/view/59/pdf

[6] A. G. Lazaropoulos, "Wireless Sensor Network Design for Transmission Line Monitoring, Metering and Controlling Introducing Broadband over PowerLines-enhanced Network Model (BPLeNM)," *ISRN Power Engineering*, vol. 2014, Article ID 894628, 22 pages, 2014. doi:10.1155/2014/894628. [Online].

Available: http://www.hindawi.com/journals/isrn.power.engineering/2014/894628/

[7] A. G. Lazaropoulos, "Improvement of Power Systems Stability by Applying Topology Identification Methodology (TIM) and Fault and Instability Identification Methodology (FIIM)–Study of the Overhead Medium-Voltage Broadband over Power Lines (OV MV BPL) Networks Case," *Trends in Renewable Energy*, vol. 3, no. 2, pp. 102-128, Apr. 2017. [Online]. Available: http://futureenergysp.com/index.php/tre/article/view/34

[8] A. G. Lazaropoulos, "Smart Energy and Spectral Efficiency (SE) of Distribution Broadband over Power Lines (BPL) Networks – Part 1: The Impact of Measurement Differences on SE Metrics," *Trends in Renewable Energy*, vol. 4, no. 2, pp. 125-184, Aug. 2018. [Online]. Available: http://futureenergysp.com/index.php/tre/article/view/76/pdf

[9] A. G. Lazaropoulos, "Detection of Energy Theft in Overhead Low-Voltage Power Grids – The Hook Style Energy Theft in the Smart Grid Era," *Trends in Renewable Energy*, vol. 5, no. 1, pp. 12-46, Oct. 2018. [Online]. Available: http://futureenergysp.com/index.php/tre/article/view/81/pdf

[10] A. G. Lazaropoulos, "Power Systems Stability through Piecewise Monotonic Data Approximations – Part 1: Comparative Benchmarking of L1PMA, L2WPMA and L2CXCV in Overhead Medium-Voltage Broadband over Power Lines Networks," *Trends in Renewable Energy*, vol. 3, no. 1, pp. 2-32, Jan. 2017. [Online]. Available: http://futureenergysp.com/index.php/tre/article/view/29/34

[11] A. G. Lazaropoulos, "Power Systems Stability through Piecewise Monotonic Data Approximations – Part 2: Adaptive Number of Monotonic Sections and Performance of L1PMA, L2WPMA and L2CXCV in Overhead Medium-Voltage Broadband over Power Lines Networks," *Trends in Renewable Energy*, vol. 3, no. 1, pp. 33-60, Jan. 2017. [Online]. Available: http://futureenergysp.com/index.php/tre/article/view/30/35

[12] A. G. Lazaropoulos and P. G. Cottis, "Transmission characteristics of overhead medium voltage power line communication channels," *IEEE Trans. Power Del.*, vol. 24, no. 3, pp. 1164-1173, Jul. 2009.

[13] A. G. Lazaropoulos and P. G. Cottis, "Capacity of overhead medium voltage power line communication channels," *IEEE Trans. Power Del.*, vol. 25, no. 2, pp. 723-733, Apr. 2010.

[14] A. G. Lazaropoulos and P. G. Cottis, "Broadband transmission via underground medium-voltage power lines-Part I: transmission characteristics," *IEEE Trans. Power Del.*, vol. 25, no. 4, pp. 2414-2424, Oct. 2010.

[15] A. G. Lazaropoulos and P. G. Cottis, "Broadband transmission via underground medium-voltage power lines-Part II: capacity," *IEEE Trans. Power Del.*, vol. 25, no. 4, pp. 2425-2434, Oct. 2010.

[16] A. G. Lazaropoulos, "Broadband transmission and statistical performance properties of overhead high-voltage transmission networks," *Hindawi Journal of Computer Networks and Commun.*, 2012, article ID 875632, 2012. [Online]. Available: http://www.hindawi.com/journals/jcnc/aip/875632/

[17] A. G. Lazaropoulos, "Towards Modal Integration of Overhead and Underground Low-Voltage and Medium-Voltage Power Line Communication Channels in the Smart Grid Landscape: Model Expansion, Broadband Signal Transmission Characteristics, and Statistical Performance Metrics (Invited Paper)," *ISRN Signal*

Processing, vol. 2012, Article ID 121628, pp. 1-17, 2012. [Online]. Available: http://www.hindawi.com/isrn/sp/2012/121628/

[18] A. G. Lazaropoulos, "Statistical Broadband over Power Lines Channel Modeling – Part 1: The Theory of the Statistical Hybrid Model," *Progress in Electromagnetics Research C*, vol. 92, pp. 1-16, 2019. [Online]. Available: http://www.jpier.org/PIERC/pierc92/01.19012902.pdf

[19] A. G. Lazaropoulos, "Statistical Broadband over Power Lines (BPL) Channel Modeling – Part 2: The Numerical Results of the Statistical Hybrid Model," *Progress in Electromagnetics Research C*, vol. 92, pp. 17-30, 2019. [Online]. Available: http://www.jpier.org/PIERC/pierc92/02.19012903.pdf

[20] A. G. Lazaropoulos, "Enhancing the Statistical Hybrid Model Performance in Overhead and Underground Medium Voltage Broadband over Power Lines Channels by Adopting Empirical Channel Attenuation Statistical Distribution," *Trends in Renewable Energy*, vol. 5, no. 2, pp. 181-217, 2019. [Online]. Available: http://futureenergysp.com/index.php/tre/article/view/96/pdf

[21] A. G. Lazaropoulos, "Main Line Fault Localization Methodology in Smart Grid–Part 1: Extended TM2 Method for the Overhead Medium-Voltage Broadband over Power Lines Networks Case," *Trends in Renewable Energy*, vol. 3, no. 3, pp. 2-25, Dec. 2017. [Online]. Available: http://futureenergysp.com/index.php/tre/article/view/36

[22] A. G. Lazaropoulos, "Main Line Fault Localization Methodology in Smart Grid–Part 2: Extended TM2 Method, Measurement Differences and L1 Piecewise Monotonic Data Approximation for the Overhead Medium-Voltage Broadband over Power Lines Networks Case," *Trends in Renewable Energy*, vol. 3, no. 3, pp. 26-61, Dec. 2017. [Online]. Available: http://futureenergysp.com/index.php/tre/article/view/37

[23] A. G. Lazaropoulos, "Main Line Fault Localization Methodology in Smart Grid–Part 3: Main Line Fault Localization Methodology (MLFLM)," *Trends in Renewable Energy*, vol. 3, no. 3, pp. 62-81, Dec. 2017. [Online]. Available: http://futureenergysp.com/index.php/tre/article/view/38

[24] A. G. Lazaropoulos, "Main Line Fault Localization Methodology (MLFLM) in Smart Grid–The Underground Medium- and Low-Voltage Broadband over Power Lines Networks Case," *Trends in Renewable Energy*, vol. 4, no. 1, pp. 15-42, Dec. 2017. [Online]. Available: http://futureenergysp.com/index.php/tre/article/view/45

[25] A. G. Lazaropoulos, "Smart Energy and Spectral Efficiency (SE) of Distribution Broadband over Power Lines (BPL) Networks – Part 2: L1PMA, L2WPMA and L2CXCV for SE against Measurement Differences in Overhead Medium-Voltage BPL Networks," *Trends in Renewable Energy*, vol. 4, no. 2, pp. 185-212, Aug. 2018. [Online]. Available: http://futureenergysp.com/index.php/tre/article/view/77/pdf

[26] A. G. Lazaropoulos, "Measurement Differences, Faults and Instabilities in Intelligent Energy Systems – Part 2: Fault and Instability Prediction in Overhead High-Voltage Broadband over Power Lines Networks by Applying Fault and Instability Identification Methodology (FIIM)," *Trends in Renewable Energy*, vol. 2, no. 3, pp. 113-142, Oct. 2016. [Online]. Available: http://futureenergysp.com/index.php/tre/article/view/27/33

[27] A. G. Lazaropoulos, "Special Cases during the Detection of the Hook Style Energy Theft in Overhead Low-Voltage Power Grids through HS-DET Method – Part 1: High Measurement Differences, Very Long Hook Technique and "Smart" Hooks," *Trends in Renewable Energy*, vol. 5, no. 1, pp. 60-89, Jan. 2019. [Online]. Available: http://futureenergysp.com/index.php/tre/article/view/82/pdf

[28] A. G. Lazaropoulos, "Special Cases during the Detection of the Hook Style Energy Theft in Overhead Low-Voltage Power Grids through HS-DET Method – Part 2: Different Measurement Differences, Feint "Smart" Hooks and Hook Interconnection Issues," *Trends in Renewable Energy*, vol. 5, no. 1, pp. 90-116, Jan. 2019. [Online]. Available: http://futureenergysp.com/index.php/tre/article/view/83/pdf

[29] A. G. Lazaropoulos, "Underground Distribution BPL Connections with (N + 1)-hop Repeater Systems: A Novel Capacity Mitigation Technique," *Elsevier Computers and Electrical Engineering*, vol. 40, pp. 1813-1826, 2014.

[30] I. C. Demetriou, "An application of best *L*1 piecewise monotonic data approximation to signal restoration," *IAENG International Journal of Applied Mathematics*, vol. 53, no. 4, pp. 226-232, 2013.

[31] I. C. Demetriou, "L1PMA: A Fortran 77 Package for Best L1 Piecewise Monotonic Data Smoothing," *Computer Physics Communications*, vol. 151, no. 1, pp. 315-338, 2003.

[32] I. C. Demetriou, "A Decomposition Theorem for the Least Squares Piecewise Monotonic Data Approximation Problem," *Springer Approximation and Optimization*, pp. 119–134, 2019.

[33] I. C. Demetriou and M. J. D. Powell, "Least squares smoothing of univariate data to achieve piecewise monotonicity", *IMA Journal of Numerical Analysis*, vol. 11, no. 3, pp. 411-432, 1991.

[34] A. G. Lazaropoulos, "Statistical Channel Modeling of Overhead Low Voltage Broadband over Power Lines (OV LV BPL) Networks – Part 1: The Theory of Class Map Footprints of Real OV LV BPL Topologies, Branch Line Faults and Hook-Style Energy Thefts," *Trends in Renewable Energy*, vol. 6, no. 1, pp. 61-87, Mar. 2020. [Online]. Available: http://futureenergysp.com/index.php/tre/article/download/112/pdf

[35] A. G. Lazaropoulos, "New Coupling Schemes for Distribution Broadband over Power Lines (BPL) Networks," *Progress in Electromagnetics Research B*, vol. 71, pp. 39-54, 2016. [Online]. Available: http://www.jpier.org/PIERB/pierb71/02.16081503.pdf

[36] A. G. Lazaropoulos, "Virtual Indicative Broadband over Power Lines Topologies for Respective Subclasses by Adjusting Channel Attenuation Statistical Distribution Parameters of Statistical Hybrid Models – Part 2: Numerical Results for the Overhead and Underground Medium-Voltage Power Grids," *Trends in Renewable Energy*, vol. 5, no. 3, pp. 258-281, Aug. 2019. [Online]. Available: http://futureenergysp.com/index.php/tre/article/view/100/pdf

[37] A. G. Lazaropoulos, "Virtual Indicative Broadband over Power Lines Topologies for Respective Subclasses by Adjusting Channel Attenuation Statistical Distribution Parameters of Statistical Hybrid Models – Part 3: The Case of Overhead Transmission Power Grids," *Trends in Renewable Energy*, vol. 5, no. 3, pp. 282-306, Aug. 2019. [Online]. Available: http://futureenergysp.com/index.php/tre/article/view/101/pdf

[38] A. G. Lazaropoulos, "Statistical Channel Modeling of Overhead Low Voltage Broadband over Power Lines (OV LV BPL) Networks – Part 2: The Numerical Results of Class Map Footprints of Real OV LV BPL Topologies, Branch Line Faults and Hook Style Energy Thefts," *Trends in Renewable Energy*, vol. 6, no. 1, pp. 88-109, Mar. 2020. [Online]. Available: http://futureenergysp.com/index.php/tre/article/download/113/pdf

[39] A. G. Lazaropoulos, "Best L1 Piecewise Monotonic Data Approximation in Overhead and Underground Medium-Voltage and Low-Voltage Broadband over Power Lines Networks: Theoretical and Practical Transfer Function Determination," Hindawi Journal of Computational Engineering, vol. 2016, Article ID 6762390, 24 pages, 2016. doi:10.1155/2016/6762390. [Online]. Available: https://www.hindawi.com/journals/jcengi/2016/6762390/cta/

[40] A. G. Lazaropoulos, "Measurement Differences, Faults and Instabilities in Intelligent Energy Systems–Part 1: Identification of Overhead High-Voltage Broadband over Power Lines Network Topologies by Applying Topology Identification Methodology (TIM)," *Trends in Renewable Energy*, vol. 2, no. 3, pp. 85-112, Oct. 2016. [Online]. Available: http://futureenergysp.com/index.php/tre/article/view/26/32

CALL FOR PAPERS

Trends in Renewable Energy

ISSN Print: 2376-2136 ISSN online: 2376-2144
http://futureenergysp.com/index.php/tre/

Trends in Renewable Energy (TRE) is an open accessed, peer-reviewed semi-annual journal publishing reviews and research papers in the field of renewable energy technology and science. The aim of this journal is to provide a communication platform that is run exclusively by scientists. This journal publishes original papers including but not limited to the following fields:

- Renewable energy technologies
- Catalysis for energy generation, Green chemistry, Green energy
- Bioenergy: Biofuel, Biomass, Biorefinery, Bioprocessing, Feedstock utilization, Biological waste treatment,
- Energy issues: Energy conservation, Energy delivery, Energy resources, Energy storage, Energy transformation, Smart Grid
- Environmental issues: Environmental impacts, Pollution
- Bioproducts
- Policy, etc.

We publish the following article types: peer-reviewed reviews, mini-reviews, technical notes, short-form research papers, and original research papers.

The article processing charge (APC), also known as a publication fee, is fully waived for the Trends in Renewable Energy.

Call for Editorial Board Members

We are seeking scholars active in a field of renewable energy interested in serving as volunteer Editorial Board Members.

Qualifications

Ph.D. degree in related areas, or Master's degree with a minimum of 5 years of experience. All members must have a strong record of publications or other proofs to show activities in the energy related field.

If you are interested in serving on the editorial board, please email CV to editor@futureenergysp.com.